Apatite-Protein Nanocomposites- From Biological to Biomimetic Materials

Dissertation zur Erlangung des

akademischen Grades eines Doktors der Naturwissenschaften

(Doctor rerum naturalium)

vorgelegt von

Knaus, Jennifer

an der

Mathematisch-Naturwissenschaftliche Sektion

Fachbereich Chemie

Konstanz, 2018

Tag der mündlichen Prüfung: 22.03.2019
1. Referentin: Dr. Elena Sturm
2. Referent: Prof. Dr. Stefan Mecking
3. Referent: Prof. Dr. Alexander Wittemann

Zusammenfassung

Die Natur hat im Laufe der Evolution eine große Bandbreite komplexer Materialien hervorgebracht, welche sehr gut an ihre Funktion angepasst sind. Die Zähne von Buntbarschen der Großen Seen Ostafrikas liefern ein gutes Model, wie Vertebraten dentale Hartmaterialien für spezialisierte Anwendungen, wie beispielsweise der Prozessierung von harter und weicher Nahrung, optimieren. Der erste Teil dieser Dissertation widmet sich der detaillierten Untersuchung der Beziehung zwischen Zusammensetzung und Eigenschaften von Zähnen des unteren Schlundkiefers unterschiedlicher Buntbarscharten, welche sich auf verschiedene Nahrungsarten spezialisiert haben. Hierbei konnten Zusammenhänge zwischen variierenden Konzentrationen von Fluor-substitutierten Hydroxylapatit mit unterschiedlichen Härten und Elastizitätsmodi hergestellt werden. Des Weiteren wurde festgestellt, dass amorphe, eisenhaltige Phasen zur Härte des resultieren Materials beitragen. Auf Basis beobachteter Ähnlichkeiten des inneren Aufbaus wurde ein einheitliches Strukturmodell erstellt, in welchem unterschiedliche Hierarchieebenen identifiziert werden konnten. Innerhalb dieses komplexen Aufbaus wurden intrinsische und extrinsische Bruchresistenzstrategien, die einen Komplettbruch des Zahnes verhindern sollen, identifiziert. Die Kombination dieses komplexen strukturellen Arrangements in Kombination mit einer spezifischen Variation der mechanischen Eigenschaften erlaubt diesen Fischen eine optimale Prozessierung ihrer Nahrung. Fischspezies, welche sich von harter Nahrung ernähren verwenden hierbei eine andere Strategie als Fische, welche sich von weicher Nahrung ernähren. Erstere verwenden molariforme Zähne, in welchem die mechanischen Eigenschaften in einem stufenförmigen Profil variieren, wohingegen letztere in papilliformen Zähnen einen linearen Gradienten verwenden.

Biomimetische Synthesen von organisch-anorganischen Hybridmaterialien unter kontrollierten Mineralisationsbedingungen sind ein wichtiger Baustein für ein vertiefendes Verständnis der Grundprinzipien der Biomineralisation und essentiell für die Entwicklung neuer bioinspirierter Materialien. Der zweite Teil dieser Arbeit führte daher vorangegangene Untersuchungen der Prinzipien zur Bildung von komplexen Kompositen anhand von biomimetischen Fluorapatit-Gelatine Kompositen fort. Ein wichtiger kationischer Substituent im Apatit-Kristallgitter ist Sr^{2+} in kristallografischen Positionen von Ca^{2+}. Man findet solche Sr^{2+}-Substitutionen in biologischen Hartmaterialien oder in geologischen Apatiten. Es wurde gezeigt, dass Sr^{2+}-Ionen sowohl *in vitro* als auch *in vivo* Knochenzellen konzentrationsabhängig stimulieren. Daher wurde in diesem Teil der Arbeit der Einfluss von Sr^{2+}-Ionen auf die Morphogenese, die Struktur, die physico-chemischen Eigenschaften als auch auf die Zusammensetzung von Fluorapatit-Gelatine Kompositmaterialien untersucht. Hierbei konnte gezeigt werden, dass die Gitterparameter *a* und *c* von isomorph substituierten Kompositen linear mit der Sr^{2+}-Konzentration steigt. Die Schwingungsmoden der Apatit-Komponenten in IR-

und Raman-Spektren zeigten eine Verschiebung zu kleineren Wellenzahlen im Vergleich zum nichtsubstituierten Fluorapatit. Thermogravimetrische Untersuchungen bestätigten den Kompositcharakter der synthetisierten Materialien. Anhand einer chemischen Analyse konnte eine empirische Formel für die Sr^{2+}-substitutierten Komposite erstellt werden. Des Weiteren wurden das Wachstumsverhalten und die Morphologie der Aggregate untersucht. Hierbei wurde ein stark anisotropes Wachstumsverhalten der Apatit-Untereinheiten beobachtet, welches sich in dünnen, stark verlängerten, nadelförmigen Apatit-Prismen darstellt. Das Wachstum der Aggregate selber verläuft über verlängerte stäbchenförmige Aggregate, welche sich über diverse hantelförmige Zwischenstufen zu einer geschlossenen Sphäre verlaufen.

In einem weiteren Teil dieser Arbeit wurden vertiefende Untersuchungen zu einer biomimetischen, Poly(etheretherketon) (PEEK)-Beschichtung durchgeführt. Diese Beschichtung basiert auf einem kovalent an die Oberfläche gebundenen Kalziumphosphat-Gelatine-Kompositmaterial. Durch XPS- XRD- und TGA-Untersuchungen konnte der knochenähnliche Kompositcharakter der Beschichtung gezeigt werden. Untersuchungen zur mechanischen Stabilität der Beschichtung haben eine gute Beständigkeit auf der Oberfläche gezeigt. Weiterführend wurden Untersuchungen zur *in vitro* Biokompatibilität für Knochenimplantatanwendungen durchgeführt. Die Kompatibilität wurde an Fibroblasten und Osteoblasten getestet, welche zwei Beispiele derer Zelltypen repräsentieren, mit welchem ein Knochenimplantat im menschlichen Körper direkt in Kontakt kommt. Hierbei konnte gezeigt werden, dass keinerlei toxische Substanzen aus dem Material gelöst werden und auch keine Kontakttoxizität existiert. Des Weiteren konnte über Adhäsions-, Viabilitäts-, und Proliferationstests eine gute Verträglichkeit des beschichteten PEEK-Materials auf die untersuchten Zelltypen bestätigt werden.

Summary

Over the course of evolution, nature has created an astonishing array of complex, functional biomaterials, which are well adapted to their respective applications. The teeth of cichlid fishes of the Great Lakes of East Africa provide a good model of how vertebrates optimize dental hard tissues for specialized ecological applications, such as processing hard or soft food. The first part of this thesis was focused on the detailed comparative investigation of the morphology-structure-chemical composition-mechanical properties relationships of the teeth of the lower pharyngeal jaws of different cichlid fish species. Varying levels of the concentration and distribution of fluoridated hydroxyapatite as the mineral component could be associated with pronounced variations in the hardness and elastic modulus of dental hard tissues.Furthermore, amorphous iron-bearing phases were found, which contribute to the hardness of the resulting material. On the basis of general similarities of the inner structure of all investigated teeth, a structure model with corresponding hierarchical levels was created. Within this complex arrangement, several intrinsic and extrinsic toughening mechanisms on multiple length scales to enhance fracture resistance against critical failure were identified. The combination of this complex structural arrangement together with specific variations of the mechanical properties within dental hard tissues of their teeth allows cichlids for optimal processing of their food. Herein, the hard diet eating species utilize a complex multilevel and multilayered structuring (incl. variation of mineralization degree) of enameloid which is reflected by a pronounced, stepwise gradient (profile) in their mechanical properties. Thus the structure of enameloid of “snail-crushing” species is optimized to significantly enhance the fracture resistance and mechanical stability of the teeth. The teeth of soft diet eating species, on the other hand, do not show this pronounced structuration in enameloid (incl. in general lower degree of mineralization) and employ a nearly linear decrease of mechanical properties from the outer part of the enameloid to dentine junction and thus specialize on grabbing of prey.

The biomimetic synthesis of organic-inorganic hybrid materials under controlled mineralization conditions is very important for the deeper understanding of the principles of biomineralization. The second part of this thesis continued previous investigations on biomimetic fluorapatite-gelatine composites on the basic principles of the formation of complex composites. One important cationic substitution in the apatite crystal structure is the Sr^{2+} in the crystallographic positions of Ca^{2+}. Such substitutions were found in natural hard tissues as well as geological apatites. In medical literature, it has been demonstrated *in vitro* and *in vivo* that the incorporation of Sr^{2+} showed a significant increase in bone cell stimulation and differentiation in a dose-dependent manner. Thus this part of the thesis was focused on investigating the influence of Sr^{2+} ions on the morphogenesis, structure, physicochemical properties and chemical composition of synthesized fluorapatite-gelatine composites. It was shown that the

lattice parameters *a* and *c* of the isomorphic substituted apatite increase monotonically with increasing strontium content. The peaks in the IR and the Raman spectra of the phosphate groups of the higher substituted apatite-gelatine composites were slightly shifted to a lower wavenumber with respect to the pure calcium fluorapatite-gelatine composites. TG-analysis confirmed that the synthesized materials have an organic-inorganic composite character, with an average gelatine content between 3-5 wt-%. Based on the chemical analysis, the empirical crystal chemical formula of the Sr^{2+}-substituted fluorapatite-gelatine composites was determined. It was shown, that the incorporation of strontium into the apatite significantly affects the morphogenesis and morphology of apatite-gelatine composite aggregates. Specifically, an increase in the anisotropy of crystal growth along *c*-axis of apatite was observed. The growth, in general, starts with an elongated rod-like aggregate (slightly distorted hexagonal prism), developing via different dumbbell shapes towards a notched sphere. Herein, it was observed that the incorporation of Sr^{2+}-ions into the apatite structure promotes branching processes already in the very early stages of morphogenesis.

The next part of this thesis continued the investigations of the characterization of a covalently bound, biomimetic calcium phosphate-gelatine composite coating on the surface of Poly(ether ether ketone) bone-implant materials. Through XPS-, XRD- and TGA-investigations, it was shown that the surface displays the general compositional characteristics of bone. The coating showed promising water contact angles and a good surface free energy for a successful bone implant. A test of the mechanical stability of the coating on the surface demonstrated reasonable stability. Furthermore, the general biocompatibility was verified using two different cell lines, fibroblasts, and osteoblasts. The fibroblasts and osteoblasts used in this study represent examples of the types of cells which bone implants will be in contact with during clinical use. Indirect and direct toxicity-assays revealed that no toxic substances were extracted from the material and no contact toxicity exists. Furthermore, viability-, adhesion- and proliferation-assays demonstrated an increase in biocompatibility of the bone-like coating in comparison with pure, non-modified PEEK.

Acknowledgments

First and foremost, I would like to express my sincere gratitude to my supervisor Prof. Dr. Helmut Cölfen, for his great support and guidance during the last years. I am very thankful that he always has an open ear for my problems and an open mind for new ideas.

I would also like to express my gratitude to my co-supervisor Dr. Elena Sturm. I learned a lot from her over the last years and greatly benefited from her guidance and scientific insights into various areas of the natural sciences.

I would also like to thank my committee members Prof. Dr. Stefan Mecking and Dr. Claudius Kratochwil for the good advice and contributions over the last years.

I also want to thank Dr. Ralf Schneider for the specimen and sample preparation and help with the fluorescence microscopy, as well as his patience when explaining the complex interrelationships of evolutionary biology in simple terms.

Further acknowledgment is addressed to Dr. Davide Carnelli, Dr. Diana Courty at the ETH Zürich for performing the nanoindentation measurements and for the good collaboration throughout the last years.

In this context, I would also like to thank Jana Segmehl and Kirstin Casdorff of the ETH Zürich for performing the confocal Raman microscopy and for their help with the data evaluation.

Furthermore, I would like to thank Dr. Baohu Wu, who was carrying out the WAXS and SAXS measurements and for his advice in the data analysis. In this context, I would like to thank Dr. Damien Faivre for kindly providing the beamtime slot.

I want to thank Tamara Schuhmacher for performing the in-vitro toxicity assays and some proliferation assay as well as her advice on all things cell culture related. I want to especially thank her for her support and for being such a good friend.

Also, I would like to thank Dr. Gudrun Auffermann at the Max-Planck-Institut für Chemische Physik fester Stoffe in Dresden for performing the ICP-OES measurements.

Also, I would like to thank Dr. Song Chen of the University of Konstanz and Dr. Sebastian Sturm at the Leibniz-Institut für Festkörper- und Werkstoffforschung in Dresden for performing several electron microscopic investigations.

Further acknowledgment is addressed to Britta Kerndl from the University of Konstanz for her assistance in the Raman spectroscopy measurements of the Sr-substituted fluorapatite-gelatine composites. Furthermore, I would like to thank Dr. Philipp Erler at the University of Konstanz for his help with the XPS measurements.

I would especially like to thank the technical staff of the University of Konstanz, especially Dr. Jochen Hentschel and Dr. Michael Laumann of the Electron Microscopy Center for introducing me to the SEM. Furthermore, I would like to thank Dr. Marina Krumova for introducing me to the AFM, TEM and microtomy technique. Furthermore, I would like to thank Matthias Hagner for preparing FIB thin cuts.
At this point I would like to especially thank all people, who corrected various parts of this dissertation, that is Dr. Elena Sturm, Dr. Song Chen, Holger Reiner, Dominik Gruber, Julian Konsek, Tamara Schuhmacher, Dr. Liangfei Tian and Maria Enders.

And of course, I would like to thank all my colleagues in the Cölfen group who made these last years such a pleasant and special time for me. Thank you all for the nice time we shared.

Words can hardly express how deeply thankful I am to my parents and my family for their love, their encouraging support and for giving me the strength to reach my goals.

Table of Contents

Chapter I General Introduction

1. Bioinspired materials

Living organisms produce inorganic-organic nanocomposite in the form of hierarchically organized biominerals, acting as functional materials. The underlying structures of these materials we observe in nature reflect good solutions for specific challenges and specialized applications, which resulted from a long adaptation process during the course of evolution. We are starting to develop a systematic understanding of several characteristics, which contribute to the exceptional mechanical performance of several biomaterials, such as a sophisticated hierarchical structure on multiple length scales, special chemical compositions and intricate distributions of these components within the material. However, we have to keep in mind that we do not know a multitude of boundary conditions in nature which are important for the development of the structures we observe.[1] We do not know if the results of adaptations are mainly to provide strong and tough materials or if it is also to solve some quite different biological problem as well or if the adaptation is the result of other unknown factors.[2] Thus, it is important to carefully study the biological systems to understand the formation process and structure-function relationships of the materials in the context of its physical and biological constraints. This knowledge can give us a better understanding to optimize synthesis parameters and design principles to solve a broad range of technical challenges. Several of such design principles have already been abstracted and applied in architecture[3], hydrodynamics[4], aerodynamics[5, 6], mechanical engineering[7-9], as well as in materials science[10] and regenerative medicine[11]. Herein a wide variety of material processing methods to mimic the properties and design principles of their natural counterparts have been developed. Herein, a broad range of methods, such as layer-by-layer deposition[12-14], electrospinning[15-17], freeze-casting/ice templating[18, 19], nanolithography[20] and 3D-printing [21-24] have been reported in the last several years.

The main components of biological hard tissues of vertebrates, such as bone and teeth, are apatite-protein nanocomposites. Over the course of evolution, nature has optimized these materials through natural selection to their respective function within the organism. In view of a high demand of bone and joint substitution materials[25, 26] and high requirements in the properties of such materials for the repair of bone and teeth defects[26, 27], these two biological hard tissues have long since been the focus of intensive research to get a better understanding of the basic principles of their formation, their material design and properties. The main inorganic component of these hard tissues of most vertebrates consists of calcium orthophosphates in the form of non-stoichiometric hydroxyapatite, that is associated with different cationic and anionic substitutions in the crystal structure.[28] The mineralization of bone and dentine itself occurs under the control of an organic matrix, which mostly contains collagenic proteins.[28, 29]

1.1 Calcium orthophosphates

Up to now, 13 non-ion substituted calcium orthophosphates are known. They and their major properties are summarized in Table 1. Only the calcium orthophosphates, which are relevant for this thesis will be described further in the following paragraphs.

Table 1: Existing calcium orthophosphates and their major properties.[30]

Ca/P molar ratio	Compound	Formula	Solubility at 25°C, -log(K_s)	Solubility at 25°C, g/L	pH stability range in aqueous solutions at 25°C
0.5	Monocalcium phosphate monohydrate (MCPM)	$Ca(H_2PO_4)_2{\cdot}H_2O$	1.14	~18	0.0–2.0
0.5	Monocalcium phosphate anhydrous (MCPA or MCP)	$Ca(H_2PO_4)_2$	1.14	~17	[c]
1.0	Dicalcium phosphate dihydrate (DCPD), mineral brushite	$CaHPO_4{\cdot}2H_2O$	6.59	~0.088	2.0–6.0
1.0	Dicalcium phosphate anhydrous (DCPA or DCP), mineral monetite	$CaHPO_4$	6.90	~0.048	[c]
1.33	Octacalcium phosphate (OCP)	$Ca_8(HPO_4)_2(PO_4)_4{\cdot}5H_2O$	96.6	~0.0081	5.5–7.0
1.5	α-Tricalcium phosphate (α-TCP)	$\alpha\text{-}Ca_3(PO_4)_2$	25.5	~0.0025	[a]
1.5	β-Tricalcium phosphate (β-TCP)	$\beta\text{-}Ca_3(PO_4)_2$	28.9	~0.0005	[a]
1.2–2.2	Amorphous calcium phosphates (ACP)	$Ca_xH_y(PO_4)_z{\cdot}nH_2O$, n = 3 - 4.5; 15 - 20% H_2O	[b]	[b]	~5–12[d]
1.5–1.67	Calcium-deficient hydroxyapatite (CDHA or Ca-def HA)[e]	$Ca_{10-x}(HPO_4)_x(PO_4)_{6-x}(OH)_{2-x}$ ($0 < x < 1$)	~85	~0.0094	6.5–9.5
1.67	Hydroxyapatite (HA, HAp or OHAp)	$Ca_{10}(PO_4)_6(OH)_2$	116.8	~0.0003	9.5–12
1.67	Fluorapatite (FA or FAp)	$Ca_{10}(PO_4)_6F_2$	120.0	~0.0002	7–12
1.67	Oxyapatite (OA, OAp or OXA)[f]	$Ca_{10}(PO_4)_6O$	~69	~0.087	[a]
2.0	Tetracalcium phosphate (TTCP or TetCP), mineral hilgenstockite	$Ca_4(PO_4)_2O$	38–44	~0.0007	[a]

[a]These compounds cannot be precipitated from aqueous solutions. [b]Cannot be measured precisely. However, the following values were found: 25.7 ± 0.1 (pH = 7.40), 29.9 ± 0.1 (pH = 6.00), 32.7 ± 0.1 (pH = 5.28). The comparative extent of dissolution in acidic buffer is: ACP >> α-TCP >> β-TCP > CDHA >> HA > FA. [c]Stable at temperatures above 100°C. [d]Always metastable. [e]Occasionally, it is called “precipitated HA (PHA).” [f]Existence of OA remains questionable.

The major component of apatite-based hard tissues, such as bone at teeth is the mineral phase in the form of hydroxyapatite. The chemical stoichiometric formula of hydroxyapatite is $Ca_{10}(PO_4)_6(OH)_2$ with a Ca/P-ratio of 1.67:1. However, biological hydroxyapatite never occurs in pure stoichiometric form and is usually associated with ionic substitutions within its crystal structure. The ions in apatites can be readily substituted with other ions and groups, e.g., Ca^{2+} = Sr^{2+}, Na^+, K^+, Mg^{2+} or OH- = F^-, CO_3^{2-} or PO_4^{2-} = CO_3^{2-} (see Table 2).[31]

Table 2: Composition of the inorganic phase of adult-human calcified tissues.[a][31]

Composition [wt-%]	Enamel	Dentine	Bone
Calcium[b]	36.5	35.1	34.8
Phosphorous[b]	17.7	16.9	15.2
Carbonate (as CO_3^{2-})[c]	3.5	5.6	7.4
Sodium[b]	0.5	0.6	0.90
Magnesium[b]	0.44	1.23	0.72
Fluoride[b]	0.01	0.01	0.03
Chloride[b]	0.3	0.06	0.13
Potassium[b]	0.08	0.05	0.03
Total inorganic[c]	97	70	65
Total organic[c]	1.5	20	25
Water[c]	1.5	10	10

[a] Because of the considerable variation found in biological samples, typical values are given in these cases. [b] Ashed samples. [c] Unashed samples

Calcium hydroxyapatite can crystallize in the hexagonal space group $P6_3/m$ and the monoclinic space group $P2_1/b$. The most common form of hydroxyapatite is hexagonal, having the space group symmetry $P6_3/m$, with the lattice parameters of $a = b =$ 9.422 Å and c = 6.883 Å.[32] Figure 1 displays the crystal structure of the hexagonal calcium hydroxyapatite as an ideal example for biological apatites. The unit cell of stochiometric crystalline hydroxyapatite is characterized by two types of crystallographic Ca-positions. Four calcium ions per unit cell are at the so-called CaI-position, which are positioned in columns along the c- axis and are coordinated by 9 oxygen atoms of the phosphate groups. CaII-atoms build equilateral triangles, which are rotated by 60° in a six-fold c-axis at z= 1/4 and 3/4. They build the so-called anion channel, which is mostly occupied by monovalent ions (e.g., OH^- in the hydroxyapatite).[32]

Stoichiometric hydroxyapatite can also occur in the monoclinic space group $P2_1/b$. The unit cell parameters are a = 9.42 Å, b=2a, c = 6.881 Å and γ= 120°.[32] The major difference between the monoclinic hydroxyapatite and the hexagonal hydroxyapatite is the ordering of the hydroxyl-groups. Theoretical and experimental data of stoichiometric hydroxyapatite showed that in the monoclinic hydroxyapatite, the OH^- ions are ordered in the same direction in the channel, and the direction is reversed in the next channel.[33] In the hexagonal form, the OH^- ions are not ordered in the channels, which can be statistically represented as a twofold disorder of the positions above mirror planes, which become glide planes in the monoclinic form.[34] These structural differences can have several implications on the physico-chemical properties of the material.[32] It is predicted that the dissolution kinetics, as well as dielectric properties, will differ for apatites with hexagonal and monoclinic crystal structure.[32, 35]

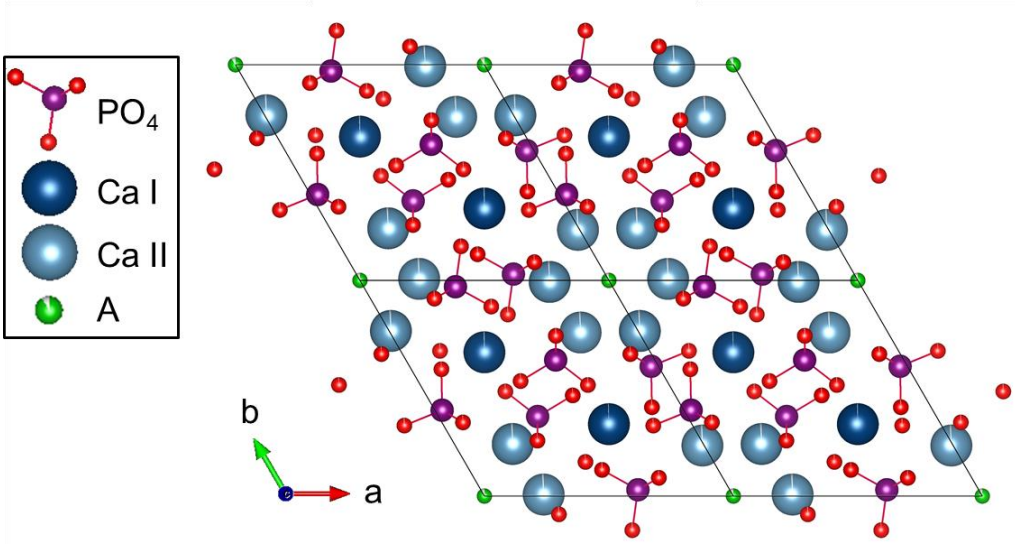

Figure 1: Crystal structure of calcium apatite space group. A: anion-channel: e.g., OH^-, F^-, Cl^-. Image created with the VESTA software package (Vers.3.4.0).

One important ionic substitute in biological apatite is fluoride. The chemical formula of pure fluorapatite is $Ca_{10}(PO_4)_6F_2$. Hydroxyapatite can be gradually substituted by fluoride, thus the formula can also be described by $Ca_{10}(PO_4)_6(OH)_{2-x}F_x$ ($0<x<2$).[36, 37] The structures of hydroxyapatite and fluorapatite are very similar. Fluorapatite occurs in the hexagonal space group $P6_3/m$ with lattice parameters $a = b = 9.367$ Å and $c = 6.884$ Å.[32] Fluorapatite has a lower solubility product than hydroxyapatite and thus is more stable, especially in acidic milieus. Hard tissues of vertebrates contain only low concentrations of fluoride (less than 0.3 wt-%).[38-45] Higher concentrations of fluoride can be found in the dental enameloids of some fishes.[46-50] The role of the fluoride ions during biological mineralization of dental or dental-like hard tissues is not yet clearly understood. In synthetic systems, material properties such as solubility can be fine-tuned by the amount of incorporated fluoride.[51] It is well known that the presence of fluoride in the apatite component decreases its reactivity and its dissolution behavior and increases the hardness of the material.[52, 53]

Another important substitute in biological hard tissues is carbonate. It is well known that biological apatites in hard tissues contain a variable amount of carbonate, which is a significant substituent in the crystal structure. Human enamel usually contains about from 1 to 9 wt-% of carbonate in the hydroxyapatite structure.[39, 54-56] It is also well known that the incorporation of carbonate into the apatite crystal structure have drastic effects on the material properties, including dissolution behavior, which is important for the process of de- and remineralization of biological hard tissues.[39, 54, 57, 58] Depending on the amount and type of the carbonate substitution in the apatite crystal structure, the lattice parameters can undergo different changes. In case of an A-type substitution the *a*-parameter increases, whereas the *c*-parameter decreases, while for B-type substitution the changes are vice versa. Consequently, carbonate ions can also influence the crystal shape and size during the growth process. The effect of carbonate on physicochemical parameters and crystal morphologies has

been studied in a synthetic system of B-type substituted carbonated fluorapatite-gelatine composites, which were grown in a double diffusion setup.[59] Herein it was reported that with increasing carbonate content, the fluorapatite-gelatine composite species (crystals and aggregates) become generally smaller and more rounded. Furthermore, the size of coherence scattering domains decreases (along [001]).

1.2 Collagen and gelatine

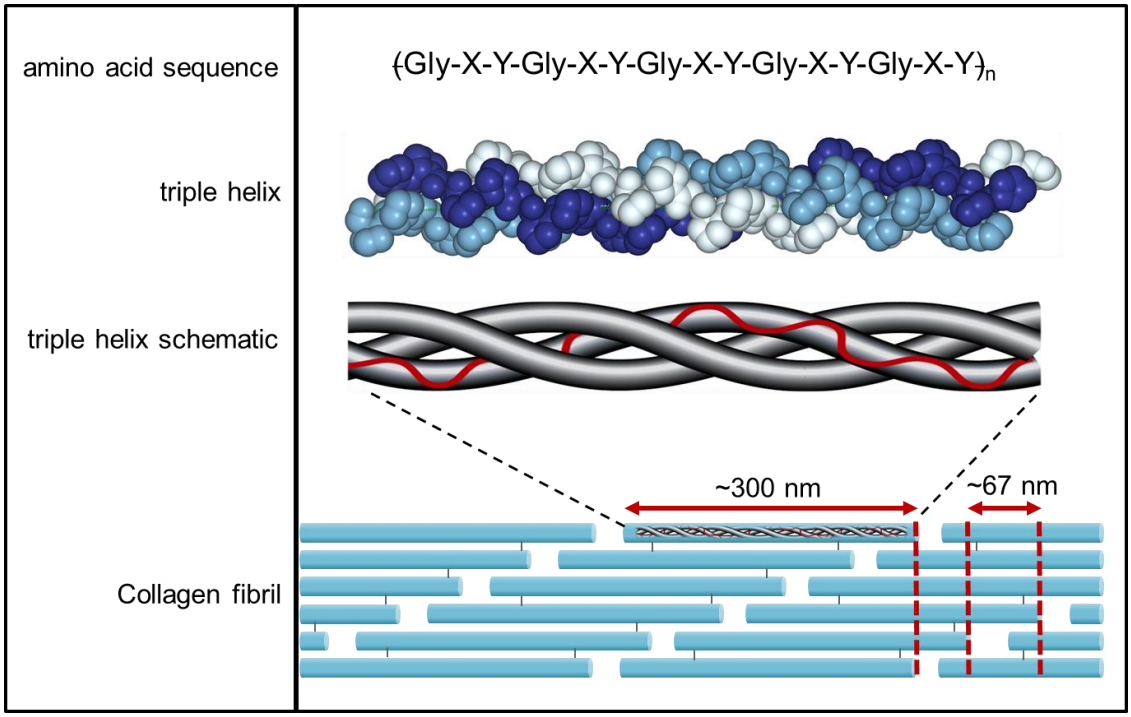

Figure 2: Side view of the structure of a polypeptide fragment, whose sequence was based on the repeating units of $(Gly\text{-}X\text{-}Y)_n$ with 9 repeating units within each chain. Herein proline frequently occurs in the X-position and hydroxyproline almost always in the Y-position The triple helix was modeled using the crystal structure data (PDB ID: 2CUO [60]) using the NGL Viewer software package.[61, 62]

Collagens are a group of ubiquitous proteins, making up about 25 - 35 % of the whole-body protein content.[63] 28 different types of collagen have been identified, of which type I collagen accounts for more than 90 % of the total amount within vertebrates.[63] Among others, Collagen type I has the ability to self-assemble into a fibrillar structure (see Figure 2).[64, 65] Typically, collagen has a uniform right-handed triple-helical conformation which generally consists of two identical polypeptide chains (α_1), comprising about 334 repetitive units of a $(Gly\text{-}X\text{-}Y)_n$ amino acid sequence and an additional chain (α_2) that differs slightly in its chemical composition.[65] This composition differs, depending on the type and origin of the collagen. Each alpha chain is coiled into a left-handed helix with about three amino acids per turn, which is mostly stabilized through hydrogen bonding.[64, 66] Proline frequently occurs in the X-position and hydroxyproline almost always in the Y-position of the $(Gly\text{-}X\text{-}Y)_n$ sequence pattern.[67] These collagen fibers are about 300 nm in length and 1.5 nm in diameter.[68] By lateral aggregation, the collagen triple-helices can form tough micron-sized collagen fibrils. In these fibrils, adjacent collagen molecules are displaced from one an-

other by about 67 nm. This staggered array causes a cross-striated effect, which can be observed by both light and electron microscopy. Covalent crosslinks are formed between hydroxylysine-residues, which further stabilize the collagen fibers and provide tensile strength.[64, 69]

Gelatine is a biopolymer, which is derived from collagen. It is obtained by physical/chemical degradation or thermal denaturation of native collagen.[70] In the manufacturing of gelatine, treatment of collagen with diluted acid or base results in a partial cleavage of the crosslinks of the collagen fibers, creating different types of collagen fragments. Depending on the method, this process usually takes a few days up to several weeks. This chemical hydrolysis can be supplemented or even replaced by the use of enzymes.[67, 70] The molecular weight fractions of alkaline-conditioned gelatine (so-called Type B-gelatine), is in the range of 100 000 g/mol and is usually derived from more complex collagen, e.g., collagen from bovine hides. Acid–conditioned gelatine (so-called Type A-gelatine) does not have a pronounced peak of its molecular weight, but a broader weight-distribution and is typically derived from less crosslinked collagen, e.g., pig skin collagen. After these pretreatments, the purified collagen is converted into gelatine in a multi-step process by extraction by either water or acid solutions at appropriate degradation temperatures of gelatine.[70] Unlike collagen, gelatine is thus soluble at a physiological pH and melts at a sol-gel transition temperature between 25°C and 30°C. Upon cooling transparent gels are formed.[70] It is completely resorbable *in vivo,* and its physicochemical properties can be suitably adjusted to the intended applications. Furthermore, gelatine is much cheaper and easier to obtain concentrated solutions in comparison to collagen.

2. Scope of this Thesis

The first part of this thesis addresses the comparative investigation of the structure-chemical composition-properties of dental hard tissues of cichlids. Cichlid fishes are textbook examples of explosive speciation, evolving stunning behavioral and morphological specializations. Studying the teeth of these cichlid fishes can provide further knowledge of the underlying mechanisms and structures for the optimization of dental hard tissues for specific ecologically relevant tasks. By studying the teeth of such different convergently evolved tooth phenotypes, we also aim to investigate whether this convergence is also reflected in the teeth's inner structure and composition. Such investigations give further insights on whether specific species differences that orchestrate bio-mineral and organic matrix deposition and hierarchical structuring might be the cause for differences in specialized food adaptations. This would argue for the central importance of regulatory evolution in rapidly evolving lineages, such as the East African cichlids.

The second part of this thesis continues previous investigations on biomimetic fluorapatite-gelatine composites of the basic principles of the formation of complex composites. The *in vivo* production of the biological hard tissues is a highly complex process, resulting in equally complex hierarchical materials. All general biological influences, such as metabolic and cellular activities during hard tissue formation are only poorly understood. To get further insight into the basic principles of biomineralization, it is thus imperative to reduce the level of complexity of the investigated system. A promising experiment to mimic the processes in bone or tooth formation is the growth of fluorapatite in gelatine matrices with a double diffusion setup. By using this approach for biomimetic synthesis, the imitation of several special building mechanisms of biological systems will be accessible. We can thus obtain composites that are ordered from the nanometer to the mesoscopic length scale and closely resemble their natural counterparts. Furthermore, these materials are attractive candidates for the development of biomimetic materials with improved functionality for possible biomedical application in hard tissue repair. To enhance the general biological performance of such apatite-based materials, the apatite is often subjected to isomorphic ionic substitutions. The investigation within this work focused on the influence of Sr^{2+} ions on the morphogenesis, structure and chemical composition of synthesized fluorapatite-gelatine composites.

The third part of this thesis continues previous investigations on the material characterization of the covalently linked, bone-like coating on the surface of Poly(ether ether ketone) (PEEK) bone-implant material. PEEK has many excellent mechanical and chemical properties, such as radiolucency and a stiffness similar to bone, making it an attractive candidate for orthopedic, trauma and spinal implants. However, its inherent bioinertness often prevents the successful ingrowth of an implant into the surrounding bone tissue. The general aim of this project was the surface functionalization and characterization of PEEK implant materials to combine the excellent bulk properties of PEEK with characteristic properties from the mineralized bone tissue. Based on the previous work, further characterization of the surface coating and an assessment of the general in vitro biocompatibility of the modified material in comparison to the non-modified version in bone implant applications was to be performed.

Chapter II Comparative Investigation of Composition-Structure-Properties Relationships of Teeth of Cichlids

1. Introduction

1.1 Cichlids

Cichlids are tropical freshwater fishes that belong to the teleost fishes, which belong to the family of Cichlidae. With an estimated number of more than 3000, they are one of the most species-rich families of all vertebrates.[71] Due to this exceptional diversity and explosive speciation, which developed within a very short time and often within geographically confined areas, they are one of the most well-known models and examples in evolutionary biology.[72-75]

Especially the cichlids of the great East African lakes (Figure 3, A) have attracted the interest of evolutionary biologists for studying the mechanisms underlying the phenomenon of adaptive radiation.[72, 73, 76-78] These lakes contain more species of fishes than any other lake in the world, of which almost all are endemic.[75] In Lake Victoria alone, for example, live approximately 500 cichlid species, which presumably evolved within less than 100,000 years.[79] Other scientists argue, that the origin of the cichlid species flock within Lake Victoria may be even younger, as the lake dried out about 15,600-14,700 years ago.[80-82] About 500-700 species have evolved in Lake Malawi within the last 2-5 million years[83], and the radiation of about 250 species in Lake Tanganyika has occurred over the last or 9-12 million years.[84, 85] However, as already mentioned, the age of the species flocks within the lakes may not correspond to the geological age of the lakes, as the climate may have changed or geological events may have caused existing species to have gone extinct.[86]

With an estimated 1800 species, the haplochromine cichlids account for about 80% of all species in these lakes and are thus the biggest and most diverse group among cichlid lineages. The species flocks of Lake Victoria and Lake Malawi are exclusively comprised of cichlids of the haplochromine tribe.[87, 88] They are a rather young lineage of cichlids that is only roughly 4 million years of age. It arose as part of the Lake Tanganyika cichlid species flock, was able to leave the confines of that lake and then gave rise to the adaptive radiations of both Lake Malawi and Victoria.[89, 90]

This evolutionary success of the cichlid fishes is remarkable, and question stands why and how the diversity of this special group of fishes and not that of other groups of fishes, which also inhabit these lakes (such as Tilapia and relatives), could have developed this drastically. Another question arising in this context is how these species are ecologically maintained without eradicating each other due to competition within these geographically confined areas.

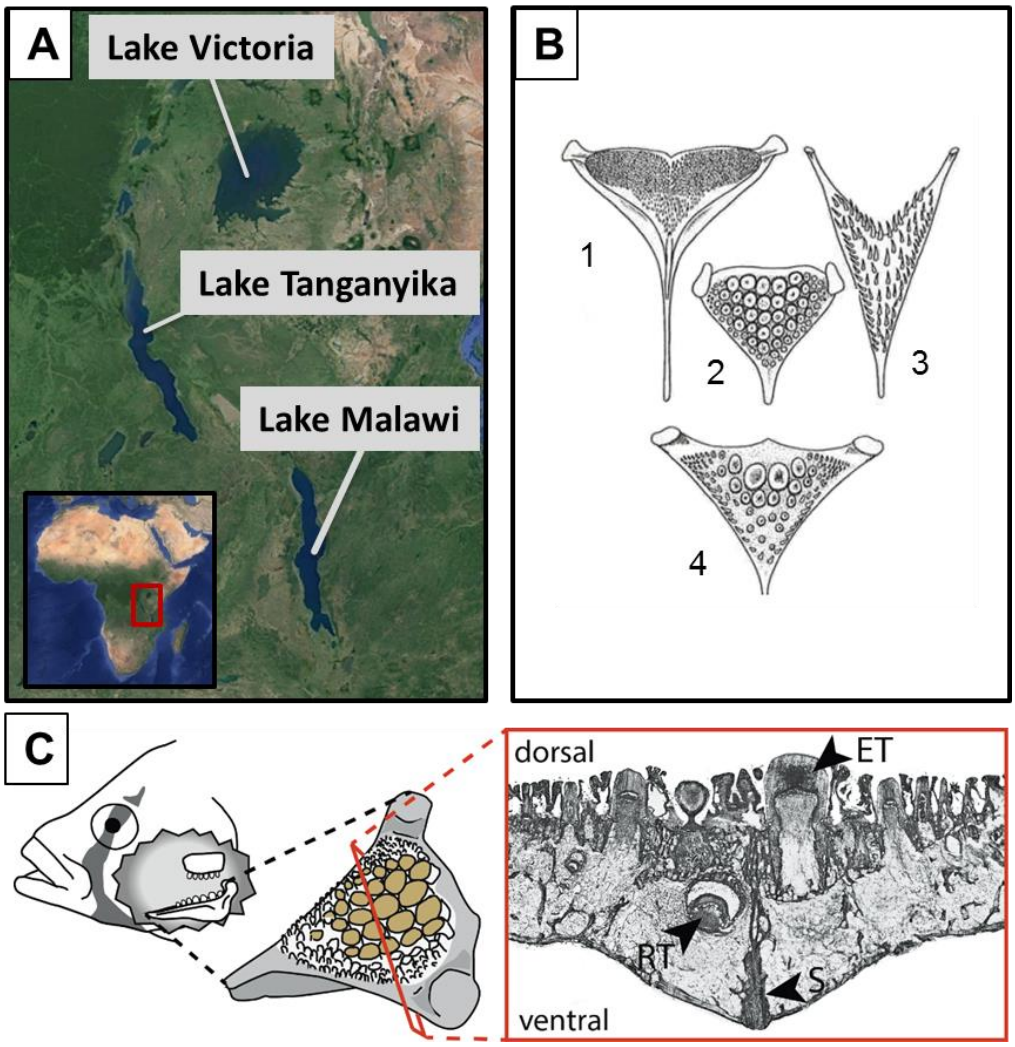

Figure 3: (A) Map of East Africa showing the great East African Lakes. (C) Scheme of the general morphological features of the skull and pharyngeal jaw apparatus of cichlid fishes (left) and a light microscopic image of a cross-section of the LPJ (ET: erupted tooth. RT: replacement tooth. S: suture). (B) Different LPJ's highlighting different morphologies of the jaws and teeth, which are specialized to their respective function: (1) *Tilapia esculenta* (L.Victoria), a phytoplankton eater; (2) *Haplochromis placodon* (L.Malawi), a mollusk crusher; (3) *Bathybates leo* (L.Tanganyika), a piscivore; (4): dorsal view of the LPJ of *Lamprologus tretocephalus* (L.Tanganyika), a mollusk crusher[75] Reprinted with permission.

One critical feature of their evolutionary success is attributed to the functional plasticity of their feeding apparatus, which allows them to occupy sometimes very narrow ecological niches, such as feeding on a very distinct food item.[91, 92] Cichlids, like many other fishes, possess in addition their oral jaw a second functional set of jaws located in their throat (see Figure 3, B and C). The latter is comprised of an upper (UPJ) and lower pharyngeal jaw (LPJ). However, cichlids have evolved a particularly effective pharyngeal apparatus in comparison to other fishes. The formerly divided four elements of the UPJ have fused to function as a unitary tooth plate and have developed a specialized protuberance, which links it with the base of the skull. It thus forms a basipharyngeal joint, which is unique to cichlids.[93] Additionally, the previous two single plates of the LPJ are fused together into a single tooth-bearing plate. The morphology of the LPJ on each rear corner evolved for the attachment of more and stronger muscles. With this, the cichlids were able to enhance the muscular force that

can be used to move the LPJ. Being a single plate and having more muscles, the LPJ can thus be used to work with the upper pharyngeal jaw to masticate prey.[94] This allowed the cichlids to exploit a wider range of food resources and adapt easier to altered feeding ecologies as the oral jaws were functionally less constraint and could evolve into highly specialized tools to extract food from the environment.[75, 76, 79, 94] The jaws and teeth of cichlids have been reported to change over the course of a few generations[75, 76, 95] or even within the lifetime of a single specimen.[96, 97] Herein it was reported that the diet can influence the size and shape of the LPJ and teeth. These studies showed that the central toothed area was affected the most by diet-induced phenotypic plasticity.[97]

As the majority of the living fishes, cichlids have polyphyodont dentition, where the teeth are replaced about every 100 days. Herein, odontogenesis and morphological features can be studied at any life stage.[76] Generally, cichlids display a wide variety of different tooth shapes (see image B in Figure 3 and Figure 6 in chapter 1.2), which can be roughly divided into three categories. Cichlids that usually feed on food that consists of tiny pieces (e.g., fragments of filamentous algae) possess delicate, long, hook-shaped teeth and have more delicate jaws. Cichlids that prey on animals (e.g., other fish or insect larvae) possess small, slender, papilliform teeth that resemble teeth in the oral jaws and also have smaller, delicate jaws. Snail eating species, which crush the hard mollusk shells or clamps, possess big molariform teeth and have massive, big jaws. The teeth can change to papilliform or even hooked towards the edge of the jaw. Molariform and papilliform jaws and teeth show a higher degree of efficiency in processing hard and soft diets, respectively.[98]

Thus, trophic morphology reflects well the feeding ecology of the respective species. As hard and soft food sources occur in all Great Lakes, phenotypes suitable to exploit these food sources also evolved multiple times, leading to a remarkable resemblance of fish species specialized on the same diet, even if they are originating from different lakes and thus radiations.[72] This phenotypic resemblance without a common ancestor sharing the specific phenotype (convergent evolution) raises the question whether similar phenotypes and their function evolved by similar underlying mechanisms (e.g., same genes and/or signaling pathways, so-called "parallel evolution") or whether the same function is achieved by different means.[99] This addresses a key question in evolutionary biology: how repeatable is evolution?[100] A common example is the independent origins of flight in insects, birds, and mammals. Convergent evolution usually creates similar phenotypes, which display similar forms or functions but were not present in the last common ancestor of those groups.[100]

The chosen species, which were investigated in this study, represent very well the specialized trophic phenotypes and reflect an ecological niche in which it is typically expressed, e.g., feeding exclusively on mollusks (hard diet) or insects (soft diet). Herein, a representative cichlid species was chosen for Lake Victoria and Lake Malawi (see Figure 4).

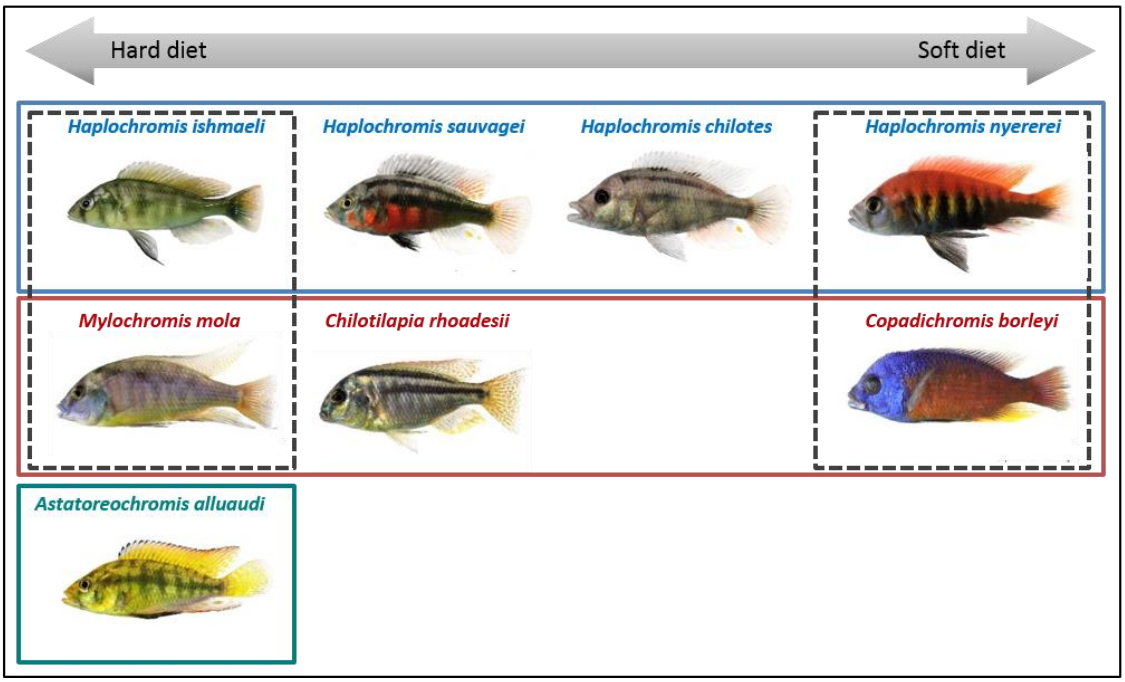

Figure 4: Images of the investigated fish species associated with the respective hardness of their diet. Species originating from Lake Victoria are marked in a blue frame, species originating from Lake Malawi are marked in a red frame, and *A. alluaudi* is marked in a turquoise frame. The *M. mola* and *H. ishmaeli* pair and *H. nyererei* and *C. borleyi* pair are comparable species from these two Lakes with respect to the hardness of their diet.

<u>*Lake Victoria radiation:*</u> *Haplochromis ishmaeli* is on the IUCN Red List of Threatened Species (IUCN 2017) and has been listed as critically endangered (possibly extinct in the wild) in 1996.[101] It occurred in inshore regions with a soft mud bottom, but a few specimens were caught over sand and shingle bottoms.[102] It feeds almost exclusively on mollusks. *Haplochromis sauvagei* is also on the IUCN Red List (2017) and has been listed in the category “vulnerable” in 1996.[103] It inhabits the littoral zone where the bottom is hard and feeds mainly on gastropods, bottom deposits, which include insect larvae, copepods and diatoms, and insects.[79] *Haplochromis chilotes* is also on the IUCN Red List (2017) and has been listed in the category “vulnerable” in 1996.[104] It occurs in sheltered sublittoral and littoral zones with a hard substrate[102] and feeds mainly on larvae[79]. *Haplcochromis nyererei*[105, 106] is mostly restricted to rocky, littoral habitats around islands, and particularly associated with shelf-like formations feeds on algae and insects.

<u>*Lake Malawi radiation:*</u> *Mylochromis* is a genus of haplochromine cichlids endemic to Lake Malawi. *Mylochromis mola* usually inhabits shallow water off sandy beaches and feeds on mollusks.[107] *Copadichromis* is also a genus of haplochromine cichlids endemic to Lake Malawi. *Copadichromis borleyi* species feed primarily on zooplankton, using a specialized suction feeding action and highly protrudable mouth.[107] *Chilotilapia* is a genus of freshwater fish in the cichlid family. It contains the sole species *Chilotilapia rhoadesii* and is also endemic to Lake Malawi. It is omnivorous but primarily feeds on snails in the wild, preferably of the genera *Melanoides* and *Lanistes*.

These snails are crushed between the pharyngeal bones as well as between the jaws. Usually, the thick end of the snail (in *Melanoides*) is bitten off.[108]
Astatoreochromis alluaudi is relatively widespread cichlid species inhabiting Lake Victoria as well as its satellite lakes and associated rivers and is basal to the modern haplochromines (see Figure 5).[109, 110] It is a generalist feeder that can consume a wide variety of food items. This adaptable feeding behavior is attributed to the wide range of phenotypic plasticity of its pharyngeal jaw apparatus, where the morphology of the LPJ is affected by the type of food.[111] Herein, two characteristic LPJ morphs have been identified for this species. One the one side, there is a molariform morph, which has a lower pharyngeal jaw with large, molar-shaped teeth. On the other side, there is a papilliform morph with a lower pharyngeal jaw with smaller delicate teeth. Molariform populations inhabit Lake Victoria, feeding primarily on hard-shelled snails, which are cracked using their robust pharyngeal jaws, while individuals from satellite lake populations are more often papilliform, ingesting a range of softer food items, with a preference for insects.[76] A cladogram of the major radiations of the cichlids, which were included in this study, is displayed in Figure 5.

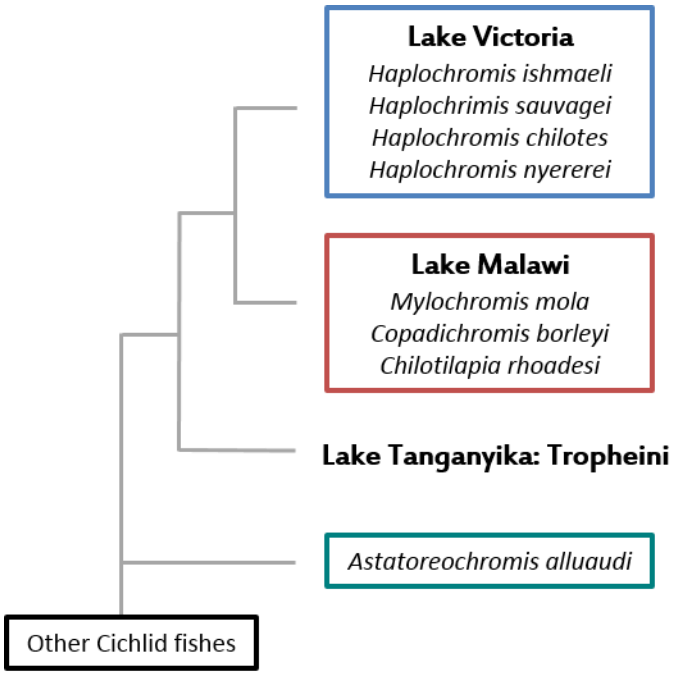

Figure 5: Cladogram of the major radiations of the East African cichlids, which were included in this study.

1.2 General structure of the teeth of lower vertebrates

Teeth are an integral part of the vertebrate feeding apparatus. They can divide the prey into manageable pieces, grip prey for reorientation, and process prey to remove inedible components. While many variations in tooth patterns (number, position, shape, and size; see Figure 6) and attachment modes exist in many vertebrates, the general structure is evolutionary conserved: a cone-like tooth surrounds a pulp cavity and consists of dentine, which is surmounted by a hard, hypermineralized layer, which is called enamel or enameloid.

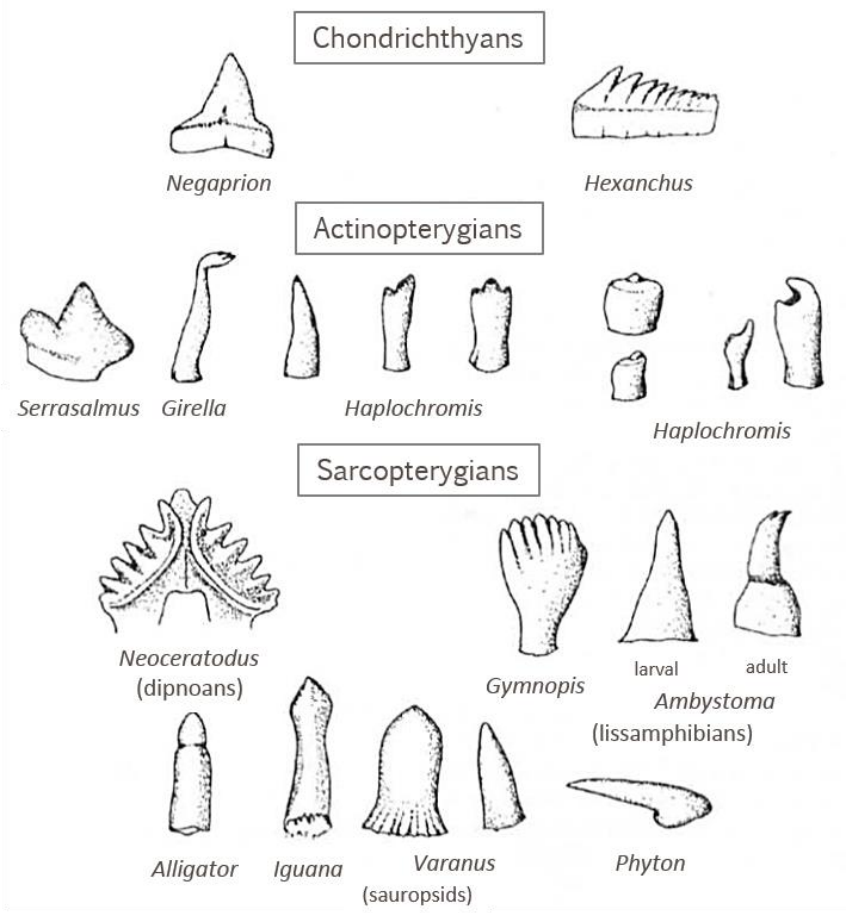

Figure 6: Survey of teeth illustrating the diversity of tooth shapes in non-mammalian vertebrates. Not drawn to scale. Redrawn after [112] and reprinted with permission.

Dentine makes up the bulk of the entire tooth and differs according to certain features, such as collagen fiber size and orientation, incorporation of vascular elements, between different vertebrates (see Figure 7).[112-115] At different times during the last decades, various researchers defined several groups of dentine types. An overview of these classifications can be seen in Table 3. The dentine type, which predominates in teleost is the so-called orthodentine (Figure 7, A), yet other types could be identified as well (Figure 7, B and C).

Similar to the bone, dentine is composed of carbonated hydroxyapatite mineral and collagen (mostly type I) and noncollagenous macromolecules. But in contrast to bone, dentine in lower vertebrates has no remodeling or self-healing properties as in bone hard tissues.[112, 116] The mineral is mostly associated with collagen and appears in plate-like irregular particles, which are situated either between the fibrils (interfibrillar) or between the fibrils (intrafibrillar). When situated intrafibrillar, the crystallographic *c*-axis is aligned with the long axis of the collagen molecules, whereas when situated intrafibrillar, the orientation is not clearly determined.[112, 117]

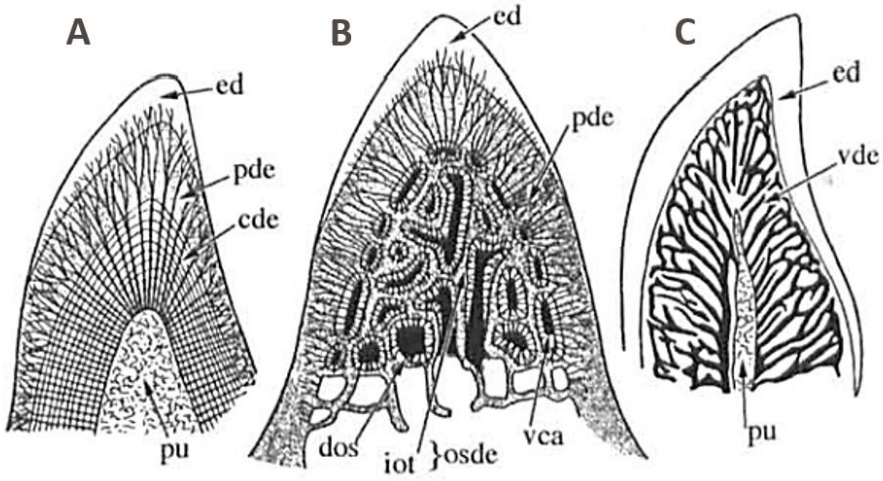

Figure 7: Schematic images of three different types of dentines found in vertebrates. A: orthodentine, B: osteodentine, C: vasodentine. In all cases, the dentine is surmounted by a layer of enameloid. Cde: circumpulpal dentine. dos: dentinal osteon. ed: enameloid. iot: interosteonal tissue. osde: osteodentine. pde: pallial dentine. pu: pulpa. vca: vascular canal. vde: vasodentine. Redrawn after [112] and reprinted with permission.

Table 3: Overview of different classifications of dentines.[113]

Tomes	Thomasett	Ørvig
Osteodentine	Osteodentines:	Osteodentines:
	a. osteodentine	a. normal
	b. pseudodentine	b. special
	c. syndentine	
Orthodentine	Dentines with an open pulp chamber:	Orthodentines:
	a. orthodentine	a. orthodentine
	b. vasodentine	b. vasodentine
Vasodentine		
Plicidentine		

Covering the dentine of most vertebrates is a hypermineralized tissue, which can be classified into two types: enamel or enameloid. As enamel/enameloid formation is a complicated process[112] and closely controlled by genetic and epigenetic factors, the structure is thought to contain much phylogenetic information.[97, 118] In fact, comparative odontology is used to identify species or describe new fossils [119, 120] or to test biogeographic hypotheses.[121] Figure 8 illustrates representative tooth structures among the major vertebrate groups. Herein, the bony fishes (Osteichthyes), where cichlids are classified into, are described to be the most diverse group of fishes regarding the tooth structure.[122] Note, that when more than one structure occurs in one group, the relative position of these structures along a branch of the cladogram is arbitrary and do not imply a transformational polarity.[122] Enamel is thought to have derived from enameloid, though this hypothesis and the phylogenetic and structural relationship between both is still largely discussed and many reviews and textbooks exist elaborating the topic in detail.[113, 114, 123-127] Therefore, only a brief overview is given here, highlighting the most prominent structural features of enamel and enameloid.

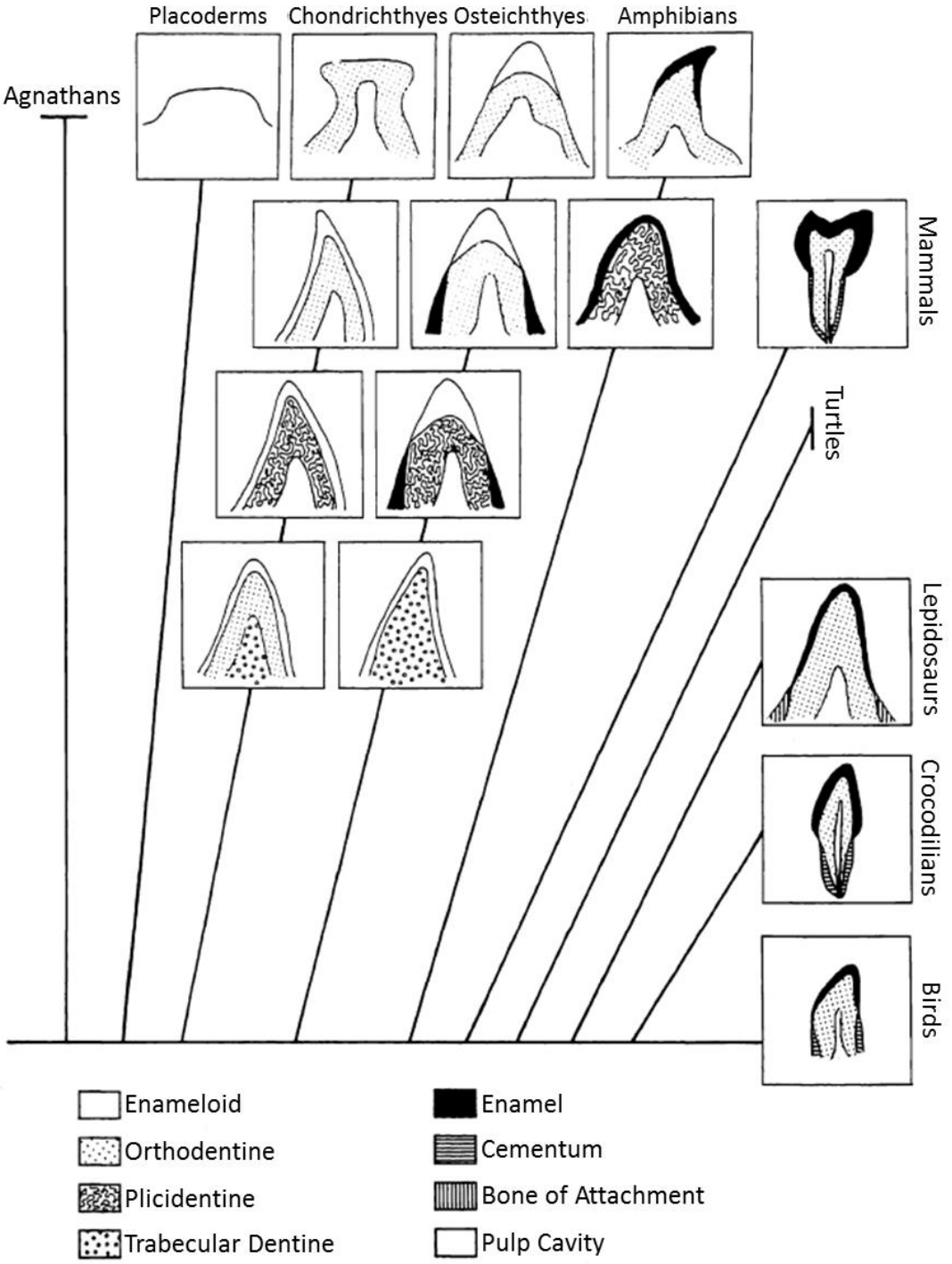

Figure 8: Highly schematic drawings of several representative tooth structures among the major vertebrate groups, which are arranged according to patterns of cladistics relationships. When more than one structure occurs in one group, the relative position of these structures along a branch of the cladogram is arbitrary and do not imply a transformational polarity. Redrawn and reprinted with permission.[122]

Enameloid covers the tooth in both cartilaginous and bony fish and is a hard tissue similar to mammalian enamel, but has a different developmental mechanism: enamel is of epithelial origin, and enameloid is predominantly of mesenchymal origin (odontoblasts and dental epithelial cells), though the contribution of both tissues is still very much debated.[112, 114] The three-dimensional arrangement so-called enamel types or layers within a tooth is called “Schmelzmuster”.[128] In mammalian enamel, the apatite

is present as structured arrays of crystals, whose boundaries are defined as “enamel prisms” or “prism sheaths”, that extend from the dentine-enamel junction to the enamel surface. Enameloid is composed of hydroxyapatite crystallites, which are arranged in bundles in different directions along the tooth. In lower vertebrates, tooth enamel is assumed to occur exclusively in primitive actinopterygians, in aquatic sarcopterygians, in dipnoans and tetrapods.[112] It comprises a thin layer, which covers the dentine, but is not very well mineralized in comparison to their mammalian counterparts or enameloid. Several types of enameloid have been identified and defined over the years for actinopterygians, such as “cap enameloid”, “acrodin cap”[126, 129] or “collar enameloid”[130], although there is much controversy about this general classification and the specific origin of these structures. An example of “cap enameloid “ and “collar enamel” within the teeth of an actinopterygian fish (*L. oculatus*) is displayed in Figure 9, A.[131] Furthermore, an example of a cross-section of a tooth of an elasmobranch shark (*I. oxyrinchus*), displaying enameloid and dentine is shown in Figure 9,B.[50]

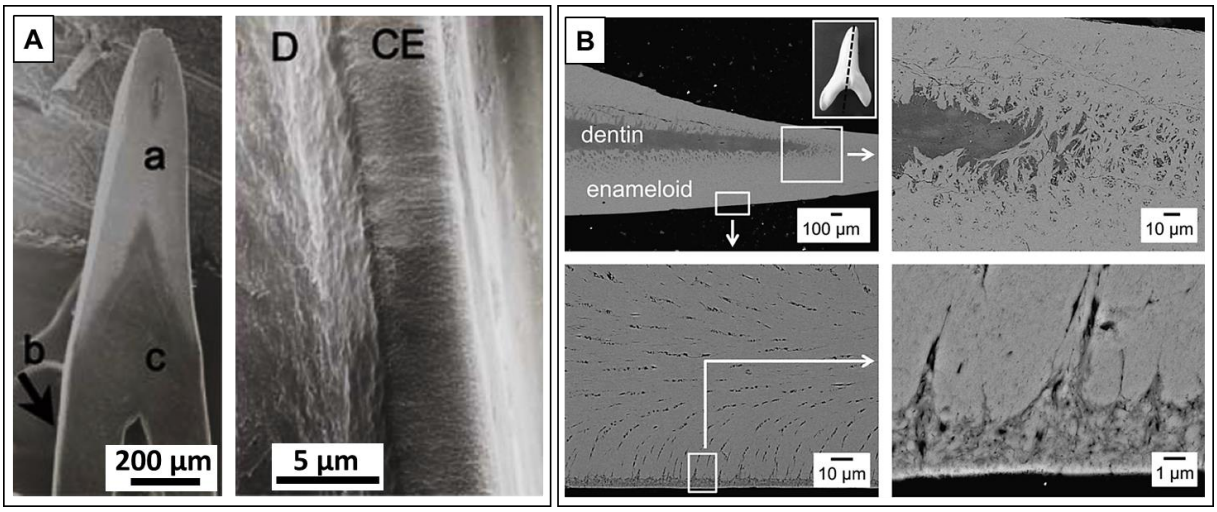

Figure 9: A: Axial cross-section of a tooth in the actinopterygian fish *L. oculatus*. The tooth consists of cap enameloid (a), collar enamel (b), dentin (c), and pulp. B: Axial cross-section of a tooth of an elasmobranch shark *I. oxyrinchus*, showing the interface between dentine and enameloid (dentin–enameloid junction) and also the topological arrangement of the apatite crystals in the enameloid in different magnifications. Reprinted with permission.[50, 131]

Some authors consider this “collar enameloid” to be true enamel (at least for some species), whereas others consider it to be enameloid. The internal structure of these types of enameloids are similar, but not the same. In contrast to enamel, enameloid contains many collagen fibers (similar to type I) and other matrix proteins as an organic matrix.[132, 133] Amelogenins are a major component of the enamel proteins in higher vertebrates. However, the presence of amelogenins in the enameloid is controversely reported in the literature.

The mineral phase of teeth of lower vertebrates is often described as carbonated fluorapatite. It has been proposed, that cichlids can be divided into two groups according to the distribution and concentration of fluoride in their teeth. One group contains species with a high (>2 wt-%) and the other species with a low fluoride concentration (0.1-0.2 wt-%).[134-137] The fluoride content in the teeth has repeatedly been suggest-

ed to be related to the phylogeny rather than the environmental water.[134] Even those fish inhabiting the marine environments only contain up to 1.4 ppm F^- in their enameloid.[138] This notion is supported by the results of LeGeros and Suga, that the incorporation of fluoride into the enameloid occurs during tooth development and not by post-eruptive addition from the environment.[139]
Furthermore, iron-bearing phases are known to be deposited in the enameloid of some teleost fishes[140, 141] and other vertebrate teeth, such as rats[142, 143], the Streamside salamander[144], shrews[145]. Famous examples are the teeth of Chitons[146] and limpets[147, 148], where the teeth comprise iron-bearing phases in the form of magnetite or goethite, respectively. Previous investigations of the iron concentration in teleostean fish teeth first suggested that the incorporation into the teeth is more related to the phylogeny of the fishes rather than to their feeding habits. [149] Similar to the fluoride content, it has been suggested that cichlids can be classified into at least two types, according to the iron distribution in the enameloid. Type A is characterized by a high iron concentration that can be detected mainly towards the occlusal part of the enameloid. In type B, the iron is deposited throughout the entire layer.[149]

1.3 Structural designs of fracture and abrasion resistant biological hard tissues

A lot of biological materials are hierarchically designed and multifunctional. The study of a lot of these materials, such as teeth, bone, seashells, antlers, crab exoskeleton, the toucan beak or scales shed light on a fascinating set of structural design elements nature has invented to produce fracture and wear resistant materials. Generally, for composites materials, a classification into intrinsic and extrinsic crack toughening mechanisms have been proposed.[150] The different toughening mechanisms, which have been proposed for bone are displayed in Figure 10. Intrinsic factors are associated with structures smaller than 1 µm and operate ahead of the crack. These factors typically reduce stress and strain through localized yielding and energy distribution. Examples have been shown for the collagen molecules in bone. Herein, energy is required to unfold the collagen molecules. When they are extended, the molecules can slide past each other and straighten. Furthermore, nano/microcracks can develop within the mineralized collagen fibrils. Additionally, collagen molecules possess so-called sacrificial bonds within or between the molecules that dissipate energy when stretched, which can be reformed after the load is released.[150-153] Such mechanisms were also identified in biological materials, which require high tensile strength of stiffness in one direction. Next to collagen in bone or tendons, further examples are chitin or silk (e.g., as spider silk[154, 155])

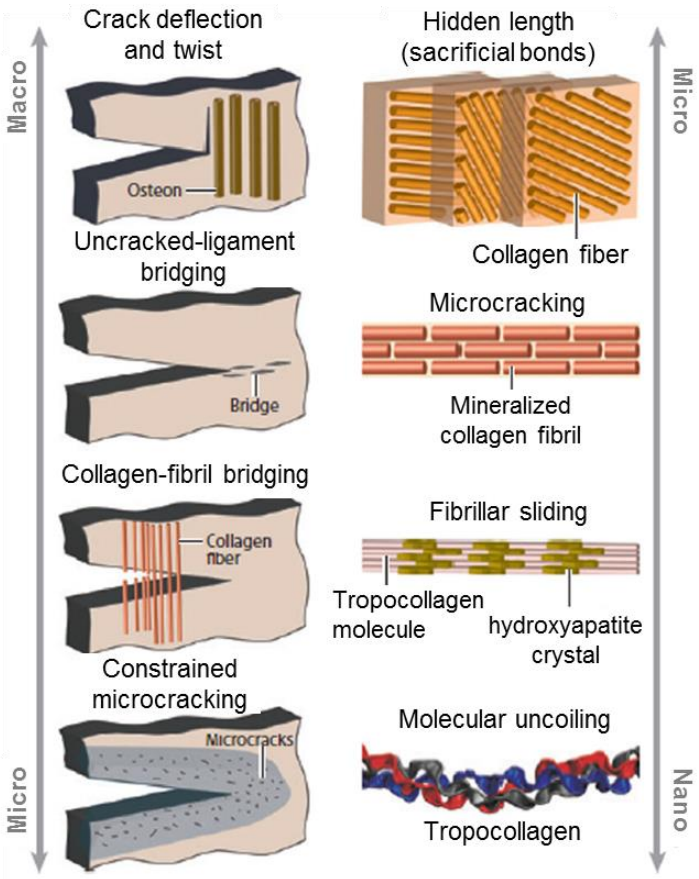

Figure 10: Fracture toughening mechanisms in the bone at different hierarchical levels, containing extrinsic and intrinsic mechanisms. Reprinted with permission.[150]

Extrinsic toughening mechanisms are associated with structures larger than 1 µm and operate behind the crack. These structures and mechanisms act to shield the crack from applied load.[156, 157] Among others, typical extrinsic mechanisms are collagen fibril crack bridging or crack-deflection.[150] Fibril crack bridging is a mechanism of collagen fibers bridging across crack gaps. Next to bone, this mechanism has been proposed for the enamel-dentine junction of human teeth.[158-160] Crack-deflection is promoted by features in the microstructure that deviate the crack from the plane of maximum driving force.[150] In bone, this is caused by the osteons, which change the angle of the original crack path.[161] In human dentine, this mechanism has been associated with the collagen fibril network.[162] Other examples of fibrous assemblies are chitin-protein fibers, which are arranged as a twisted plywood structure within the cuticle of the lobster *Homarus americanus*.[163] Further crack deflecting mechanisms are associated with granular structures. Nanogranularity is a widespread structural trait of biominerals (e.g. in shells of gastropod molluscs[164], cephalopods[165, 166], bone[151], enamel[167]). These grain boundaries in biominerals are often detected using phase contrast atomic force microscopy and display similar diameters between approximately 50-120 nm.[168] Grain boundaries are considered to constitute to planes of reduced fracture resistance and thus, crack propagation often follows along these boundaries.[169] It has been pointed out, that nanogranularity is not a universal trait of all biominerals, although a lot of biominerals featuring this structural property.[168]

2. Results

2.1 Astatoreochromis alluaudi

2.1.1 Morphology of LPJ and teeth

LIGHT MICROSCOPY AND HR-SEM

The morphology of the teeth was investigated by Light microscopy and HR-SEM to get an overview of the macroscopic structure of the tooth. The LPJ of *Astatoreochromis alluaudi* (Figure 11, A, B) has a triangular shape. The dorsal side is almost completely covered with functional teeth. The biggest teeth of the hard diet treated specimen are in the middle of the plate. The tooth size tended to diminish from mediostral to laterocaudal (see Figure 11, B). The biggest teeth have a robust and molariform shape with relatively flat crowns (B, inset). The teeth in the outer region are small and papilliform. The tips of the teeth appear reddish to brownish. This coloring is more pronounced in the biggest central teeth in comparison to the outer, smaller teeth (Figure 11, B).

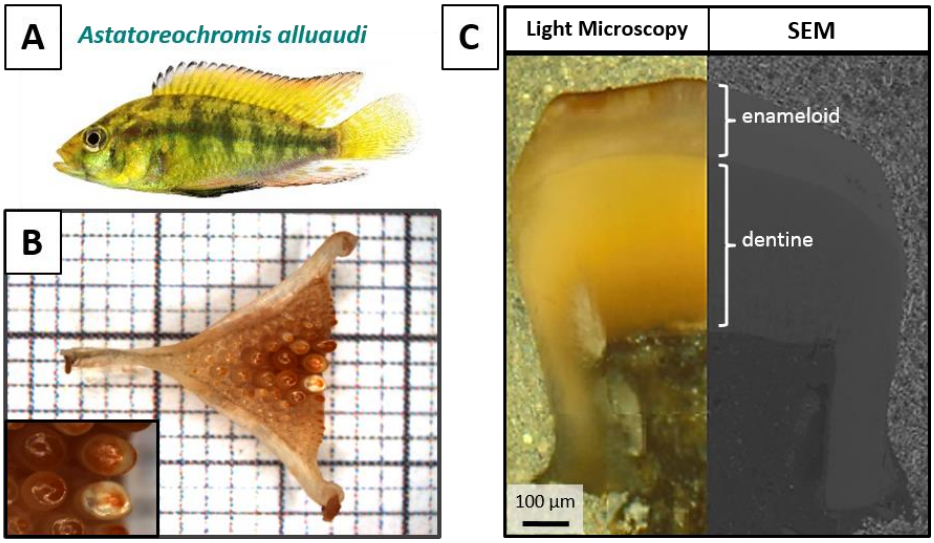

Figure 11: A: Photo of the East African cichlid *Astatoreochromis alluaudi.* B: Lower pharyngeal jaw of *A. alluaudi*, inset: biggest central teeth of the lower pharyngeal jaw. C: A merge of a light microscope image and SEM image of a polished cross-section of a central tooth of the LPJ.

Light microscopic and SEM investigations of polished cross-sections (Figure 11, C) showed the presence of different distinct areas inside the teeth. These can generally be divided into the enameloid and dentine area. The red pigmentation is strongest as a thin area at the top surface of the tooth. The thickness of the pigmentation reaches, depending on the lateral position, about 20-30 µm into the sample.

2.1.2 Chemical composition and distribution

EDXS

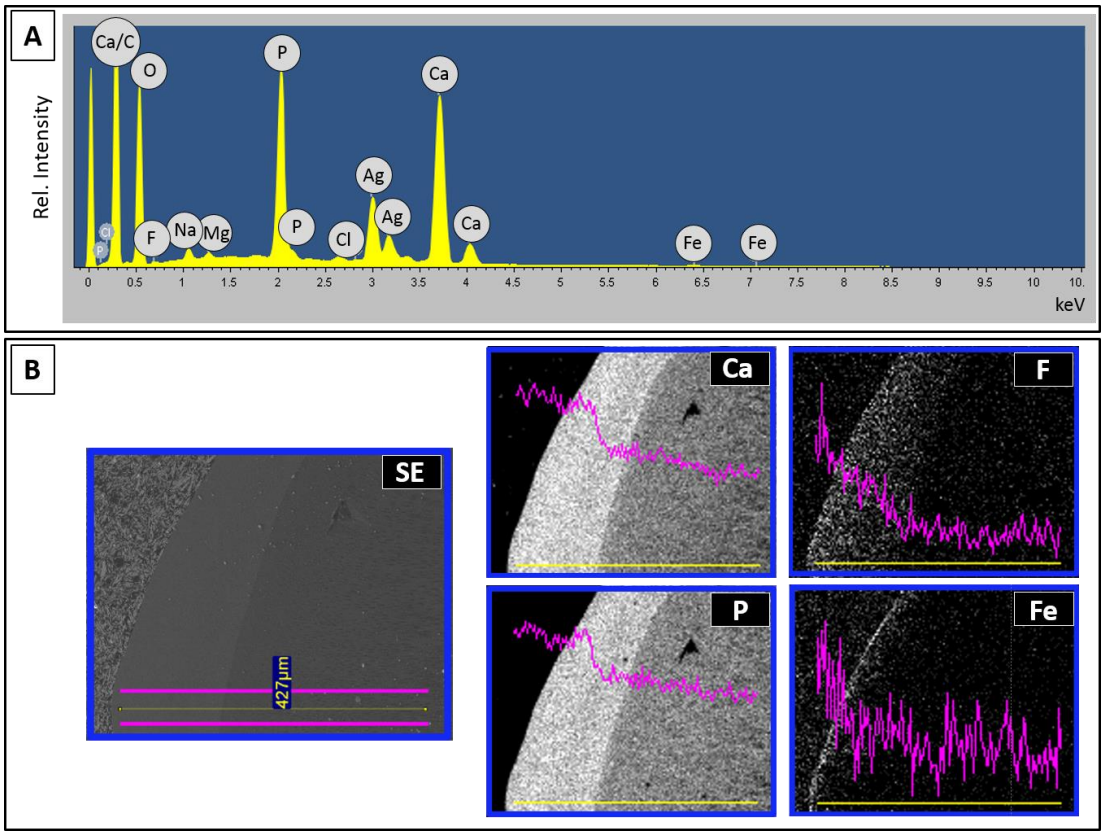

Figure 12: EDXS-measurements on polished cross-sections of a tooth of *A alluaudi.* A: sum spectrum of elemental analysis; B: elemental mappings and corresponding line scans of Ca, P, F and Fe on the surface as displayed in the SEM-micrograph displayed on the left side.

Elemental analysis and mapping were performed using EDXS on the polished surface of the cross-sectional tooth sample to get an overview of the elemental composition and -distribution within the tooth. The elements carbon, oxygen, calcium, phosphorous, fluorine, iron, magnesium, sodium, chlorine, and silver could be detected (see Figure 12, A). The silver originates from the conducting embedding resin. A mapping of the major elemental components within the polished longitudinal cross-section can be found in Figure S 1. Line scans within these mappings revealed a high concentration of calcium and phosphorous in the enameloid area of the tooth (Figure 12, B). Furthermore, the concentration of both elements varies in a non-linear, stepwise fashion. A high concentration can be found directly at the occlusal surface. The intensity falls to a local minimum, rises slightly again and falls abruptly to a low value upon the border to the dentine area. The mapping further revealed that fluorine is enriched in the enameloid, decreasing in a nearly linear fashion and falling to nearly zero on the border to the dentine area. A high concentration of iron could be found in a very thin area at the occlusal part of the enameloid. As can be seen in the mapping in Figure S 1, the signals for the elements carbon, magnesium, and sodium all show an enriched intensity over the entire thickness of the dentine.

RAMAN MICROSCOPY

Raman microscopy was performed on the polished axial cross-section of a tooth of *A. alluaudi* to get additional insight into the distribution of ionic groups within the teeth. The measured area is displayed with a frame in Figure 13, A. The spectra along the length of the measured area are displayed in Figure 13, B. The presence of characteristic apatite vibration modes could be detected at about 963 cm^{-1} ($[PO_4]^{3-}$ v_1), ~430 cm^{-1} ($[PO_4]^{3-}$ v_2), ~1042 cm^{-1} ($[PO_4]^{3-}$ v_3), 589 cm^{-1} ($[PO_4]^{3-}$ v_4) and 1003 cm^{-1} ($[HPO_4]^{2-}$).[170-172] Characteristic signals of the organic component could be identified at 1660 cm^{-1} (amide I), 1262 cm^{-1} (amide II) and 1453 cm^{-1} (C-H bending mode).[173, 174] A band at ~1070 cm^{-1} indicates a carbonate substitution in the apatite- component[173, 174], although the signal intensity is very low. The observed vibration signals and peak assignments are summarized in Table S 1 in the appendix A. An overlay of all collected Raman spectra of the phosphate v_1 band of the cross-section additionally revealed a small shift in wavenumbers of about 3 cm^{-1} towards lower wavenumbers from the occlusal area of the enameloid towards the dentine (see Figure S 2).

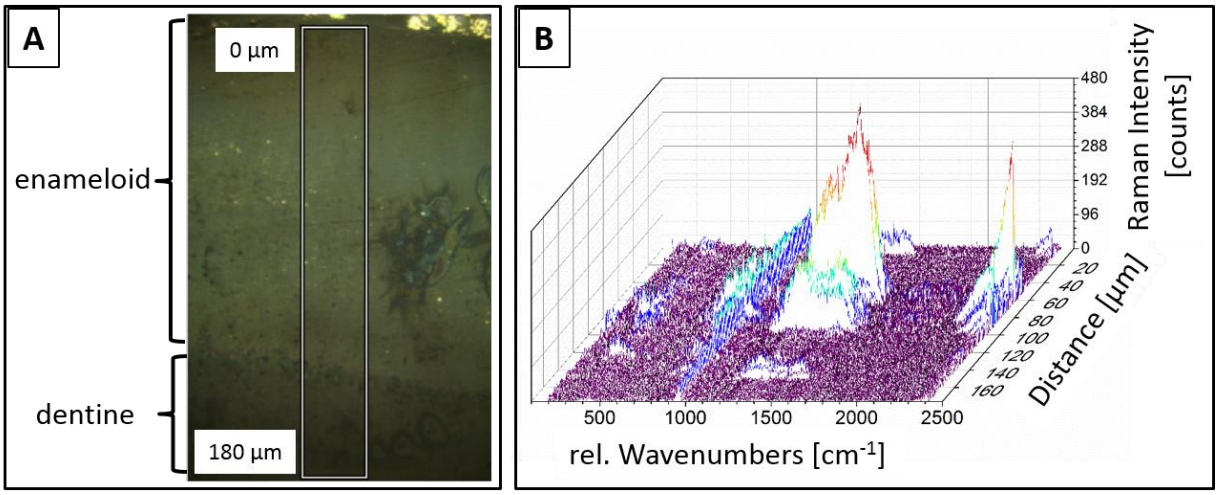

Figure 13: A: Light microscopic image of a polished cross-section of a tooth of *A. alluaudi*. The frame indicates the area for the Raman-measurements. B: Summarized Raman spectra along the length of the frame, as indicated in A.

In order to better display the distribution of the different components, selected vibration modes were extracted and displayed as a function of the distance from the top of the tooth. These single spectra are shown in appendix A in Figure S 3. In the face of the relatively high noise, the signal in a range of about 2-5 wavenumbers was displayed to get a representative intensity profile along the tooth. The signal intensity of the phosphate v_1 vibration mode was significantly higher in the enameloid area as in the dentine area. Local variations in the signal of the phosphate peak intensity could be observed. The signal intensity slightly drops within the first 20 µm, before slightly rising again and decreasing again towards the dentine area.
At position 60 µm and 90 µm, the signal displays a sharp signal increase. The trend is not as clear as the phosphorous signal for the EDX measurements although the general steps are in accordance with the different measurement types.

A band at about 238 cm^{-1}, which could relate to iron oxide phase[175, 176], showed a slight increase in the first 10 µm from the top of the tooth and a second maximum between 60 µm - 90 µm into the tooth, although the general intensity is very low. All signals relating to the organic component of the tooth display a sharp maximum between 50 µm - 100 µm from the top with a local maximum at about 60 µm.

FT-IR-SPECTROSCOPY

To gain additional complementary information on the ionic groups, and to gain further knowledge about the carbonate component of the apatite, several teeth of *A. alluaudi* were crushed, and the resulting powder was investigated by FT-IR spectroscopy. The results of the main signals are summarized in Table S 2 in appendix A. The IR spectrum exhibits three modes at 962 cm^{-1} ($[PO_4]^{3-}$ v_1),1090 cm^{-1} ($[PO_4]^{3-}$ v_3) and 1162 cm^{-1} ($[PO_4]^{3-}$ v_3), which can be attributed to the internal vibration of the phosphate group.[177] Furthermore, the IR peaks at 1644 cm^{-1}, 1549 $cm^{-1,}$ and 1238 cm^{-1} can be attributed to the amide l, amide II and the amide III respectively.[178-180] Additionally, amide A and B bands at 3070 – 3300 cm^{-1}, which overlap with the stretching modes of the water molecules could be observed.[178] The strong vibration modes of the CH groups were found at 2854 cm^{-1}, 2924 $cm^{-1,}$ and 2959 cm^{-1}. Furthermore, the IR spectrum also shows characteristic carbonate bands at 720 cm^{-1}, 875 cm^{-1}, 1416 $cm^{-1}$and 1457 cm^{-1}, indicating a B-type substitution in the apatite crystal structure.

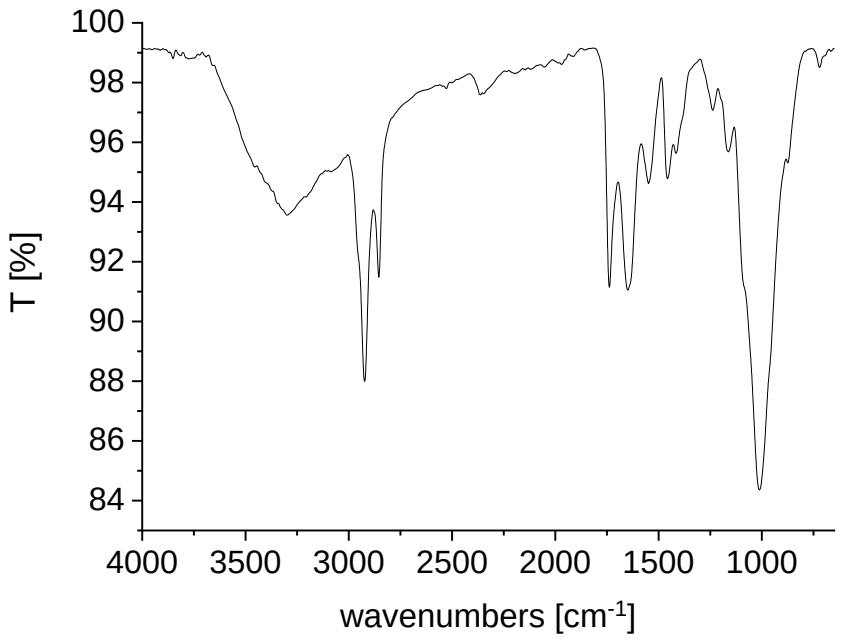

Figure 14: IR spectrum of a powdered mix of several teeth of the LPJ of *A. alluaudi.*

2.1.3 Ultrastructure of the teeth

HR-SEM

In order to get insight into the inner tooth structure, HR-SEM was performed on a polished axial cross-section of a tooth and fractured teeth of *A. alluaudi*. The SEM images of the polished cross-section are displayed in Figure 15. It was observed that the bulk of the enameloid consists of highly interwoven fibers. In the distal part of the enameloid, about approx.45 µm measured from the top of the tooth, these woven fibers were not observed. In the dentine area a lot of pores were observed, which originate from the dentinal tubules.

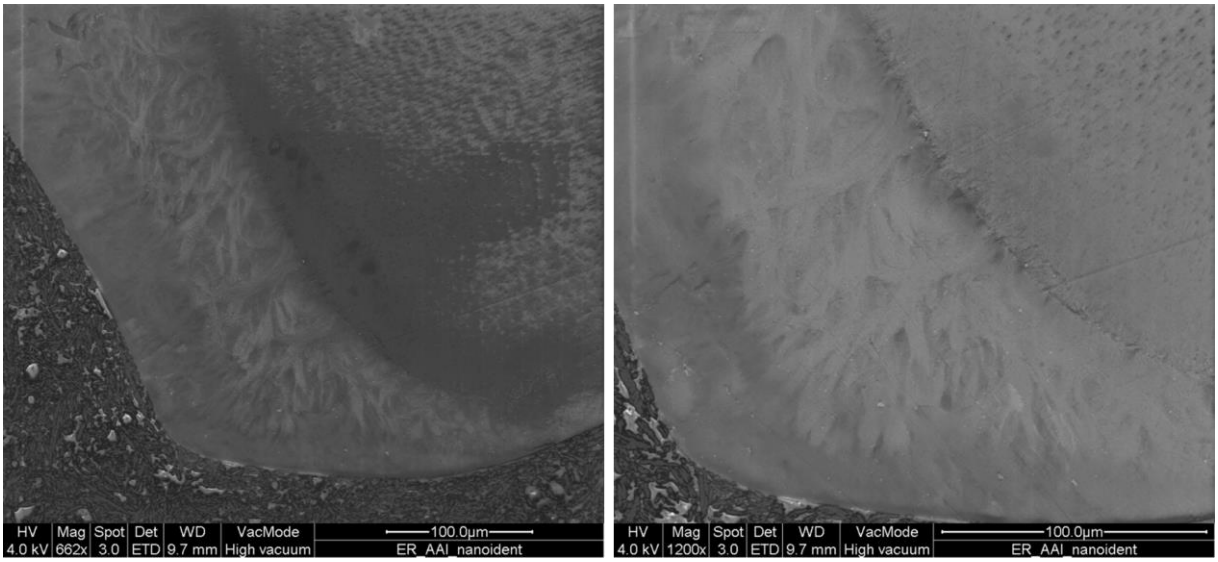

Figure 15: HR-SEM micrographs of a polished axial cross-section of a molar tooth of *A. alluaudi*.

SEM images of the fractured teeth are displayed in Figure 16. These investigations showed that the molar tooth consists of different structural elements. A thin, about 1-1.5 µm thick, and dense mineralized surface layer was found to cover the outside of the teeth (marked as (sl) in Figure 16, A). Within this layer, the crystallites are oriented parallel to each other and their long axis is oriented perpendicular to the tooth surface. Following this thin superficial layer is an area within the enameloid, where mineralized fibers are oriented roughly parallel to each other and their long axis perpendicular to the surface (marked with (1) in images A-C). These fibers become more decussated from the top of the tooth towards the inside. About 8-10 µm within the tooth, measured from the outer surface, these crystallites are interwoven with ribbons of fibrous mineralized bundles which run along the long axis of the tooth and are perpendicular to the long axis of the mentioned crystallites of the layer 1. This arrangement creates an interwoven plywood-structure (Figure 16, B-D, marked with (2)). These bundles cover the full length of the tooth. The innermost layer of the enameloid, which describes the junction between the enameloid and dentine, consist of less organized bundles of tangled, mineralized fibers, which are more densely packed and slightly oriented towards outer areas of the tooth (marked with (3)).

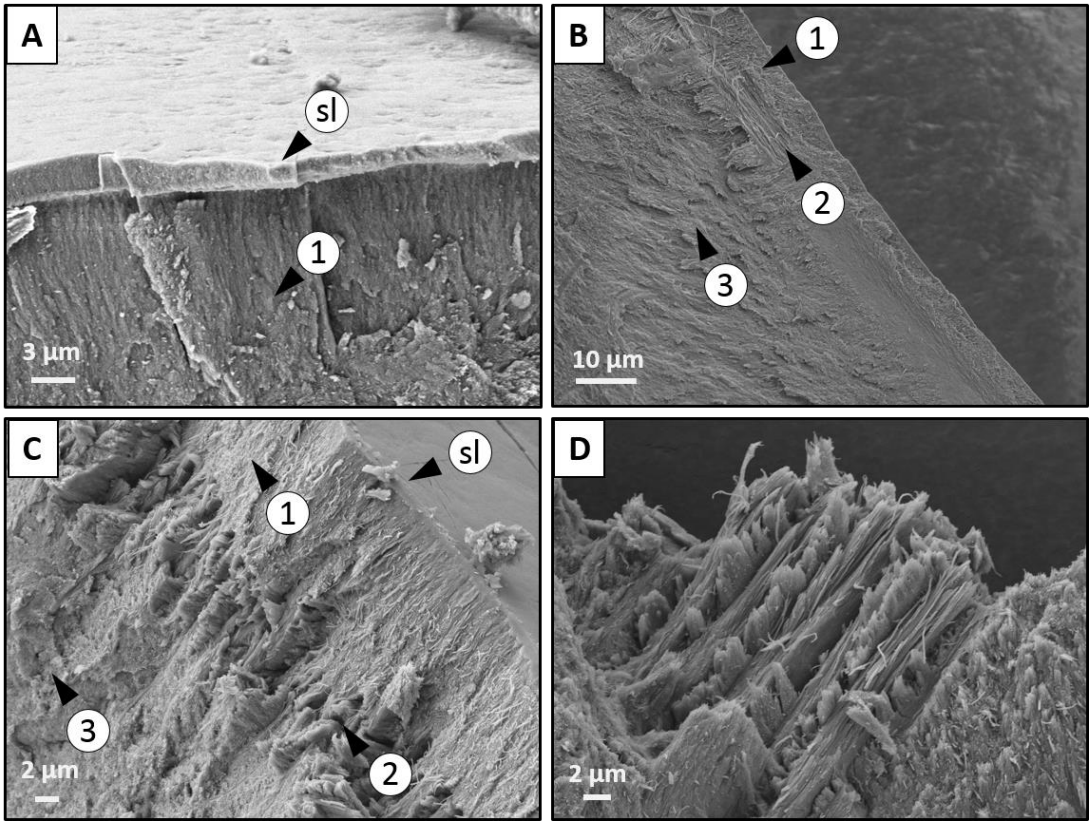

Figure 16: Scanning electron micrographs of fracture areas of crushed teeth of *A. alluaudi.* Labels (sl), (1)-(3) highlight the different structural layers as described in the text.

The dentine is composed of thin crystallized bundles, which are oriented in a nearly random fashion. Dental tubules (appendix A Figure S 4), which have a diameter of about 1-2 µm were observed. These channels perforate the entire structure and radiate outwards from the pulp. The tubules are surrounded by a fibrous network of concentrically arranged fibers.

FLUORESCENCE MICROSCOPY

To get more information about the organic component of the tooth and its distribution and orientation fluorescence microscopy was utilized on a demineralized and stained cross-section. The images revealed that an organized organic matrix is present within the whole tooth, which roughly follows the previously described structural elements of the SEM investigations on fractured teeth. The structure of the dentinal tubules can be clearly recognized. They reach from the pulpa through the dentine towards the occlusal area within the enameloid (see Figure 17, A). A high fluorescence intensity could be detected within the dentine close to the pulpa, indicating an organic layer, which separates the dentine from the pulpa. Furthermore, a high intensity could be detected within a layer between 10- 20 µm, measured from the occlusal surface within the tooth. This location coincides with the described interwoven plywood-structure, which was described above.

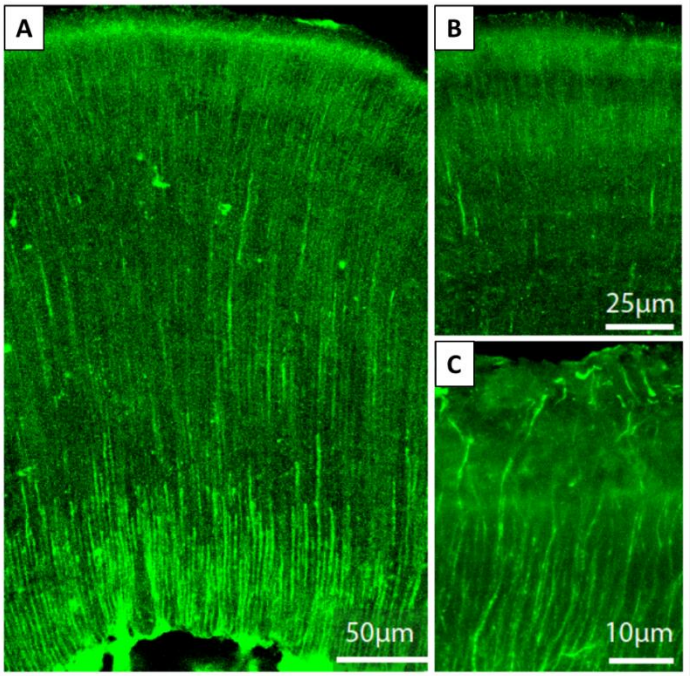

Figure 17: Fluorescence microscope images of a decalcified and stained cross-sectional cut of a tooth of *A. alluaudi.*

µ-BEAM WAXS/SAXS

To obtain deeper insight into the nature and distribution of the mineral phase, thin slices of an axial and a transverse cross-section of a molar tooth of *A. alluaudi* was investigated using µbeam WAXS and SAXS measurements.
The results of the µbeam WAXS and SAXS measurements on the transverse cross-section are displayed in Figure 18. Image A illustrates the position of the investigated slice in the tooth sample and the measurement direction. Note, that the shown tooth in this illustration was not the exact same tooth, which was taken for the measurement. Image B shows a light microscopic image of both sides of the embedded slice of the tooth. Caution has to be taken when interpreting the data, as the measurement was performed in transmission mode and the results represent an overlay of all structural features throughout the tooth section. As the slice was polished close to the occlusal surface of the tooth, the upper side (side a) displays a red surface, while the bottom side (side b) is completely white. The measured area is illustrated with a frame in the SEM image in image D. In order to obtain an overview of the preferred orientation in this tooth section, the 2D SAXS scans were arranged to form a map of the recorded CCD images of the tooth (image C). Herein, each square indicates one 2D SAXS pattern.
It has to be mentioned that this mapping is constructed using the raw data of the measurement. In this image, the observed texture direction does not necessarily show the real preferred orientation of the crystallites and fibers. If a thin section of a biomaterial with such a complex composite structure is scanned in two directions perpendicular to the X-ray beam, the fiber axis will not necessarily be perpendicular to the beam at each measured point. Therefore, as was already discussed and described in previous works by P. Fratzl and co-workers[181-183], an expression would be

required to describe the relationship between the direction of the diffracting fibers and the diffraction pattern as measured with an area detector. This calculation for the adjustment of the texture patterns was not performed within this work. However, the results of the electron microscopic investigations show, that in the outer part of the enameloid *c*-axis of apatite is generally oriented roughly perpendicular towards the surface of the tooth. The same tendency is also clearly visible in diffraction patterns of enameloid which measured in a straight perpendicular direction (vertical or horizontal) within the tooth section plane.

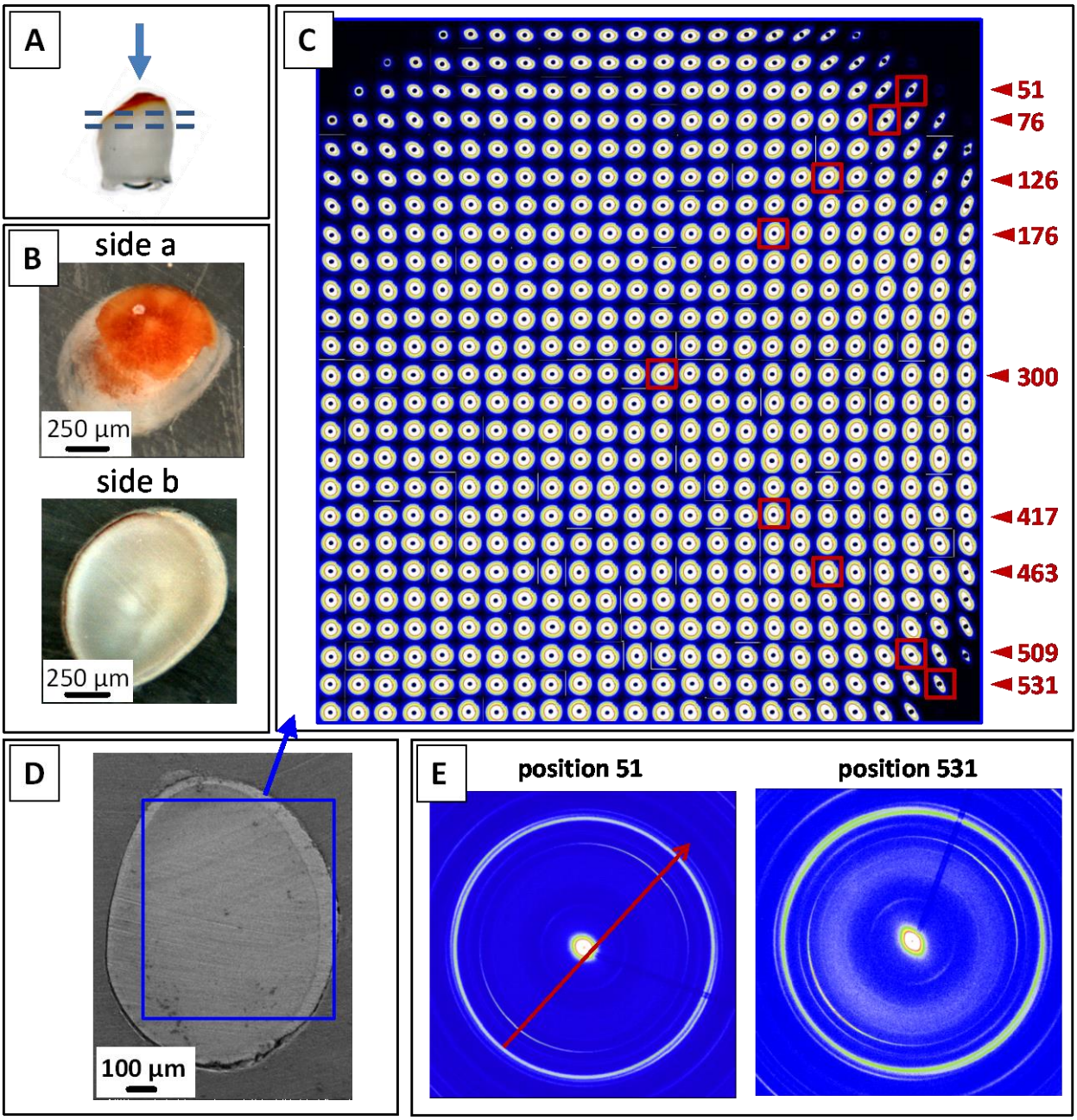

Figure 18: Results of the µbeam WAXS and SAXS measurements on a transverse cross-section of *A. alluaudi.* A: scheme illustrating the measurement direction and view on the sample; B: light microscope image of both sides of the polished sample. C: Overview of the 2D SAXS pattern maps (raw data); D: SEM image displaying the scanned area; E: Exemplary SAXS/WAXS images on selected positions displaying different types of texture like patterns.

Several positions were selected for further investigations, as is indicated with the red squares in image C. Generally, in all positions, which were within the enameloid area, strong texture effects along [001] direction of apatite were observed, while there were no texture effects in the position, which belonged to the dentine (within the size of the beam). In image E, two representative 2D WAXS patterns for the enameloid area are shown, illustrating the orientational change of texture direction of apatite crystallites (positions 51, 531). The intensity pattern the 002 reflection of apatite was used to evaluate the texture direction. The intensity was integrated over 360° in a narrow band containing the 002 reflection and plotted versus the azimuthal angle. Figure 19 shows the graphs of the resulting curves.

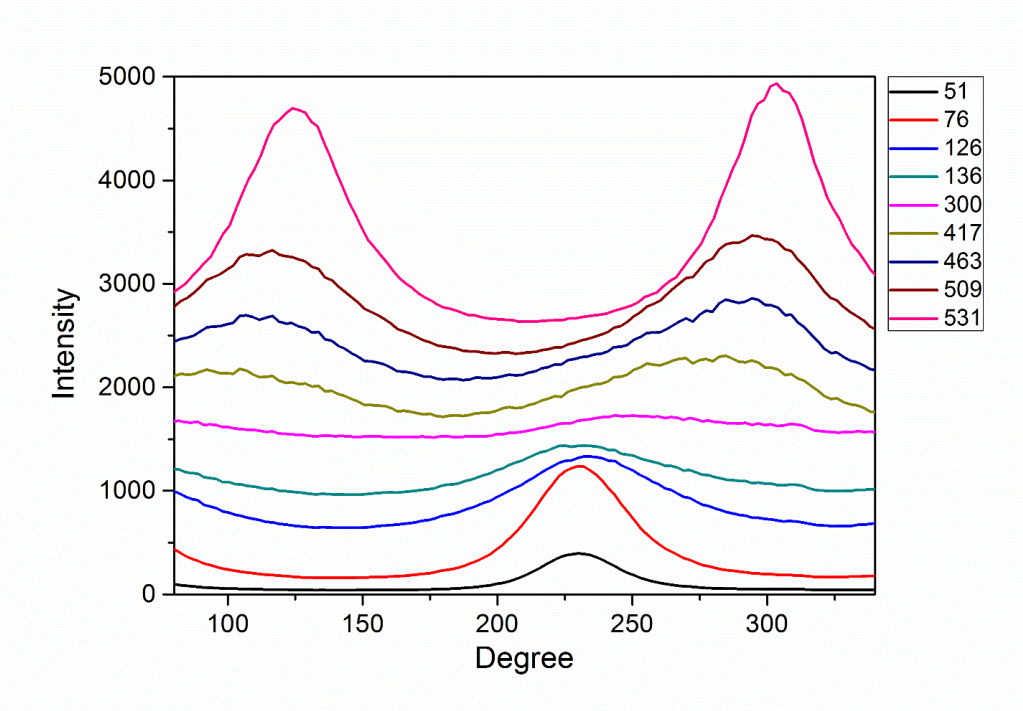

Figure 19: Azimuth plot of the 002 reflection in the selected positions as indicated in D in Figure 18.

Two pronounced peaks, which are separated by about 180° can be found in the patterns recorded from the enameloid areas. This indicated, that while there was no significant anisotropy in the dentine area, there was an increasing azimuthal variation towards all enameloid regions.

In order to evaluate the phase composition of the dental hard tissues, the radial integration of the intensity of 2D WAXS patterns as a function of the scattering vector q was performed. A typical two-dimensional and corresponding one-dimensional diffraction pattern of position 300 (dentine) is shown in Figure 20, A. The integrated one-dimensional diffraction patterns of all selected positions are shown in B. All 2D patterns of the selected positions are displayed in appendix A in Figure S 5. The analysis of WAXS patterns showed that the enameloid and dentine gave well-resolved apatite pattern. Reflections corresponding to other crystallite phases were not identified.

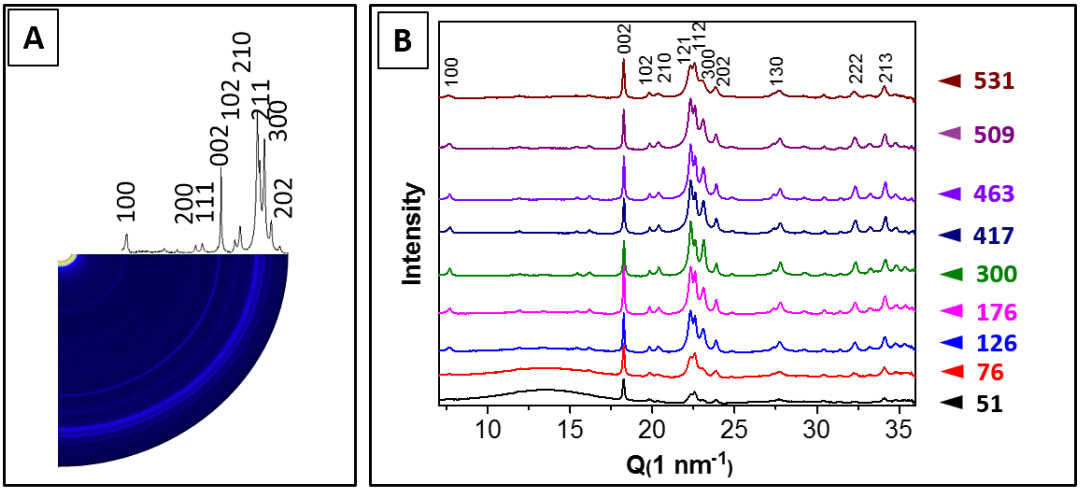

Figure 20: A: exemplary 2D-WAXS and corresponding integrated 1D- XRD in the position 300 (as marked in Figure 18, C). B: Integrated 1D patterns of all selected positions.

The sizes of coherent scattering domains (CSD) of apatite in the selected positions (see figure Figure 18, C) were calculated with the Scherrer equation using the one-dimensional WAXS pattern after correcting instrumental peak broadening. The method used was the same as that reported in the previous literature.[184] The results are summarized in Table 4. The apatite crystallite domains show a slight elongation in the *c*-direction, as is indicated by the narrowing of 00l diffraction peaks. The calculation of the apatite lattice parameters showed, that the parameter *a* slightly decreases in the apatite crystals from the enameloid toward the dentine, while the *c*-parameter remains nearly the same. The results are summarized in Table 5.

Table 4: Crystallite sizes of selected positions (in nm) of selected positions (as indicated in Figure 18, C).

Sample	51	76	126	176	300	417	463	509	531
(100)	-	-	12,1	12,7	13,9	12,5	12,3	11,0	8,4
(002)	18,1	18,2	20,6	20,9	20,7	18,5	20,0	19,7	17,8
(202)	12,4	12,2	13,2	13,4	14,2	14,6	14,1	12,0	12,4
(222)	9,2	10,9	11,1	11,6	12,1	12,2	12,3	11,6	10,8

Table 5: lattice parameters a and c (in Å) of selected positions (as indicated in Figure 18, C).

Parameter	51	76	126	176	300	417	463	509	531
a	9.41 ±0.01	9.412 ±0.003	9.407 ±0.002	9.412 ±0.003	9.405 ±0.001	9.41 ±0.002	9.398 ±0.002	9.416 ±0.008	9.4 ±0.002
c	6.89 ±0.01	6.885 ±0.005	6.883 ±0.002	6.882 ±0.003	6.88 ±0.002	6.88 ±0.002	6.878 ±0.003	6.893 ±0.009	6.873 ±0.002

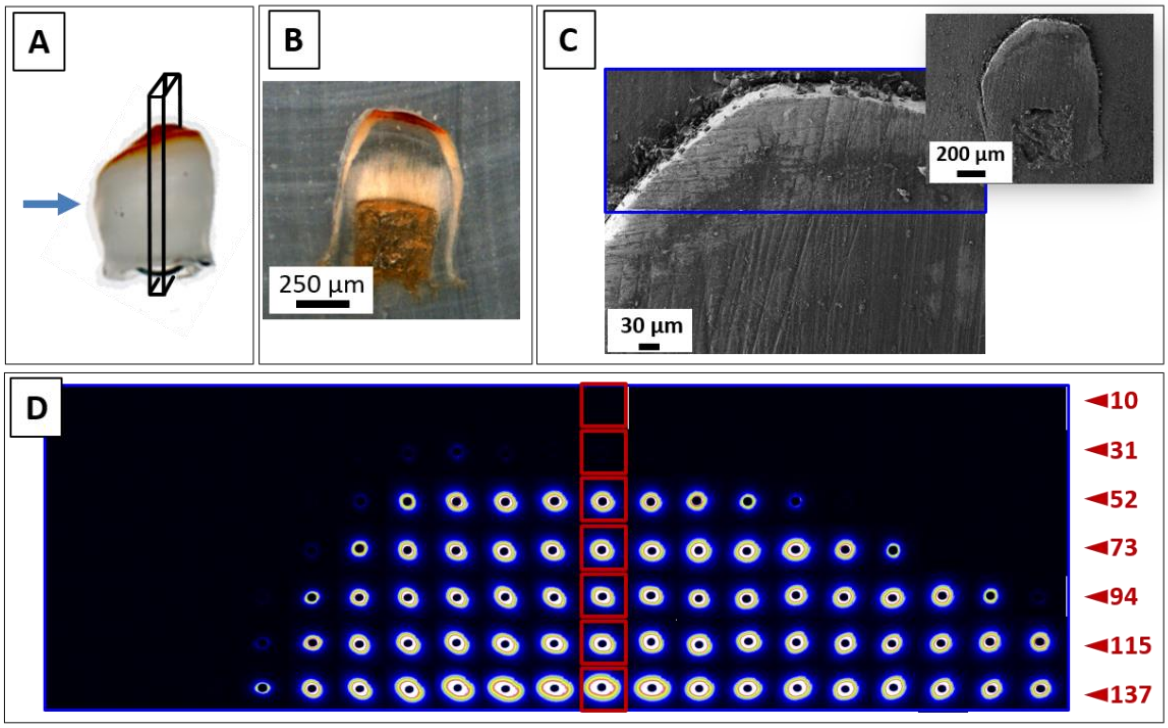

Figure 21: Results of the µbeam WAXS and SAXS measurements on an axial cross-section of *A. alluaudi.* A scheme illustrating the measurement direction and view on the sample; B: Light microscope image of the thin and embedded tooth slice; C: A SEM micrograph displaying the scanned area. D: Overview of the 2D WAXS pattern maps.

The results of the µbeam WAXS and SAXS measurements on an axial cross-section are displayed in Figure 21. Image A illustrates the sample cross-section of the tooth sample and general measurement direction. Note, that the shown tooth in the illustration was not the exact same tooth, which was taken for the measurement. Image B shows a light microscope image of the embedded tooth-slice. The occlusal side shows a thin, red area. The µbeam WAXS and SAXS measurements were performed within a small area within this reddish part, as is indicated with the blue frame in image C. In order to obtain an overview of the preferred orientation in this tooth section, the 2D SAXS scans were arranged to form a map of the recorded CCD images of the tooth (image D). Herein, each square indicates one 2D SAXS pattern. Several positions were selected for further investigations, as is indicated with the red squares in image D. Generally, in all positions, which were within the enameloid area, strong texture effects along [001] direction of apatite were observed. The intensity pattern of the 002 of apatite was used to evaluate the texture direction of apatite crystallites.
The intensity was integrated over 360° in a narrow band containing the 002 reflection and plotted versus the azimuthal angle (Figure 22) Two pronounced peaks, which are separated by about 180° and two smaller peaks, which are shifted about 90° to the pronounced peaks, were found in the patterns recorded from the outer occlusal enameloid areas (position 137). The intensity of the two pronounced peaks was decreased towards the inner area of the tooth, further away from the occlusal top. This indicated, that while there was no significant anisotropy in the dentine area, there was an increasing azimuthal variation towards outer enameloid regions.

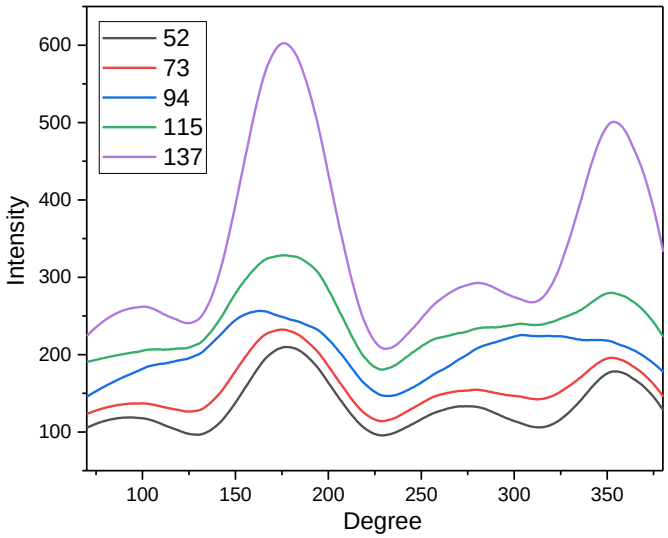

Figure 22: Azimuth plot of selected figures as indicated in D in Figure 21.

In order to evaluate the phase composition within this area, the radial integration of the intensity of the 2D WAXS patterns as a function of the scattering vector q was performed. A typical two-dimensional and one-dimensional diffraction pattern of position 52 is shown in image A of Figure 23. All 2D patterns of the selected positions are displayed in Figure S 6 in appendix A. The integrated one-dimensional diffraction patterns of different selected positions are summarized in image B of Figure 23.The analysis of the WAXS patterns showed that the enameloid gave well-resolved apatite patterns. Reflections corresponding to other crystalline phases were not identified.

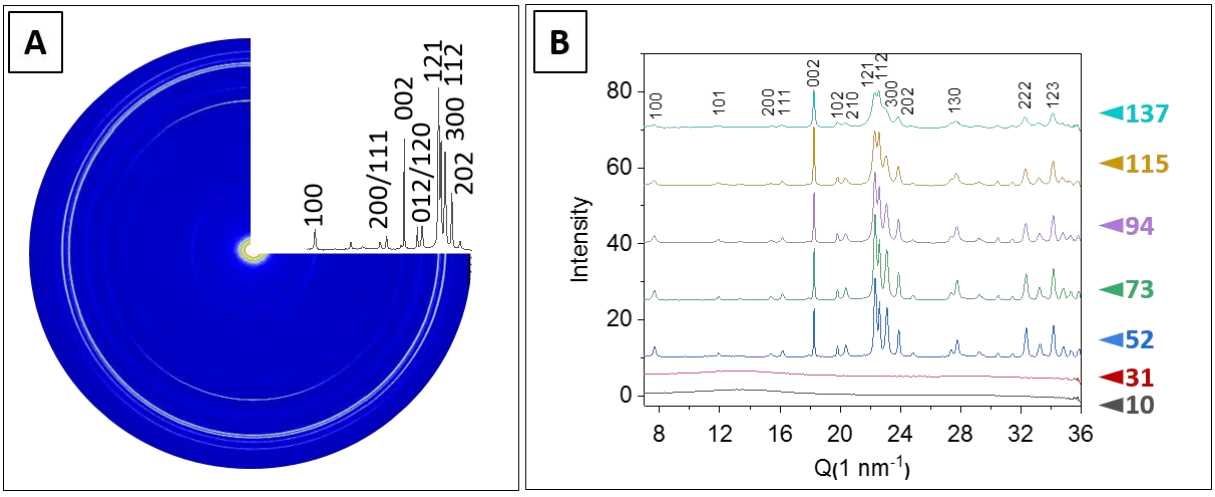

Figure 23: A: exemplary 2D- and integrated 1D- XRD. B: Integrated 1D patterns of the selected positions (as marked in Figure 21, D).

The sizes of the coherent scattering domains (CSD) of apatite in the selected positions were calculated with the Scherrer equation using the one-dimensional WAXS pattern after correcting instrumental peak broadening. The method used was the same as that reported in the previous literature.[184] The results are summarized in Table 6. The apatite crystallite domains show no elongation in the *c*-direction, which

would be indicated by a narrowing of 00l diffraction peaks. The calculation of the apatite lattice parameters showed, that the parameter *a* slightly increases in the apatite crystals from the enameloid toward the dentine, while the *c*-parameter remains nearly the same. The results are summarized in Table 7.

Table 6: Crystallite sizes of selected positions (in nm) of selected positions (as indicated in Figure 21, D).

position	52	73	94	115	137
(002)	24.8	26.7	25.1	24.0	21.3
(202)	20.2	19.7	18.3	17.9	-
(222)	14.0	16.0	15.5	14.5	12.1
(100)	21.5	19.0	17.1	15.5	12.9

Table 7: lattice parameters *a* and *c* (in Å) of selected positions (as indicated in Figure 21, D).

Parameter	52	73	94	115	137
a	9.404 ± 0.002	9.421 ± 0.006	9.428 ± 0.006	9.438 ± 0.007	9.447 ± 0.004
c	6.874 ± 0.002	6.874 ± 0.008	6.872 ± 0.008	6.875 ± 0.008	6.879 ± 0.004

TRANSMISSION ELECTRON MICROSCOPY

TEM investigation can give valuable insight into the inner structure of the teeth on a nanometer-size scale and provide further information about the crystal morphology, -orientation and phase composition.
TEM investigations were carried out on an ultrathin FIB-cut, which was prepared at the edge of the tooth within the enameloid using an axial cross-section of the polished molar tooth sample, which was also used for the µ-beam WAXS and SAXS measurements (see Figure S 7). The images show elongated apatite rods, which are aligned parallel to their *c*-axis (see image Figure 24, A). An analysis of the electron diffraction pattern identified apatite as the main mineral component within the investigated area (image B). The pattern shows a distinct texture effect along the [001] direction. Electron energy loss (EELS) spectra taken from these areas showed the presence of iron-bearing phases (see image C). However, the selected area electron diffraction (SAED) pattern showed only the reflections of the apatite component, the presence of other crystalline phases were not identified. Based on this observation, it can be concluded, that the iron-bearing phase is amorphous.

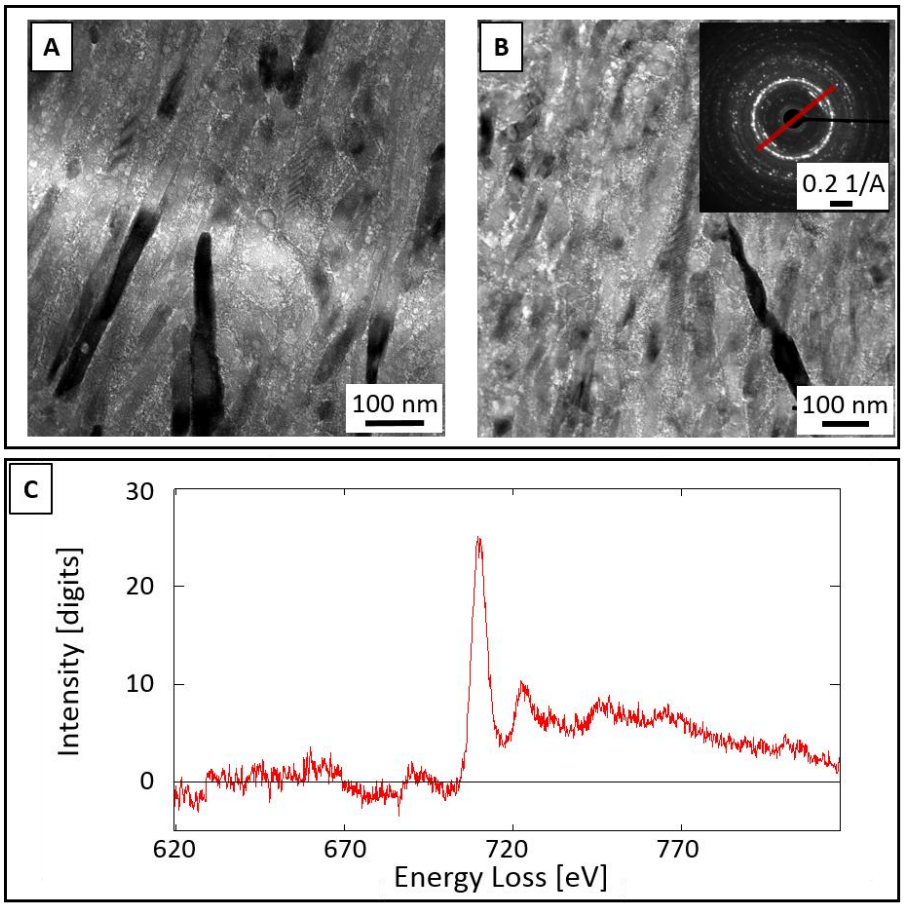

Figure 24: TEM images of a FIB-cut prepared from an axial embedded toot of *A. alluaudi* displaying aligned and elongated apatite rods in the plane of observation B: TEM image displaying the elongated crystallites with corresponding SAED pattern, which identified apatite as the main mineral phase. Highlighted is the texture effect along the [001] direction. C: Electron energy loss spectrum identified the presence of iron-bearing phases within the enameloid.

2.1.4 Mechanical properties

NANOINDENTATION

The local mechanical properties of the central tooth of the Lower pharyngeal jaw of *A. alluaudi* were investigated by nanoindentation. The mapping revealed that the highest values for the hardness and elastic modulus were found in the enameloid at the very tip of the tooth. The results of the single measurements for the hardness and elastic modulus are displayed in Figure 25 (A and B). The values follow a distinct nonlinear, stepwise gradient along the length of the measured lines. Average values of the hardness and elastic modulus changes from 5.61 ± 0.26 GPa and 105.89 ± 2.98 GPa respectively in the occlusal part the tooth. The values fall then to a local minimum of 2.82 ± 0.09 GPa and 70.84 ± 7.2 GPa respectively upon reaching an area, which appears to be non-pigmented and porous (see Figure 25, C). Afterwards, the values rise again to a local maximum of 3.35 ± 0.19 GPa and 78.24 ± 3.78 GPa respectively in the basal area of the enameloid. The values of the hardness and elastic modulus show a notable reduction upon reaching the enameloid-dentine junction, dropping to values of about 1.38 ± 0.04 GPa and

33.66 ± 1.72 GPa, respectively. The values in the porous area of the dentine displayed a quite high deviation of the absolute values and were not considered in the determination of the hardness and elastic modulus in that area.

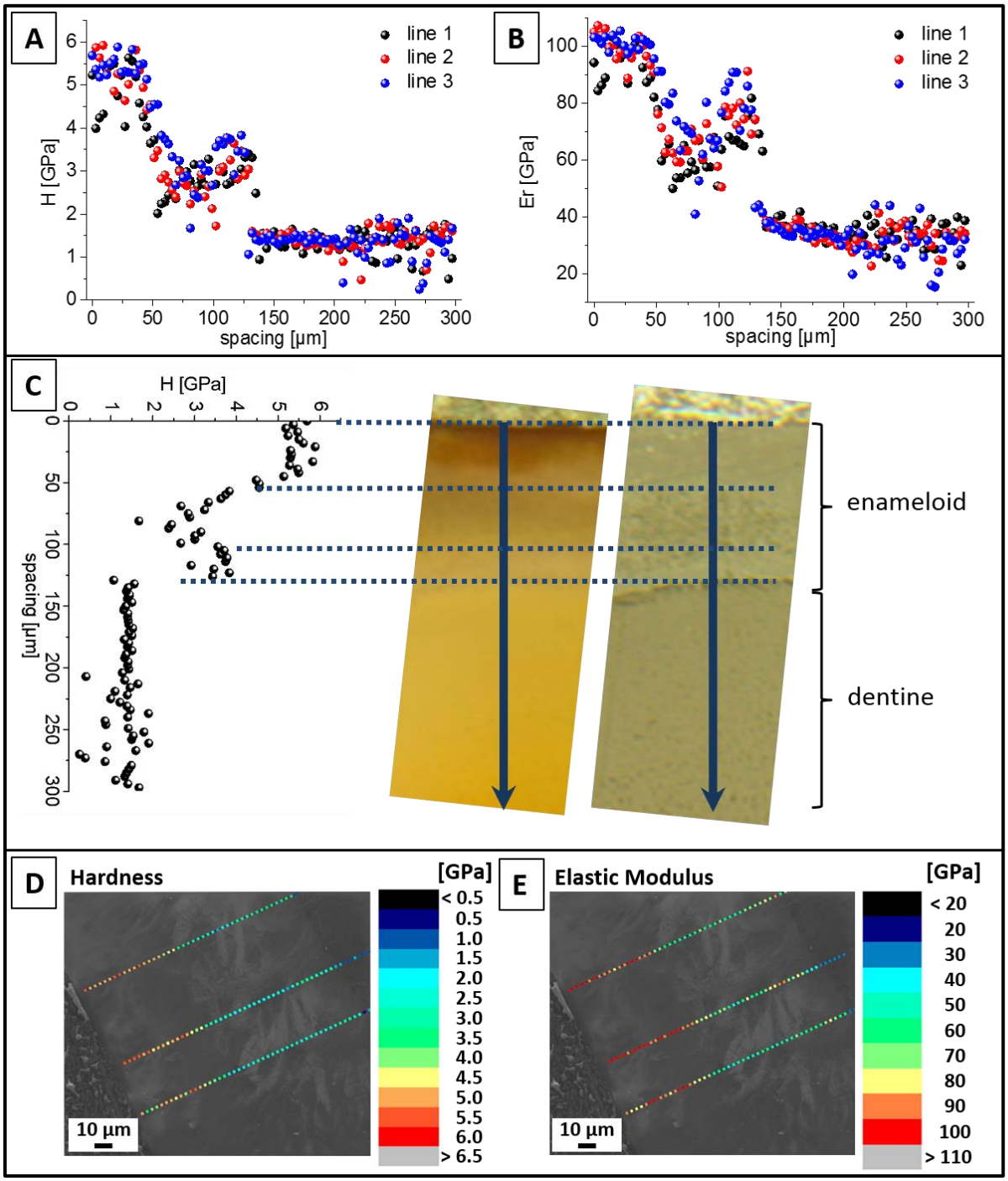

Figure 25: Mechanical properties derived from nanoindentation experiments across the axial cross-section of a tooth of *A. alluaudi.* A: results of hardness measurements of the single line scans; B: results of elastic modulus measurements of the single line scans; C: mean values of the hardness across the sample length correlated with light microscopic images (left: bright field, right: polarized light) of the cross-section of the tooth; D: colour coded hardness values directly overlayed with the positions of the corresponding indents displayed with SEM images of the polished cross-section; E: colour coded values of the elastic modulus directly overlayed with the positions of the corresponding indents displayed with SEM images of the polished cross-section.

Image D and E in Figure 25 displays an overlay of a SEM image of the axial cross-section with the color-coded hardness and elasticity values, respectively, of each indent along the length of the sample. This representation reveals that the decrease in the values correlates with an area within the enameloid, which appears highly fibrous in the SEM images.

HR-SEM AND AFM OF INDENTS

Investigating the residual impression of the indents can present other useful information about the material to assess their intrinsic mechanical properties. Thus, the indents were investigated with HR-SEM and AFM. Figure 26 displays the results of the investigation. The SEM images (Figure 26, A) revealed no cracks on the edges of the indents and the shape of the indents appear homogeneous along the sample. No obvious pile-ups under the administered loads could be observed. AFM height topology and phase contrast image of the residual indents (Figure 26, B) also revealed no obvious cracks. The edges of the investigated indents remained smooth with no obvious pile-ups around the corners of the indents. The average indent depth was around 70 nm, and the indent shape was very broad and irregular. The phase contrast image revealed a homogeneous (in composition) surface of the indents.

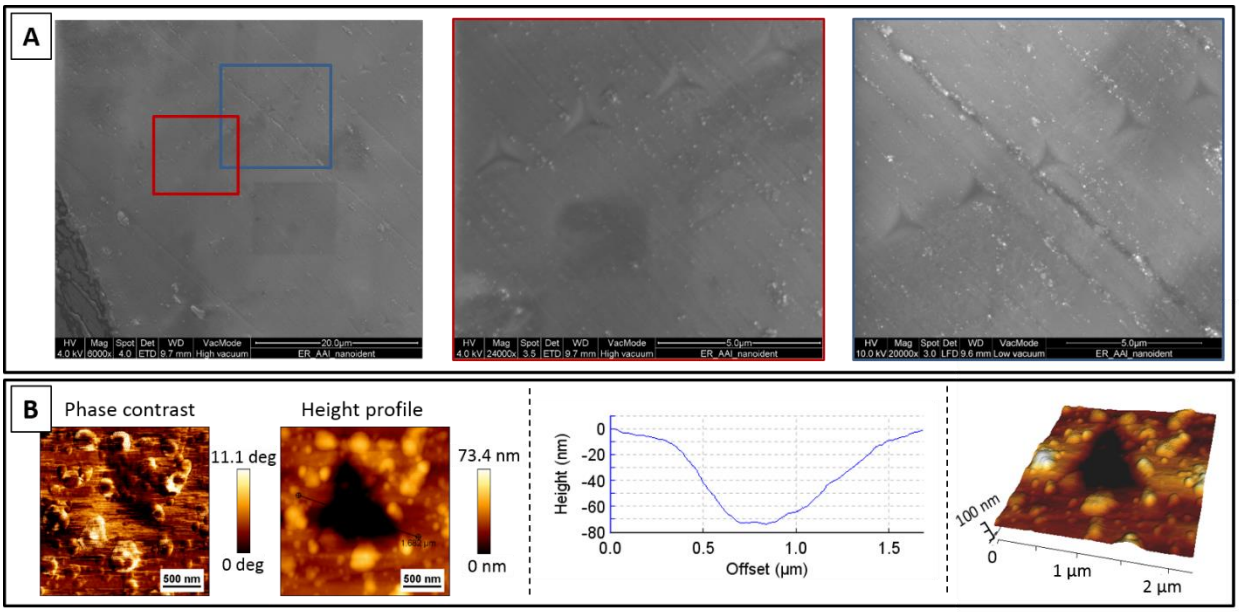

Figure 26: Images of indents of the nanoindentation measurements. A: SEM images of indents on selected positions; B: AFM images (phase contrast and height topography) of an indent with indent cross-section profile and 3D visualization.

2.2 Lake Victoria cichlids

2.2.1 *Haplochromis ishmaeli*

2.2.1.1 Morphology of LPJ and teeth

LIGHT MICROSCOPY AND HR-SEM

Haplochromis ishmaeli (Figure 27, A) is a representative of a hard diet eating species of Lake Victoria. The morphology of the LPJ (see Figure 27, B) is the same as was described for *A. alluaudi* in chapter 2.1.1. The jaw has a big massive shape with big, molariform teeth (image B, inset). The teeth in the outer region are smaller than in the inner, central area. In contrast to *A. alluaudi*, the teeth in the outer region are not papilliform but remain molariform, but generally decrease in size towards the outer area of the jaw. The occlusal top of the teeth is more rounded than the ones of *A. alluaudi.*

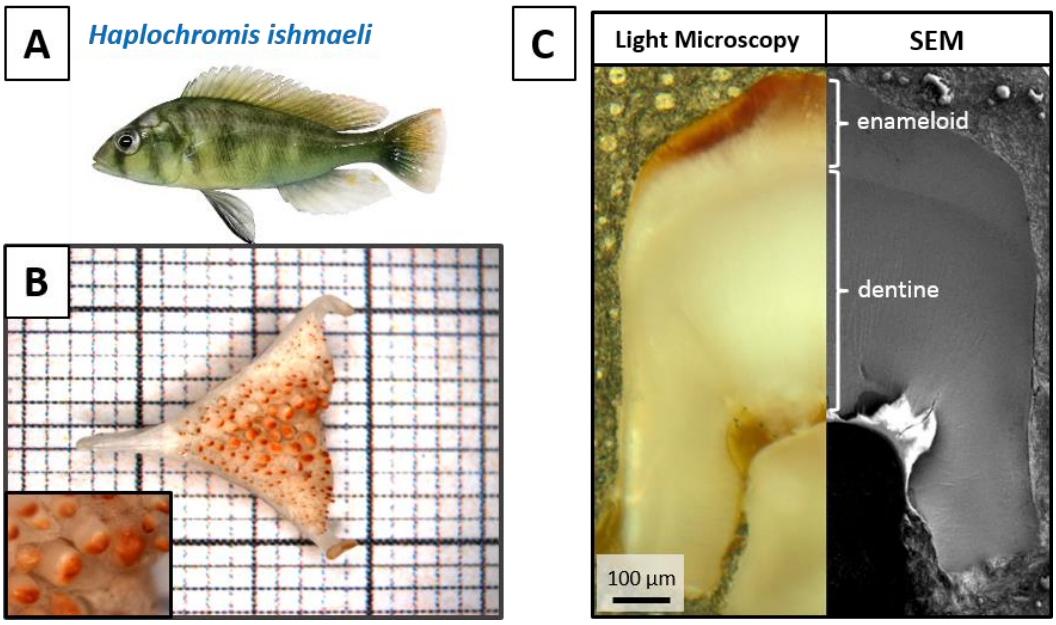

Figure 27: A: Photo of the East African cichlid *Haplochromis ishmaeli.* B: Light microscope image of the LPJ of *H. ishmaeli*, inset: biggest central teeth of the lower pharyngeal jaw. C: A merge of a light microscope image and SEM image of a polished cross-section of a central tooth of the LPJ.

Light microscopic and SEM investigations of polished cross-sections (Figure 27, C) also showed the presence of different distinct areas, identified as enameloid and dentine. The tooth cusp is more convex than the one of *A. alluaudi*. The red pigmentation is strongest in a thin line at the top surface of the tooth. This pigmentation reaches, depending on the lateral position, about 20-30 µm into the sample.

2.2.1.2 Chemical composition and distribution

EDXS

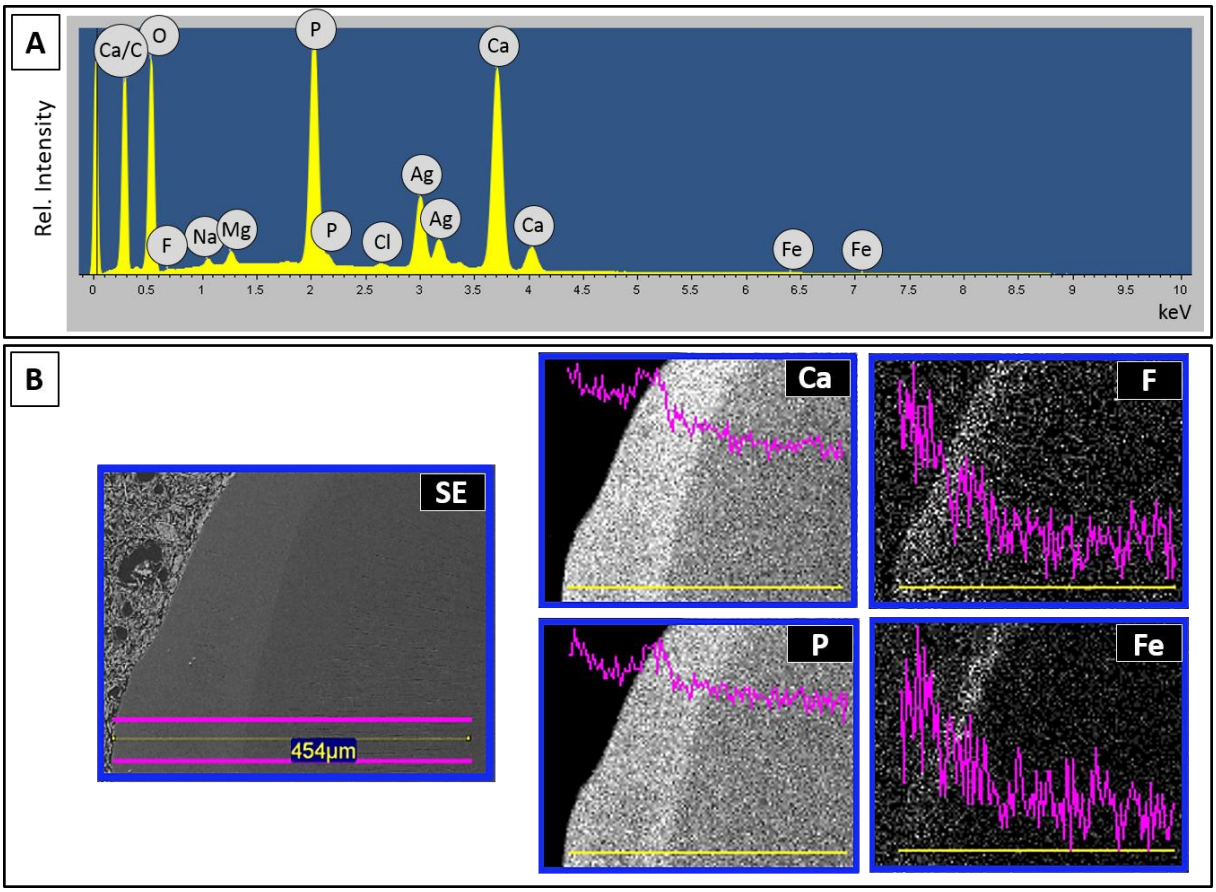

Figure 28: EDXS-measurements on polished cross-sections of a tooth of *H. ishmaeli.* A: sum spectrum of elemental analysis; B: elemental mappings and corresponding line scans of Ca, P, F and Fe in the tooth as displayed in the SE-image on the left side.

To compare the general elemental composition of this species with the other cichlids in this study an EDXS analysis was performed on the polished surface of a tooth. Qualitatively, the general elemental composition and distribution were the same for this species as was found for *A alluaudi* (see Figure 28, A). The mappings of all major elemental components and their distribution within the cross-section can be found in Figure S 8. Line scans within these mappings revealed that the teeth of *H. ishmaeli* also show a non-linear, stepwise distribution of Ca and P within the enameloid area of the tooth (Figure 28, B). They further revealed that fluorine is enriched in the enameloid, with the concentration decreasing in a non-linear fashion from the occlusal surface to the enameloid- dentine junction and falling to nearly zero in dentine area. A high concentration of iron could be found within the first 40 µm, measured from the occlusal top of the tooth, of the tooth. The thickness of the iron layer appears to be larger than the one found for *A. alluaudi*. It was also noted, that the carbon content is increased within an area between 30-110 µm, measured from the occlusal top, with a maximum at about 75 µm (see Figure S 9).

RAMAN MICROSCOPY

As was the case for the dental hard tissues of *A.alluaudi*, Raman microscopy was performed on the polished axial cross-section of *H. ishmaeli*. The measured area is displayed with a frame in Figure 29 A. The spectra along the length of the measured area are displayed in Figure 29 B. They showed the presence of characteristic apatite vibration modes at about 961 cm^{-1} ($[PO_4]^{3-}$ v_1), ~423 cm^{-1} ($[PO_4]^{3-}$ v_2), 1042 cm^{-1} ($[PO_4]^{3-}$ v_3), 592 cm^{-1} ($[PO_4]^{3-}$ v_4) and 1004 cm^{-1} ($[HPO_4]^{2-}$).[170-172] Characteristic signals of the organic component could be identified at 1438 cm^{-1} (C-H bending mode), and 1658 cm^{-1} (amide I).[173, 174] The results and peak assignments are summarized in Table S 3.

In order to better display their distribution, selected vibration modes were extracted and displayed as a function of the distance from the top of the tooth. These single spectra are shown in Figure S 11. All phosphate related modes show a significant increase in intensity from about 40 µm to 140 µm into the sample. This corresponds to the whitish, lighter colored area within the enameloid. This increase in intensity coincides with the increase in the P signal of the EDX line scan measurements. All signals relating to the organic component of the tooth are very weak and could only be detected between 40 µm – 140 µm, measured from the occlusal top of the tooth. It has to be noted, however, that this general increase in signal intensity within this area might also be a result of an increased fluorescence due to an increase in organic content, as is indicated by the increase in carbon content measured by EDX-line scans.

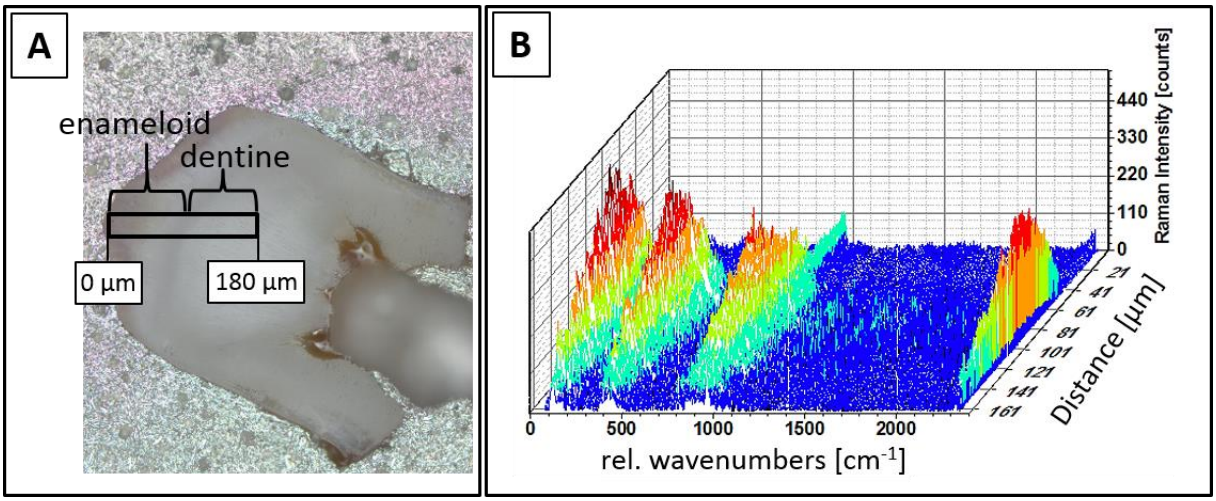

Figure 29: Light microscopic image of a polished cross-section of a tooth of *H. ishmaeli*. The frame indicates the area for the Raman-measurements. B: Summarized Raman-spectra along the length of the frame, as indicated in A.

FT-IR-SPECTROSCOPY

Complementary to Raman-microscopy, IR-spectroscopy was used to get further information about the composition of the teeth of *H. ishmaeli*. Thus, several teeth were crushed, and the resulting powder was investigated by FT-IR spectroscopy (see Figure 30). The results of the main signals are summarized in Table S 4. The IR spectrum exhibits three modes at 963 cm^{-1} ($[PO_4]^{3-}$ v_1), 1092 cm^{-1} ($[PO_4]^{3-}$ v_3) and 1155 cm^{-1} ($[PO_4]^{3-}$ v_3), which were attributed to the internal vibration of the phosphate group.[177] The IR peaks at 1643 cm^{-1}, 1549 $cm^{-1,}$ and 1238 cm^{-1} can be attributed to the amide I and the amide II and amide III respectively.[178-180] Additionally, amide A and B bands at 3070 – 3300 cm^{-1}, which overlap with the stretching modes of the water molecules were found.[178] Strong vibration modes of the CH groups were found at 2855 cm^{-1}, 2925 $cm^{-1,}$ and 2961 cm^{-1}. Furthermore, the IR spectrum revealed characteristic carbonate bands at 714 cm^{-1}, 873 cm^{-1}, 1415 $cm^{-1,}$ and 1452 cm^{-1}, indicating a B-type substitution.

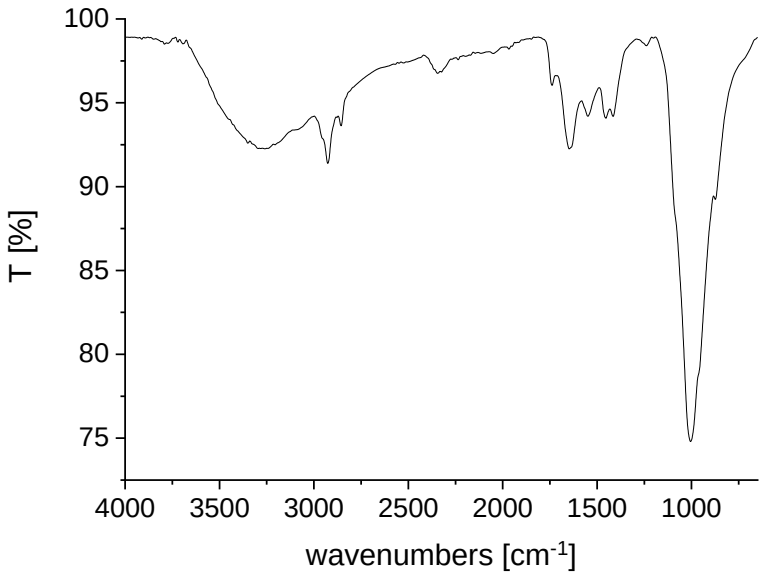

Figure 30: IR spectrum of a powdered mix of several teeth of a LPJ of *H. ishmaeli.*

2.2.1.3 Ultrastructure of the teeth

HR-SEM

In order to get insight into the inner tooth structure, HR-SEM was performed on a polished cross-section of a tooth sample and fractured teeth samples of *H. ishmaeli*. The inner structural elements were similar to the ones, which were identified for the teeth of *A. alluaudi*. SEM micrographs of the polished cross-section are displayed in Figure 31. It was observed, that similar to the ultrastructure of *A. alluaudi,* the bulk of the enameloid consists of a highly interwoven fibrous structure. The brightness is higher at the occlusal surface of the tooth, indicating a higher mineralization within the first 25 µm, measured from the occlusal top.

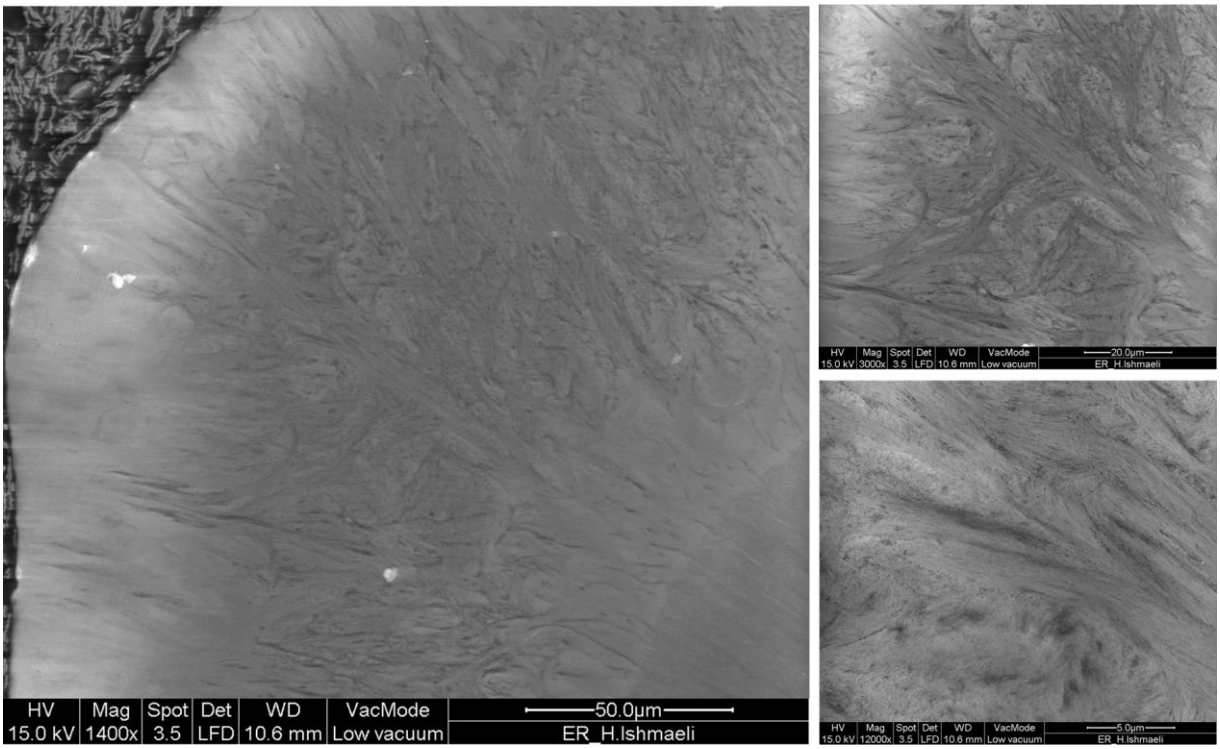

Figure 31: SEM images of a polished cross-section of a molar tooth of *H. ishmaeli*.

At the enameloid-dentine junction, the fibers appear more densely packed. This area at the junction is accompanied by a slightly higher image contrast, which indicates a slightly higher degree of mineralization within that area.

The results of the SEM investigation on fractured teeth are summarized in Figure 32. Similar structural elements were observed as for the hard diet eating morph of *A. alluaudi*. Image A displays a cross-section of a fractured tooth. Image B and C highlight the main structural motifs of the outer area of the tooth. The outer area consists of crystallites, which are oriented parallel to each other and with their long axis roughly perpendicular to the surface of the tooth (this layer is marked with (1) in the image). These crystallites are pervaded by ribbons of mineralized fibrous bundles, which run along the whole length of the long axis of the tooth (marked with (2) in the image). This arrangement creates an interwoven plywood-structure. Directly beneath these ribbons are mineralized fibers, which are oriented with their long axis perpendicular to the surface and roughly parallel to each other (marked with (3)).Image D-F highlight the pores and direction of the channels of the dentinal tubules, which run from the pulpa, through the dentine towards the enameloid area.

The images of fracture surfaces of *H.ishmaeli* revealed more clearly the structure of the dentine. The inner structure of the dentine also resembles that of *A. alluaudi.* In Figure S 12, C, the network of concentrically arranged fibers around the dentinal tubules can be clearly recognized.

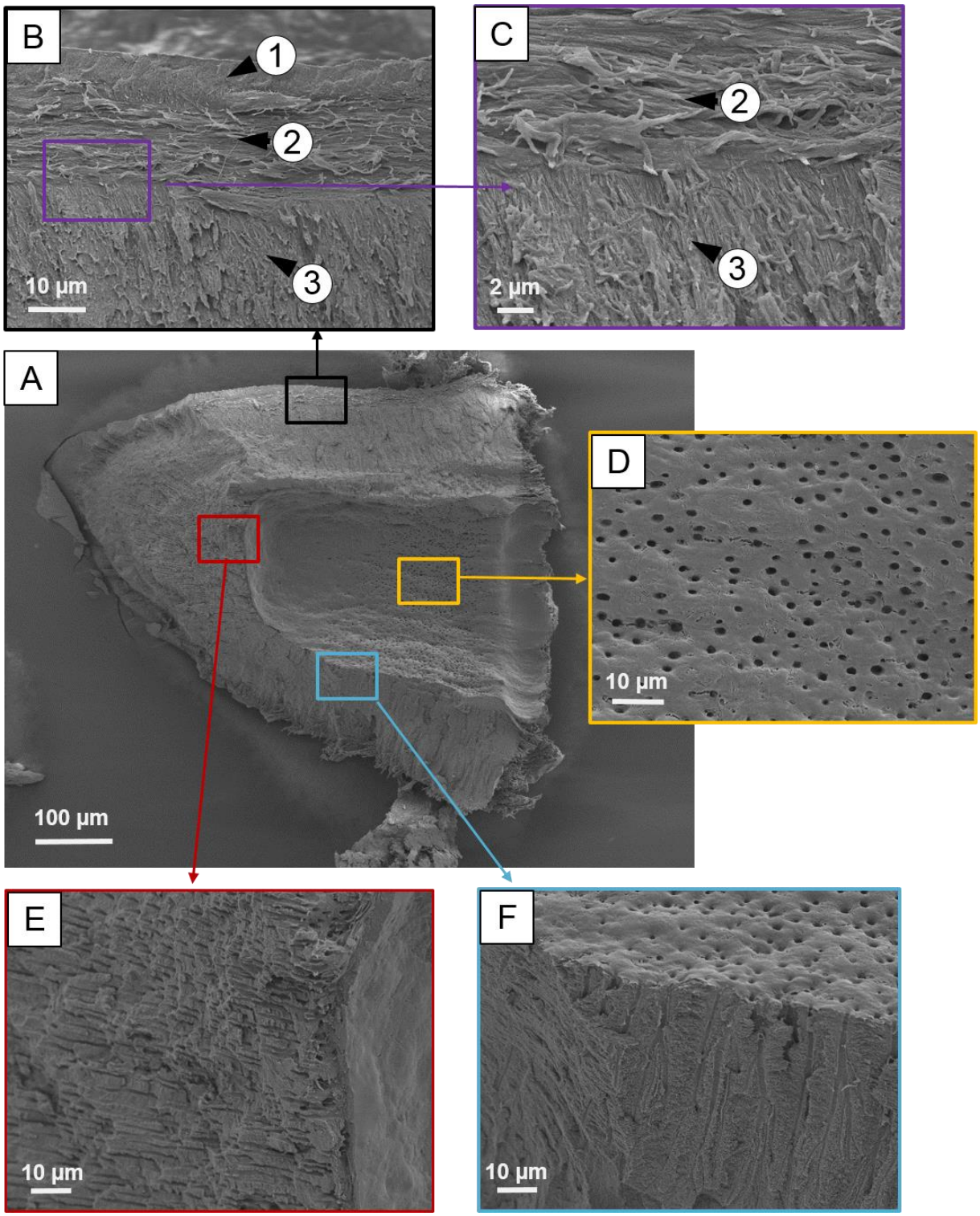

Figure 32: SEM images of fractured areas of a tooth of the LPJ of *H. ishmaeli* displaying an overview of the inner structure. A: Overview of a cross-section of the whole tooth. B: Enlargement of the outer, cervical area of the tooth. C: Enlargement of the transition of the perpendicular to the outer crystallites intergrown, fibers, which create a plywood-like structure. D: Porous area within the dentine, which show the beginnings of dentinal tubules. These tubules reach across the dentine towards the enameloid (F). Labels (1)-(3) highlight the different structural layers as described in the text.

TRANSMISSION ELECTRON MICROSCOPY

Ultrathin microtome sections of partially demineralized teeth were prepared and analyzed by TEM and HR-TEM. As the amount of provided jaws was limited for most species, this investigation was only performed for the teeth of *H.ishmaeli* within the group of investigated species of Lake Victoria.

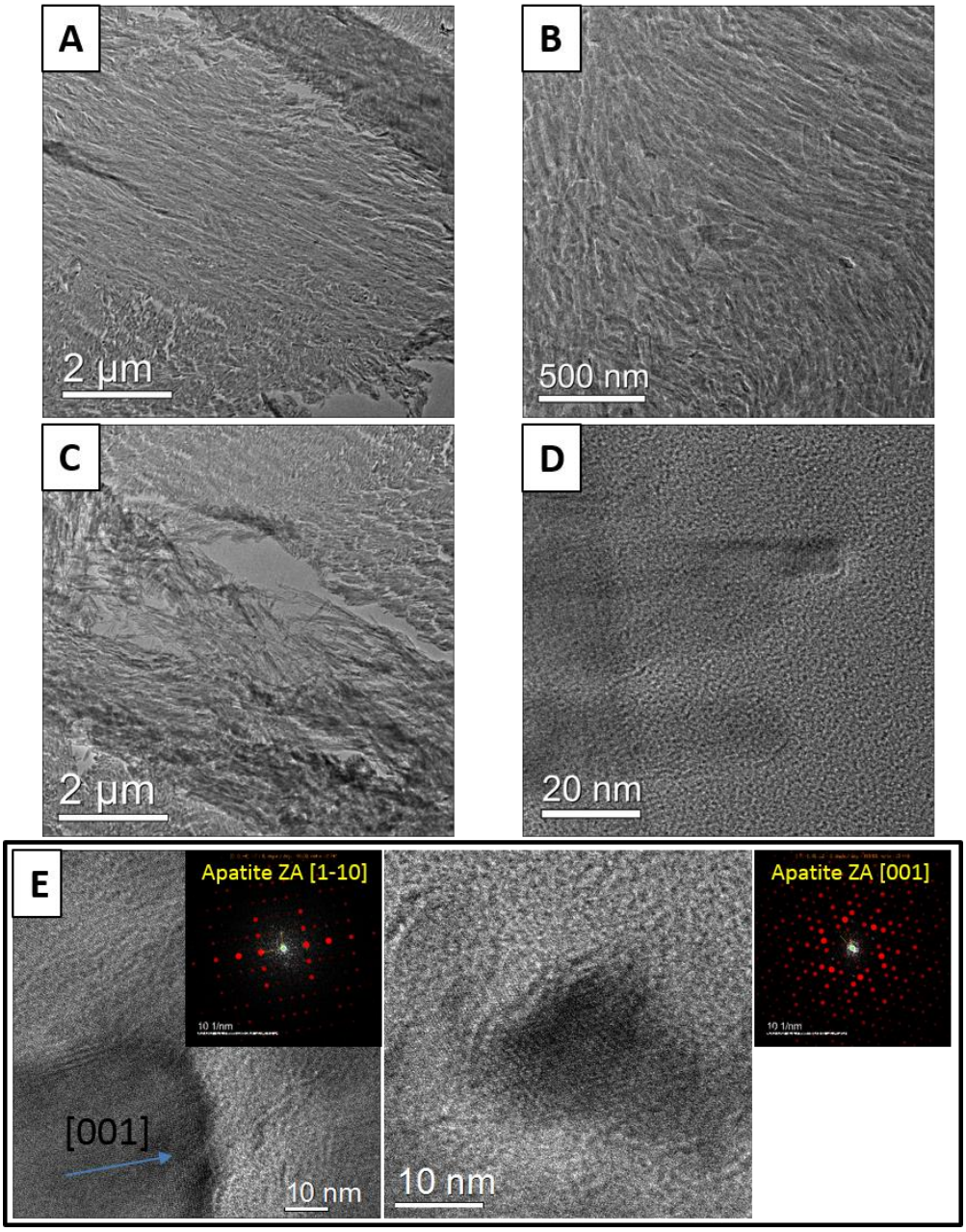

Figure 33: TEM images of a cross-section of the enameloid area of a tooth of *H. ishmaeli* A-C: elongated crystals are packed together and are oriented within the enameloid; D: structure of individual nanorods; E: HR-TEM images of single crystallites and SAED-patterns (inset).

Figure 33 displays TEM images of an ultramicrotome cross-section prepared from the enameloid of a tooth of *H. ishmaeli*. The tooth enameloid consists of tightly packed bundles of thin, elongated apatite rods (Figure 33, A-D and Figure S 14). These bundles of crystallites are generally oriented with their crystallographic *c*-axis along the elongation of the tooth towards its surface. In some areas, these crystallites follow an

intriguing pattern (image B). Figure E shows the HRTEM images and corresponding Fast Fourier transform (FFT) patterns of apatite crystallites imaged along [1-10] and [001] zone axes. These images confirmed that apatite rods are elongated along [001] direction. Figure 34 displays an overview of a transverse cross-section of a completely demineralized tooth at the outer surface of the enameloid. Here, the orientation of the fibrous bundles of collagen fibers could be observed. The outer enameloid layer is regularly pervaded by the distal ends of these bundles of collagen fibers, which originate from the dentine of the tooth. These fibers have a diameter of about 30 nm and a lateral spacing of about 63 nm periodicity of the fiber cross-striation (see Figure 34 C, D and Figure S 13). Interspacing these collagen bundles are smaller, less oriented fibrils. Similar observations were made with the fluorescence microscope images of stained, demineralized sections of teeth of *A. alluaudi* (see chapter 2.1.3).

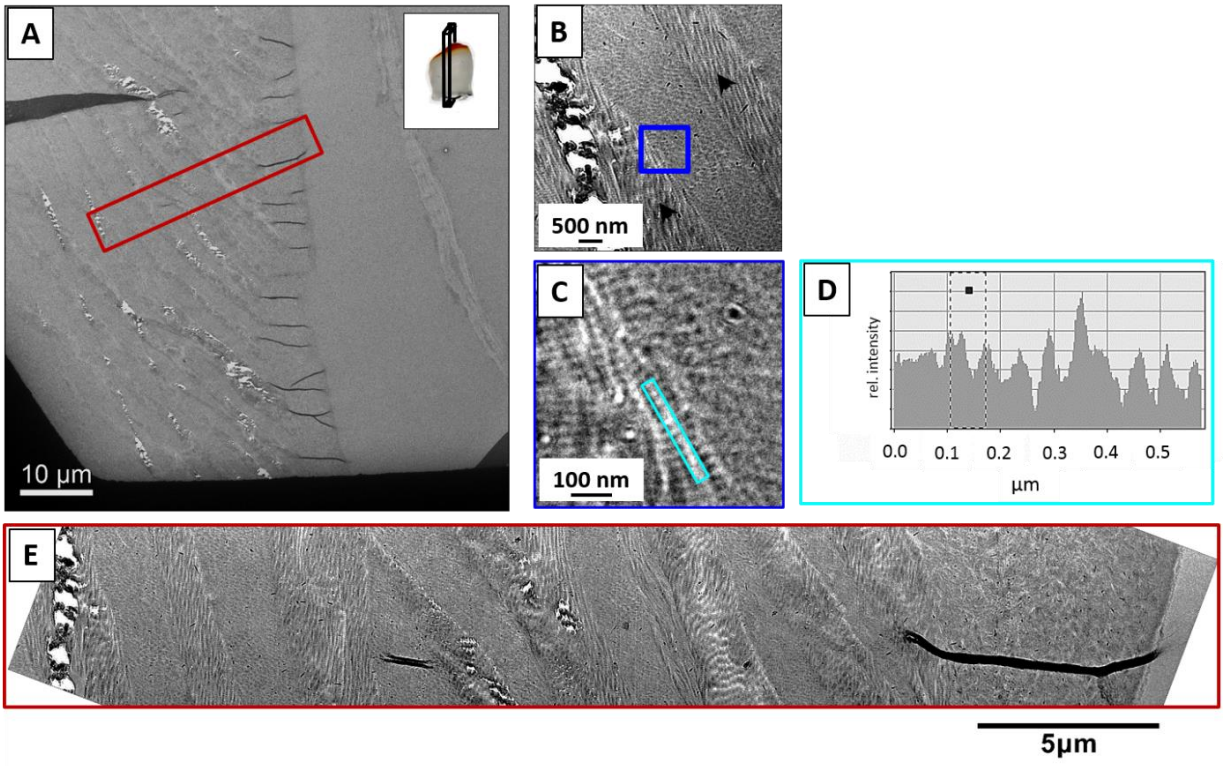

Figure 34: TEM images of a cross-section of an enameloid area of a tooth of *H. ishmaeli* .A: Overview of the outer, cervical area of the tooth. B,C: Enlargements of the interwoven, plywood-like structure towards within the enameloid. D: Graph highlighting the periodicity of the fibers. E: Detailed enlargement of the cross-section as indicated with the red frame in A.

Generally, the crystallites are arranged in bundles as well, which follow the general orientation of the collagen fibrils. This was observed with TEM images of partially demineralized sections (see Figure S 14), which showed the elongated bundles of crystallites inside the tooth structure.

ATOMIC FORCE MICROSCOPY

AFM measurements of the topography on completely demineralized microtome cuts of a tooth of *H. ishmaeli* revealed a lot of fibrous structures (see Figure 35). These fibers are partially bundled aligned but generally have a random orientation in the measured areas within the investigated area within the enameloid. Due to the low resolution of the attached microscopic setup, the exact location within the tooth could not be clearly identified.

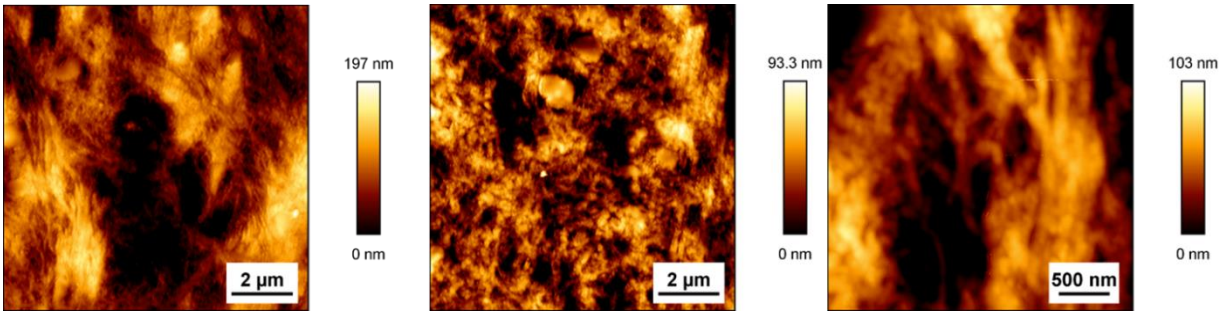

Figure 35: AFM topography image of the surface of a partially demineralized microtome cut of a tooth of *H. ishmaeli.*

2.2.1.4 Mechanical properties

NANOINDENTATION

The mechanical properties of the central molariform tooth of the lower pharyngeal jaw of *Haplochromis ishmaeli* were investigated by nanoindentation. The mapping revealed a similar stepwise profile of the mechanical properties as was found for *A. alluaudi*. The results of the single measurements for the hardness and elastic modulus are displayed in Figure 36 (A and B). The highest averaged values for the hardness, and elastic modulus were found in the enameloid at the very tip of the tooth. The general average values of the hardness and elastic modulus are 4.6 ± 0.33 GPa and 82.1 ± 3.14 GPa, respectively, at the very occlusal part tooth. The values then fall to a local minimum of 2.04 ± 0.12 GPa and 49.99 ± 3.18 GPa, respectively, of the area, that appears to be non-pigmented and less bright in the light microscope image (see Figure 36, C). Afterwards, the values rise again to a local maximum of 2.65 ± 0.06 GPa and 67.19 ± 0.29 GPa, respectively, in the basal area of the enameloid. The values of the hardness and elastic modulus show a notable reduction upon reaching the enameloid-dentine junction, dropping to a value of about 1.19 ± 0.01 GPa and 28.46 GPa, respectively. The values of the indents between approximately 250 µm- 300µm the line scans, which correlate to the quite porous area within the dentine, displayed a relatively high deviation in the absolute values. Within this area, the indenter might have hit the pores of the dentinal tubules. The results of these indents thus showed lower, not representative values and were thus not considered in the determination of the hardness and elastic modulus for that area.

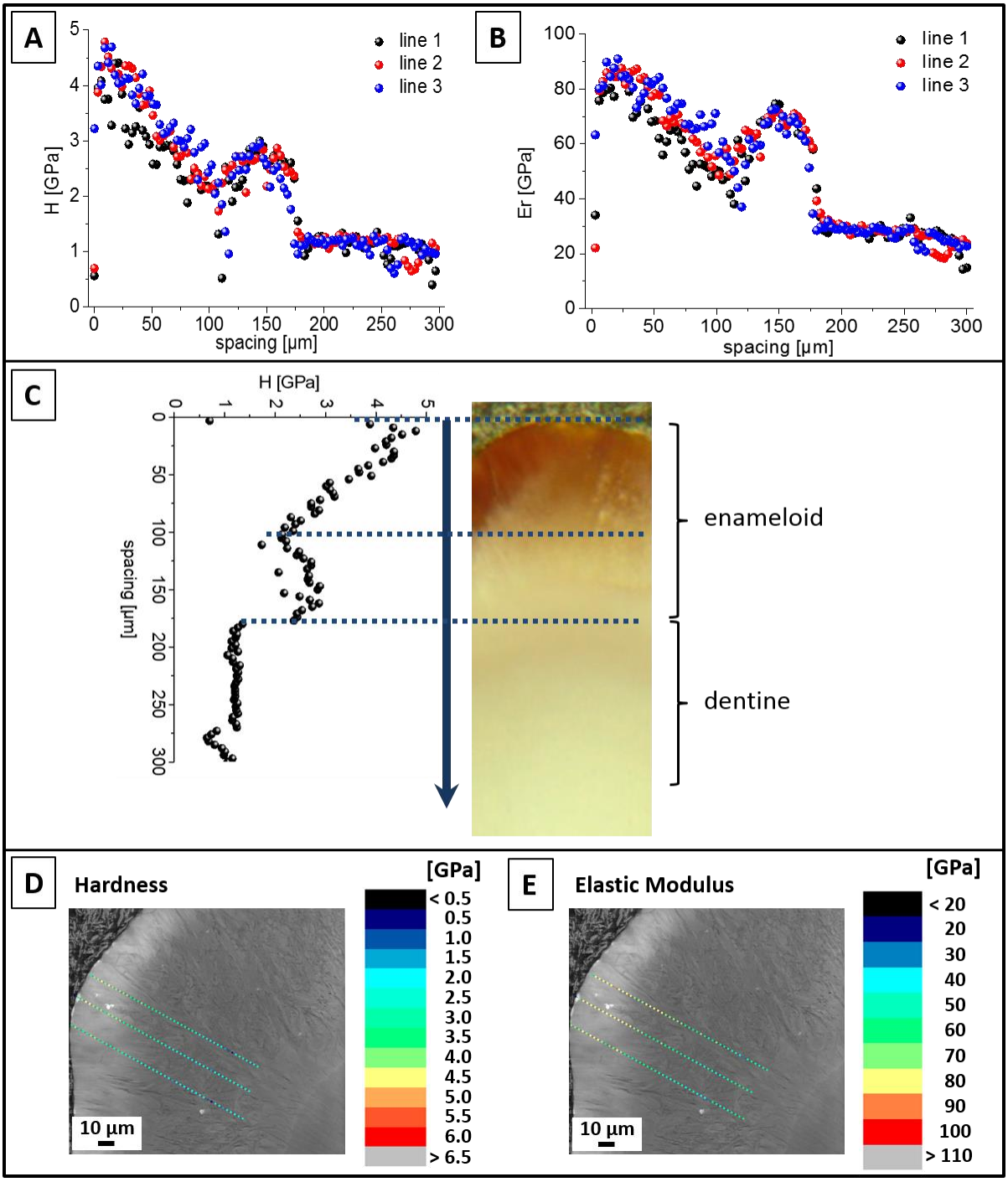

Figure 36: Mechanical properties derived from nanoindentation experiments across the axial cross-section of a tooth of *H. ishmaeli.* A: results of hardness measurements of the single line scans; B: results of elastic modulus measurements of the single line scans; C: mean values of the hardness across the sample length correlated with light microscopic images (left: bright field, right: polarized light) of the cross-section of the tooth; D: colour coded hardness values directly overlayed with the positions of the corresponding indents displayed with SEM images of the polished cross-section; E: colour coded values of the elastic modulus directly overlayed with the positions of the corresponding indents displayed with SEM images of the polished cross-section.

Figure 36 displays an overlay of a SEM image of the axial cross-section with the color-coded hardness (Figure D) and elasticity values (Figure E) of each indent along the length of the sample. Note, that the color-code is the same as the one used for *A. alluaudi*. This representation reveals that the step-wise decrease in the values correlates with a decrease in mineral content. This can be assumed due to the weaker contrast in the SEM image.

AFM OF INDENTS

Figure 37 displays the AFM height topology and phase contrast images of the residual imprints of the indents made on the surface of the polished tooth (full summary in Figure S 15). The investigation revealed no obvious cracks at the edges of the indents. At the very top and about 90 µm into the sample, slight pile-ups around the edges of the indents could be observed. The surface of the sample in between the indents and the edges of the indents remained smooth (see indent profiles in Figure 37 and Figure S 15). The triangular shape of the indents could be clearly recognized. About 50 µm, measured from the occlusal top of the enameloid towards the dentine, granular structures could be observed on the surface. These grains had a diameter of approx. 80-120 nm. The appearance of these grains coincides with the end of the reddish, iron-bearing area. No change in phase contrast, which could indicate a change in the material composition, could be detected.

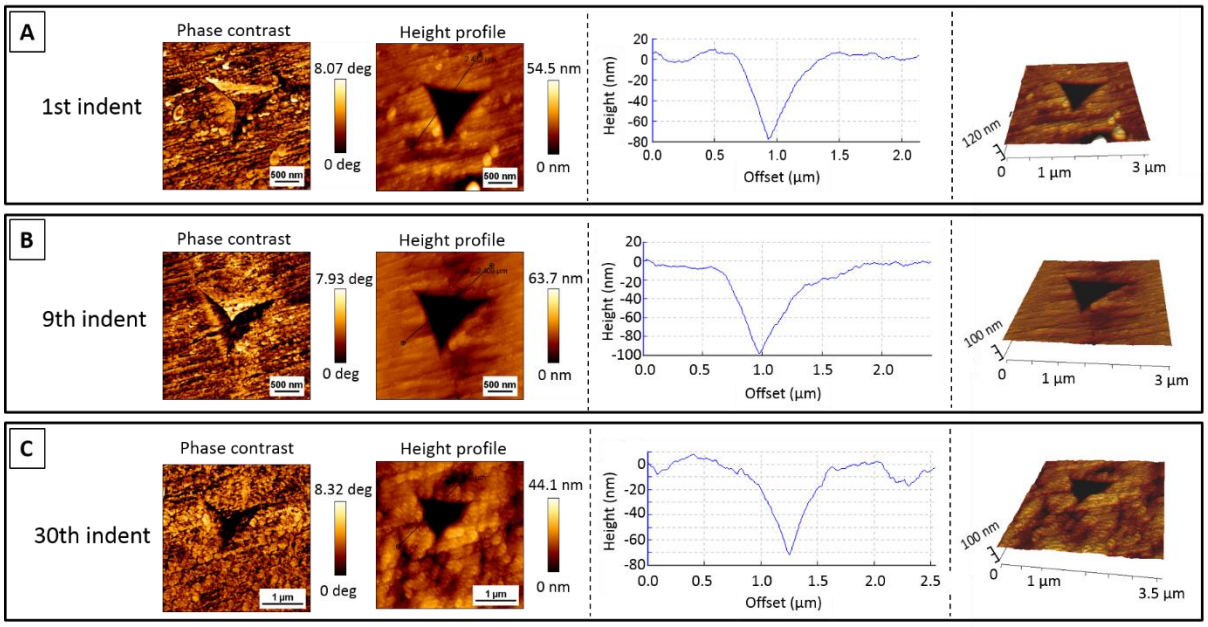

Figure 37: AFM images (phase contrast and height topography) with corresponding cross-section profiles of the indents and 3D visualizations of selected indents on the cross-section of a tooth of *H. ishmaeli*.

2.2.2 *Haplochromis sauvagei*

2.2.2.1 Morphology of LPJ and teeth

LIGHT MICROSCOPY AND HR-SEM

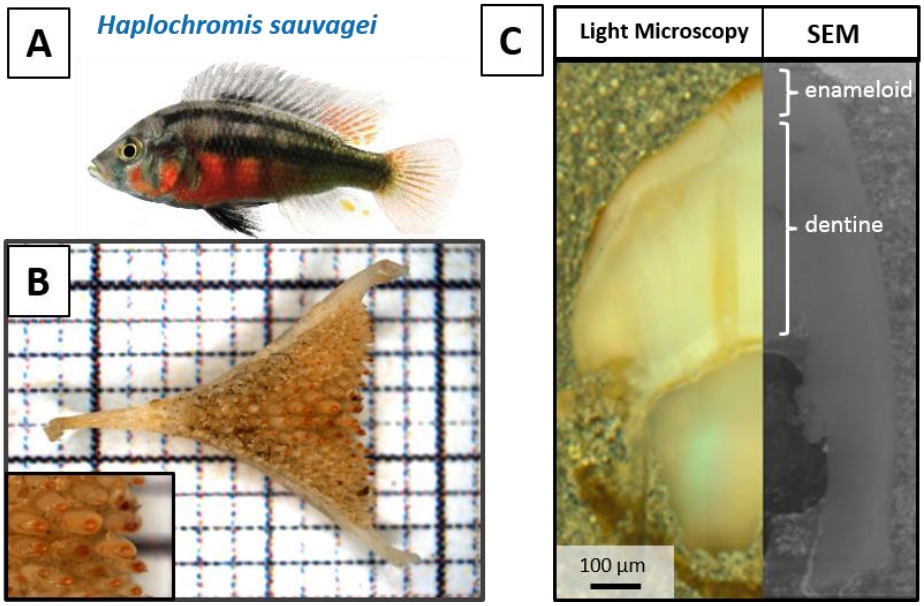

Figure 38: A: Photo of the East African cichlid *Haplochromis sauvagei*. B: Lower pharyngeal jaw of *H. sauvagei*, inset: biggest central teeth of the LPJ. C: Merge of a light microscope image and SEM image of a polished cross-section of a central tooth of the LPJ.

Haplochromis sauvagei (Figure 38, A) is an example of a species, which feeds on a hard-soft diet mix. The macroscopic morphology was investigated with Light microscopy and SEM. The morphology of the LPJ (see Figure 38, B) is the same as was described for *A. alluaudi* in chapter 2.1.1. The jaw has size and shape appeared less robust than the pure hard diet eating species. The tooth shape of the biggest central teeth are not clearly molariform but are larger and more robust than pure soft diet eating species (see chapter 3.2.3.1 or chapter 3.2.4.1). The morphology resembles a mix of molariform and papilliform teeth. The central teeth appear more elongated in the axial direction. The tips of the teeth also appear red to brown. Light microscopy and SEM (Figure 38, C) revealed that the teeth are structured in at least two areas, which can be assigned to the enameloid and dentine area. The thickness of the enameloid is a mix of the molariform and papilliform teeth as well. Specifically, the enameloid has a slightly elongated tip, similar to that of the soft diet eating fish species, it is still a lot thinner than the big molariform teeth of the hard diet eating cichlids. The red color appears only at a small area at the very tip of the tooth in the enameloid region.

2.2.2.2 Chemical composition and distribution

EDXS

Elemental analysis was also performed for this species using EDXS on the polished surface of a tooth sample. Qualitatively. the general elemental composition and distribution were the same for this species as was found for *A alluaudi* and *H. ishmaeli* (see Figure 39, A). In addition, sulfur could be detected, although the signal intensity is very low. The mappings of all major elemental components and their distribution within the cross-section are displayed in Figure S 16. The lines can within these mappings revealed that the teeth of *H. sauvagei* do not show a clear non-linear, stepwise distribution of Ca and P within the enameloid area of the tooth (Figure 39, B). The concentrations of Ca and P remain on a similar high level within the enameloid. As for the other cichlid species, the scans also show that fluorine is enriched in the enameloid, which decreases from the occlusal surface towards the enameloid-dentine junction and falling to nearly zero in the dentine area. A high concentration of iron could be found in a distinct area in the first 25 µm measured from the occlusal top of the tooth.

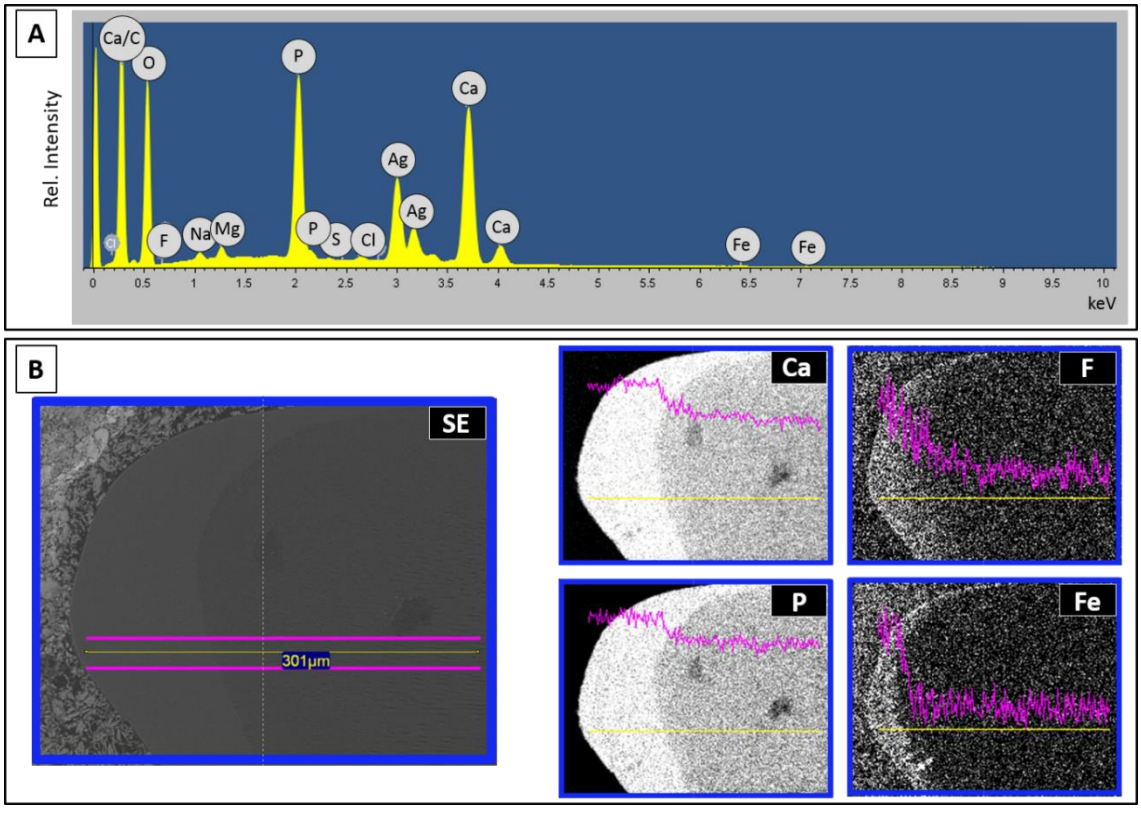

Figure 39: EDXS-measurements on polished cross-sections of a tooth of *H. sauvagei.* A: sum spectrum of elemental analysis; B: elemental mappings and corresponding line scans of Ca, P, F and Fe in the tooth as displayed in the SEM-image on the left side.

RAMAN MICROSCOPY

The polished axial cross-section of *H. sauvagei* was also investigated with Raman microscopy. The measured area is marked with a frame in image A in Figure 40. The measured Raman-spectra along the length of the sample are displayed in image B. It was observed, that except for the $[PO_4]^{3-}$ v_1- vibration the intensity of all peaks were very low. However, the presence of characteristic apatite vibration modes could be detected at 962 cm^{-1} ($[PO_4]^{3-}$ v_1), 430 cm^{-1} ($[PO_4]^{3-}$ v_2), 1045 cm^{-1} ($[PO_4]^{3-}$ v_3) and 589 cm^{-1} ($[PO_4]^{3-}$ v_4).[170-172] An overlay of all collected Raman spectra of the phosphate v_1 band of the cross-section additionally revealed a small shift in wavenumbers of about 3 cm^{-1} towards lower wavenumbers from the occlusal area of the tooth towards the dentine (see Figure S 17).
Similar to the procedure of the previous samples, selected vibration modes were displayed as a function of the distance from the top of the tooth in order to better display their distribution. However, due to the low intensity of the signal, no characteristic distributions patterns could be observed, except for the $[PO_4]^{3-}$ v_1- vibration.

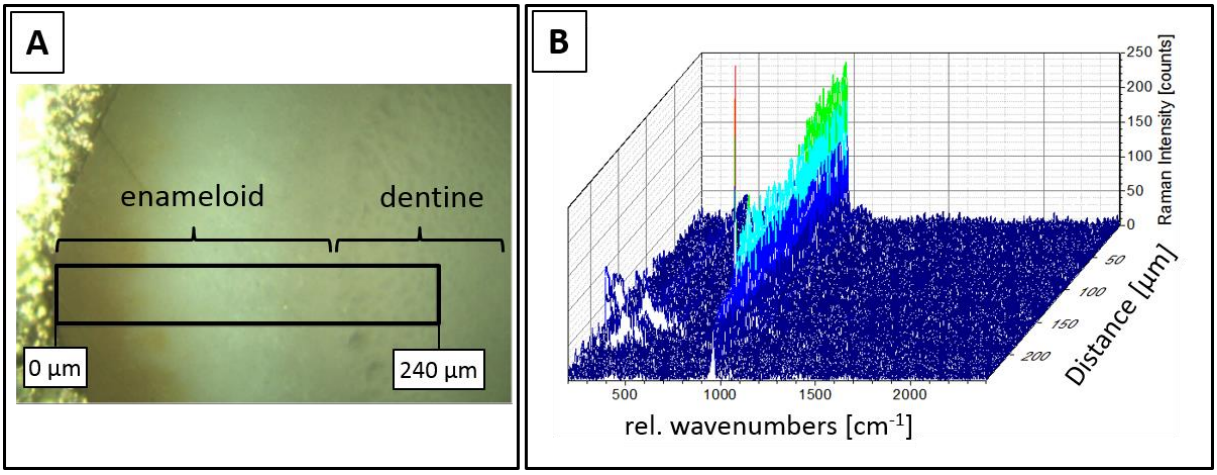

Figure 40: Light microscopic image of a polished cross-section of a tooth of *H. sauvagei.* The frame indicates the area for the Raman-measurements. B: Summarized Raman-spectra along the length of the frame, as indicated in A.

Thus, 5 additional measurements were performed in distinct positions in small areas along the length of the tooth as is indicated with the frames in Figure 41, A. The respective spectra are displayed in B. In addition to the phosphate related peaks, an additional signal of the organic component could be identified at 1453 cm^{-1} (C-H bending mode).[173, 174] Furthermore, the spectra also showed a characteristic carbonate band at 1070 cm^{-1}. The results and peak assignments are summarized in Table S 5 in appendix A. These measurements confirm that the phosphate related peaks are shifted about 3 cm^{-1} towards lower wavenumbers and the signal intensity drops from the occlusal area at the top of the tooth towards the dentine area (see image C).

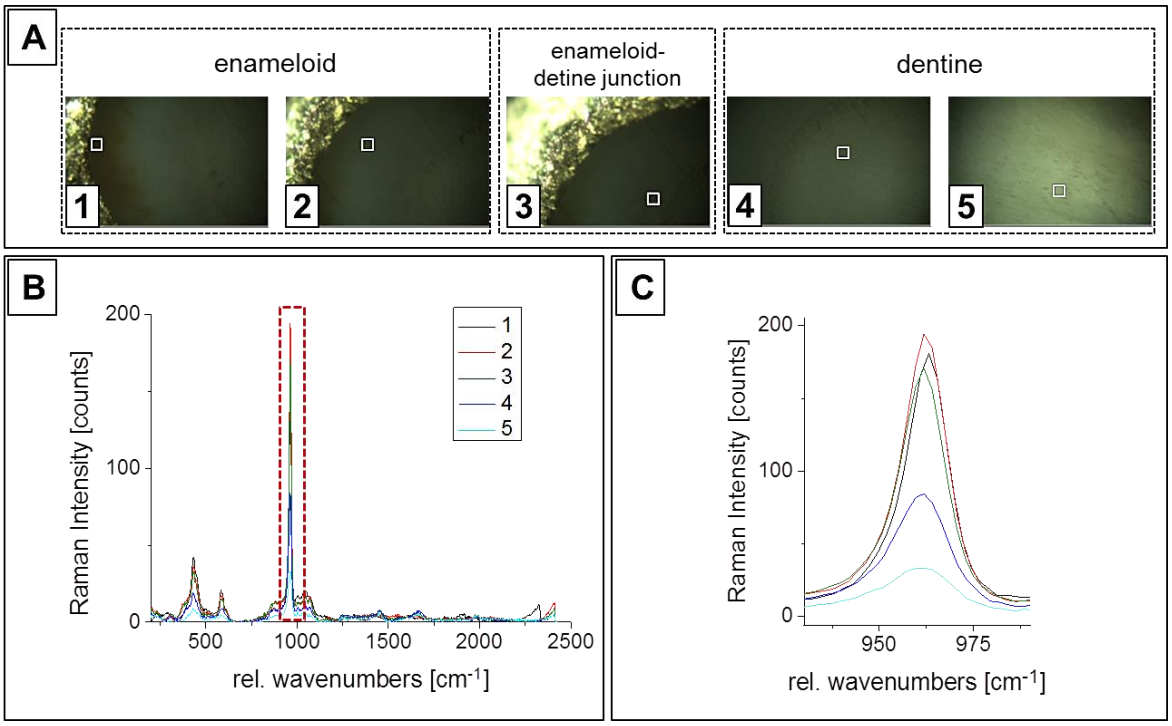

Figure 41: Results of the Raman measurements on selected areas on the polished tooth cross-section of *H. sauvagei.* A: light microscopic images of the surface of the tooth. The measurement positions are indicated with a white frame. B: Corresponding Raman spectra on the positions as indicated in A. C: enlargement of the phosphate v_1 vibration mode as indicated with the red frame in B.

FT-IR-SPECTROSCOPY

Teeth of the LPJ of *H. sauvagei* were crushed, and the resulting powder was investigated by FT-IR spectroscopy. The results are summarized in Table S 6 in the appendix A. In the IR spectrum (Figure 42) three modes at 963 cm^{-1} ($[PO_4]^{3-}$ v_1), 1093 cm^{-1} ($[PO_4]^{3-}$ v_3) and 1155 cm^{-1} ($[PO_4]^{3-}$ v_3) could be observed, which were attributed to the internal vibration of the phosphate group.[177] The IR peaks at 1642 cm^{-1}, 1544 $cm^{-1,}$ and 1238 cm^{-1} were attributed to the amide I, amide II and amide III respectively.[178-180] Furthermore, amide A and B bands at 3070 – 3300 cm^{-1}, which overlap with the stretching modes of the water molecules, could be observed.[178] Strong vibration modes of the CH groups were found at 2856 cm^{-1}, 2926 $cm^{-1,}$ and 2964 cm^{-1}. These IR measurements confirm the presence of carbonate by measuring characteristic bands at 714 cm^{-1}, 871 cm^{-1}, 1415 $cm^{-1,}$ and 1452 cm^{-1}, indicating a B-type substitution.

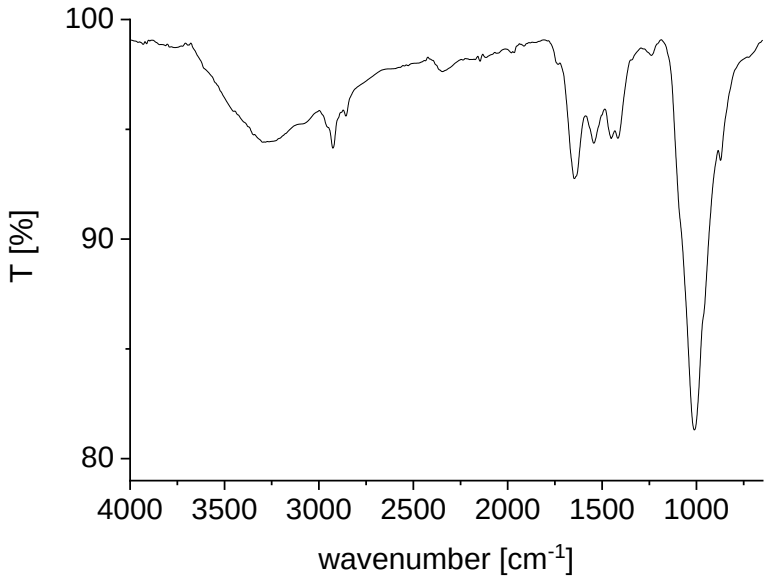

Figure 42: IR spectrum of a powdered mix of teeth of a LPJ of *H. sauvagei.*

2.2.2.3 Ultrastructure of the teeth

HR-SEM

In order to get insight into the inner structure of the teeth of *H. sauvagei* HR-SEM was performed on a polished cross-section of an axial tooth and fractured tooth samples. The SEM images of the polished cross-section are displayed in Figure 43.

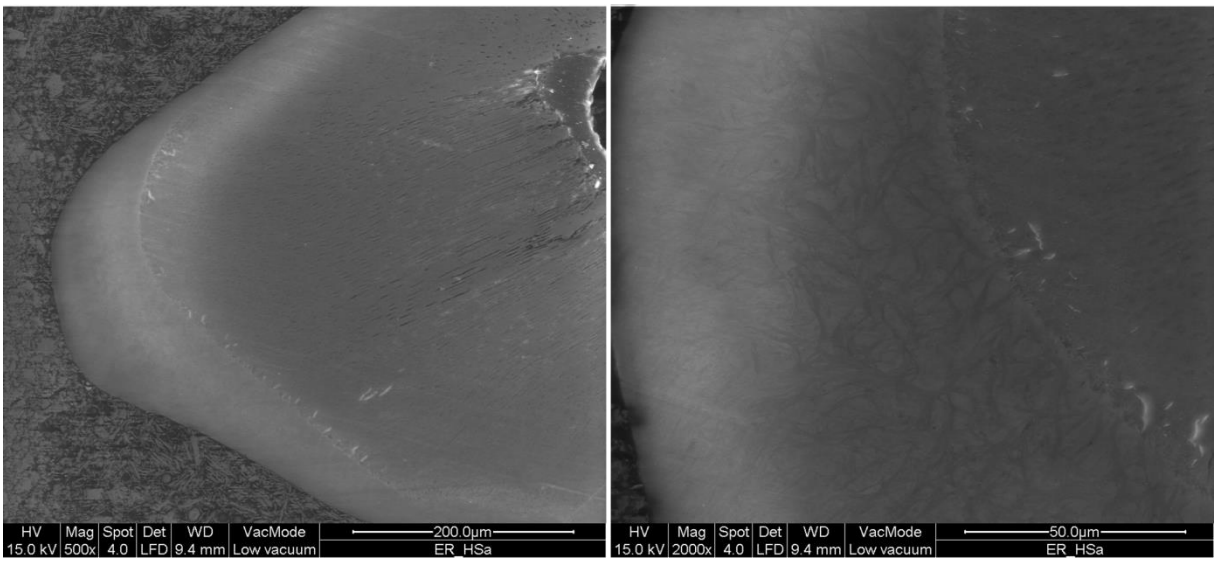

Figure 43: SEM images of a polished cross-section of a tooth of *H. sauvagei*.

These results show that similar to the teeth of the other investigated species, the bulk consists of a tangled arrangement of mineralized fibers. The mineral content, as is indicated by the brighter areas within the image, appears to be higher towards the occlusal surface of the tooth within the first approx. 40 µm, measured from the top. The dentine shows the typical arrangement of the dentinal tubules, which range from the pulpa, through the dentine, towards the enameloid. A similar structural setup was observed for the hard diet eating species.

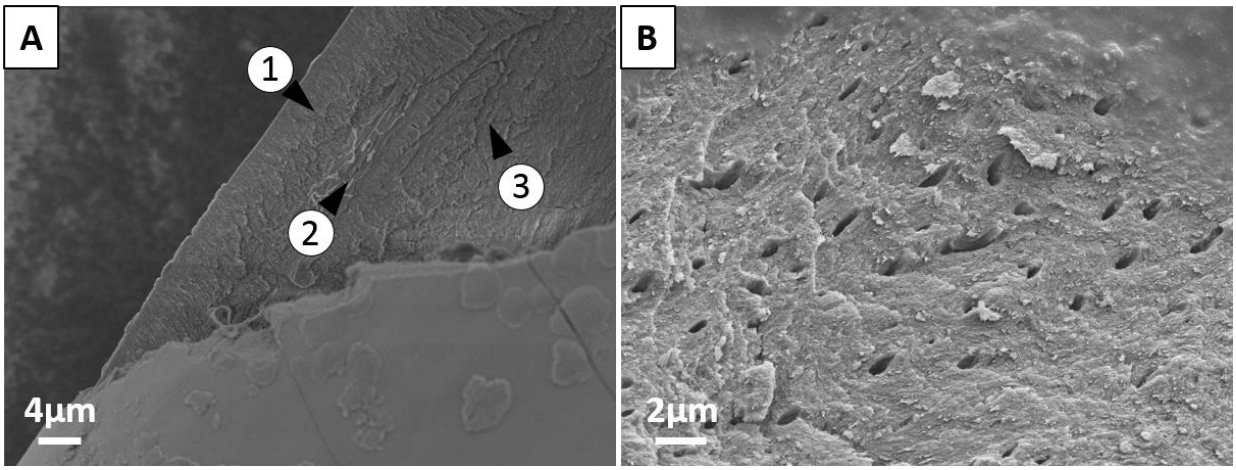

Figure 44: Scanning electron micrographs of fracture areas of crushed teeth of *H. sauvagei.* A: Overview of the main structural elements, which were identified for the outer area of the tooth. Labels (1)-(3) in A highlight the different structural layers as described in the text. B: Holes of the dentinal tubules within the dentine.

The SEM micrographs of the fractured teeth are displayed in image A and B of Figure 44. The teeth showed similar structural elements, which were identified within the teeth of the LPJ's of *A. alluaudi* and *H. ishmaeli*. Image A of Figure 44 exemplarily highlights the main features of the outer tooth area. The very outer surface has a thin mineralized layer. Following this layer is an arrangement of crystallites, whose long axes are nearly perpendicular to the surface and which are roughly parallel to each other (marked as (1) in image A). Directly beneath this layer are the interwoven fibers, which run along the long axis of the tooth and are perpendicular to the mentioned crystallites of the previous layer (marked with (2) in image A). This arrangement creates an interwoven-plywood structure. Following this arrangement is an area with even more decussated crystallites, whose orientation borders on a near random orientation (marked as (3) in image A). Image B in Figure 44 highlights the porous area within the dentine, which stem from the dentinal tubules, which run along the length of the tooth.

2.2.2.4 Mechanical properties

NANOINDENTATION

The mechanical properties of the central tooth of the LPJ of *Haplochromis sauvagei* were investigated by nanoindentation. The results of the single measurements for the hardness and elastic modulus are displayed in Figure 45 (A and B). The highest averaged values for the hardness, and elastic modulus were found in the enameloid at the occlusal area of the tooth. The values also follow a distinct nonlinear, step-wise gradient along the length of the measured lines although the single steps are not as pronounced as for the pure hard diet eating species. Average values of the hardness and elastic modulus were 4.94 ± 0.25 GPa and 95.58 ± 2.74 GPa, respectively, at the very tip of the tooth. The values then fall to a local minimum of 2.54 ± 0.06 GPa and 67.94 ± 2.32 GPa, respectively, at about 60 µm from the occlusal top. The values then rise again to a local maximum of 2.87 ± 0.07 GPa and 66.9 ± 3.09 GPa in the basal area of the enameloid, which is about 100 µm from the top of the tooth (see Figure 45, C). At the enameloid-dentine junction a notable reduction of the values to about 1.26 ± 0.07 GPa and 29.51 ± 1.33 GPa, respectively, was measured. From the light microscopic images, it was observed, that the highest values correlate with the slightly red pigmented area at the occlusal surface of the tooth.
Figure 45 displays an overlay of a SEM image of the axial cross-section with the color-coded hardness (Figure D) and elasticity values (Figure E) of each indent along the length of the sample. Note, that the color-code was kept the same for all investigated species for comparison reasons. This representation does not indicate any correlation of the hardness and elastic modulus with structural elements, except their drastic reduction upon reaching the dentine area. However, the previous SEM investigations on the polished sample revealed (see Figure 43) that the mineral content appeared to be higher towards the occlusal surface of the tooth within the first approx. 40 µm, as was indicated by the brighter areas within the image. This area coincides with the highest values of the hardness and elastic modulus within the distal area of the enameloid, which were determined by these line scan measurements.

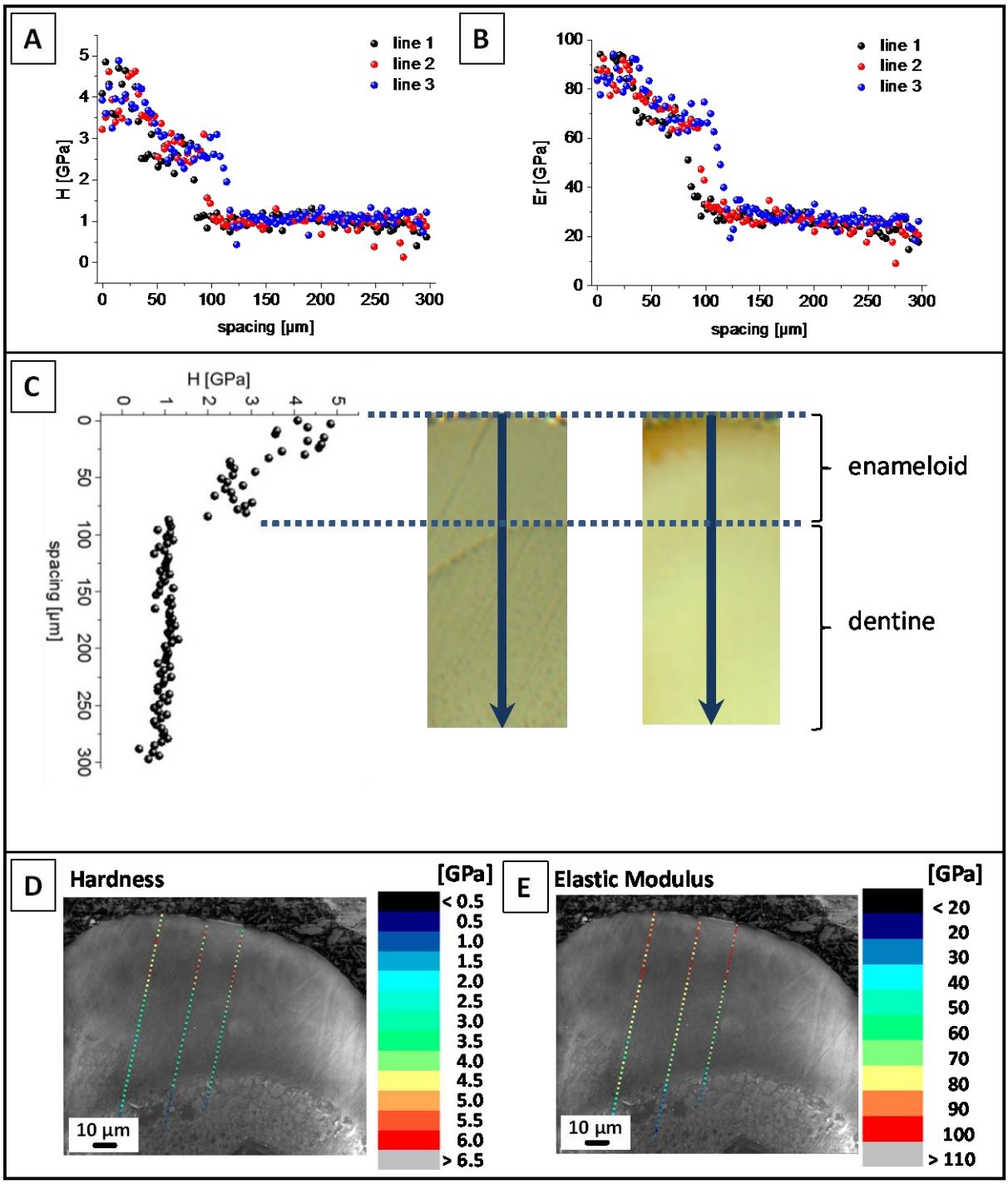

Figure 45: Mechanical properties derived from nanoindentation experiments across the axial cross-section of a tooth of *H. sauvagei.* A: Results of hardness measurements of the single line scans; B: Results of elastic modulus measurements of the single line scans; C: Mean values of the hardness across the sample length correlated with light microscopic images (left: bright field, right: polarized light) of the cross-section of the tooth; D: Colour coded hardness values directly overlayed with the positions of the corresponding indents displayed with SEM images of the polished cross-section; E: Colour coded values of the elastic modulus directly overlayed with the positions of the corresponding indents displayed with SEM images of the polished cross-section.

AFM OF INDENTS

Figure 46 displays the AFM height topology and phase contrast images of the residual indents made on the surface of the polished tooth (full overview in Figure S 15). The residual intents showed a very irregular shape when compared to the hard diet cichlid species, e.g., *H. ishmaeli*. Especially the indents close to the occlusal surface show this irregular shape. A comparison of the indent-profiles revealed that the cross sections of the indents increased in width from the occlusal top towards the dentine area. With the help of the phase contrast images, it was observed, that the surface has a very grainy structure. The diameter of these grains is about 80-120 nm. The investigation revealed some small cracks at the edges of some indents. The cracks follow the boundaries of the nanograins. No obvious pile-ups at the edges of the indents could be observed by extracting a height profile along the length of the indents. No increased phase contrast, which could indicate a change in material composition, could be observed from the occlusal area of the tooth towards the dentine. However, the general phase shift is a bit higher as compared with the sample of the hard diet eating species.

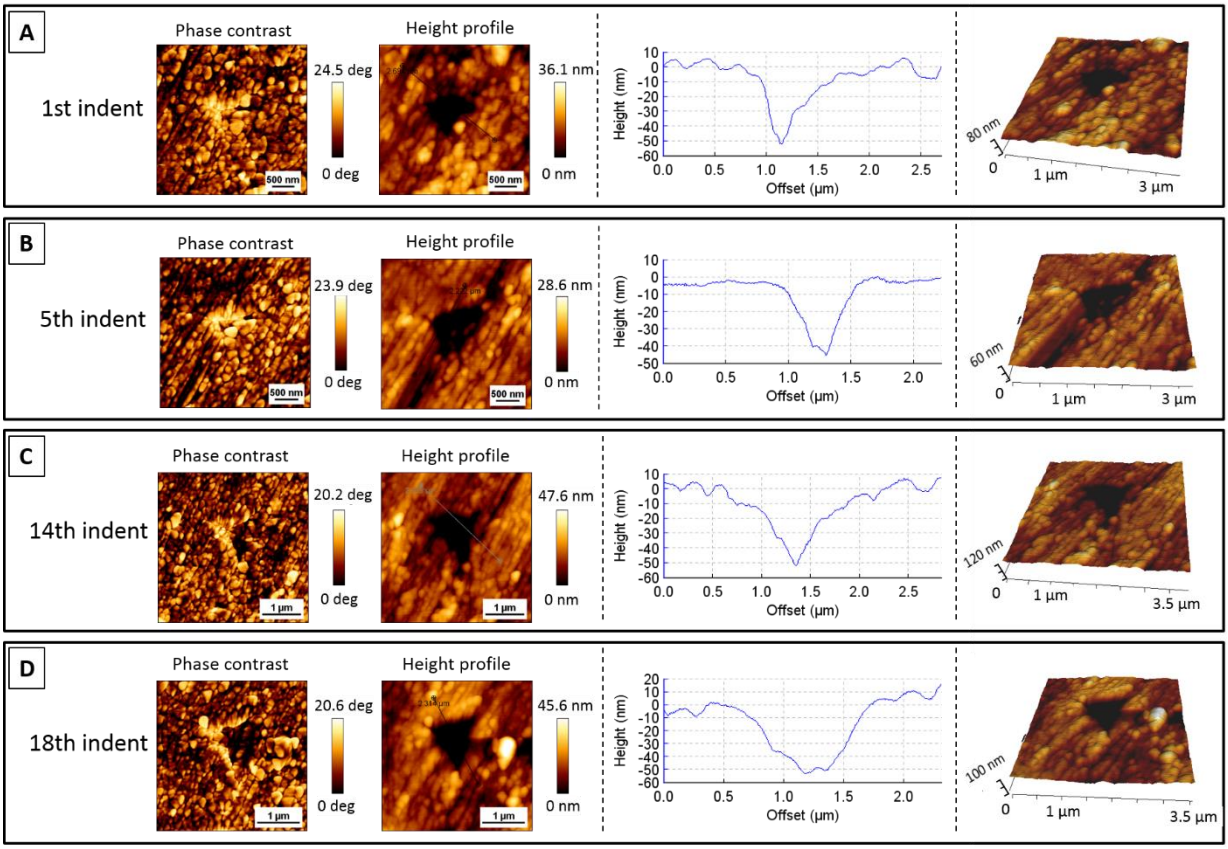

Figure 46: AFM images (phase contrast and height topography) of selected indents the axial cross-section of a tooth of *H. sauvagei* along the length of the sample, with indent cross-section profiles and 3D visualization.

2.2.3 *Haplochromis chilotes*

2.2.3.1 Morphology of LPJ and teeth

LIGHT MICROSCOPY AND HR-SEM

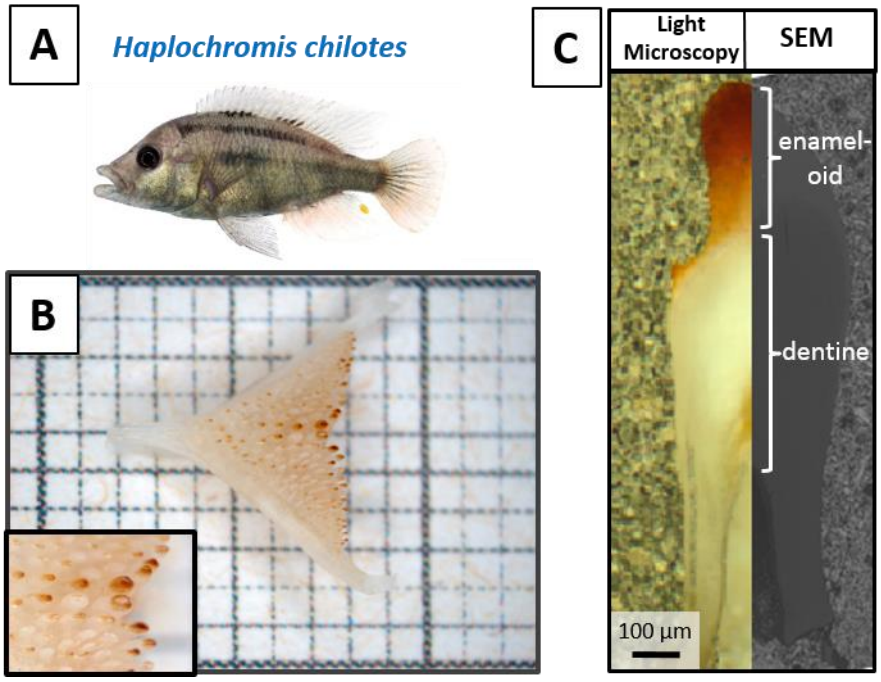

Figure 47: A: Photo of the East African cichlid *Haplochromis chilotes.* B: Lower pharyngeal jaw of *H. chilotes*, inset: biggest central teeth of the lower pharyngeal jaw. C: Merge of a light microscope image and SEM image of a polished cross-section of a central tooth of the LPJ.

Haplochromis chilotes is an example of the soft diet eating species (Figure 47, A, B). The macroscopic morphology was investigated with Light microscopy and SEM. The morphology of the LPJ (see Figure 47, B) is the same as was described for *A. alluaudi* in chapter 2.1.1. The jaw itself appeared small and delicate, and the tooth shape of the biggest teeth was fine and papilliform. The tips of the teeth also appear a deep red to brown. This coloring is more pronounced in the biggest central teeth in comparison to the outer, smaller teeth (inset Figure 47, B). Light microscopy and SEM on a polished cross-section (Figure 47, C) revealed that these teeth are also structured in at least two areas, which can be assigned to the enameloid and dentine area. The deep brown/red color is the most intense at the occlusal surface of the tooth but reaches throughout the entire enameloid. In contrast to the molariform teeth of the hard diet eating species, the enameloid resembles a rather big, elongated cap on the dentine.

2.2.3.2 Chemical composition and distribution

EDXS

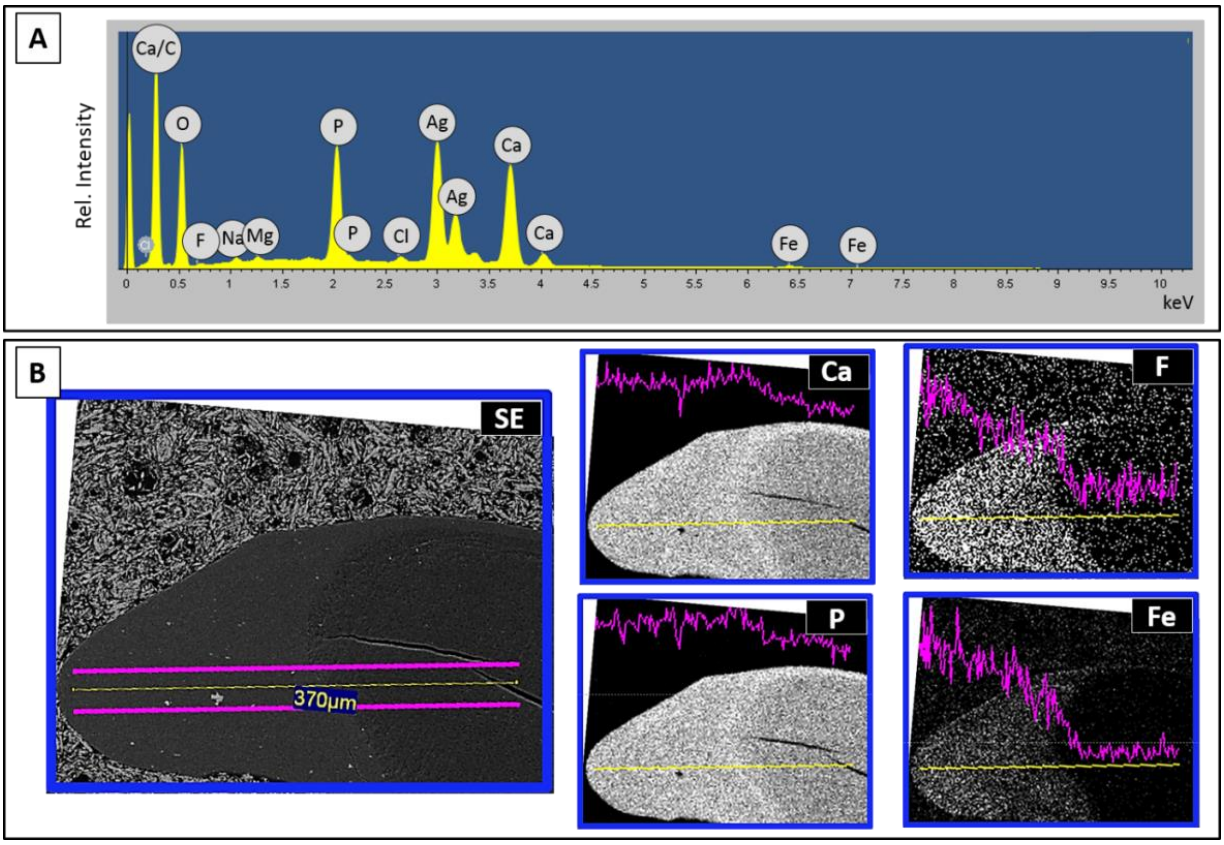

Figure 48: EDXS-measurements on polished cross-sections of a tooth of *H. chilotes*. A: sum spectrum of elemental analysis; B: elemental mappings and corresponding line scans of Ca, P, F and Fe in the tooth as displayed in the SE-image on the left side.

Elemental analysis was also performed for this species using EDXS on the polished surface of a tooth sample. The general elemental composition (Figure 48, A) and distribution were the same for this species as was found for previously described cichlid species. The mappings of all major elemental components and their distribution within the cross-section are displayed in Figure S 18 in appendix A. In contrast to the hard diet eating cichlid species, the line scans within these mappings revealed, that the Ca and P concentrations do not vary in a stepwise fashion and remain mostly the same within entire enameloid (Figure 48, B). As for the other cichlid species, the scans also show that fluorine is enriched in the enameloid, especially at the occlusal surface of the tooth. After approximately 90 µm, measured from the top of the tooth, the F-concentration decreases to a lower level before falling to nearly zero in the enameloid-dentine junction. A high concentration of iron could be found along the whole length of the enameloid. The concentration is decreasing in a nearly linear fashion along the length of the enameloid before decreasing to nearly zero at the enameloid-dentine junction.

RAMAN MICROSCOPY

Raman microscopy was performed on the polished axial cross-section of a central tooth of *H. chilotes*. The measured area along the tooth in the enameloid area is displayed with a frame in A in Figure 49. The area along the length of the enameloid-dentine junction is shown in Figure S 19 in appendix A. The Raman-spectra were plotted as a function of the distance from the top of the tooth (see Figure 49, B). The presence of characteristic apatite vibration modes could be detected at about 961 cm^{-1} ($[PO_4]^{3-}$ v_1), 420 cm^{-1} ($[PO_4]^{3-}$ v_2), 1045 cm^{-1} ($[PO_4]^{3-}$ v_3) and 590 cm^{-1} ($[PO_4]^{3-}$ v4).[170-172] Additionally, a signal at 1004 cm^{-1}, which corresponds to $[HPO_4]^{2-}$, could be detected. Characteristic signals of the organic component could be identified at 1455 cm^{-1} (C-H bending mode) and 1262 cm^{-1} (amide II).[173, 174] The results and peak assignments of the main peaks are summarized in Table S 7. An overlay of all collected Raman spectra of the phosphate v_1 band of the cross-section additionally revealed a small shift in wavenumbers of about 1-2 cm^{-1} towards lower wavenumbers from the occlusal area of the tooth towards the dentine (see Figure S 20).

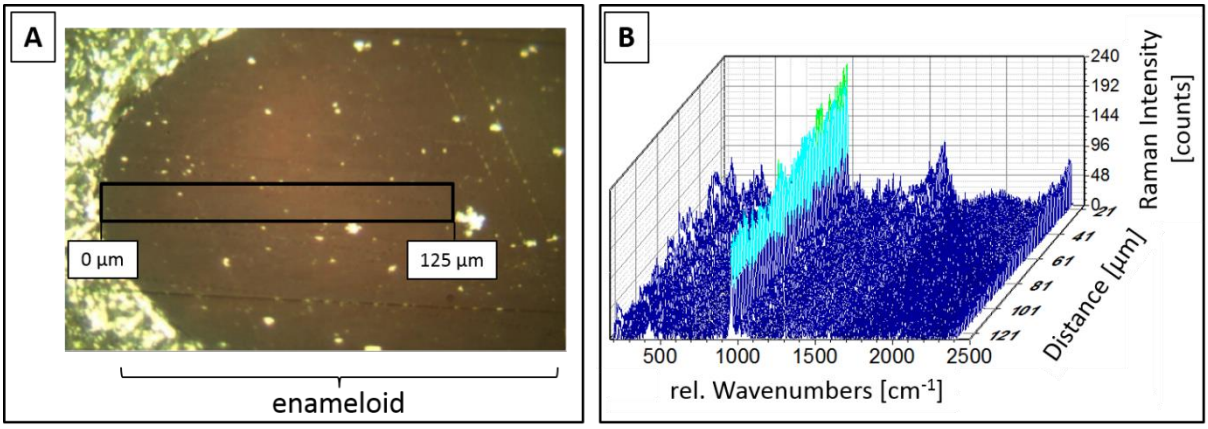

Figure 49: A: Light microscopic image of a polished cross-section of a tooth of *H. chilotes*. The frame indicates the area for the Raman-measurements. B: Summarized Raman-spectra, which were taken along the length of the frame, as indicated in image A.

In order to better display the distribution of the different components, selected vibration modes were extracted and displayed as a function of the distance from the top of the tooth. These single spectra are shown in Figure S 21 in appendix A. The first 7 µm showed a massively increased signal intensity within the whole spectral range. This might be due fluorescence originating from the silver-epoxy-resin used for the embedding material. Therefore, the signal intensities were plotted and interpreted from about 7 µm (measured from the occlusal top of the tooth) onwards. The signal intensity of the phosphate v_1 vibration mode was increased in the first 20 µm of the sample and slowly decreasing in a nearly linear fashion towards the enameloid-dentine junction.

All signals relating to the organic component of the tooth displayed a slight increase of the intensity within in the first 20 µm of the sample as well. A weak band at 308 cm^{-1}, which could relate to a characteristic iron oxide phase, showed a slight increase in the first 10 µm from the top of the tooth. Additional weak signals could be detected at 1070 cm^{-1} and 1125 cm^{-1}. The intensity profile of these peaks along the length of the investigated sample did not show significant changes and thus a distribution profile.

FT- IR-SPECTROSCOPY

Teeth of *H. chilotes* were crushed, and the resulting powder was investigated by FT-IR spectroscopy. The presence of the apatite specific ions and the amide signals of the protein molecules could be confirmed and are summarized in Table S 8 in appendix A. The IR spectrum (Figure 50) exhibits three modes at 963 cm^{-1} ($[PO_4]^{3-}$ v_1), 1093 cm^{-1} ($[PO_4]^{3-}$ v_3) and 1155 cm^{-1} ($[PO_4]^{3-}$ v_3), which can be assigned to the internal vibration of the phosphate group.[177] The IR peaks at 1646 cm^{-1}, 1542 $cm^{-1,}$ and 1240 cm^{-1} were attributed to the amide I, amide II and amide III, respectively.[178-180] Also, amide A and B bands at 3070 – 3300 cm^{-1}, which overlap with the stretching modes of the water molecules were observed.[178] Furthermore, the IR spectrum also shows characteristic CH bands at 2854 cm^{-1}, 2924 $cm^{-1,}$ and 2955 cm^{-1}. Additionally, the spectrum confirms the presence of a B-type carbonate substitution by showing peaks at 874 cm^{-1} (v_2), 1413 cm^{-1} (v_3), 1456 cm^{-1} (v_3) and 702 cm^{-1} (v_4).

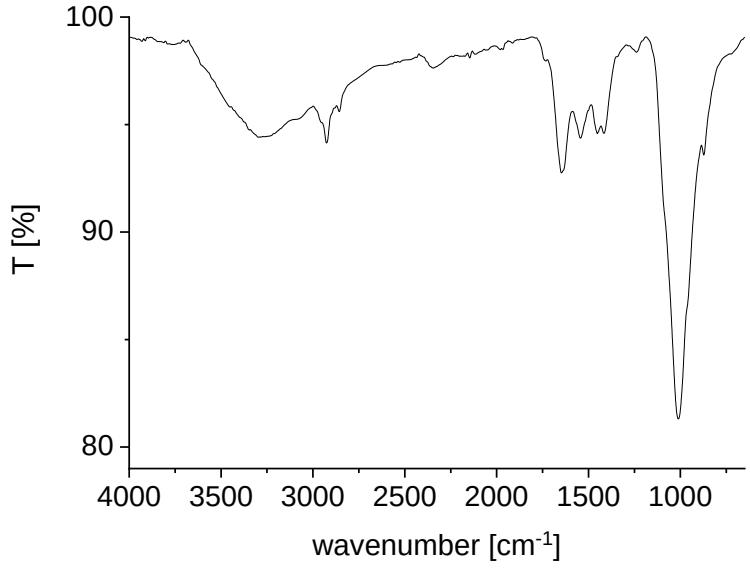

Figure 50: IR spectrum of a powdered mix of teeth of a LPJ of *H. chilotes.*

2.2.3.3 Ultrastructure of the teeth

HR-SEM

To get insight into the inner structure of teeth of *H. chilotes* HR-SEM was performed on a polished cross-section of an embedded, polished tooth and on fractured tooth samples. The results of the SEM investigation on the polished axial cross-section are displayed in Figure 51. These investigations revealed that the bulk area of the enameloid of the papilliform teeth is also composed of a tangled arrangement of mineralized fibrils. However, in contrast to the hard diet eating species, this tangled fibril array seems to span through the whole enameloid area.

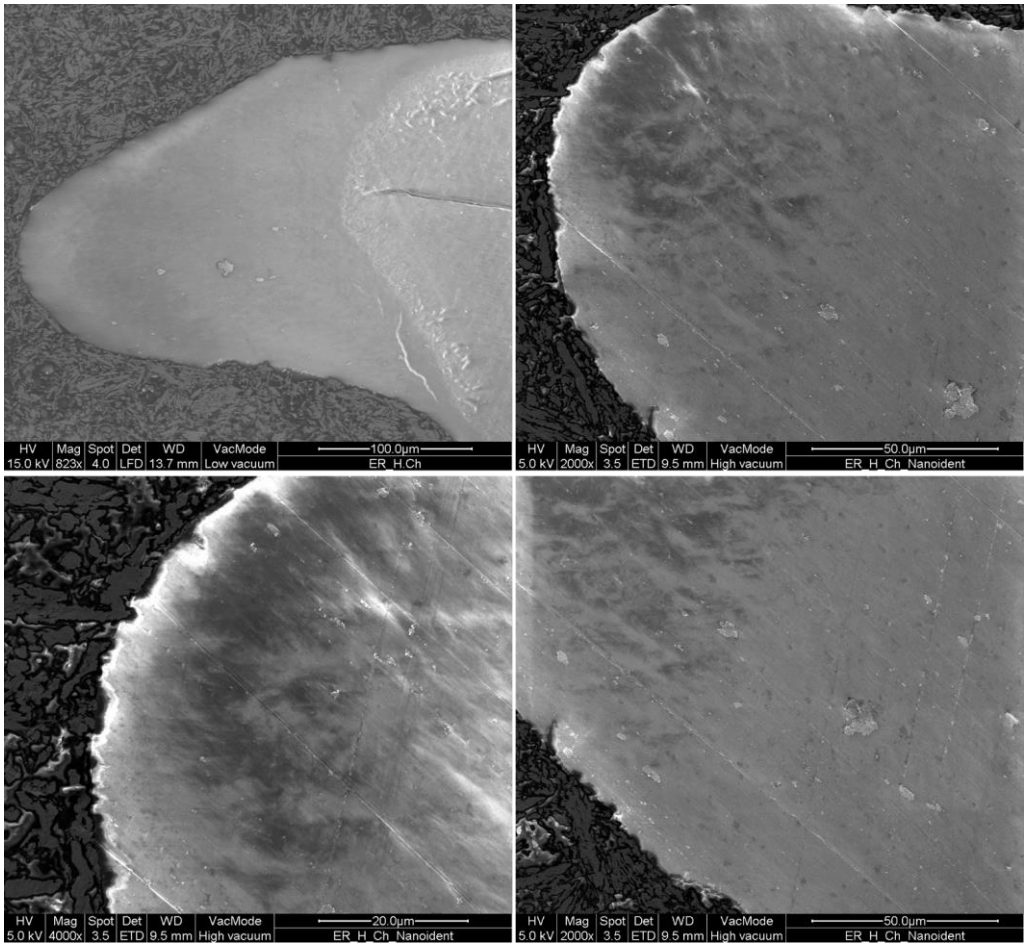

Figure 51: SEM images of a polished cross-section of a tooth of *H. chilotes*, highlighting different areas within the enameloid area.

The results of the SEM investigation on the fractured teeth are displayed in Figure 52. The ultrastructure displayed a similar set of structural motifs as the molariform teeth of the hard diet eating species. The surface is covered with a thin and dense layer of crystallites, which are aligned parallel to each other and their long axis roughly perpendicular to the surface (see marking (sl) in image A). In contrast to the molariform teeth of the hard diet species, this layer appears to be only about 200-400 nm thick. Directly beneath this superficial layer are long mineralized fibers, which are roughly parallel to each other and whose long axis is oriented perpendicular to the

surface (marked with (1) in image A-C). These fibers become more decussated from the outside of the tooth towards the inside. Within approx. 5-8 µm into the tooth, measured from the outer surface, these mineralized fibers are interwoven with ribbons of other mineralized fibers, whose long axis run parallel to the surface. These ribbons run along the whole length of the tooth and thus build an interwoven plywood structure (marked with (2) in images B and C). Within the next layer, the mineralized fibers are smaller and oriented in a nearly random fashion (this layer is marked with (3) in images B and C). This area is pervaded with the channels of the dentinal tubules (marked with (dt) in image B). Image D shows the dentine as viewed from within the pulpa. This demonstrates that the dentine is composed of many fibers. These fibers are oriented concentrically around the holes of the dentinal tubules.

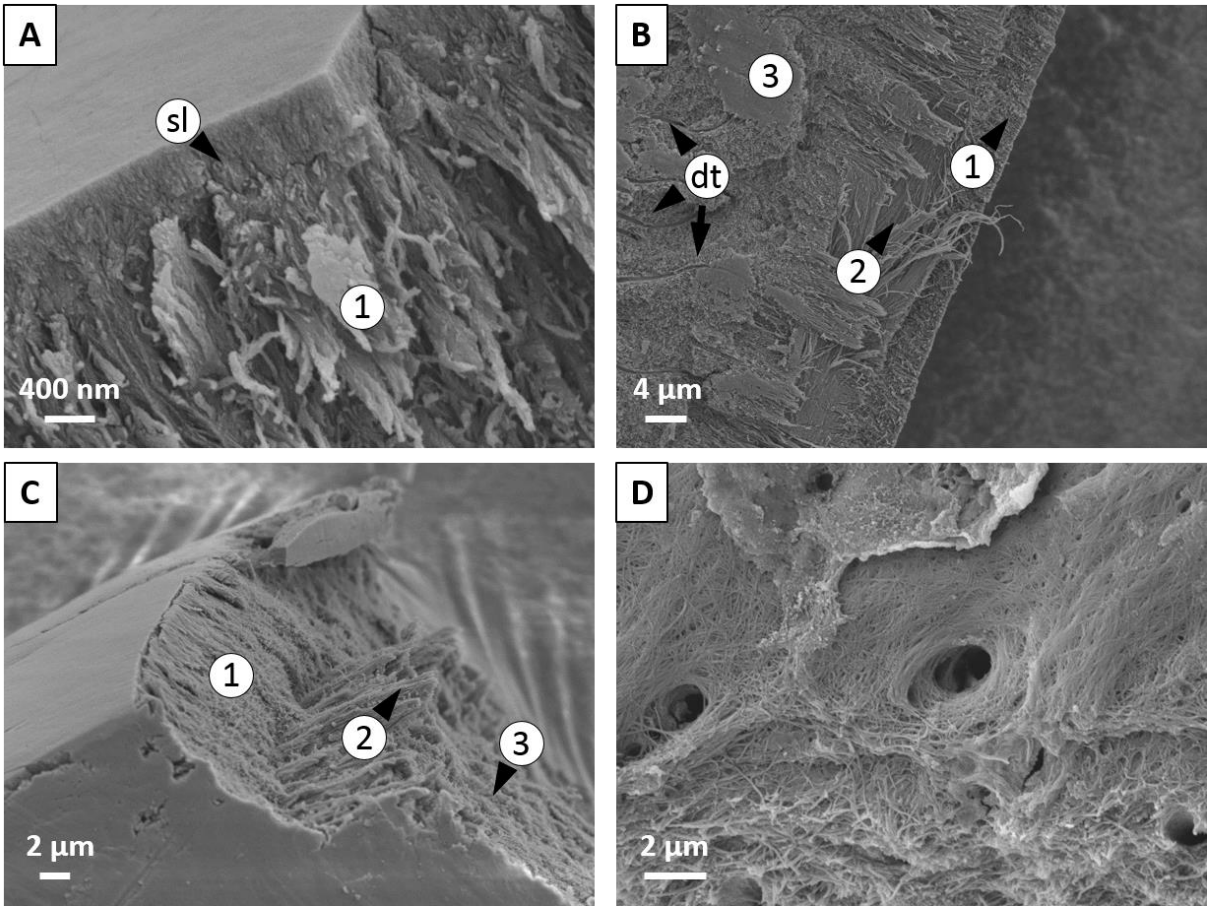

Figure 52: Scanning electron micrographs of fracture areas of crushed teeth of *H. chilotes*. A: Occlusal surface of the tooth, displaying the first 2 layers within the enameloid. B,C: Overview of the structure of the outer 3 layers. D: Holes of the dentinal tubules, highlighting the concentrically arranged fibers around the holes. Labels (sl), (1)-(3) highlight the different structural layers as described in the text.

2.2.3.4 Mechanical properties

NANOINDENTATION

The mechanical properties of a central tooth of *Haplochromis chilotes* were investigated by nanoindentation. The results of the single measurements for the hardness and elastic modulus are displayed in Figure 53 (A and B). It was observed that the values have a high deviation to each other in comparison to the hard diet eating species. The highest values for the hardness and elastic modulus were found in the enameloid at the tip of the tooth. The values gradually decrease over the length of the enameloid with a weak almost linear gradient. Specifically, the hardness and elastic modulus changes from 4.12 ± 0.39 GPa and 80.87 ± 8.91 GPa respectively in the very occlusal part of the tooth to 3.12 ± 0.12 GPa and 66.99 ± 1.59 GPa respectively in the basal area of the enameloid. Upon reaching the enameloid-dentine junction, the hardness and elastic modulus show a notable reduction, dropping to a value of about 1.19 ± 0.32 GPa and 34.41 ± 10.36 GPa. Upon reaching the less pigmented area within the enameloid (see Figure 53, C), the values appear to also reach a local minimum for measurement line 2. The actual values within this area are 2.54 ± 0.25 GPa and 58.8 ± 2.49 GPa respectively. However, line 1 shows a more linear profile.
Figure 53 displays an overlay of a SEM image of the axial cross-section with the color-coded hardness (Figure D) and elasticity values (Figure E) of each indent along the length of the sample. Note, that the color-code is the same as the one used for the other investigated cichlid species. This representation does not indicate any correlation of the hardness and elastic modulus with structural elements, except their drastic reduction upon reaching the dentine area. However, the previous SEM investigations on the polished sample showed (see Figure 51) that the bulk area of the enameloid of the papilliform teeth is composed of an interwoven arrangement of mineralized fibrils. However, in contrast to the hard diet eating species, this tangled fibril array seems to span through the whole enameloid area.

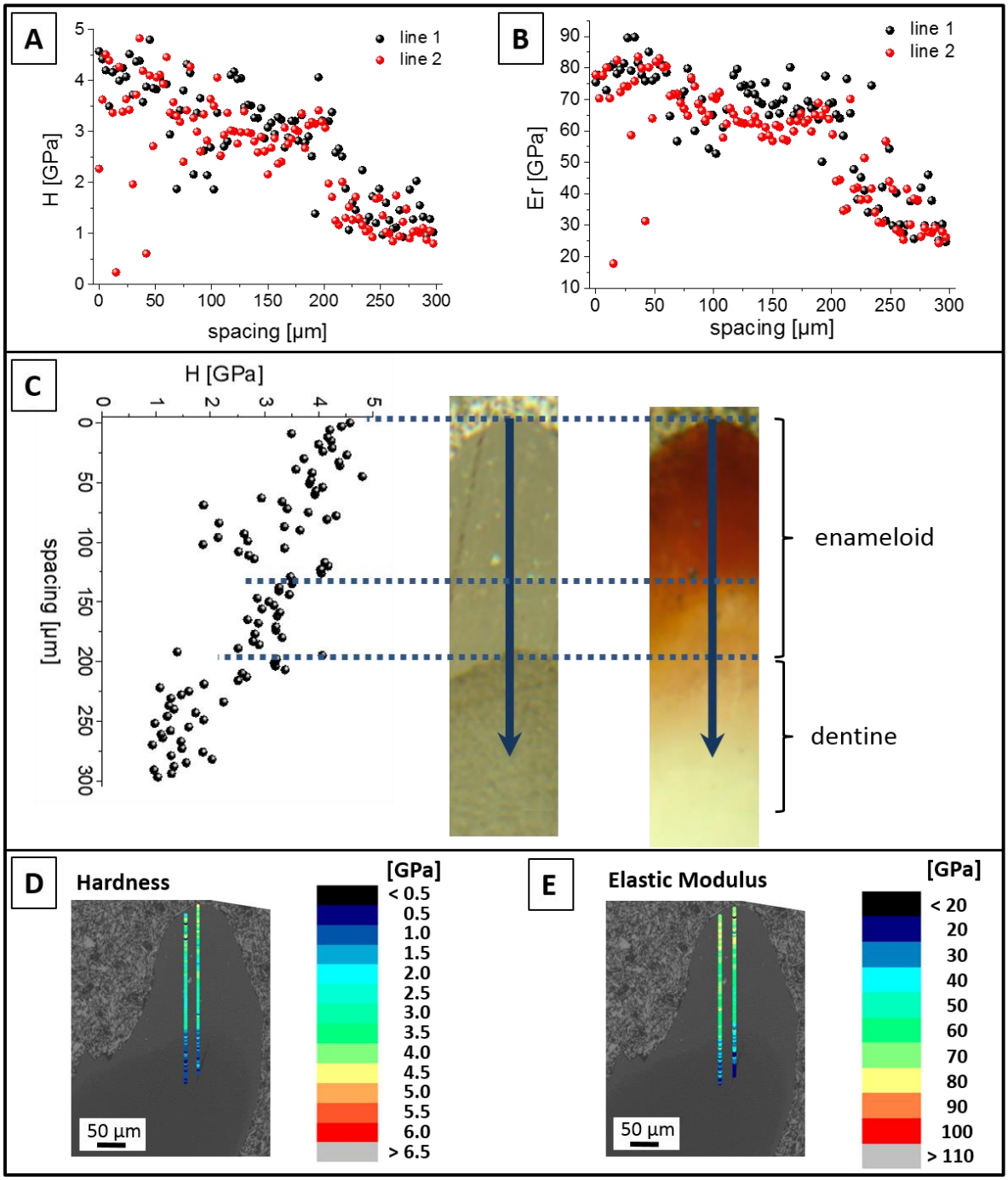

Figure 53: Mechanical properties derived from nanoindentation experiments across the axial cross-section of a tooth of *H. chilotes*. A: Results of hardness measurements of the single line scans; B: Results of elastic modulus measurements of the single line scans; C: Mean values of the hardness across the sample length correlated with light microscopic images (left: bright field, right: polarized light) of the cross-section of the tooth; D: Colour coded hardness values directly overlayed with the positions of the corresponding indents displayed with SEM images of the polished cross-section; E: Colour coded values of the elastic modulus directly overlayed with the positions of the corresponding indents displayed with SEM images of the polished cross-section.

2.2.4 *Haplochromis nyererei*

2.2.4.1 Morphology of LPJ and teeth

LIGHT MICROSCOPY AND HR-SEM

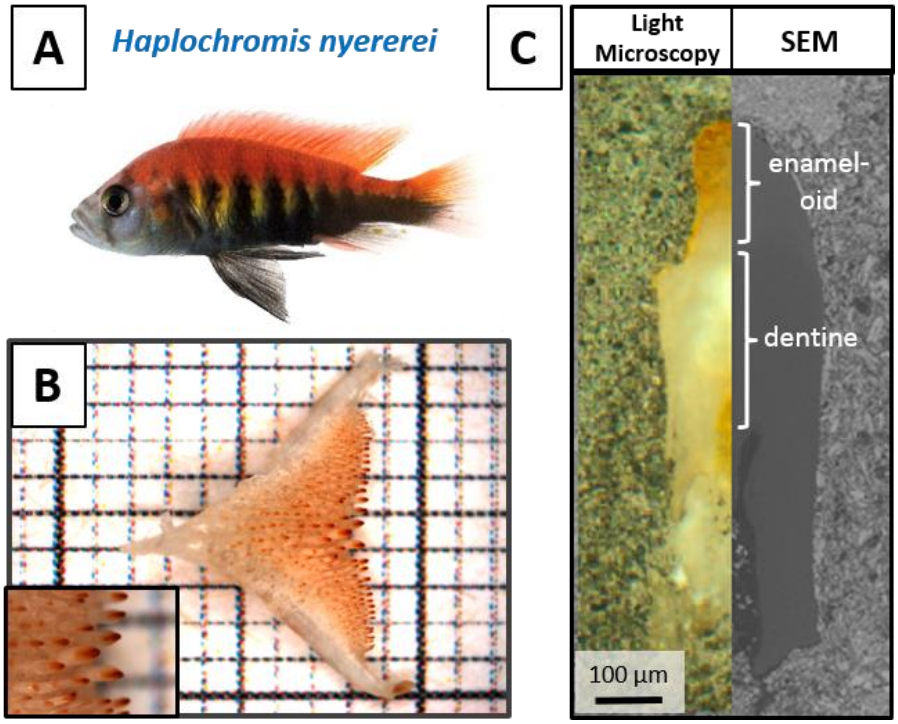

Figure 54: A: Photo of the East African cichlid *Haplochromis nyererei.* B: Lower pharyngeal jaw of *H. nyererei*, inset: biggest central teeth of the lower pharyngeal jaw. C: Merge of a light microscope image and SEM image of a polished cross-section of a central tooth of the LPJ.

Haplochromis nyererei is another example of a soft diet eating species. (Figure 54, A, B). The macroscopic morphology was investigated with Light microscopy and SEM. *H. nyererei* has a smaller and more delicate LPJ than the hard diet eating species, but the general morphology of the LPJ (see Figure 54, B) is the same as was described for *A. alluaudi* in chapter 2.1.1. The tooth shape of the biggest teeth is fine, papilliform and appear even smaller than the teeth of the other soft diet eating cichlid species *H. chilotes*. The enameloid of these papilliform teeth are also elongated and resemble a cap on the dentine. The tips of the teeth also appear red to brown, at some points nearly black. Light microscopy and SEM on a polished cross-section (Figure 54, C) revealed that these teeth are also structured in at least two areas, which can be assigned to the enameloid and dentine area. Within the polished cross-section, the coloring appears less pronounced but is distributed along the whole length of the enameloid

2.2.4.2 Chemical composition and distribution

EDXS

Elemental analysis was performed using EDXS on the polished axial cross-section of a central tooth of the LPJ of *H. nyererei*. Qualitatively, the general elemental composition was the same for this species as was found for previously described cichlid species (see Figure 55, A). The mappings of all major elemental components and their distribution within the cross-section are displayed in Figure S 22 in appendix A. Similar to *H.chilotes* and in contrast to the hard diet eating cichlid species, the elemental line scans within these mappings revealed, that the Ca and P remain nearly constant within the whole of the enameloid (Figure 55, B). As for the other cichlid species, the scans also show that fluorine is enriched in the enameloid, which decreases in a linear fashion from the occlusal surface towards the enameloid-dentine junction and falling to nearly zero in the dentine area. A high concentration of iron could be found along the whole length of the enameloid, although it displays a relatively high concentration at the very outer area of the enameloid at the occlusal surface. Similar *to H.chilotes* the iron concentration is also decreasing in a nearly linear fashion.

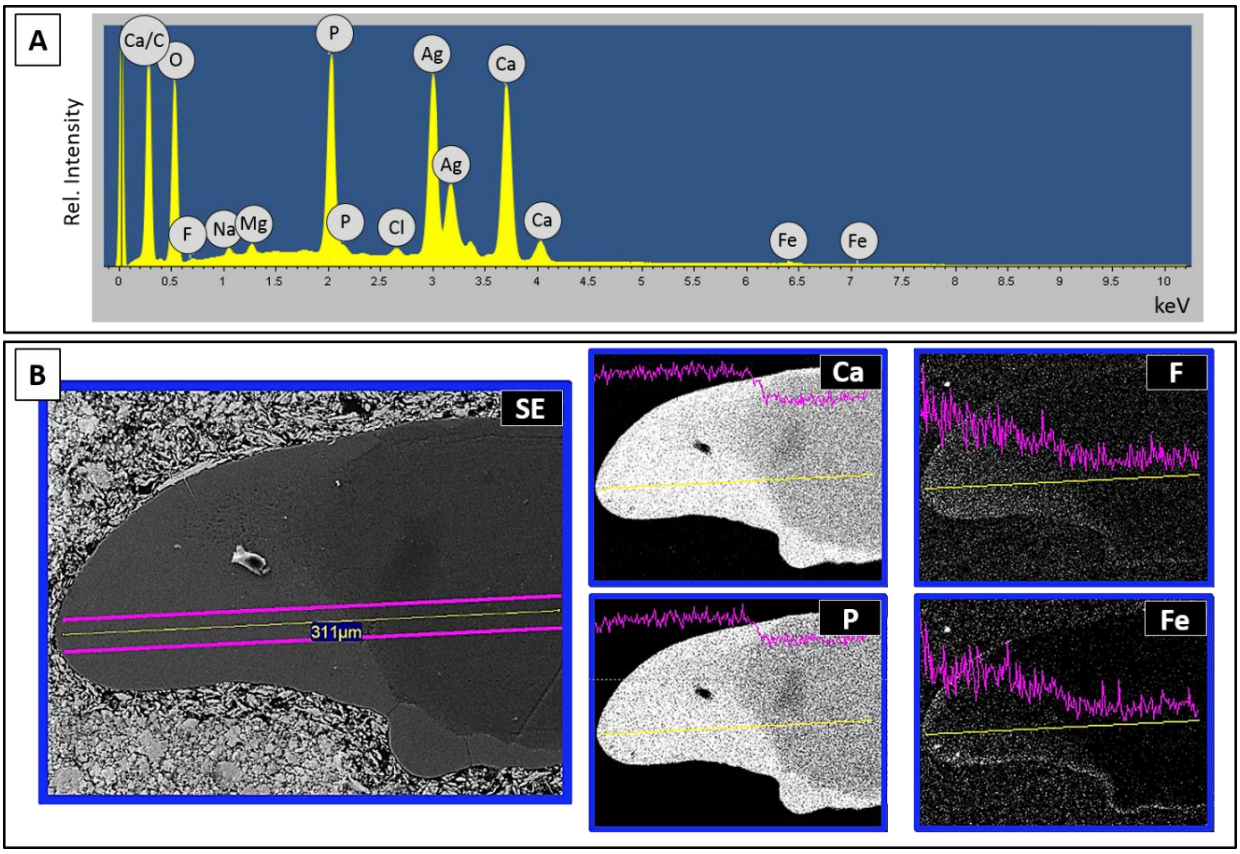

Figure 55: EDXS-measurements on polished cross-sections of a tooth of *H. nyererei.* A: sum spectrum of elemental analysis; B: elemental mappings and corresponding line scans of Ca, P, F and Fe in the tooth as displayed in the SE-image on the left side.

RAMAN MICROSCOPY

As was the procedure for the other investigated cichlid species, Raman microscopy was performed on the polished axial cross-section of a central tooth of the LPJ of *H. nyererei*. The measured area along the tooth in the enameloid area is displayed with a frame in Figure 56, A. The Raman-spectra were plotted as a function of the distance from the top of the tooth (see Figure 56, B). The measured area along the length of the enameloid-dentine junction can be seen in image A in Figure S 23. The presence of characteristic apatite vibration modes could be detected at 962 cm^{-1} ($[PO_4]^{3-}$ v_1), 431 cm^{-1} ($[PO_4]^{3-}$ v_2), 1043 cm^{-1} ($[PO_4]^{3-}$ v_3) and 587 cm^{-1} ($[PO_4]^{3-}$ v4).[170-172] A characteristic signal of the organic component could be identified at 1438 cm^{-1} (C-H bending mode).[173, 174] The results and peak assignments of the main peaks are summarized in Table S 9. In contrast to the other studied tooth samples, an overlay of all collected Raman spectra of the phosphate v_1 band of the cross-section did not show a shift in wavenumbers (see Figure S 24 in appendix A).

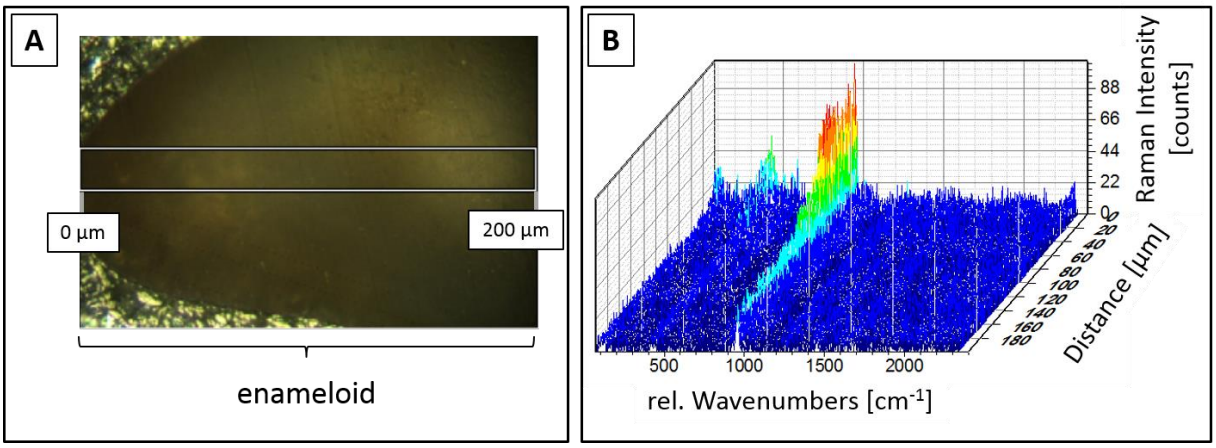

Figure 56: Light microscopic image of a polished cross-section of a tooth of *H. nyererei*. The frame indicates the area for the Raman-measurements. B: Summarized Raman-spectra along the length of the measured area as indicated in A.

In order to better display the distribution of the components, selected vibration modes were extracted and displayed as a function of the distance from the top of the tooth. These single spectra are shown in Figure S 25 in appendix A. The signal intensity of all apatite related vibration modes are significantly higher in the enameloid area and decreases gradually in the enameloid-dentine junction (see Figure S 23, B). Similar to all other investigated cichlids, local variations in the signal intensity could be observed. The signal slightly drops within the first 10 µm, before slightly rising again and keeping a quite stable intensity within this area upon reaching the dentine. All signals relating to the organic component of the tooth display a slight increase of the intensity of 5-10 µm of the sample, measured from the occlusal part of the enameloid.

FT-IR-SPECTROSCOPY

Teeth of *H. nyererei* were crushed, and the resulting powder was investigated by FT-IR spectroscopy. The presence of the apatite specific ions and the amide signals of the protein molecules could be confirmed and are summarized in Table S 10. Two modes at 964 cm^{-1} ($[PO_4]^{3-}$ v_1), 1093 cm^{-1} ($[PO_4]^{3-}$ v_3) were observed, which were attributed to the internal vibration of the phosphate group.[177] The IR peaks at 1649 cm^{-1}, 1547 $cm^{-1,}$ and 1240 cm^{-1} were attributed to the amide l, amide II and the amide III respectively.[178-180] Additionally, amide A and B bands were observed at 3070 – 3300 cm^{-1}, which overlap with the stretching modes of the water molecules.[178] The strong vibration modes of the CH groups were found at 2857 cm^{-1}, 2929 cm^{-1}, 2953 cm^{-1}. Furthermore, the IR spectrum also shows characteristic carbonate bands at 871 cm^{-1}, 1415 $cm^{-1,}$ and 1454 cm^{-1}, indicating a B-type substitution in the apatite.

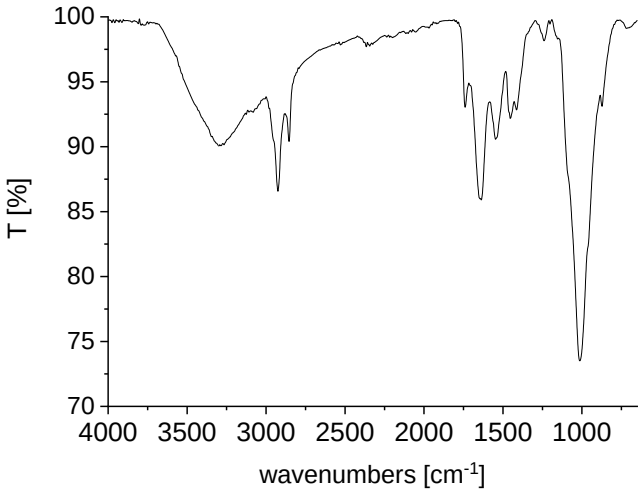

Figure 57: IR spectrum of a powdered mix of teeth of a LPJ of *H. nyererei.*

2.2.4.3 Ultrastructure of the teeth

HR-SEM

To get further insight into the inner structure of the teeth of the LPJ of *H. nyererei* HR-SEM was performed on an embedded and polished cross-section and fractured tooth samples. The SEM micrographs of the polished cross-section are shown in Figure 58. These investigations confirm the results of the other soft diet eating species *H. chilotes*. The images showed that the bulk of the enameloid is composed of a tangled, interwoven arrangement of fibrous mineralized bundles and that these interwoven fibrils span through the whole of the enameloid. The outermost 25 µm appear to be higher mineralized as is indicated by the higher brightness of the images.

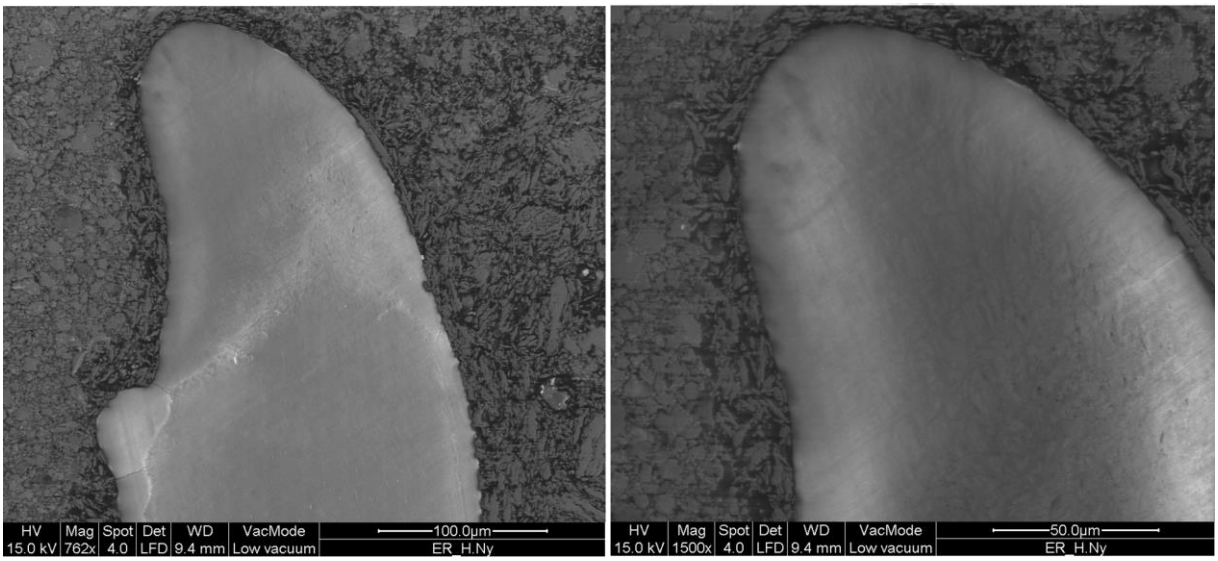

Figure 58: SEM images of a polished cross-section of a tooth of *H. nyererei.*

A SEM micrograph of a fractured tooth of H. ishmaeli is shown in Figure 59. It was observed, that the teeth of *H. chilotes* display similar structural motifs as was identified for the other investigated cichlid species. The surface of the tooth is covered by a very thin, dense layer of crystallites (marked as (sl) in Figure 59). Directly beneath the superficial layer are nearly randomly oriented, thin mineralized fibers (marked with (1) in Figure 59). About 6-8 µm within the tooth, measured from the tooth surface, mineralized fibrous bundles run along the long axis of the tooth (marked with (2)). These ribbons create an interwoven plywood-structure. Beneath this ribbons is a layer with randomly oriented mineralized fibers (marked with (3) in the image).

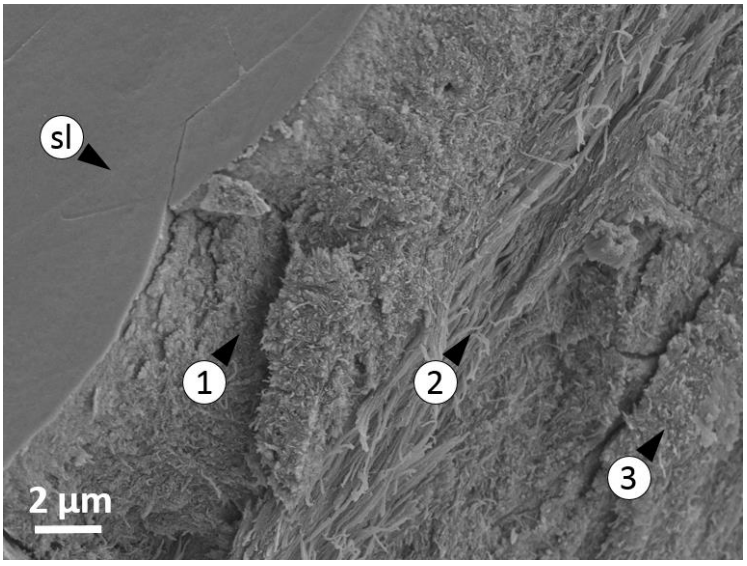

Figure 59: SEM image of a fracture area of a tooth of the LPJ of *H. nyererei*. Labels (sl), (1)-(3) highlight the different structural layers as described in the text.

2.2.4.4 Mechanical properties

NANOINDENTATION

Nanoindentation was performed on the cross-section of a central tooth of the LPJ of *Haplochromis nyererei*. The results of the single measurements for the hardness and elastic modulus are displayed in Figure 60 (A and B). One of the three measured profiles showed a drastically different trend than the other two lines, which were measured within this tooth (see Figure S 26 in appendix A) and the observed general trend of the other investigated samples. This line partially went through the epoxy resin of the embedding material (see red arrow in Figure 60, D) and was thus not included in the determination of the averaged values of the hardness and elastic modulus. The values gradually decrease over the length of the enameloid with a weak, almost linear gradient. This trend is similar to the other soft diet eating species *H. chilotes*. Similar to all investigated species, the highest values for the hardness and elastic modulus were found at the tip of the tooth. Specifically, the hardness and elastic modulus changes from 5.42 ± 0.13 GPa and 83.96 ± 9.63 GPa in the very tip of the tooth to 4.35 ± 0.67 GPa and 83.52 ± 8.82 GPa in the basal area of the enameloid. Upon reaching the enameloid-dentine junction, the values of the hardness and elastic modulus show a notable reduction, dropping to a value of about 1.29 ± 0.06 GPa and 32.83 ± 0.71 GPa. Just before the dentine area, the values briefly fall to a local minimum of 2.20 ± 1.20 GPa and 51.65 ± 23.96 GPa.

Image D and E in Figure 60 display an overlay of a SEM image of the axial cross-section with the color-coded hardness and elasticity values of each indent along the length of the sample. Similar to the other soft diet eating species *H. chilotes* this representation does not indicate any correlation of the hardness and elastic modulus with structural elements, except their drastic reduction upon reaching the dentine area. The previous SEM investigations on the polished sample showed (see Figure 58) that the bulk area of the enameloid of the papilliform teeth, is composed of an interwoven arrangement of mineralized fibrils and that in contrast to the hard diet eating species, this tangled fibril array spans through the whole enameloid area.

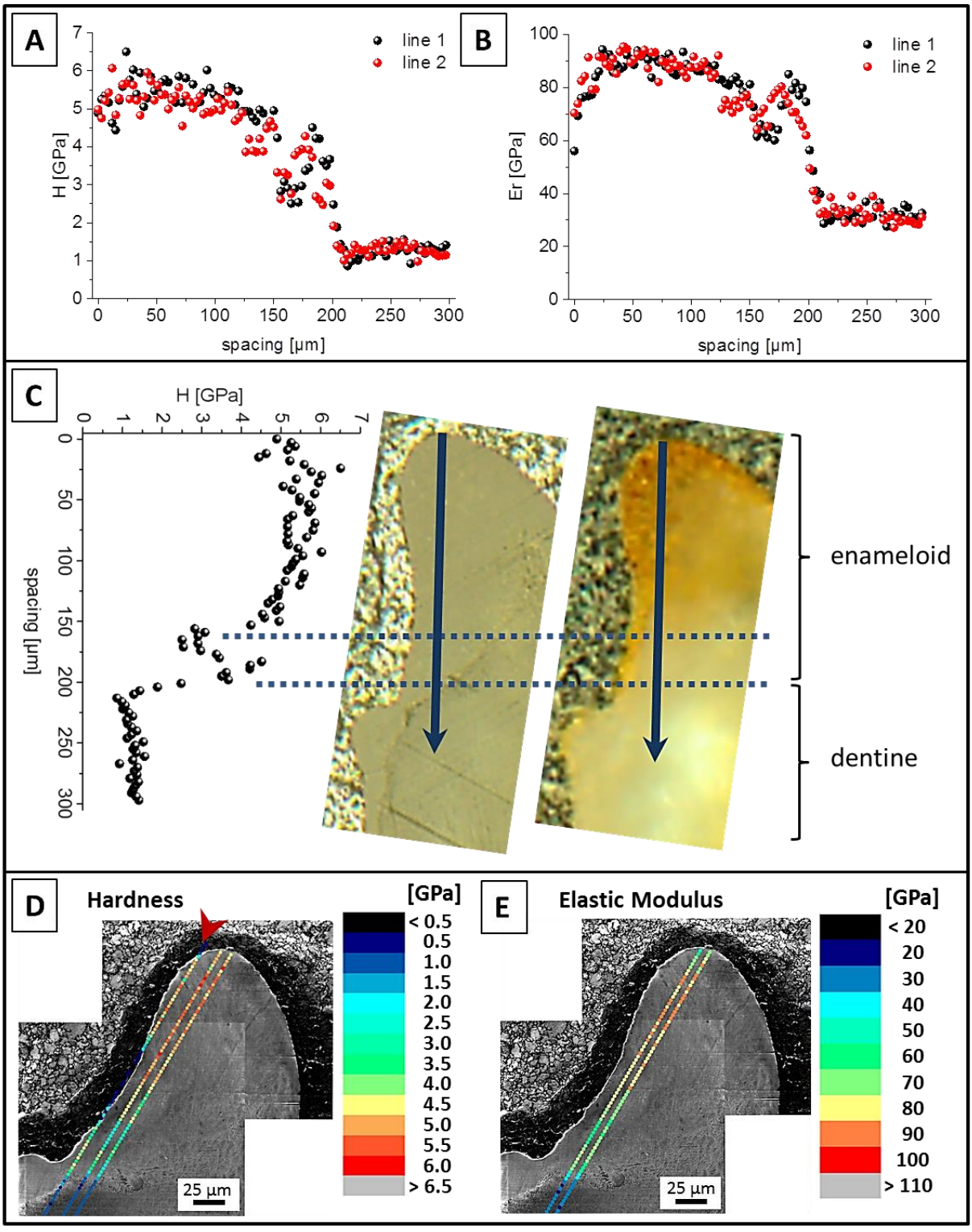

Figure 60: Mechanical properties derived from nanoindentation experiments across the axial cross-section of a tooth of *H. nyererei.* A: Results of hardness measurements of the single line scans; B: Results of elastic modulus measurements of the single line scans; C: Mean values of the hardness across the sample length correlated with light microscopic images (left: bright field, right: polarized light) of the cross-section of the tooth; D: Colour coded hardness values directly overlayed with the positions of the corresponding indents displayed with SEM images of the polished cross-section; E: Colour coded values of the elastic modulus directly overlayed with the positions of the corresponding indents displayed with SEM images of the polished cross-section.

AFM OF INDENTS

Figure 61 displays the AFM height topology and phase contrast images of the residual indents made on the surface of the polished tooth. Due to the instrumental setup, all investigated indents were measured from one indent line within a 100 µm length from the occlusal surface. In the case of *H. nyererei*, this implies, that all investigated indents remain in the reddish-brown area within the enameloid cap. The investigation revealed no obvious cracks. No pile-ups at the edges could be observed by extracting a height profile along the cross-section of the indents. A noticeable change in phase contrast without a change in height was observed in a gradient increasing from the occlusal area of the tooth towards the dentine. This might indicate a change in the composition of the measured material.

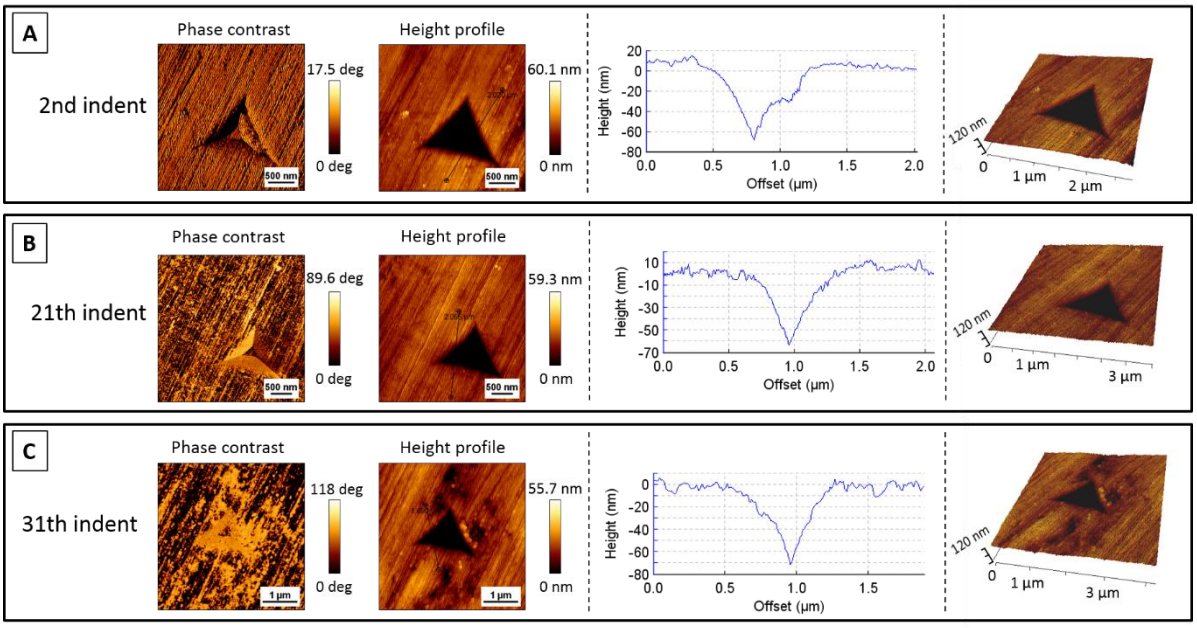

Figure 61 AFM images (phase contrast and height topography) of selected indents the axial cross-section of a tooth of *H. nyererei* along the length of the sample, including indent cross-section profiles and 3D visualization.

2.3 Lake Malawi cichlids

As hard and soft food sources occur in all Great Lakes of East Africa, specialized trophic phenotypes also evolved multiple times. This led to a remarkable resemblance of fish species specialized on the same diet, even if they are originating from different lakes and thus radiations. In order to address the question, whether this resemblance is also reflected in the inner structure and composition of the teeth or whether the same function was realized by different underlying methods, the teeth of specialized representatives of cichlids from Lake Malawi were investigated.

2.3.1 *Mylochromis mola*

2.3.1.1 Morphology of LPJ and teeth

LIGHT MICROSCOPY

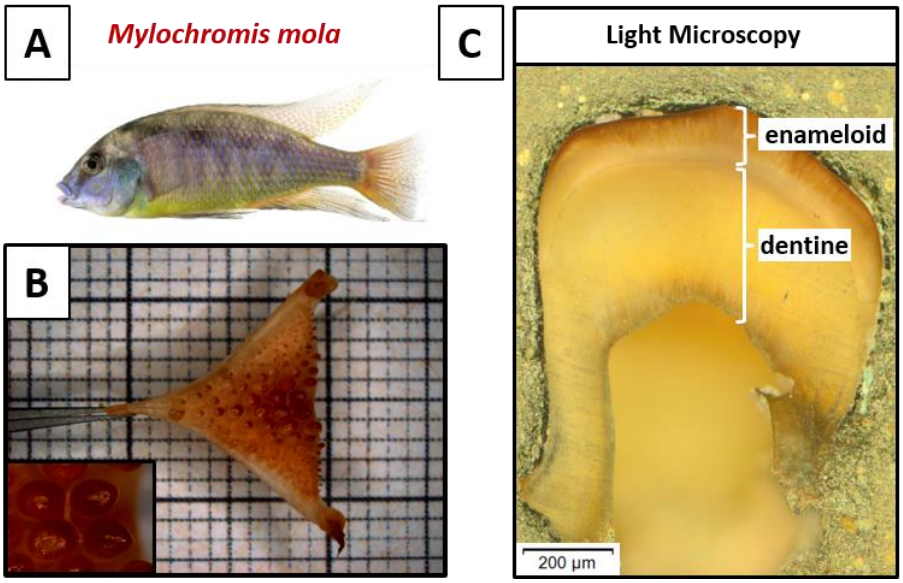

Figure 62: A: Photo of the East African cichlid *Mylochromis mola.* B: Lower pharyngeal jaw of *M. mola*, inset: biggest central teeth of the lower pharyngeal jaw. C: Merge of a light microscope image of a polished cross-section of a central tooth of the LPJ.

Mylochromis mola (Figure 62, A) is a hard diet eating example of the investigated species of Lake Malawi, which would be comparable to the hard diet eating species *H. ishmaeli* of Lake Victoria or the hard diet phenotypic morph of *A. alluaudi*. The big and robust morphology of the LPJ (see Figure 62, B) resembles remarkably the one, which was described for *A. alluaudi* in chapter 2.1.1 and that of the hard diet eating species of Lake Victoria *H.ishmaeli*. The biggest central teeth have big, molariform shape (image B, inset) and the surface appears a red/brown color.
Light microscopic investigations of polished cross-sections (Figure 62, C) also showed also the presence of different distinct areas, identified as enameloid and dentine. The red pigmentation is strongest in a small area at the top of the tooth. This pigmentation reaches, depending on the lateral position, about 30-40 µm into the

sample. A lighter area could be identified directly at the border between the enameloid and dentine, which describes the enameloid-dentine junction.

2.3.1.2 Chemical composition and distribution

ATR-IR Microscopy

The embedded and polished cross-section of a tooth of *M. mola* was investigated by ATR-IR microscopy. As indicated in image A in Figure 63, three different positions within the cross-section were measured, which are representative for the enameloid, the enameloid-dentine junction, and the dentine area. Each circular measurement area is 120 µm in diameter. The corresponding spectra of each position are displayed in image B. From these the presence of the apatite specific ions, and the amide signals of the protein molecules could be confirmed and are summarized in Table S 11. The spectra exhibit two modes at 960 cm^{-1} ($[PO_4]^{3-}$ v_1), 1014 cm^{-1} ($[PO_4]^{3-}$ v_3), which were assigned to the internal vibration of the phosphate group.[177] The signals at 1649 cm^{-1}, 1549 $cm^{-1,}$ and 1241 cm^{-1} can be assigned to the amide I, amide II and amide III, respectively.[178-180] Furthermore, amide A and B bands at 3070 – 3300 cm^{-1} were observed, which overlap with the stretching modes of the water molecules.[178] The spectra also show characteristic CH bands at 2856 cm^{-1} and 2926 cm^{-1}. Characteristic carbonate peaks were found at 866 cm^{-1} (v_2), 1416 cm^{-1} (v_3) and 1451 cm^{-1} (v_3), indicating a B-type carbonate substitution in the apatite component. It was observed that signals, which are related to the organic component are clearly stronger within the dentine area and increased from the occlusal surface to the dentine area.

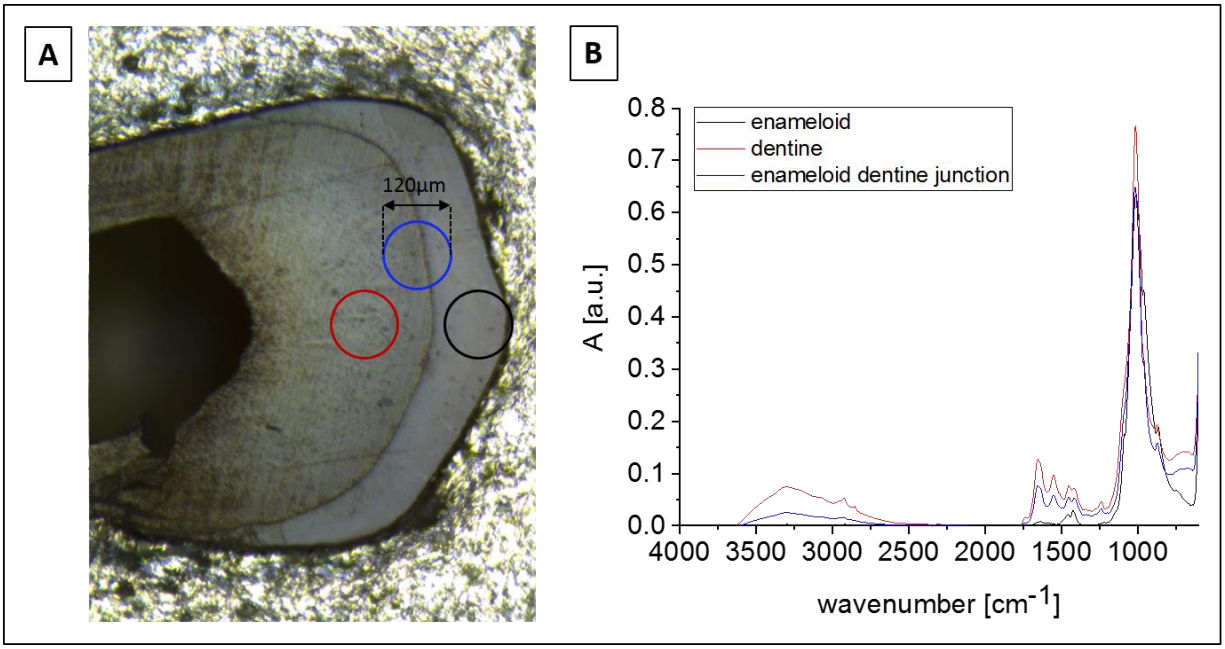

Figure 63: Results of the ATR-IR measurements on an embedded tooth of *M. mola*. A: Light microscopic image with circles indicating the measured area. B: Corresponding IR-spectra of the different measured area as indicated in image A.

2.3.1.3 Ultrastructure of the teeth

HR-SEM

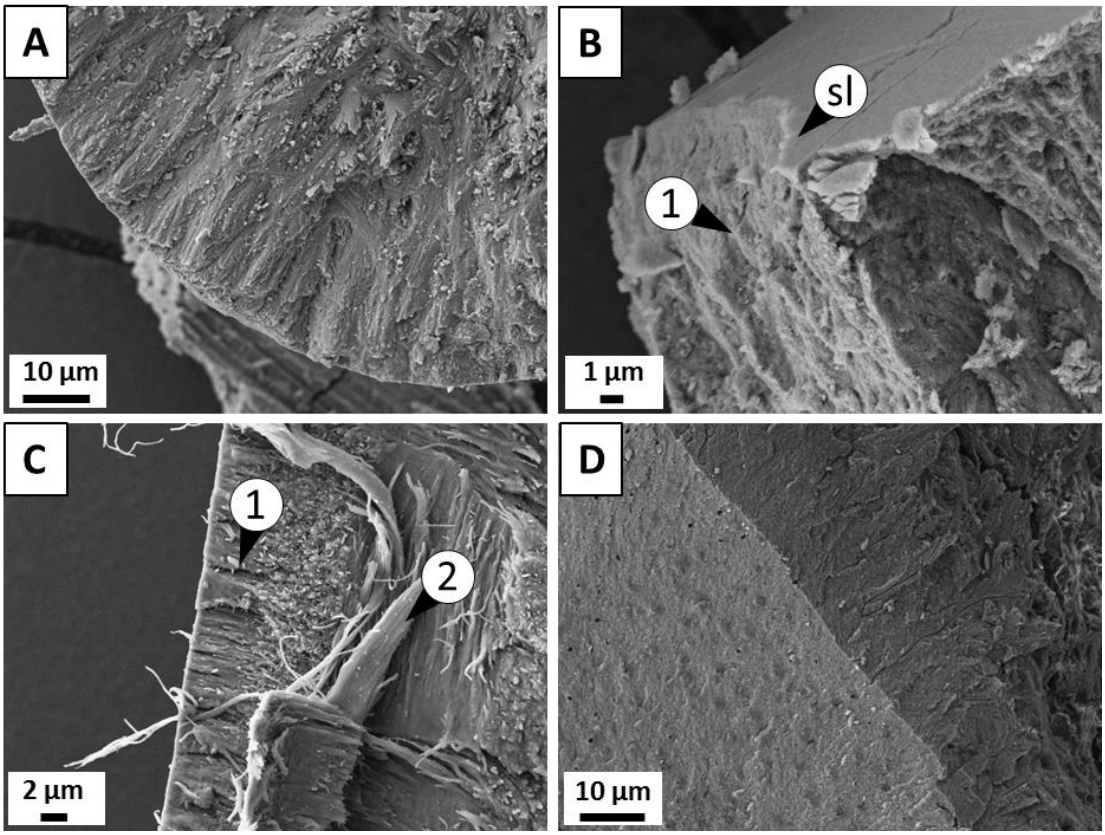

Figure 64: Overview of the main structural features of different teeth of the lower pharyngeal jaw of crushed teeth of *M. mola* as was investigated by HR-SEM.

HR-SEM investigations were performed on fractured teeth of the LPJ of *M. mola* as a representative of a hard diet eating species with big, molariform teeth. The results are summarized in Figure 64. These investigations showed that the bulk of the enameloid is composed of thick interwoven bundles of mineralized fibers (see image A). The outer surface of the tooth is covered by a dense, mineralized layer (marked with (sl) in image B). Directly beneath this layer are mineralized fibers, which are oriented with their long axis perpendicular to the surface and parallel to each other (marked as (1) in image C). These fibers are pervaded by ribbons of mineralized fibers, which run parallel to the long axis along the whole length of the tooth (marked as (2) in image C). This structure creates an interwoven plywood-structure. Image D shows the pores and channels of the dentinal tubules within the dentine. Thus it was shown, that the molariform teeth of this hard diet eating species show similar structural motifs, which were identified for the teeth of the species of Lake Victoria.

2.3.2 *Chilotilapia rhoadesii*

2.3.2.1 Morphology of LPJ and teeth

LIGHT MICROSCOPY AND HR-SEM

Chilotilapia rhoadesii (Figure 65, A) is an example of a mixed diet eating species and would be comparable with *H. sauvagei* from the Lake Victoria species flock. The morphology of the LPJ is the same as for all other investigate cichlid species (see image B). The biggest central teeth of the LPJ have a papilliform shape, although a more massive and thicker than the teeth of the purely soft diet eating fish like but not as molariform as the pure hard diet eating species. Light microscopic and scanning electron microscopic investigations of polished cross-sections (Figure 65, C) showed the typical structures of the enameloid and dentine area. The thickness of the enameloid is a mix of the molariform and papilliform tooth shape. Specifically, the enameloid has a slightly elongated tip, similar to that of the soft diet eating fish species, it is still a lot thinner than the big molariform teeth of the hard diet eating cichlids. The red pigmentation is strongest at the occlusal surface at the top of the tooth. This pigmentation reaches, depending on the lateral position, up to about 100 µm into the sample. Between this reddish/brownish area and the dentine-border, a white area was observed, which might describe the dentine-enameloid junction.

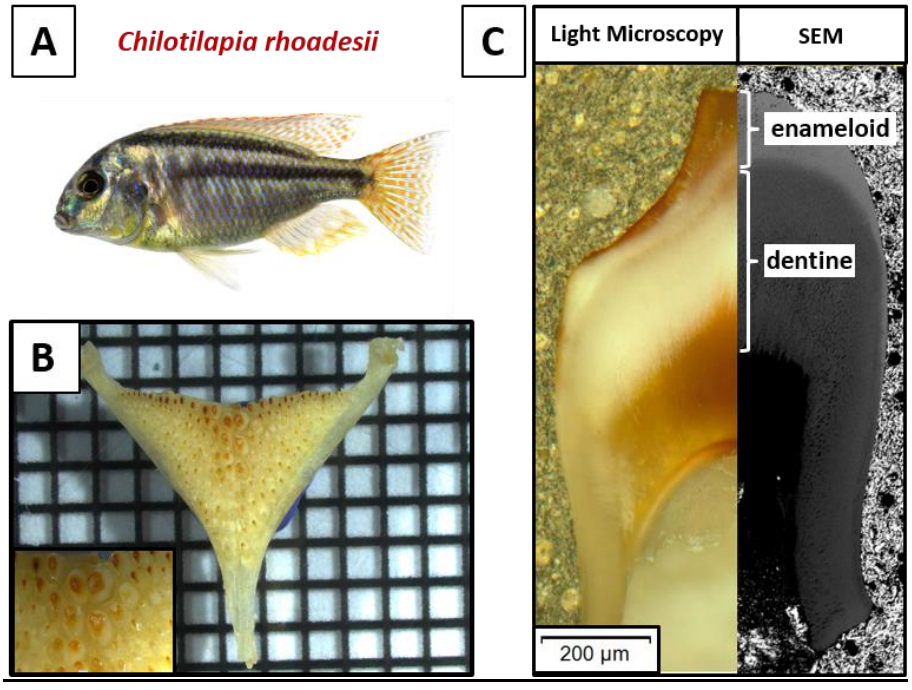

Figure 65 A: Photo of the East African cichlid *Chilotilapia rhoadesii.* B: Lower pharyngeal jaw of *H. ishmaeli* , inset: biggest central teeth of the lower pharyngeal jaw. C: Merge of a light microscope image SEM image of a polished cross-section of a central tooth of the LPJ.

2.3.2.2 Chemical composition and distribution

EDXS

Elemental analysis was performed using EDXS on the polished surface of the tooth sample. The general elemental composition (Figure 66, A) was the same for this species as was found for previously described cichlid species. The mappings of all major elemental components and their distribution within the cross-section are displayed in Figure S 22 in appendix A. Similar all soft diet eating species the elemental line scans within these mappings revealed that the Ca and P remain mostly constant within the whole of the enameloid (Figure 66, B). However, the Ca concentration rises again near the enameloid-dentine junction. As for the other cichlid species, the scans also show that fluorine and iron are enriched in the enameloid. The concentration of F nearly remains constant over the length of the enameloid towards the enameloid-dentine junction and falling to nearly zero in the dentine area. The iron signal shows an increased intensity near the enamel-dentine junction. As can be estimated from the mapping, the actual position of the line scan might not be the most representative as the intensity in other positions is the highest near the occlusal surface of the tooth. From that, a decrease in iron concentration from the top of the tooth towards the dentine can be estimated.

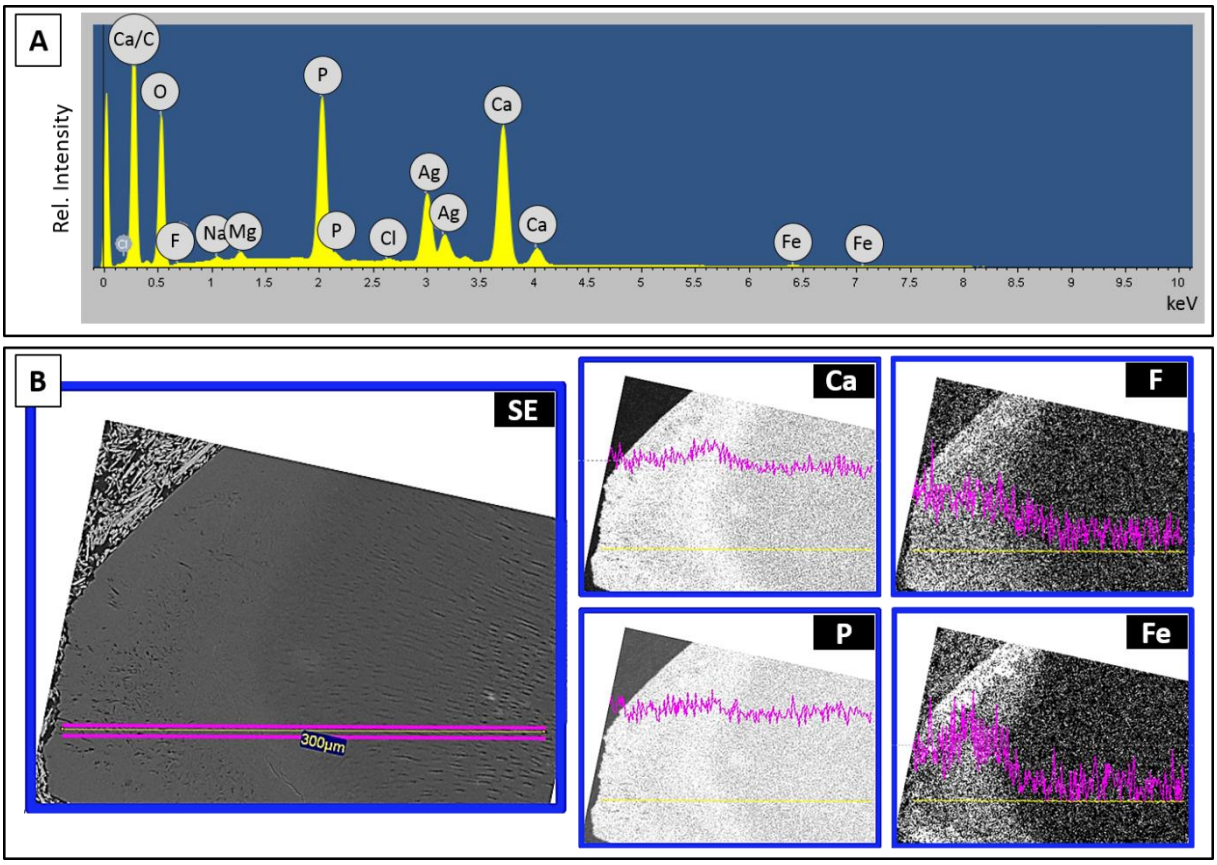

Figure 66: EDXS-measurements on polished cross-sections of a tooth of *C. rhoadesii.* A: sum spectrum of elemental analysis; B: elemental mappings and corresponding line scans of Ca, P, F and Fe in the tooth as displayed in the SE-image on the left side.

FT-IR-SPECTROSCOPY

Teeth of *C. rhoadesii* were crushed, and the resulting powder was investigated by FT-IR spectroscopy (Figure 67). The presence of the apatite specific ions and the amide signals of the protein molecules could be confirmed and are summarized in Table S 12. The IR spectra exhibit two modes at 960 cm^{-1} ($[PO_4]^{3-}$ v_1), 1090 cm^{-1} ($[PO_4]^{3-}$ v_3), which can be attributed to the internal vibration of the phosphate group.[177] The IR peaks at 1645 cm^{-1}, 1546 $cm^{-1,}$ and 1240 cm^{-1} can be attributed to the amide I, amide II and amide III respectively.[178-180] Additionally, amide A and B exhibit bands at 3070 – 3300 cm^{-1}, which overlap with the stretching modes of the water molecules.[178] A vibration mode of the CH groups was found at 2933 cm^{-1}. Furthermore, the IR spectrum also indicates characteristic carbonate bands at 871 cm^{-1}, 1417 $cm^{-1,}$ and 1455 cm^{-1}, indicating a B-type substitution in the apatite component.

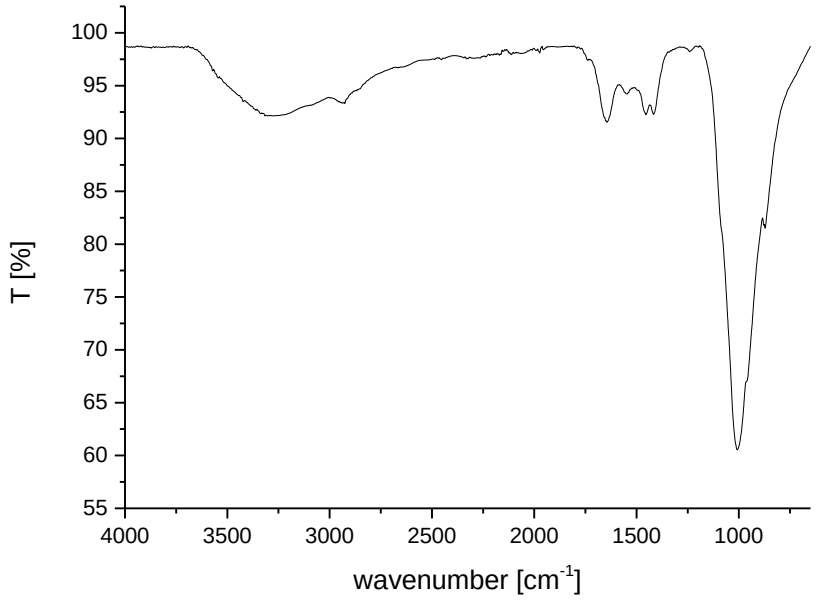

Figure 67: IR spectrum of a powdered tooth sample of *C. rhoadesii.*

2.3.2.3 Ultrastructure of the teeth

In order to get insight into the inner tooth structure, HR-SEM was performed on fractured teeth samples of *C*. *rhoadesii*. An overview of the inner structure of the tooth is displayed in image A in Figure 68, showing both a lateral and axial cross-section of a broken tooth. Image B and C highlight the channels of the dentinal tubules within the dentine, which run along the long axis of the tooth The position within the tooth is indicated with a green and blue frame, respectively, in image A. These tubules originate at the border of the dentine and the pulpa (see also image A Figure S 28 in appendix A). The whole dentine is comprised of thin mineralized and randomly interwoven fibers (see Figure S 26, B). Image D highlights the main structural elements, which were identified for the outer area of the enameloid at the surface of the tooth. The immediate surface is comprised of a thin layer of densely packed crystallites.

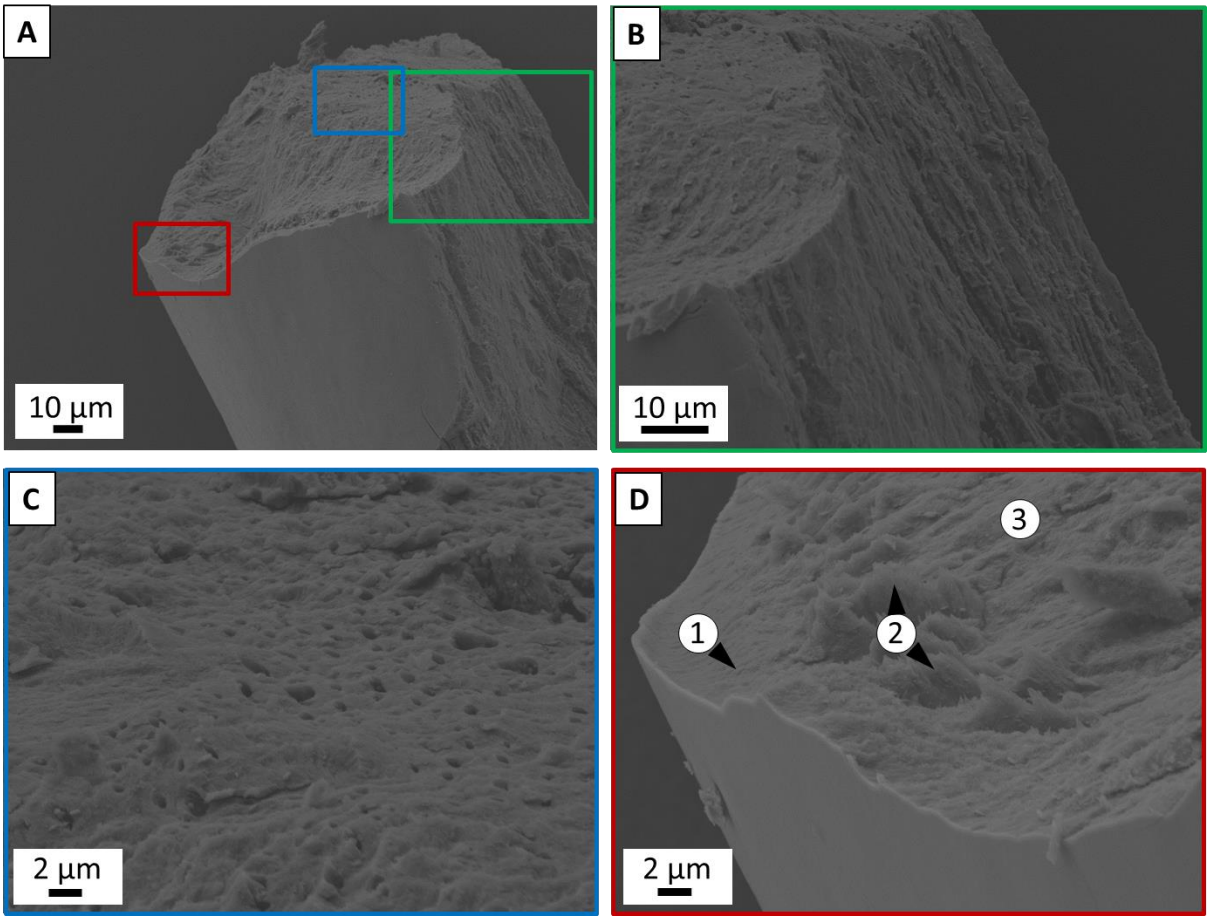

Figure 68: Scanning electron micrographs of fracture areas of crushed teeth of *C. rhoadesii*. A: Overview of a longitudinal and axial cross-section of a fractured tooth. B: Enlargement of the inner tooth area, highlighting the dentinal tubules, which run along the long axis of the tooth. The position is indicated with the green frame in A. C: Holes of the dentinal tubules within the dentine area, as indicated with the blue frame in A. D: Enlargement of the outer area of the tooth, highlighting the outer areas of the tooth structure. The position within the tooth is indicated with the red frame in A. Labels (1)-(3) highlight the different structural layers as described in the text.

Directly beneath this surface layer follows a layer of mineralized fibers, which appear less densely packed, and with their long axis oriented perpendicular to the surface (labeled as (1) in image D). Approx.4-6 µm within the tooth, measured from the surface, ribbons of mineralized fibers are interwoven with the fibers of layer 1 (labeled as (2) in image D). These ribbons are parallel oriented to each other and run along the entire length of the tooth (see Figure S 26, C and D in appendix A). These results show that the teeth of *C. rhoadesii* show similar structural motifs as the other investigated cichlid species.

2.3.2.4 Mechanical properties

NANOINDENTATION

The mechanical properties of the central tooth of the lower pharyngeal jaw of *Chilotilapia rhoadesii* were also investigated by nanoindentation. The mapping revealed that the highest values for the hardness and elastic modulus were found in the enameloid at the very tip of the tooth. The results of the single measurements for the hardness and elastic modulus are displayed in Figure 69 (A and B). It was observed that the values of line 2 and 3 have a high variation. The approximate average values of all maximum values of the hardness and elastic modulus at the very tip of the tooth are 4.01 ± 0.49 GPa GPa and 78.61 ± 8.09 GPa, respectively. Generally, these high values correlate with the red pigmentation within the enameloid (see Figure 69, C). The values then drop to a local minimum. As the values within this area show a high deviation only the lowest values were used for the determination of the hardness and elastic modulus, which is 2.21 ± 0.21 GPa and 55.62 ± 5.93 GPa, respectively. This area appears to be highly porous, which can be correlated with the help of the SEM images in Figure 69 (D and E). As can be further determined by the SEM images, the observed increase of the values of the mechanical properties coincides with a denser, less porous area, which is positioned directly before the dentine. Within this area, the averaged values of the hardness and elastic modulus are 2.76 ± 0.32 GPa and 75.73 ± 7.82 GPa, respectively.
The high deviation of these values might be due to the indenter hitting a pore and thus detecting a lower value during the measurement. Under this assumption, the actual trend along the length of the tooth cannot be clearly determined. Thus, it can also not be determined, if the trend of the mechanical properties within these teeth correspond more to the step-wise profile of the hard diet eating species or the soft diet eating species, which employ a linear gradient within their teeth.
As was the case for all investigated cichlid species the values of the hardness and elastic modulus then show a notable reduction upon reaching the enameloid-dentine junction, dropping to values of about 0.92 ± 0.08 GPa and 23.66 ± 2.56 GPa, respectively.

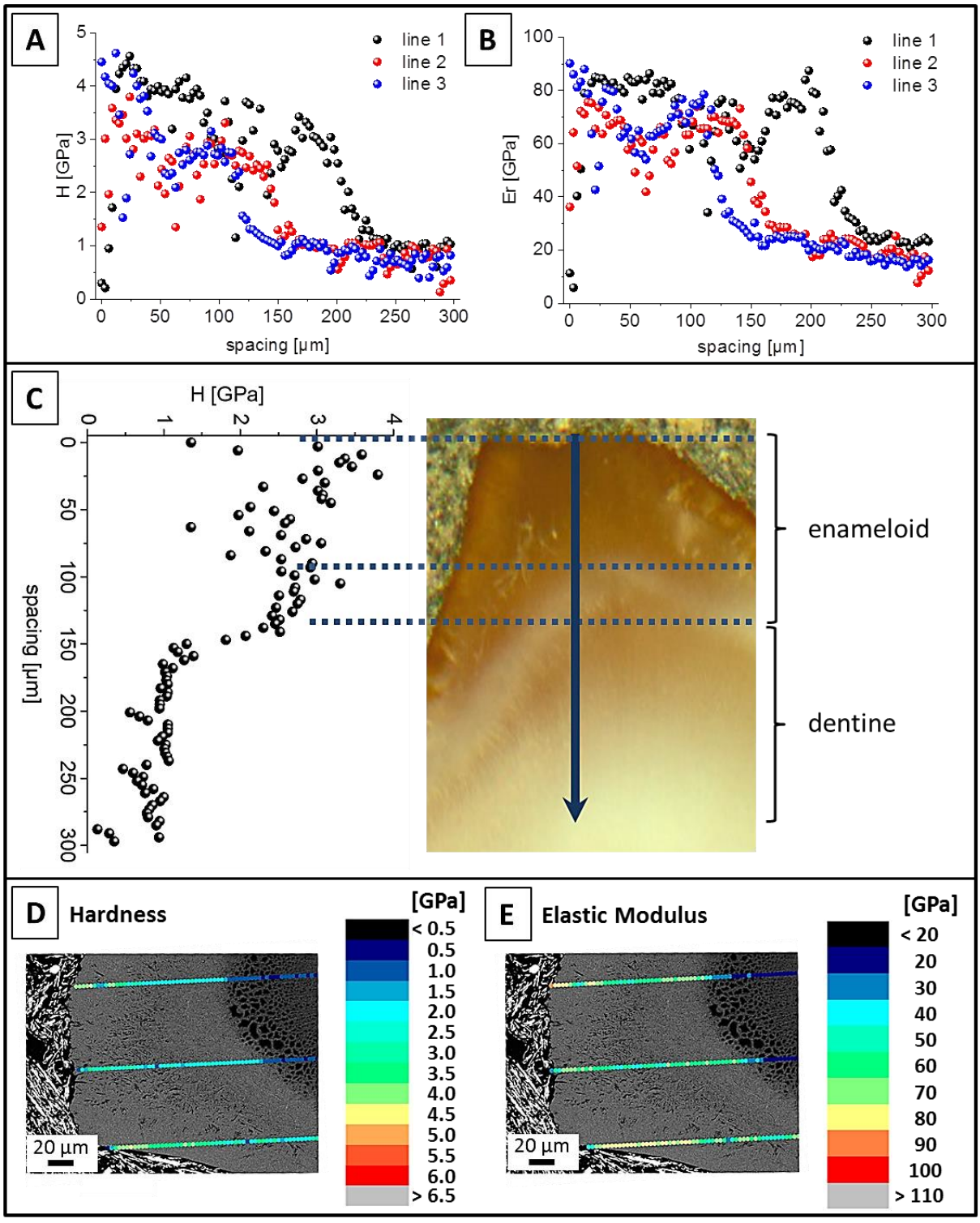

Figure 69: Mechanical properties derived from nanoindentation experiments across the axial cross-section of a tooth of *A. alluaudi.* A: Results of hardness measurements of the single line scans; B: Results of elastic modulus measurements of the single line scans; C: Mean values of the hardness across the sample length correlated with light microscopic images of the cross-section of the tooth; D: Colour coded hardness values directly overlayed with the positions of the corresponding indents displayed with SEM images of the polished cross-section; E: Colour coded values of the elastic modulus directly overlayed with the positions of the corresponding indents displayed with SEM images of the polished cross-section.

AFM OF INDENTS

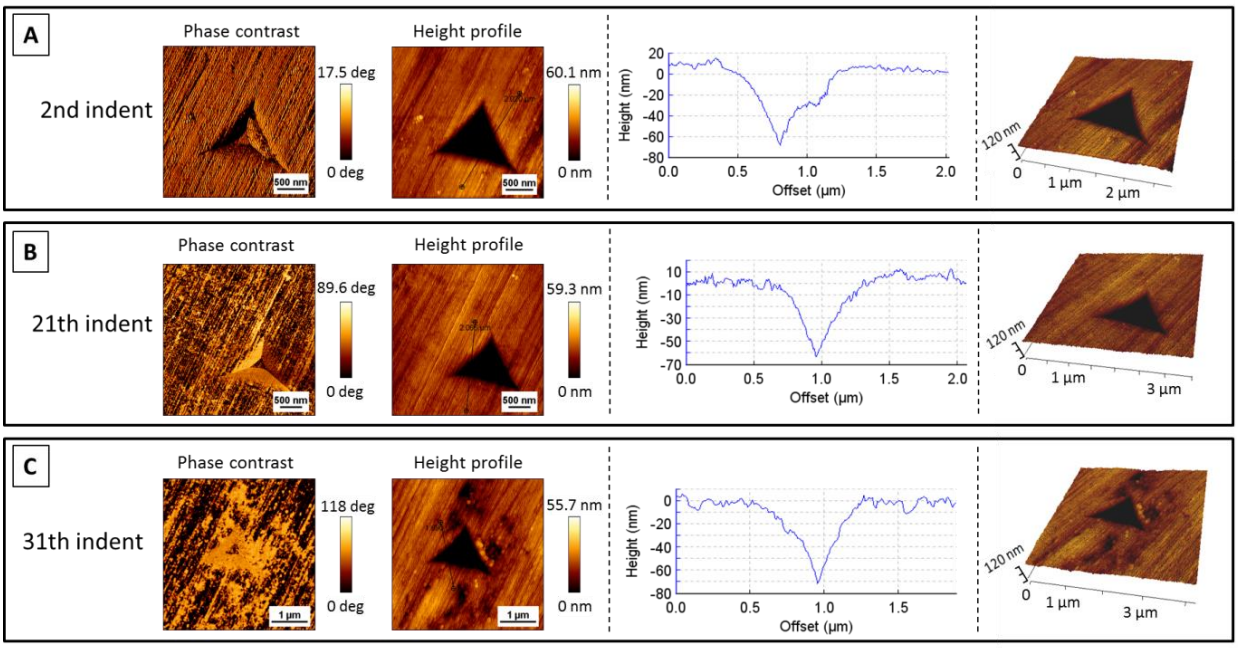

Figure 70: AFM images (phase contrast and height topography) of selected indents the axial cross-section of a tooth of *C. rhoadesii* along the length of the sample, with indent cross-section profiles and 3D visualization.

Figure 70 displays the AFM height topology and phase contrast images of the residual indents made on the surface of the polished tooth (full summary in Figure S 29). The investigation revealed no obvious cracks. Within the measured samples, no pile-ups around the edges of the indents could be observed. The surface of the sample and the edges of the indents remained smooth (see indent profiles in Figure 70 and Figure S 29). Similar to the soft diet eating species and in contrast to the hard diet eating species, no nanogranular structures were observed on the surface. With increasing distance from the top of the tooth, an increase in phase contrast could be observed. These can be seen as stripes along the length of the images in the phase contrast images of the AFM measurements. As there is no drastic topological change on the polished surface, this change could originate from a change in material composition.

2.3.3 *Copadichromis borleyi*

2.3.3.1 Morphology of LPJ and teeth

LIGHT MICROSCOPY

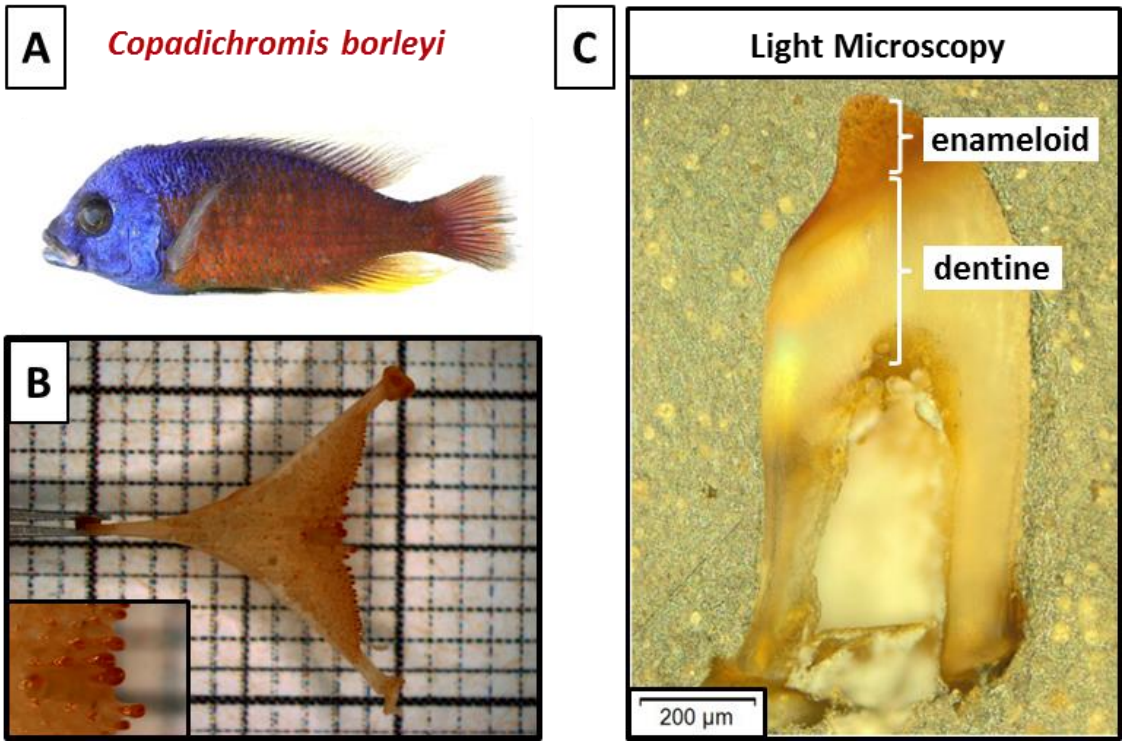

Figure 71: A: Photo of the East African cichlid *Copadichromis borleyi.* B: Lower pharyngeal jaw of *C. borleyi*, inset: biggest central teeth of the lower pharyngeal jaw. C: Merge of a light microscope image of a polished cross-section of a central tooth of the LPJ.

Copydichromis borleyi (Figure 71, A) is a soft diet eating example of Lake Malawi. The shape and color distribution of the LPJ of *C. borleyi* (image B) is similar to the jaws of the soft diet eating species of Lake Victoria. Generally, all teeth are small and papilliform. The biggest central teeth are larger and a bit thicker than the ones investigated for the other soft diet species (e.g., *H. nyererei*). A light microscopic image of a polished axial cross-section of a big central tooth (image C) showed that it is also comprised of an enameloid and dentine area. The enameloid itself appears not as elongated as the caps of the other investigated soft diet eating species.The red/brown pigmentation is strongest at the occlusal top of the tooth but reaches throughout the entire enameloid area.

2.3.3.2 Chemical composition and distribution

ATR-IR Microscopy

The embedded and polished cross-section of a tooth of *C. borleyi* was investigated by ATR-IR microscopy. As indicated in image A in Figure 72, three different positions within the cross-section were measured. Each measurement area is 120 µm in diameter. The corresponding spectra of each position are displayed in image B. From these the presence of the apatite specific ions, and the amide signals of the protein molecules could be confirmed and are summarized in Table S 13. The spectra exhibit two modes at 958 cm^{-1} ($[PO_4]^{3-}$ v_1), 1015 cm^{-1} ($[PO_4]^{3-}$ v_3) and 1088 cm^{-1} ($[PO_4]^{3-}$ v_3). These were assigned to the internal vibration of the phosphate group.[177] The signals at 1650 cm^{-1}, 1550 cm^{-1}, and 1240 cm^{-1} were assigned to the amide I, amide II and amide III, respectively.[178-180] Additionally, amide A and B bands at 3070 – 3300 cm^{-1} were observed, which overlap with the stretching modes of the water molecules.[178] Furthermore, the spectra also show characteristic CH bands at 2852 cm^{-1} and 2925 cm^{-1}. Characteristic carbonate peaks were found at 867 cm^{-1} (v_2), 1419 cm^{-1} (v_3) and 1451 cm^{-1} (v_3), indicating a B-type substitution in the apatite component. Similar to the tooth sample of *M. mola*, it was observed that the signals corresponding to the carbonate and organic component were stronger within the dentine area and decreased in intensity towards the top of the tooth.

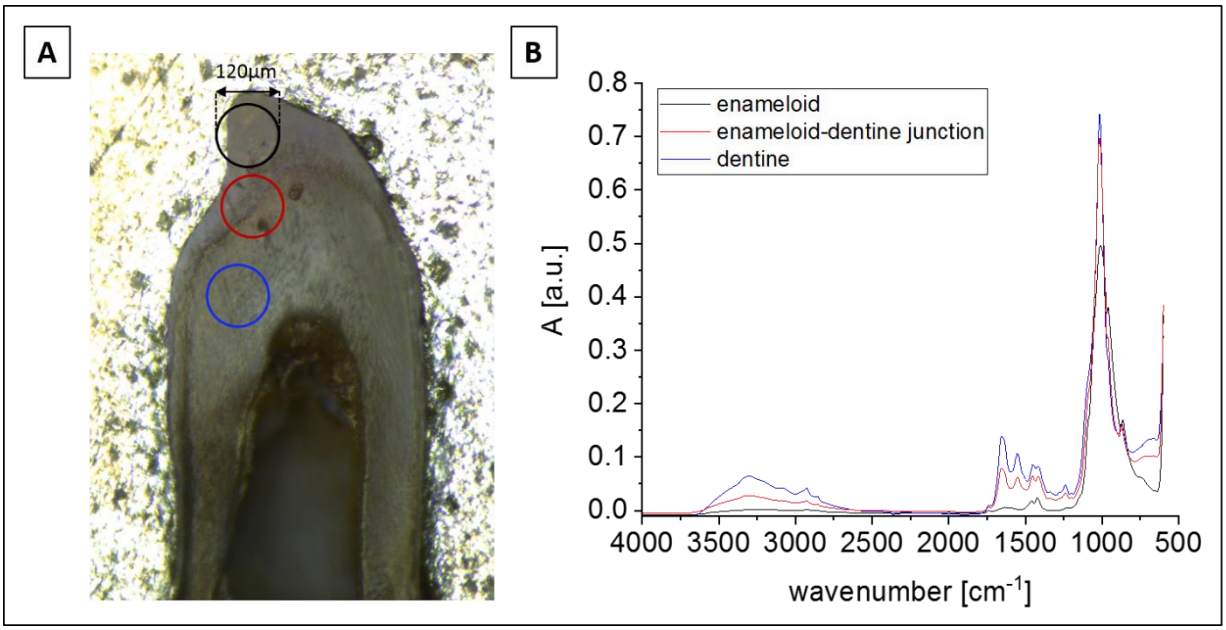

Figure 72: Results of the ATR-IR microscopic measurements on an embedded tooth of *C. borleyi*. A: Light microscopic image with circles indicating the measured area. B: Corresponding IR-spectra of the different measured area as indicated in image A.

2.3.3.3 Ultrastructure of the teeth

HR-SEM

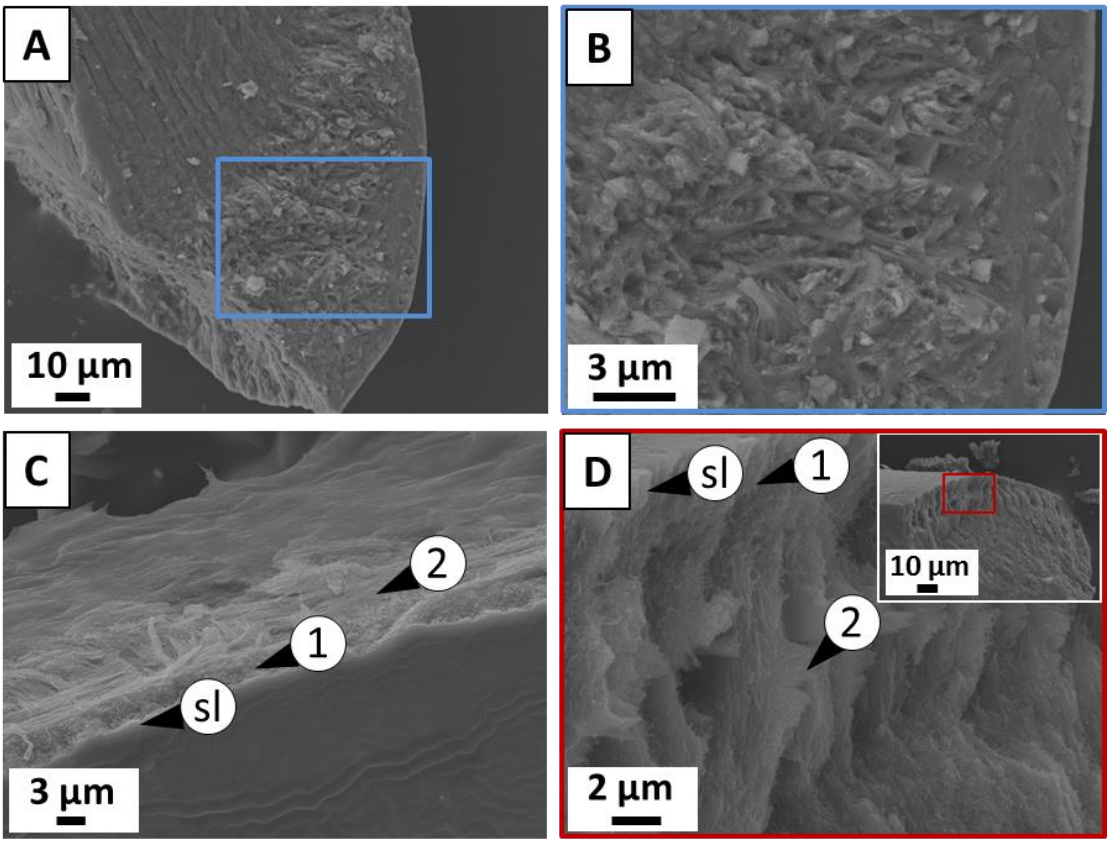

Figure 73: Scanning electron micrographs of fracture areas of crushed teeth of the lower pharyngeal jaw of *C. borleyi.* A: Overview of an axial cross-section of a tooth, displaying the fibrous enameloid area and the dentine area with dentinal tubules, which run along the long axis of the tooth. B: Enlargement of the outer enameloid area as indicated with the blue frame in image A. C: Outer area of an axial cross-section of a tooth, highlighting the outer structural elements. D: Axial cross-section of a fractured tooth, highlighting the outer characteristic structural elements. The position within the tooth is marked with a red frame in the inset, which shows the whole cross-section. Labels (sl), (1) and (2) mark the different structural layers as described in the text.

HR-SEM investigations were performed on fractured the teeth of *C. borleyi* as a good representative of a soft diet eating species of Lake Malawi in order to determine their inner structure. The results are displayed in Figure 73. These investigations revealed that the bulk of the enameloid is composed of thick, randomly oriented mineralized bundles of fibers, which are tightly interwoven in an intriguing pattern (see image A and B in Figure 73). The outer area of the tooth has a dense mineralized layer at the surface of the tooth (see the label (sl) in image C and D). Directly beneath this dense layer are thin, mineralized fibers. These fibers are oriented parallel to each other and perpendicular to the surface (see the label (1) in image C and D in Figure 73). Directly following is a layer of fibrous ribbons which are aligned parallel to each other (see label (2) in image C and D). These ribbons run along the whole length of the tooth, creating an interwoven plywood structure with the previously mentioned mineralized fibers of layer 1. These results generally show that the teeth of *C. borleyi* have similar structural motifs as were identified for the other cichlid species.

3. Discussion

3.1 Inner structure and hierarchical levels

The results of all investigations of this study on fractured and polished tooth samples reveal a complex structure with several different hierarchical levels at different length scales. The investigated hard and soft diet eating species show several similar structural motifs within the ultrastructure of their teeth, however, their arrangement and distribution, as well as the degree of mineralization, significantly vary. Such similarities are not common as it has been reported that within a single dentition similar teeth (e.g., premolars and molars) commonly share the same schmelzmuster, but teeth with significant morphological differences and function (e.g., incisors) often have their own schmelzmuster.[185] In view of the observed similarity in the inner structure of the teeth of all investigated specimen, the structure is summarized in a single, simplified structure model, showing the basic structural units (Figure 74, A.)
The outer surface consists of a dense, thin mineralized layer, where the crystallites are densely packed parallel to each and with their long axis perpendicular to the surface. Directly beneath this superficial layer are mineralized fibers, which are roughly parallel aligned and perpendicular oriented towards the surface (labeled as (1) in Figure 74). These fibers become more decussated from the top of the tooth towards the inside. This area resembles the so-called “shiny layer” and “parallel-fibered layer”, as previously described for the outer region of shark teeth.[48, 186] TEM investigations showed, that the fibers have a diameter of about 30 nm and lateral spacing of about 60-64 nm periodicity of their fiber cross-striation, which is a bit smaller than for human collagen fibrils. These results are however consistent with reports of the structure of the dental epithelium and odontoblasts during enameloid matrix deposition of the cichlid *Cichlasoma cyanoguttatum*.[187] Herein, it was reported, that the enameloid matrix of several teleosts, such as cichlids, consists of small-diameter collagen fibers, in contrast to shark enameloid matrix, which consists of large-diameter collagen fibers. It has been hypothesized that in cichlids small differences in the collagen type may inhibit the formation of strong cross-links, which can result in small, more soluble enameloid fibrils.[187, 188]
About 5-10 µm within the tooth, depending on the species, these crystallites are interwoven with ribbons of fibrous mineralized bundles which run along the long axis of the tooth and are perpendicular to the long axis of the mentioned crystallites of the layer 1. This arrangement creates an interwoven plywood-structure (labeled with (2) in Figure 74). These bundles cover the full length of the tooth. The innermost layer of the enameloid, which describes the junction between the enameloid and dentine, consist of less organized bundles of tangled, mineralized fibers, which are more densely packed and slightly oriented towards outer areas of the tooth (D, marked with (3)). The dentine itself is composed of finely crystallized bundles oriented in a random fashion and contains channels, the so-called dental tubules, which have a diameter of about 1-2 µm. These tubules are surrounded by a fibrous network of concentrically arranged fibers. Generally, the structure of the dentine resembles that of or-

thodentine. Orthodentine is discussed to predominate in teleost fishes, such as the cichlids investigated in this study.[112, 113] As is typical for orthodentine, these tubules radiate outwards from the pulp and perforate the entire tooth. The bulk of the enameloid consists of highly interwoven mineralized fibers. Generally, it was observed, that all crystallites follow the long axis of the collagen fibers. This has also been observed in TEM studies on the structure of the dental epithelium during enameloid mineralization of the cichlid *Cichlasoma cyanoguttatum*.[189] Similar to their results, slightly compressed/distorted hexagonal prisms, which are elongated along [001] of the apatite were observed within the enameloid. These prisms are not as perfectly hexagonal in cross-section as is the case for the fluorapatite crystals in elasmobranchs, e.g., in the shark enameloid.[190]

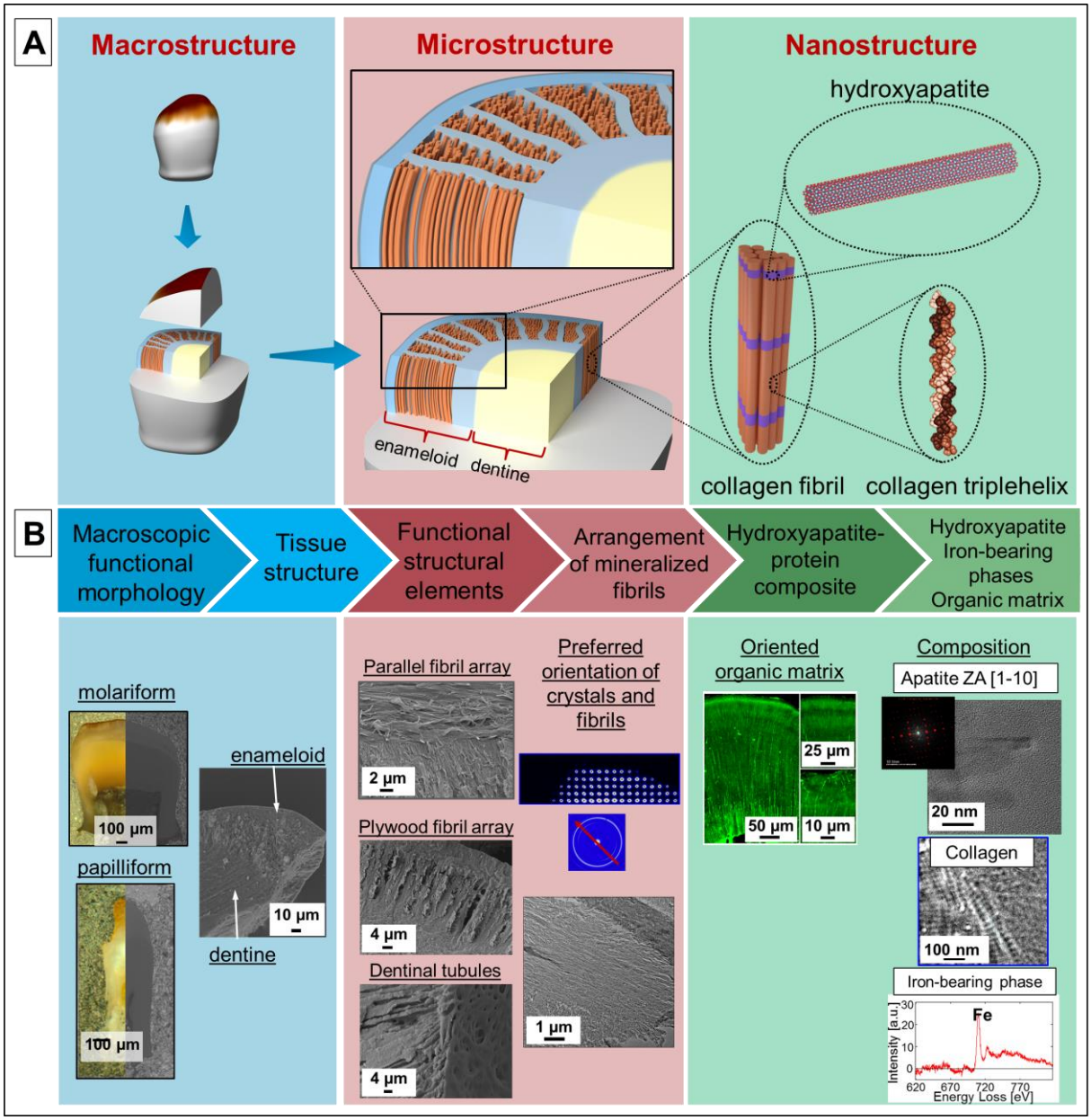

Figure 74: A: Structure model of the inner structure of the teeth of the investigated cichlids. B: Different hierarchical levels, which were identified for the teeth of the investigated species. Below are examples of different analysis results of this study, which correspond to the respective hierarchical levels.

Despite the apparent similarities in the structure, the teeth of the investigated cichlid species show differences in the thickness and distribution of these structural elements. The molariform teeth of the hard diet eating species utilize a comparably thin enameloid. Thus, the diffuse, interwoven fibrillary arrangement within the enameloid is generally thinner as well and spread out over a large area. In contrast, the thin and pointed papilliform teeth of the soft died eating species show an elongated enameloid cap.

The complex structure of these teeth can be classified into different hierarchical levels comprising several length scales. On the lowest hierarchical level, the basic components are the hydroxyapatite phase, the iron-bearing phases and the organic molecules (e.g.,collagen). µ-beam WAXS and SAXS investigations on an axial and transversal cut revealed that sizes of coherent scattering domains (CSD) show a slight elongation in the *c*-direction, as was indicated by the narrowing of 00l diffraction peaks. The calculation of the apatite lattice parameters showed, that the parameter *a* slightly decreases in the apatite crystals from the enameloid toward the dentine, while the *c*-parameter remains nearly the same. These variations in lattice parameters and CSD can be caused by several ionic substitutions within the apatite crystal structure.[32]

The next higher level is described by the apatite-collagen composite structure, which is specifically ordered within the different hard tissues of the tooth and packed into tight bundles. These mineralized bundles already describe the next hierarchical level on the microscale. These different bundles or fiber arrays are arranged in different structural motifs. Herein, different fibrillary arrays could be identified. These are summarized in Figure 75. There are arrays of parallel fibrils, which can be found at the outer collar of the enameloid area (see A in Figure 75). The next fibril pattern is a plywood-like fiber arrangement. Here, the parallel oriented fibrils are arranged in fiber ribbons, which are interwoven with perpendicularly oriented fibers. Plywood-like structural motifs are very common in nature. In natural biological hard tissues, this motif can be encountered in bone, tooth cementum or certain fish scales (many of which are mineralized).[117] Another pattern is a tangled fiber arrangement. Here, the fibrils are arranged into bundles, which are loosely packed and poorly oriented. Such a woven fiber structure can also be found in woven bone.[117] In the cichlid teeth, this arrangement is typical for the bulk of the enameloid area. The last arrangement is a radial fiber arrangement. This pattern is characteristic of the bulk of dentine.[117]

The next hierarchical level is described by the tissue structure, which consists of the enameloid, with its complex structure, and the dentine. The shape of the whole macroscopic tooth describes the last level of the hierarchy, where the shape itself is application-oriented (e.g., molariform for crushing or papilliform for grabbing prey). The impact on these different hierarchical layers on the mechanical performance of the tooth will be discussed in chapter II, 3.5.

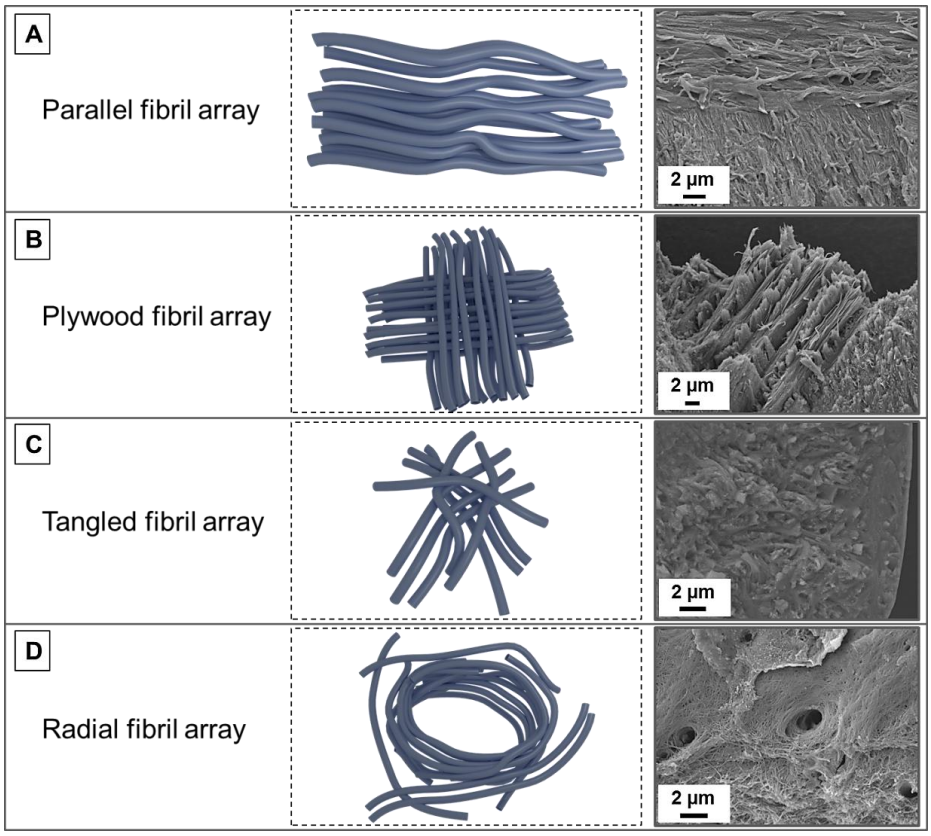

Figure 75: Different fibril arrays with their SEM examples within the cichlid teeth. A: Parallel fibril array, which can be found at the outer collar of the enameloid area. B: Plywood fibril array. This layer is interwoven with the parallel fibers of the parallel fibril array at the distal area of the enameloid. C: Tangled fibril array, which is characteristic for the bulk area of the enameloid. D: Radial fibril array, which can be found around the dentinal tubules in the dentine.

3.2 Composition

Qualitatively the dental hard tissues of the teeth of all investigated fish species have the same element and phase composition. The main inorganic component of enameloid and dentine is carbonated hydroxyapatite, which is substituted by fluoride at the occlusal surface of the enameloid. Furthermore, the enameloid contains iron-bearing phases, which are enriched at the occlusal surface of the teeth. The main organic component of the enameloid and dentine is collagen.

There is generally a higher amount of calcium and phosphate in the enameloid than the dentine. The hard diet eating species display a distinct, step-wise distribution pattern of the calcium and phosphate along the length of their teeth. Specifically, a very high concentration of both elements was found at the occlusal top of the tooth. The concentration falls to a local minimum, before rising again to a local maximum, and finally to a low concentration within the dentine. The soft diet eating species, on the other hand, show a nearly linear decrease of calcium and phosphate from the occlusal top towards the dentine, before falling to a low concentration within the dentine.

The relative carbon content, as was determined by EDXS line scans, showed a homogeneous distribution along the length of the enameloid. The amount increases drastically upon reaching the enameloid-dentine junction. The carbon stems from the

organic matrix but also might also be attributed to the carbonate ions within the apatite crystal structure. As element mappings based on EDX are not able to differentiate between different ionic groups and ionic substitutions, vibration spectroscopy, especially utilized as a microscopy technique, is a powerful complementary tool to identify these and clarify their distribution across the sample. However, the interpretation of IR- and Raman- bands of complex systems such as teeth can be quite challenging and require various considerations. The positions of the infrared absorption bands of carbonate indicate a B-type carbonate substitution. Carbonate substitution could, however, be barely detected in the Raman spectra, as the signal to noise ratio is very high and some bands quite broad, in all performed measurements. Thus, no reliable distribution along the length of the sample could be determined in most cases. It is well known that biological apatites in hard tissues contain a variable amount of carbonate, which is a significant substituent in the crystal structure. It is also well known that the incorporation of carbonate into the apatite crystal structure have drastic effects on the material properties, such as its dissolution behavior, which is important for the process of de- and remineralization of biological hard tissues.[39, 54, 57, 58] Depending on the amount and type of the carbonate substitution in the apatite crystal structure, the lattice parameters can undergo different changes. In case of an A-type substitution the *a*-parameter increases, whereas the *c*-parameter decreases, while for B-type substitution the changes are vice versa. Consequently, carbonate ions can also influence the crystal shape and size during the growth process. The effect of carbonate on physicochemical parameters and crystal morphologies has been studied in a synthetic system of B-type substituted carbonated fluorapatite-gelatine composites, which were grown in a double diffusion setup.[59] Herein it was reported that with increasing carbonate content, the fluorapatite-gelatine composite species (crystals and aggregates) become generally smaller and more rounded. Furthermore, the size of coherence scattering domains decreases (along [001]).

Fluorine could be detected in all teeth of this study, indicating a gradual fluoride substitution of the hydroxyl groups in the channels of the apatite crystal structure. The general distribution within the teeth is the same for the hard and soft diet eating species. The fluoride content is generally higher in the apatite within the enameloid at the occlusal surface of the teeth, which gradually decreases towards the dentine. The results of the Raman microscopy measurements of the phosphate v_1 band, especially of the *H. sauvagei* sample, indicate a small shift towards higher wavenumbers. This could indicate a higher degree of fluoride substitution in the apatite component.[191-193] The F- profile scans of the EDXS measurements confirm, that there is indeed an increase of fluorine towards the surface of the tooth, whereas there is no shift in the dentine part of the samples. However, due to the high signal to noise ratio, care has to be taken, when interpreting such small shifts in wavenumbers within biological hard tissues. The fluoride content in the teeth of fishes has repeatedly been suggested to be related to the phylogeny rather than the environmental water.[134]

In all investigated teeth of the different cichlid species, iron could be detected in the enameloid, although the distribution varies depending on the species. Soft diet fish, which have small, papilliform teeth, show a tendency to have an iron gradient along the length of the whole enameloid, which drops to nearly zero at the enameloid-

dentine junction. Whereas *H. chilotes* has a continuous nearly linear gradient towards the dentine, *H. nyererei* shows locally very high variations in the concentrations of iron at the very tip between the first 10 µm into the tooth. Except for *A. alluaudi*, the species bearing molariform teeth show a narrow layer of iron of about 10-20 µm into the enameloid. As mentioned in the introduction cichlids have been suggested to be classified into two types. Type A is characterized by a high iron concentration that can be detected mainly towards the occlusal part of the enameloid. In type B, the iron is deposited throughout the entire layer.[149] Within this classification, the hard diet eating species clearly showed a preference towards type A, whereas the soft died eating species could be assigned to type B. Those species employing a mix of soft and hard diet showed different results: whereas *H. sauvagei* tended to display a type A distribution similar to the hard diet eating species, *C. rhoadesii* showed a distribution better fitting within the type B category.

Identification of the iron phase proved to be challenging. No method utilized in this study (µbeam WAXS, Electron diffraction in TEM, Vibration spectroscopy) was able to identify any crystalline iron-bearing phase. For Raman-spectroscopy, scientists reported, that different iron oxides and -hydroxyoxide phases display different vibration mode positions in Raman spectroscopy.[194] While some bands in positions of characteristic iron-containing mineral phases could be found within the cichlid teeth, the exact identification of the iron phase and the distribution along the investigated samples were not conclusive. A severe problem is the fact that some iron minerals transform easily into other phases when applying laser powers of 1 mW or more.[176] Herein, it was reported, that most of the iron (oxy)hydroxides are converted to haematite. In this study, some signals could be assigned to typical haematite signals, others to magnetite. It was thus not possible to identify the origin of the iron-bearing phase in the material with Raman-microscopy. Gordon and co-workers reported the presence of intergranular amorphous iron phosphate within rodent tooth enamel.[195] From EXAFS spectra, this amorphous phase was estimated to amount to 42%, the other phase being a “ferrihydrite-like material”. It was discussed, that amorphous phases can be very accommodating of substituents, and thus this amorphous iron phase may be described as a mixture of ferrihydrite and amorphous iron-calcium phosphate.[195] This agrees with results from another beaver enamel study of *Myocastor coypus*.[196] The results of Dumont *et al*. indicate magnetite as the iron-phase for the pigmented enamel of the shrew *Blarina brevicauda*.[145] Within these studies, they reported that the magnetite phase might be present as ultrafine grained material, which is close to amorphous. Both studies, enamel of beaver and shrew, agree that the iron-rich phase is distributed around the hydroxyapatite crystals and that iron does not substitute calcium in the apatite lattice structure. A similar ultrafine grained iron-phase could also be present within the teeth of the investigated cichlid species. However, further studies are necessary to verify this hypothesis.

All investigated samples showed the presence of sodium and magnesium. Both ions can substitute for Ca in the apatite crystal structure.[197, 198] Generally, the sodium concentration was increased in the apatite of the enameloid of the teeth and dropping at the border towards the dentine. The magnesium displayed the exact opposite

trend. All investigated samples had an increased amount of magnesium in their dentine, with an increase at the border towards the enameloid.

3.3 Mechanical properties

Nanoindentation measurements were performed on the polished axial cross-section of the cichlid specimen teeth from the tip to the dentine area to measure the local penetration resistance, as well as elastic and plastic mechanical properties. The small scale of this method allows correlating these properties with the structural and/or chemical features of the investigated samples. The results of the averaged hardness and elastic modulus in different areas along the length of the teeth are summarized in Table 8 and Table 9 respectively. The determination and definition of the different areas A-D can be exemplarily seen in Figure S 31. Herein, area A was assigned as the hardest outermost area of the enameloid and D was assigned to the dentine. A positional shift of the values within the sample has been taken into account, where only values pertaining to the same layer were averaged.

Table 8: Averaged values of the hardness along axial cross-sections of different cichlid species as were determined by nanoindentation measurements (left) and the ratios of the different areas to each other (right).

Hardness [GPa]					Ratio:		
species/area	A	B	C	D	A/D	B/D	C/D
A. alluaudi	5.61 +/- 0.26	2.82 +/-0.09	3.35 +/- 0.19	1.38 +/- 0.04	4.07	2.04	2.43
H. ishmaeli	4.6 +/- 0.33	2.04 +/- 0.12	2.65 +/- 0.06	1.19 +/- 0.01	3.87	1.71	2.23
H. sauvagei	4.94 +/- 0.25	2.54 +/- 0.06	2.87 +/- 0.07	1.26 +/- 0.07	3.92	2.02	2.28
H. chilotes	4.12 +/- 0.39	-	3.12 +/- 0.12	1.27 +/- 0.18	3.24	-	2.46
H. nyererei	4.08 +/- 0.13	-	4.35 +/- 0.67	1.29 +/- 0.06	3.16	-	3.37
C. rhoadesii	4.01 +/- 0.49	-	2.80 +/- 0.18	0.92 +/- 0.08	4.36	-	3.04

Table 9: Averaged values of the elastic modulus along axial cross-sections of different cichlid species as were determined by nanoindentation measurements (left) and the ratios of the different areas to each other (right).

Elastic modulus [GPa]					Ratio:		
species/area	A	B	C	D	A/D	B/D	C/D
A. alluaudi	105.89 +/- 2.98	70.84 +/- 7.20	78.24 +/- 3.78	33.66 +/- 1.72	3.15	2.10	2.32
H. ishmaeli	82.1 +/- 3.14	49.99 +/- 3.18	67.19.+/- 0.29	28.46 +/- 0.36	2.87	1.76	2.36
H. sauvagei	95.58 +/- 2.74	67.94 +/- 2.32	66.90 +/- 3.09	29.51 +/- 1.33	3.24	2.30	2.23
H. chilotes	80.87 +/- 8.91	-	66.99 +/- 1.59	34.41 +/- 2.41	2.35	-	1.95
H. nyererei	83.96 +/- 9.63	-	83.52 +/- 8.82	32.83 +/- 0.71	2.56	-	2.54
C. rhoadesii	78.61 +/- 8.09	-	72.26 +/- 4.38	23.66 +/- 2.56	3.32	-	3.07

The results showed that the hard diet eating fish species displayed the hardest enameloid and the soft food eating fish species showed the softest enameloid, with a gradual decrease of hardness from hard diet towards soft diet, when looking at the averaged values. The values for the species that feed on a mix of hard and soft food, like H. *sauvagei* and *C. rhoadesii* are in between pure soft and hard diet eating spe-

cies. This is also reflected in the A/D ratio. As the hardness of the dentine and elastic modulus are generally similar for all tooth bearing vertebrates, which utilize apatite as a basis for the inorganic mineral component within their teeth, using these values as a normalization factor lowers the systematic error of the measurement. [199-203] The slightly lower hardness within the enameloid of *H. ishmaeli* do not fit into the expected trend, as it feeds on a hard diet. This might be due to the fact, that the nanoindentation measurements were taken in an area, which has less iron incorporated within its composition. This can be seen from the light microscope images of the tooth surface as well as the EDX-line scans. In fact, measuring EDX- line scans slightly shifted within the red area (Figure S 10 in appendix A) shows an increased iron content at the occlusal top of the tooth. Thus, the measured hardness for *H. ishmaeli* might not be representative of the whole tooth and could be underestimated. Generally, some caution has to be taken when interpreting absolute values of nanoindentation measurements and comparing the results to other studies. It has to be considered, that only one chosen tooth of each jaw of each specimen has been investigated in this study. Thus, no biological variations between each tooth of each jaw and even between different individuals of each species could be taken into account, which has been shown to vary slightly in mammalian teeth.[203, 204] Furthermore, all values are averaged on the assumption of a homogeneous distribution of the elements along the length of the analysis volume, which might not be the case for natural samples. Examples of the inhomogeneity of the elemental composition of the teeth can be seen in the light microscopic images of the teeth, where the red/brown pigmentation is not exactly the same for adjacent teeth (see Figure 11 (B)) or within one tooth (Figure S 10). Additionally, due to different indentation techniques and procedures used in literature the values can differ due to the method of indentation, sample preparation or load applied, which can greatly influence the interpretation of the results.[48, 50, 205, 206]

General trends for the hardness and elastic modulus throughout the axial cross-sections of the teeth could be observed for the hard diet and soft diet eating species respectively. Hard diet eating fishes show a clear step-wise profile along the tooth. They have high values at the occlusal top of the teeth, dropping to a local minimum, rising again to a local maximum and dropping at the enameloid-dentine junction to a generally low value in the dentine. The soft diet eating species, on the other hand, show a linear decrease from the occlusal top towards the dentine. The associated elastic modulus follows the same trend as the local hardness. *H. sauvagei* who utilizes its teeth both for hard and soft food displays a profile that resembles more the profiles of the pure hard diet eating species. The profile of *C. rhoadesii* could not clearly be assigned. The dentine area displayed roughly the same hardness in all investigated samples, that is about 1.3 GPa on average of all investigated species. Generally, it was observed, that the hardness of the material correlates with the amount and distribution of the apatite-component and the iron-bearing phase within the teeth.

When a sharp, stiff indenter tip is used for the measurement, the plastic deformation initially occurs at the direct contact area. When abrasion is produced in this scenario, the abrasion resistance approximately scales with the hardness. Under the assumption that abrasion damage is proportional to the material property group $K_{Ic}^4 /(HxE^2)$,

and K_{Ic} is similar for all investigated teeth, a low increment of fracture toughness significantly improves the abrasion resistance.[207, 208] This has also been demonstrated for other biomaterials such as nacre and shells.[207, 209] Comparing the single values of the investigated species (see Table 10) it can be seen, that all of them are in the same range, with the value of *A. alluaudi* being a bit lower than the other samples. This implies that all teeth show the same abrasion tolerance.

Table 10: Materials property parameters for the teeth of the investigated and various biominerals and ceramics.

	H [Gpa]	Er[Gpa]	1/H Er^2 [1/GPa^3]	Reference
A. alluaudi	5.61	105.89	1.6×10^{-5}	This study
H. ishmaeli	4.6	82.1	3.2×10^{-5}	This study
H. sauvagei	4.94	95.58	2.2×10^{-5}	This study
H. chilotes	4.12	80.87	3.7×10^{-5}	This study
H. nyererei	4.08	83.96	3.5×10^{-5}	This study
Radular teeth from *C. stelleri* (Chiton)	9-12	90-125	$7 \times 10^{-5} – 1.4 \times 10^{-5}$	[146]
Magnetite	10.5	175	7×10^{-6}	[146]
Aragonite (Abalone and Conch shells)	3-4	70-75	6.3×10^{-5}	[206]
SiC	20-30	410-480	$1.5 \times 10^{-7} – 3 \times 10^{-7}$	[210, 211]
B4C	30	430-480	1.6×10^{-7}	[211, 212]

However, it has to be noted, that biological mineral composite materials often have fracture toughness enhancement mechanisms during crack propagation compared with brittle materials that generally have a single value of fracture toughness (K_{Ic}). Such resistance-curve or “R-curve behavior” has also been reported for bulk enamel, which exhibits increasing fracture toughness with crack extension.[213] The results pointed out, that the average fracture toughness, as was quantified from the maximum critical stress intensity, was on average 2.07 ± 0.22 MPa $m^{0.5}$. These values were more than twice the estimates, which were obtained from indentation fracture resistance measurements of other studies. Thus, care has to be taken, when abstracting fracture toughness modes for such complex materials. The single fracture toughness enhancement mechanisms, which were observed within the teeth of the investigated cichlid species, will be discussed in the next chapters.

The AFM investigations of the residual impressions after the indentation showed no or only slight pile-ups and seldom cracks around the edges of the indents. Some studies have reported, that the occurrence of larger pile-ups at the edges of indents might lead to an overestimation of H and E with the Oliver-Pharr method due to the difference between the true contact area of the indenter tip to the contact area acquired during the calibration. [214-217]

3.4 Implications of macroscopic morphology on mechanical properties

Tooth morphology has long since been linked to the tooth function and even prey preference.[218, 219] When comparing the actual performance of teeth, hardness and strength are not the only factors to consider. The macroscopic tooth design is also important, as the teeth must also perform well according to their intended function, e.g., crushing or penetrating prey. The “snail-crushing” species of this study show convex tooth cusps, which have a high mineral content with a high hardness. The soft diet eating species show short, papilliform tooth shapes, which are optimized for piercing or grabbing the prey. These smaller teeth are not highly mineralized, thus their flexibility is higher, and the risk of tooth fracture is minimized. The morphology of the teeth of the species that feed on a mix of harder and softer food, like *H. sauvagei* and *C. rhoadesii* are morphological in between pure soft and hard diet eating fishes.
Researchers tried to quantify the relationship between the force of penetration and the sharpness of the teeth.[220] Strong or stiff foods (e.g., cuticles of insects) are most efficiently broken down by minimizing the contact area between the tooth and the food, thus maximizing the jaw forces onto a single spot.[219-221] At the same time, the tooth must not be brittle to penetrate into the prey without breaking. Short teeth with high curvatures are therefore optimized for this application. For molariform teeth, it was predicted, that “blunt cusps” can break more brittle foods equally effectively, while reducing the risk of tooth tip fracture.[221] Based on the results of measurements of a series of aluminum tooth models, which varied in concavity and morphology, it was found, that the most effective tooth shape for breaking snail shells is flat or convex with a tall skinny cusp.[222] The teeth of the cichlid fishes, therefore, show a good example of adaptation of tooth morphology to their respective function.

3.5 Implications of the inner structure and tooth morphology on mechanical properties

Biomechanical properties usually emerge from contributions of structural elements across multiple length-scales throughout the material. These structural elements are attributed to improve different mechanical properties, such as strength, stiffness, flexibility, fracture toughness, wear resistance and energy absorption. As already mentioned in the introductions, such mechanisms of biological composite materials are typically divided into intrinsic and extrinsic mechanisms. The intrinsic mechanisms are typically associated with structures smaller than 1 µm. Within the cichlid teeth, the lowest hierarchical level is represented by a single crystallite and the molecular structure of the collagen fibers. The hardness of poly-nanocrystalline composite materials was reported to be influenced by the orientation of the crystals and the degree of crystallinity.[50, 186, 223-228]
As the TEM and SAXS/WAXS investigations of the enameloid indicate, the apatite crystals are arranged with their crystallographic long-axis oriented perpendicular towards the surface of the tooth. On the assumption that the orientation of the crystals does play a role in the resulting hardness of a material, this should reinforce the material and optimize the nanohardness and modulus towards the surface. Apatite be-

longs to the hexagonal crystal system which displays an anisotropic stiffness[229]. Theoretically, this results in a higher modulus in the direction parallel to the crystallographic *c*-axis. In consequence, this should result in significantly improved wear resistance and fracture tolerance. This has been proposed for the anisotropy of the crystallites in human dental enamel due to different orientations of the enamel prisms.[167, 230] However, it has also been repeatedly reported, that the crystallite orientation did not play a major role in the resulting hardness of a material.[50, 230-232] Braly *et al.* performed nanoindentation experiments on human molar teeth with distinct prism orientations (perpendicular and parallel to the long axis of the prisms) and found no correlation between the crystallite orientation and the hardness and elastic modulus.[231] However, they also caution, that their results do not exclude the possibility of such orientational properties, which were determined with other methods. As such indentations generally create radial and not uniaxial deformations, the properties, such as hardness and elastic modulus, tend to be averaged over multiple crystallite orientations.[231, 233] Thus even measurements on highly anisotropic materials might result in relatively small variations in hardness and elastic modulus.[234] Generally, all these studies agree on the thesis, that the chemical composition of the teeth is more with regards to hardness and elastic modulus.

Further toughening mechanisms on this hierarchical level belong to the collagen component within the teeth. It has been demonstrated for collagen that the general mechanism arises from the energy required for the collagen molecule to unfold.[235] When the chains are extended, they are able to slide past each other.[236] Additionally, cracks can develop within the collagen fibrils.[236, 237] Furthermore, it has been demonstrated that there are sacrificial bonds within or between the collagen molecules that dissipate energy when they are stretched and are reformed after the load is released.[168, 236]

A further crack deflecting mechanism is associated with the nanogranular structure, which was identified by AFM imaging. An example of crack-propagation is displayed in image A of Figure 76, which shows the AFM topography and phase contrast images of the residual imprint on the surface after nanoindentation of a tooth of *H. sauvagei.* The single grains can be clearly recognized and display diameters between approximately 80-100 nm. The cracks at the edges of the imprint follow the boundaries around the grains (see white arrows in image A). Grain boundaries are generally considered to constitute to planes of reduced fracture resistance, and thus, cracks can follow along these boundaries. This allows for further energy dissipation by significantly enlarging the crack pathway (see scheme in image B in Figure 76).[168, 238-241]

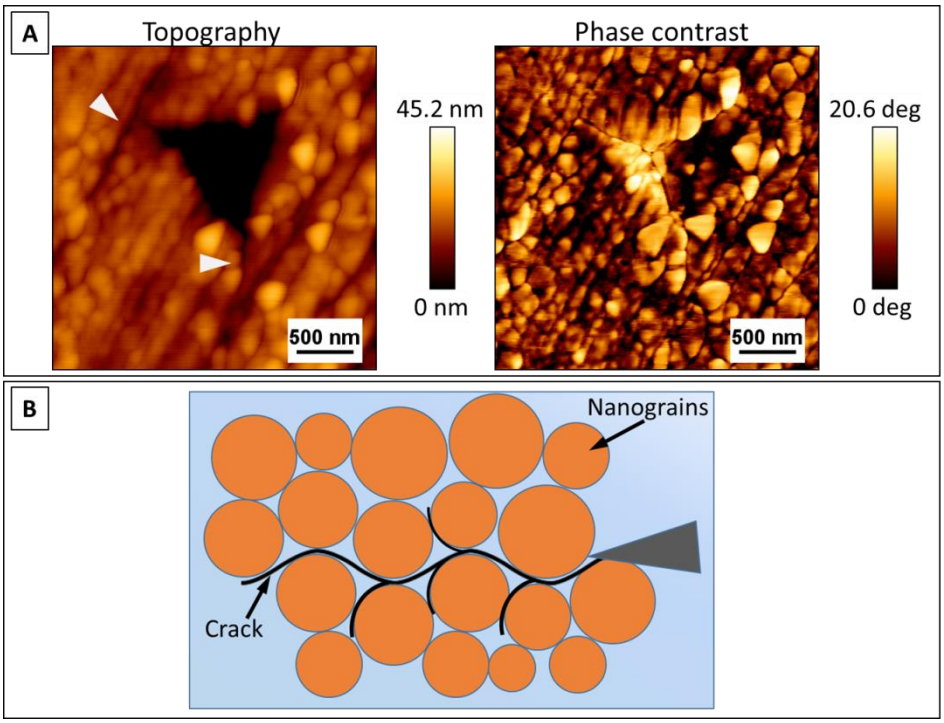

Figure 76: A,B: AFM topography and phase contrast image of H. sauvagei after nanoindentation highlighting the nanogranular structure. B: Scheme illustrating the crack propagation in nanogranular structures.

Typical crack toughening mechanisms, which are associated with the higher hierarchical levels within the tooth belong to the so-called extrinsic toughening mechanisms. The relevant structural elements, which were observed from the occlusal surface to the enameloid-dentine area of the teeth of cichlids, are displayed in Figure 77. One factor consists of the crystalline outer surface, which densely packed apatite crystallites, as schemed in A and B. In previous studies on the crack growth resistance of human enamel, it has been concluded that cracks are guided through areas with straight prisms towards the inner, more decussated region in the dentine, where the cracks encounter crystallites, which are more oblique to the crack path (crack deflection) and are finally arrested.[213]. During this process the surface layer is delaminated. In the teeth of elasmobranchs, similar structures have been hypothesized to impart tensile strength.[242] This energy-dissipating mechanism is repeated in the inner areas of the enameloid, as indicated in image D in Figure 77. Another extrinsic toughening mechanism, which is present in the cichlid teeth is the so-called collagen-fibril crack bridging. Towards the occlusal area within the enameloid, the collagen fibers are arranged as a plywood structure, as is indicated in the inset in image C in Figure 77. At the same time, these fibers can act to diffuse the crack force within this layer. Should cracks still continue towards the inner enameloid areas, they can, as already mentioned, be arrested due to the even more diffuse structure directly before the enameloid-dentine junction. From the phase contrast images of the AFM measurements, a fine nanogranular structure was noticed within that area. Such structures have been observed within the architecture of the inner layers of some brachiopods and have been assumed to direct noncontinuous microfractures and jagged crack fronts to promote energy dissipation and thereby prevent catastrophic brittle fractures.[168, 243]

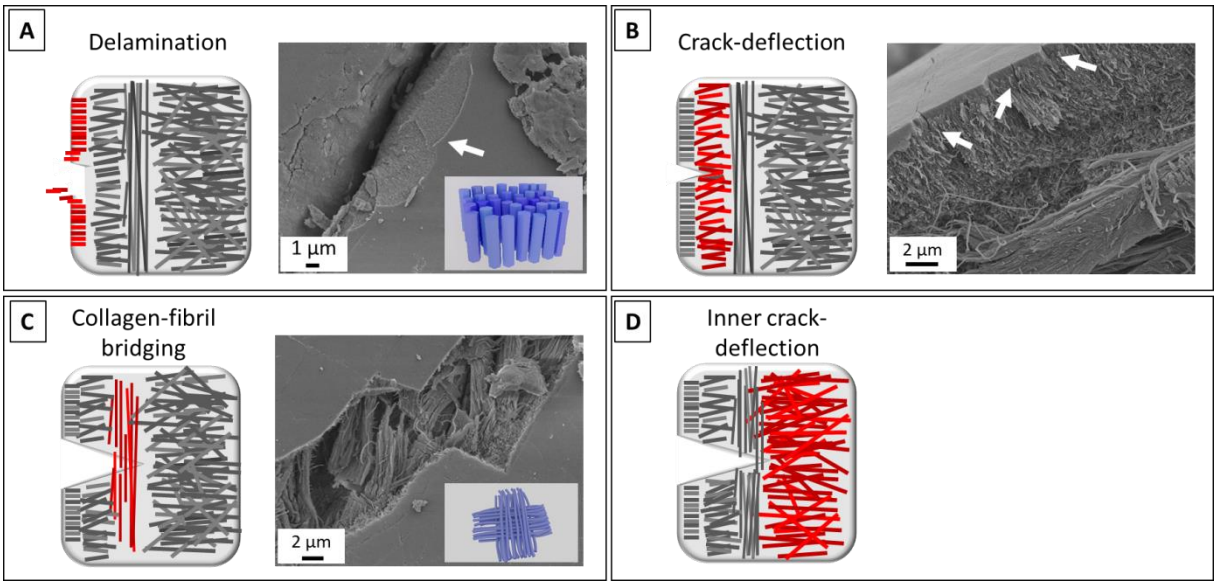

Figure 77: Schemes and SEM examples of extrinsic toughening mechanisms, which were observed for the cichlid teeth: A: Delamination. B: Crack-deflection; the arrows mark cracks, which have been arrested due to the crack-deflection properties of this structural element. C: Collagen-fibril crack bridging, D: Inner crack-deflection.

Another extrinsic defense mechanism against critical cracking failure is represented within the dental-tubule system along the length of the tooth. In teeth, these tubules usually provide the nutrients and allow for cellular activity. These structures can also serve as scattering centers, which decrease the amplitude of longitudinal stress, which can be generated during an impact or pressure on the material.[181] The overall orientations of the tubules to each other and towards the surface of the tooth is concluded to result in a more energy absorbing material during an impact than a solid material without it. Indeed, it has been reported, that the fracture toughness of dentine was over 50% higher in the direction parallel to the tubules compared to the perpendicular direction, which was attributed to extensive crack bridging.[162, 244] It was suggested, that mechanical properties, such as fracture resistance, is linked with the tubule orientation. Due to the fact, that these tubules are embedded within a network of mineralized collagen fibers, this link is rather indirect. It was reported that the elastic properties within the dentine of the narwhal tusk varied with the change in collagen orientation.[245]

3.6 Implications of chemical composition on mechanical properties

Most of the influence of the hardness of the enamel/enameloid is often attributed to a high degree of mineralization.[230, 246, 247] The results of this study indeed indicate a positive correlation of the hardness with the Ca and P content inside the teeth. The correlation of the fluorine and iron content from the EDX-line scans of the hard diet eating species with the hardness and reduced elastic modulus implies that the hardness and elastic modulus is furthermore influenced by the concentration. The results show that in areas with high F and Fe concentrations the hardness values reach a maximum. In areas with less/ no Fe and F, but with high Ca and P concentrations,

the hardness, and elastic modulus is still quite high, but never the less still lower than in the presence of F and Fe. Fluorapatite is reported to be harder and stiffer than pure hydroxyapatite and has further advantageous properties for teeth, e.g., a better resistance to acids, providing a higher resistance to abrasion during tooth wear.[248] However, studies on the hardness of shark teeth, which employ pure fluorapatite inside their teeth, showed that the incorporation of fluoride into the apatite lattice had no effect on the micro- or nanohardness of the teeth.[50] Similar to fluoride, various biological roles for the iron deposition in teeth have been proposed by authors. In general, it is assumed that iron, in whichever form present, improves the mechanical properties of enamel and enameloid in different ways, such as increasing the enamel hardness[142], developing a better resistance to acids [142, 249, 250], providing a higher resistance to abrasion during tooth wear [249, 251] and reducing tooth abrasion and cracking[252].

This results in periodic variations in the mechanical properties within the length of the tooth. A higher degree of mineralization makes materials stronger and stiffer (higher modulus of elasticity), but it usually lowers the toughness; that is, it is less capable of absorbing shock and strain energy, which is important during the crushing of hard food.[247] However, the hardest area, of the molariform teeth is relatively thin in comparison to the elongated, papilliform teeth. Thus the ability to absorb the shocks of the stains during the crushing would not be impaired. Similar strategies have been reported for highly impact resistant biomaterials, such as the dactyl clubs of a “smasher”-type stomatopod, where the impact surface is enhardened with a thin layer of fluorapatite.[253, 254] Thus this variation in mechanical properties inside these teeth may contribute to the general toughness of the material and provide mechanical stress relieve and crack-resisting mechanisms.[255-257]

The enameloid of the soft diet eating species display a gradual decrease in mineral content and thus hardness and elastic modulus. Because of this linear correlation, the direct influence of the iron phase and fluoride cannot be directly estimated. Such linear gradient structures are generally discussed to provide toughness, increase wear resistance and/or arrest crack growth.[238, 258-267]

Another gradient can also be found within the transition of the mechanical properties at the junction from the enameloid to the dentine of all investigated fish species of this study. The enamel-dentine junction within mammalian molar teeth has been shown to be a good example of the transition of properties within biomaterials. Herein, the well-bonded interface creates a gradient barrier between the stiff enamel and tough dentine phase.[160, 268] A further example can be found in the squid beak, where the hardness gradually decreases over 100 times towards the interior of the beak.[269]

4. Summary and conclusion

Cichlid fishes are a text-book examples for explosive speciation and rapid evolution that resulted in a stunning array of behavioral and morphological phenotypes. A main driver of cichlid diversity is ecological specialization to sometimes very narrow niches, such as feeding on a very distinct food item. Famously, trophic phenotypes (such as specialized pharyngeal dentition) can be observed recurrently across the cichlid phylogeny. The teeth of these cichlid fishes provide a good model of how vertebrates optimize dental hard tissues for specialized ecological applications. Within this study, the teeth of the lower pharyngeal jaws of different cichlid fish species from the major radiations of the East African cichlids, which have adapted to different food resources, were investigated in detail on their chemical composition and distribution, their macroscopic and inner structure as well as their mechanical properties to determine the structure-property relationships. Across the investigated cichlid species, the general inner tooth structure is conserved. On the basis of the observed similarities, a structure model with corresponding hierarchical levels of structural elements was created. Within this complex hierarchical arrangement, several intrinsic and extrinsic toughening mechanisms on multiple length scales enhancing fracture resistance against critical failure and wear resistance were identified.
Varying levels of the concentration and distribution of fluoridated hydroxyapatite as the mineral component could be associated with pronounced variations in the hardness and elastic modulus of dental hard tissues. Furthermore, amorphous iron-bearing phases were found, which contribute to the hardness of the resulting material. On the basis of general similarities of the inner structure of all investigated teeth, a structure model with corresponding hierarchical levels was created. Within this complex arrangement, several intrinsic and extrinsic toughening mechanisms on multiple length scales to enhance fracture resistance against critical failure were identified. The combination of this complex structural arrangement together with specific variations of the mechanical properties within dental hard tissues of their teeth allows cichlids for an optimal processing of their food. Herein, the hard diet eating species utilize a complex multilevel and multilayered structuring (incl. variation of mineralization degree) of enameloid which is reflected by a pronounced, stepwise gradient (profile) in their mechanical properties. Thus the structure of enameloid of “snail-crushing” species is optimized to significantly enhance the fracture resistance and mechanical stability of the teeth. The teeth of soft diet eating species, on the other hand, do not show this pronounced structuration in enameloid (incl. in general lower degree of mineralization) and employ a nearly linear decrease of mechanical properties from the outer part of the enameloid to dentine junction and thus specialize on grabbing of prey.
Furthermore, as radiations are monophyletic, the investigated phenotypes evolved convergently. Thus, the results of this investigation also imply, that species differences in cellular activities that orchestrate mineral and to a lesser part -matrix deposition might be the likely cause for different biomechanical properties of cichlid teeth, arguing for the central importance of regulatory evolution in rapidly evolving lineages, such as the East African cichlids.

Chapter III Synthesis and Characterization of Strontium Substituted Fluorapatite-Gelatine Composites

1. Introduction

Biomimetic syntheses of organic-inorganic hybrid materials under controlled mineralization conditions are very important for the deeper understanding of the principles of biomineralization. Mimicking artificial composite materials with the aid of synthetic and natural polymers, highlighting morphogenetic, structural and/or compositional relations to biogenic materials as essential points, is a highly researched field.[270-277] However, only few research groups are working in the direction of understanding not only structural features but also morphogenetic aspects of the formation of hybrid materials closely related to biogenic materials.[276-279] Such approaches give insights into the basic principles of nucleation, self-organization, as well as the formation of hierarchical composite patterns and hold the potential for a deeper understanding of the basic principles of biomineralization. Therefore, such approaches also give further information for the development of biomimetic materials with improved functionality for biomedical applications. The main inorganic component of the hard tissues such as bone or teeth of the most recent vertebrates (including humans) consists of carbonated hydroxyapatite, which is associated with different isomorphic substitutions in the crystal structure. The number of ionic substitutions in bioapatites is generally smaller than for geological apatites, due to the limited number of elements present in body fluids. Performing ionic substitutions in the apatite crystal structure has gained much interest to better understand biomineralization processes and improve material properties, such as size and morphology of the crystals, mechanical performance, as well as solubility and biocompatibility.[280]

1.1 Cationic substitution: Strontium vs. Calcium

One important cationic substitution in the apatite crystal structure is the Sr^{2+} in the crystallographic positions of Ca^{2+}. In medical literature, strontium is also known as “bone-seeking element”, while 99.1% of the total body content is associated with bones.[281] Furthermore, it also has been demonstrated that the incorporation of Sr^{2+} affects the mechanical properties of hydroxyapatite.[282] *In vitro* investigations showed a significant increase in osteoblast stimulation and differentiation in a dose-dependent manner in a range of 3-7 at-%.[283, 284] Strontium has also been reported to stimulate the *in vivo* bone formation[285] and was recently used to treat osteoporotic spinal fractures and other related osteoporosis.[286]
The Sr^{2+} ion, which is larger than Ca^{2+}, can isomorphically substitute calcium completely in the apatite crystal structure, forming the whole range of solid state solutions without a solubility limit. It was reported that for the partially substituted apatite the

CaII site of the crystal structure is slightly more preferable for the Sr^{2+} ions.[54] However, recently performed DFT calculations on hydroxyapatite show that at a high-temperature the most energetically preferred substitution pattern is a mixed CaI and CaII substitution. In case of a low-temperature synthesis, the mixed state is still slightly more preferable, while at 20 wt-%, the occupation of CaII site is dominated.[287] Furthermore, it was suggested that partial incorporation of Sr^{2+} ions can lower the crystal symmetry of apatite from $P6_3/m$ to $P6_3$ and even to non-centrosymmetric $P2_1$. Therefore, the doping of apatite with Sr^{2+} can potentially enhance its pyroelectric and piezoelectric properties.[288]

1.2 Fluorapatite-gelatine nanocomposites

As the *in vivo* production of biological hard tissues is a highly complex process, it is challenging to account for all general biological influences, such as the metabolic and cellular activities during hard tissue formation. Thus, to get further insight into the basic principles of biomineralization, it is detrimental to reduce the level of complexity of the investigated system. A promising experiment to mimic the processes in bone or tooth formation is the growth of fluorapatite in gelatine matrices with a double diffusion setup.

The shape development of the fluorapatite-gelatine nanocomposites, which were synthesized by the double-diffusion technique within gelatine gel matrices, was investigated and described in detail from the nano- to the micrometer-scale.[278, 289, 290] The morphogenesis starts with the mineralization of triple-helical fiber protein bundles, followed by the formation of aggregates with more or less parallel alignment of nanoboards. This process then leads to the formation of a hexagonal prismatic seed with perfect parallel alignment of the nanoboards (see the green box in Figure 78).[289] It was also shown that the nanocomposite seed, which can be described as highly-mosaic controlled superstructure, bears already the intrinsic code for the further shape development on the µm-scale. One a critical size of the bundles of nanoboards is reached, an intrinsic electric dipole field develops, which can be detected by electron holography (see the blue box in Figure 78).[278, 289] This electric field can further direct the growth process, leading to an even more parallel alignment of the polar nanoboards. This field additionally controls the formation of a hierarchical pattern of the protein fibrils within the composite (see red box in Figure 78). Finally, the growth process leads to the development of a notched sphere via several growing dumbbell states.

In order to synthesize the material which is even more closely related to biological hard tissues, the biomimetic synthesis of carbonated fluorapatite-gelatine-nanocomposites was performed with the double-diffusion technique.[290] Herein, the carbonated fluorapatite-gelatine composites were synthesized with a variable carbonate content (from 0.3 to 7.5 wt-%) at the phosphate-position in the fluorapatite crystal structure (so-called B-type substitution). Compared with non-carbonated specimens the shapes of carbonated composite aggregates became significantly rounded and compressed with increasing carbonate content. Furthermore, it was observed,

that the incorporation of carbonate into the composite causes dramatic effects with respect to the size of the nano-subunits, which are building the mesoscopic and macroscopic aggregates. The overall chemical composition of the as-grown materials was closely related to dental enameloid of sharks (as well as conodont hard tissues) and even human enamel, although the latter contains hydroxyapatite instead of fluorapatite as the inorganic component.

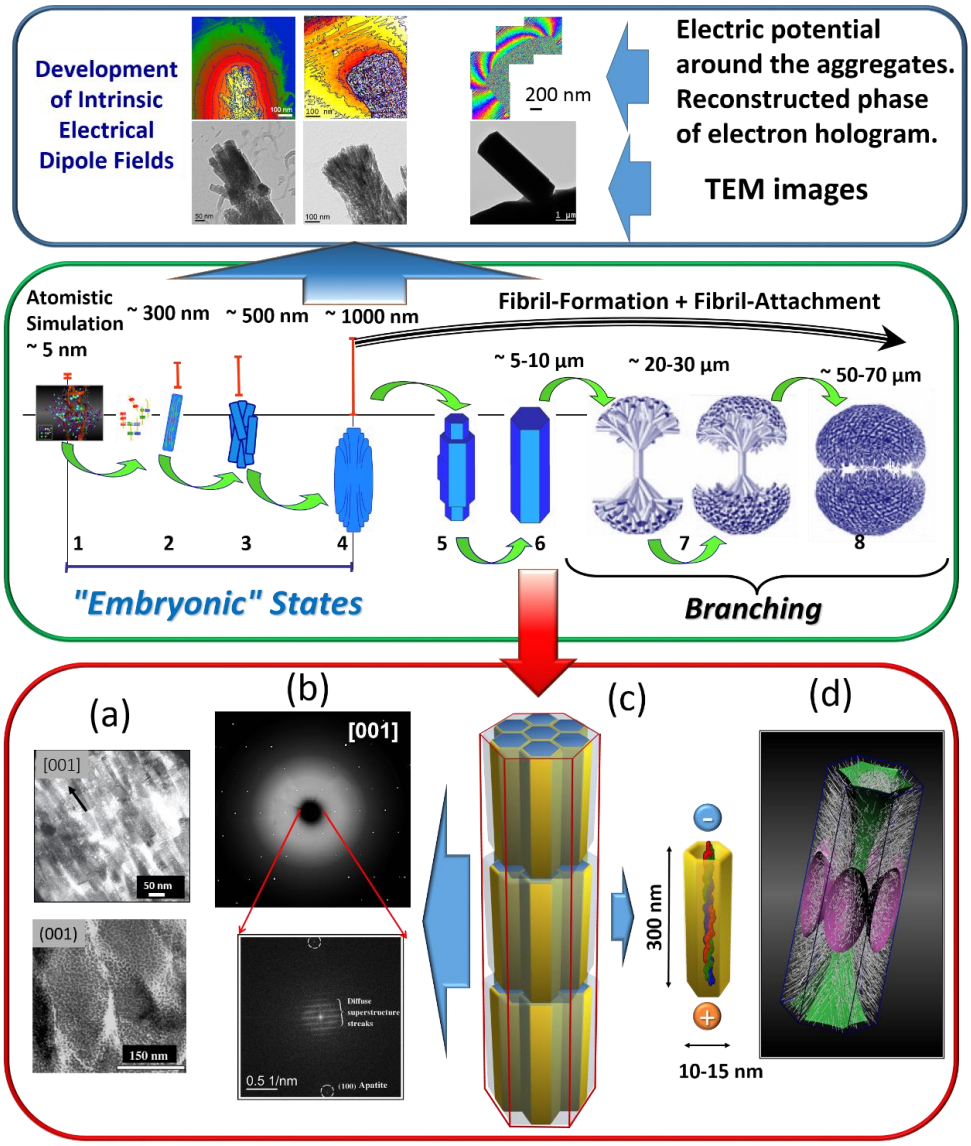

Figure 78: (Blue box): (a–c) Fluorapatite–gelatine composites in different stages of morphogenesis. Bottom row: TEM images; top row: reconstructed phase images of electron holograms showing the electric potential distribution around the corresponding composite aggregates. (Green box): Schematic illustration of the morphogenesis process of fluorapatite–gelatine composites. (Red box): Structural features of the hexagonal-prismatic entities: (a) TEM images of ultra-thin slices oriented along and perpendicular to [001]; (b) X-ray diffraction pattern (wide angle) and FFT of the HRTEM image (superstructure –small angle) obtained perpendicular to [001]; (c) schematic illustration of the nanocomposite superstructure; (d) simulated 3D fibril pattern revealing the areas separating fibrils with different orientations.Reprinted with permission.[291]

2. Results and Discussion

2.1 Liesegang band positions

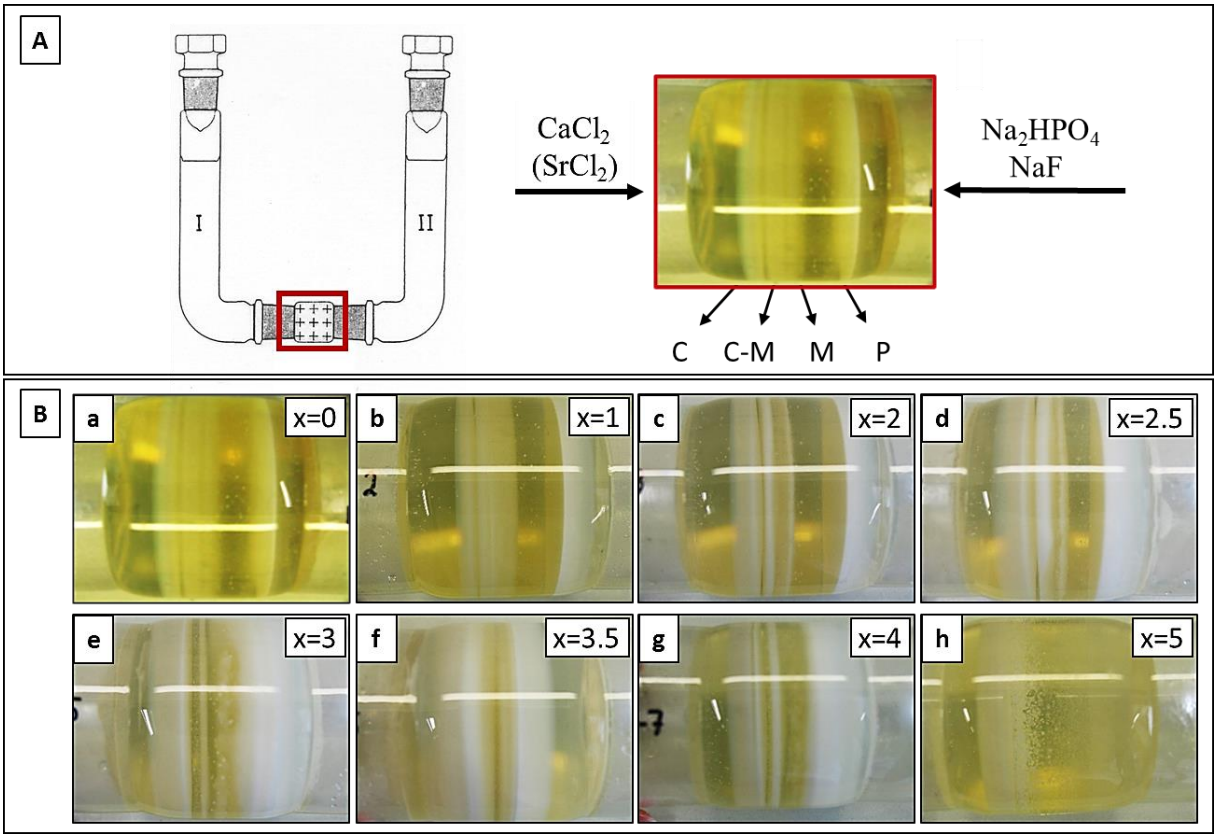

Figure 79: A: Scheme of the double diffusion setup (left) and an example of the Liesegang bands within the gelatine gel. The bands are described as C-, M-, P- bands, showing their position within the gelatine plug. B: Photos of the calcium/strontium fluorapatite substitution gelatine gels. Molar ratios ranging from x=0 (a) to x= 5 (h) with Ca:P:Sr:F = 5-x:5:x:1.

Image A in Figure 79 illustrates the setup of the double diffusion with a scheme and an example of the periodic growth of Sr^{2+}-substituted fluorapatite-gelatine aggregates within the gelatine gel. The bands are described as C-, M-, and C-bands according to their position within the diffusion tube. Image B in Figure 79 shows the photos of the Liesegang bands within the gelatine gel after 21 days of crystallization. The molar ratios were ranging from x=0 (image a) to x= 5 (image h) with Ca:P:Sr:F = 5-x:5:x:1. With increasing strontium concentration the P-band gets more pronounced and increases in size (compare image a-g). The M-bands are clearly separated in the lower strontium concentrations (image a and b) and become blurred and ticker in the higher Sr^{2+}-concentration range (image c-g). Two bands could be observed between the C- and P-bands. Herein, the thicker bands were always labeled M-band. The other band in image a (with x=0) was labeled C-M-band and the bands in images b-g (with 1<x<4) M-P-bands. Only a single band on the C-side and small crystallites throughout the gel could be observed in all series of Ca/Sr substitution experiment (x=5, image h).

2.2 pH of the bands in the gel

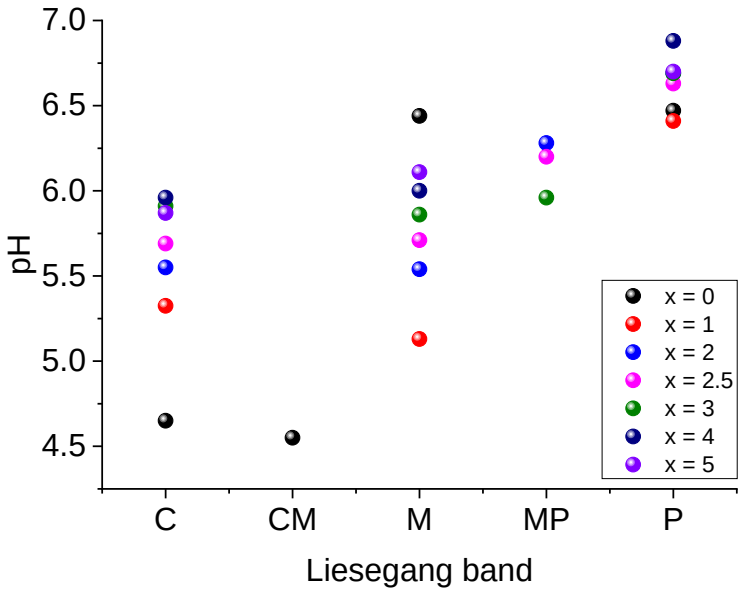

Figure 80: pH of the isolated Liesegang bands of the calcium/strontium fluorapatite substitution gelatine gels. Molar ratio x in solution ranging from x=0 (A) to x= 5 (H) with Ca:P:Sr:F = 5-x:5:x:1. C: C-Liesegang band, which is near the calcium-containing solution. P: P-Liesegang band, which is near the phosphate-containing solution. M: M-Liesegang band, which is in the middle of the gel and both calcium and phosphate containing solution. CM: Liesegang band, which is located in between C- and M- band. MP: Liesegang band, which is located in between M- and P-band.

The results of the pH-measurements of the isolated Liesegang bands in the gelatine gel matrix are shown in Figure 80. The starting pH of the gel was ~3.4, and the starting pH of the solutions was 7.4. During the composite growth, a slow, gradual increase of the pH within the gel was desired. Generally, after 21 days, the lowest pH values were found in the C-bands. A rise in the pH values from the C-bands of the calcium-rich side to the phosphate-rich side were observed in all substitution experiments. The creation of different calcium phosphate phases inside a gelatin gel is dependent on the local ionic concentrations and the pH inside the gel. The phase analysis (see chapter 3.1.4) showed that all aggregates of all isolated Liesegang bands are apatite.

2.3 Chemical composition

The chemical composition of the Sr^{2+}-substituted fluorapatite-gelatine composites, which were isolated from the M-Liesegang band, were investigated by inductively coupled plasma-optical emission spectroscopy (ICP-OES) and CHNS-analysis. All N and C signals originate from the gelatine. The N and C contents of pure gelatine were determined to be 16.84 (±1.2) wt-% and 44.32 (±3.6) wt-% respectively. The amount of gelatine was thus determined on the basis of the N-content of the analysis and corresponds to about 3.2-4.5 wt-% gelatine in the composites. The results of the elemental analysis of the inorganic component are summarized in Table 11.

Table 11: Chemical composition of Sr^{2+}-substituted fluorapatite-gelatine composites, which were isolated from the M-Liesegang bands (wt-%).

Starting Sr^{2+}-concentration (x) in solution [a]	0	1	2	2.5	3	4	5
Ca	36.39	25.97	17.8	14.36	12.74	3.89	0.00
Sr	0.00	14.82	27.26	31.61	33.86	48.04	54.55
P	17.36	15.98	14.76	14.18	13.96	12.64	12.41
Na	0.609	0.467	0.416	0.404	0.375	0.358	0.358
F	3.64	3.19	2.84	2.61	2.56	2.05	2.09
N	0.64	0.50	0.45	0.47	0.56	0.54	0.60
Gelatine	3.74	3.15	3.33	3.68	4.10	4.57	3.74
(Ca+Sr+Na)/P	1.67	1.63	1.63	1.61	1.60	1.62	1.59

[a] (molar ratios Ca:P:Sr:F = 5-x:5:x:1)

Figure 81 (A) shows the relationship between the strontium content in the composites, which were isolated from the M Liesegang bands and the starting strontium concentration (x) in solution (molar ratios Ca:P:Sr:F = 5-x:5:x:1). The strontium content increases linearly with an increase of the initial strontium concentration in solution. The calculated distribution coefficient for the Sr^{2+} substitution series remains nearly 1 for all composite materials Figure 81 (B). The distribution of the Sr^{2+} ions in solution and in the crystal remains constant, thus no excess of Sr^{2+} ions is needed for the ionic substitution into the apatite crystal structure.

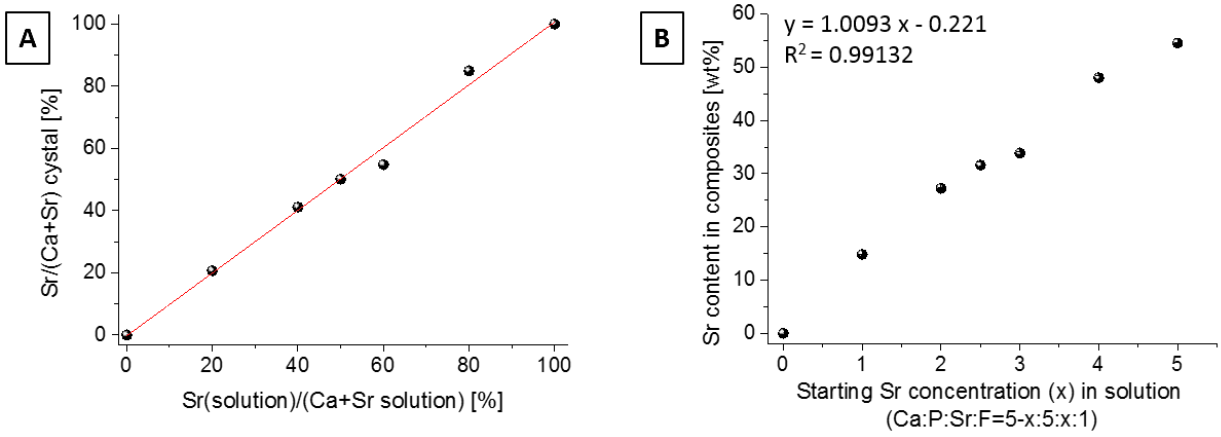

Figure 81: Distribution coefficient between the Sr^{2+}-content in the crystal and the Sr^{2+}-concentration in solution (A) and the relationship between the strontium content in the composites and the starting strontium concentration (x) in solution (molar ratios Ca:P:Sr:F = 5-x:5:x:1) (B).

The calculated (Ca+Sr+Na)/P molar ratio on the basis of the complete chemical analysis is decreasing with increasing Sr^{2+}-content in the apatite. However, this tendency is developing not in a perfectly linear fashion (Figure S 32 in appendix B). This points to a slight increase of cationic deficiencies in crystallographic positions of Ca^{2+} within the apatite crystal structure. Thus according to substitution scheme I, the partial heterovalent substitution of $[PO_4]^{3-}$ by $[HPO_4]^{2-}$ can also cause the formation of vacancies on the Ca^{2+} sites, in combination with the creation of $F^-(OH^-)$ vacancies and/or the incorporation of H_2O molecules in the channels of the apatite crystal structure. The results of the chemical composition show a clear decrease of the molar F^--content in the apatite upon increasing strontium content, further pointing to the formation of F^- vacancies (or substitution by OH- or H_2O).
Additionally, the chemical analysis indicated the presence of Na^+ in the apatite. Sodium can also partially substitute Ca^{2+} ions.[198, 290] This heterovalent substitution can be balanced by an additional opposite charged heterovalent substitution of $[PO_4]^{3-}$ by $[HPO_4]^{2-}$ (in accordance with substitution scheme II). Furthermore, the incorporation of Na^+ into the apatite can cause the formation of further F^- vacancies and/or additional incorporation of H_2O in the channels of apatite (substitution scheme III).[197, 198]

$$Ca^{2+} + [PO_4]^{3-} + F^-(OH^-) \leftrightarrow \square_{Ca2+} + [HPO_4]^{2-} + (\square_{F^-(OH^-)}; H_2O) \quad (I)$$

$$Ca^{2+} + [PO_4]^{3-} \leftrightarrow Na^+ + [HPO_4]^{2-} \quad (II)$$

$$Ca^{2+} + F^- \leftrightarrow Na^+ + \square_{F^-} + (H_2O) \quad (III)$$

According to literature, the process of a $[PO_4]^{3-}$ substitution by $[CO_3]^{2-}$ (so-called B-type substitution) can cause the formation of vacancies on the Ca^{2+} site according to substitution scheme IV.[198, 292, 293] Incorporation of Na^+ is also able to maintain the charge balance in apatite during the incorporation of $[CO_3]^{2-}$ according to substitution scheme V. As the amount of carbonate was generally low or not detectable (by FT-IR and Raman spectroscopy, see chapter 2.1.5), this substitution scheme V was not included in the determination of the crystal chemical formula of apatite.

$$Ca^{2+} + [PO_4]^{3-} + F^-(OH^-) \leftrightarrow \square_{Ca} + [CO_3]^{2-} + (\square_{F^-(OH^-)}; H_2O) \quad (IV)$$

$$Ca^{2+} + [PO_4]^{3-} \leftrightarrow Na^+ + [CO_3]^{2-} \quad (V)$$

The calculated chemical composition per unit cell formula of Sr^{2+}-substituted fluorapatite-gelatine composites, which were isolated from the M-Liesegang bands are summarized in Table 12.

Table 12: Calculated chemical composition of Sr^{2+}-substituted fluorapatite-gelatine composites, which were isolated from the M-Liesegang bands (per unit cell formula: $(Ca_xSr_yNa_z\square_{10-(x+y+z)})$ $\{[PO_4]_{6-n}$ $[HPO_4]_n\}$ x $\{F_p$ $[OH]_s$, $(\square, H_2O)_{2-(s+p)}\})$.

Starting Sr^{2+}-concentration (x) in solution [a]	0	1	2	2.5	3	4	5
Ca	9.72	7.56	5.61	4.71	4.24	1.43	0.00
vac Ca	0.00	0.24	0.24	0.33	0.39	0.27	0.44
Sr	0.00	1.97	3.92	4.73	5.15	8.07	9.33
P	5.73	5.33	5.40	5.31	5.21	5.64	5.25
HPO_4	0.27	0.67	0.60	0.69	0.79	0.36	0.75
OH	0.00	0.05	0.12	0.20	0.20	0.41	0.35
HPO_4 (+OH)	0.28	0.71	0.72	0.89	1.00	0.77	1.10
Na	0.28	0.24	0.23	0.23	0.22	0.23	0.23
F	2.00	1.95	1.88	1.80	1.80	1.59	1.65

[a] (molar ratios Ca:P:Sr:F = 5-x:5:x:1)

The determination of a general apatite formula is thus based on the assumption, that the phosphate sites are fully occupied by $[PO_4]^{3-}$ and $[HPO_4]^{2-}$ groups, wherein the total content of them is set to six according to the stoichiometric apatite formula.[54] Na^+ is assigned to the Ca^{2+} site, and no carbonate is present in the apatite formula. Thus, charge balance can be maintained by the replacement of $[PO_4]^{3-}$ by $[HPO_4]^{2-}$ ions, as well as by the formation of vacancies in the Ca^{2+} and F^- sites. The empirical crystal chemical formula for the Sr^{2+}-substituted fluorapatite can be described as following based on the experimental determination of the chemical composition:

$(Ca_xSr_yNa_z\square_{10-(x+y+z)})$ $\{[PO_4]_{6-n}$ $[HPO_4]_n\}$ x $\{F_p$ $[OH]_s$, $(\square, H_2O)_{2-(s+p)}\}$

For pure fluorapatite: x=9.72, y=0, z=0.28, n=0.27, s=0, $(x+y+z) \leq 10$, $(p+s) \leq 2$

For pure strontium-apatite: x=0, y=9.33, z=0.23, n=7.5, s=0.35; $(x+y+z) \leq 10$, $(p+s) \leq 2$

The empirical formula for all Sr^{2+}-substituted fluorapatites can be found in Table S 14 in appendix B.

2.4 Phase analysis

X-Ray diffraction patterns of all prepared Sr^{2+}-substituted fluorapatite-gelatine composite powders, which were isolated from the M-Liesegang bands, are shown in Figure 82 (A). The XRD diffraction patterns of the Sr^{2+}-substituted fluorapatite-gelatine composite aggregates, which were isolated from the P- and C-band, are displayed in

Figure S 33 in appendix B. The analyses showed that the composites, which were synthesized with initial molar ratios (x) of strontium ions in solution from 0 to 5, gave well-resolved apatite patterns for the inorganic component of the composite materials grown in all Liesegang bands. Reflections belonging to other calcium phosphates or minerals, e.g., calcium fluoride were not observed. A clear shift in reflex positions towards lower angles with increasing Sr^{2+}-content was observed (Figure 82, B), indicating an increase of d-spacings and hence lattice parameters due to the incorporation of Sr^{2+} ions in the apatite crystal structure. Homovalent strontium substitution of calcium cations cannot directly cause a charge imbalance in the apatite structure. Thus, no charge neutralizing substitution schemes are expected. However, as was stated in the previous paragraph, some vacancies in the crystallographic positions of Ca^{2+}, and F^- can be formed due to the incorporation of $[CO_3]^{2-}$ and $[HPO_4]^{2-}$. The formation of vacancies in the channels along the *c*-axis would reduce their diameter and consequently reduce the *a* lattice parameter. However, in case these positions are filled by H_2O molecules, the lattice parameter *a* increases.

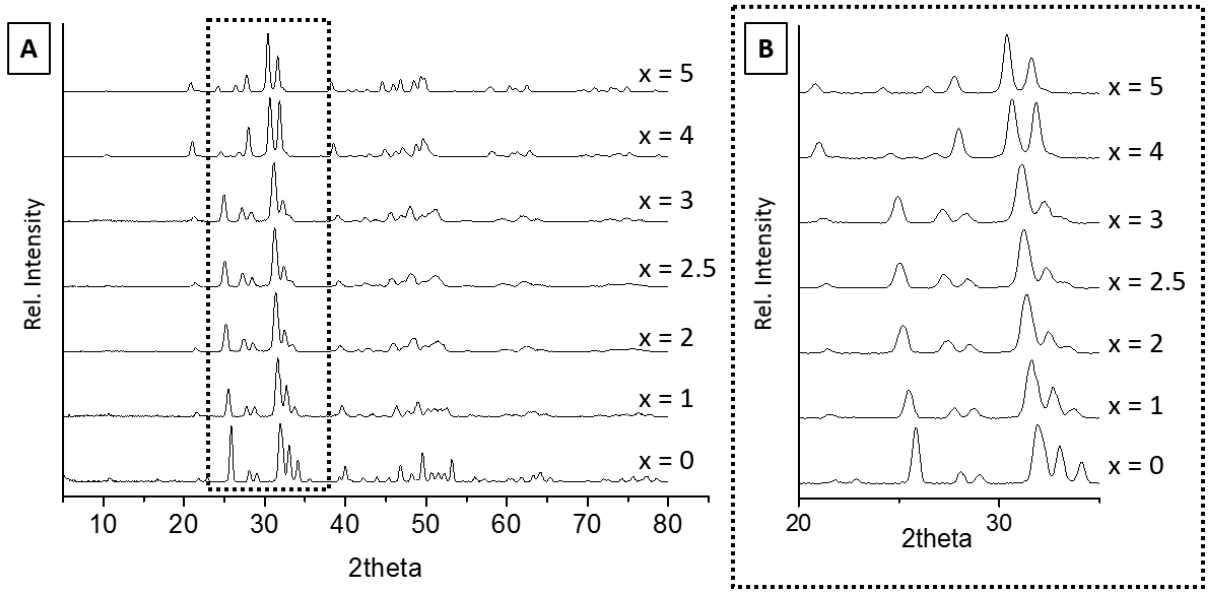

Figure 82: Results of the pXRD-measurements of Sr^{2+}-substituted fluorapatite-gelatine composites with increasing Sr^{2+}-substitution (with molar ratios Ca:P:Sr:F = 5-x:5:x:1) (A) and an enlargement of a range of 15 2theta to visualize the shift in reflex-positions upon increasing Sr^{2+}-incorporation into the apatite (B).

The calculated *a*- and *c*-lattice parameters as well as unit cell volume of the Sr^{2+}-fluorapatite-gelatine composites, which were isolated from the M-band, are gradually increasing with the Sr^{2+}-content (Figure 83, Table 13). These findings are consistent with the assumption of the larger strontium ions entering the apatite structure and are in general accordance with results reported in the literature.[294-297] The changes in lattice parameters and cell volume are within the ranges of predicted values of different atomic scale modeling techniques (see Figure 83). In the lower Sr^{2+}-concentration rage, the *a*-parameter and the cell volume generally follow the values of *ab initio* DFT simulations for the configurationally averaged cation site distribution of Ca^{2+} and Sr^{2+} to either the MI or MII site in the apatite lattice upon increasing Sr^{2+}-substitution in the fluorapatite.[298] In this range, the model predicts only a slight ener-

getic preference for Sr^{2+} to occupy the MII site. In consequence, the distribution to either the MI or MII site is random. As there are more MII sites than MI sites the occupation of MII is statistically more probable. In the higher Sr^{2+}-concentration range our experimental values fit more to the predicted values of Goryaeva *et al.*.[299] They employed a semi-empirical approach using Buckingham, Morse and a three-body interatomic potential parameters variation of atomic configurations of Sr^{2+}-bearing fluorapatite solid solutions with different distributions to predict the changes in lattice parameters.

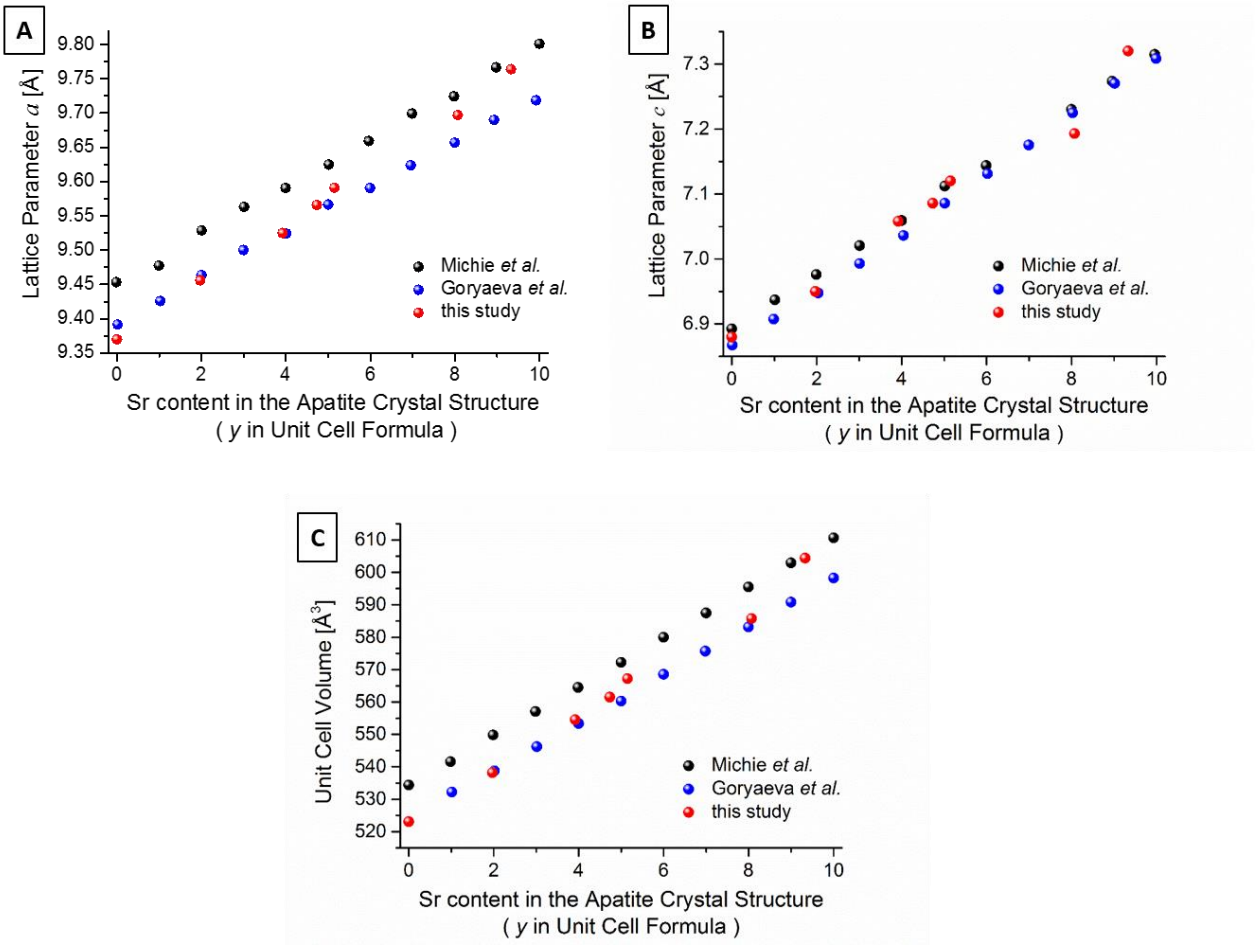

Figure 83: Lattice parameters *a* (A), *c* (B) and unit cell volume (C) of Sr^{2+}-substituted fluorapatite-gelatine composites as a function of *y* in the unit cell formula compared with literature studies.[298, 300]

Lattice parameters *a* and *c* of the composites, which were isolated from the other Liesegang bands, increase as well with increasing Sr^{2+}-content (Figure S 34 in appendix B). While the lattice parameters of the composites of the M- and P-Liesegang bands increase linearly upon the degree of strontium substitution, the parameters of the composites in the C-bands increase in a nonlinear fashion (image A and B in Figure S 34). The *c*/*a* ratio generally increases with increasing Sr^{2+}-incorporation into the apatite (image C in Figure S 34). All this indicates a change in the substitution schemes in this case. As was demonstrated in substitution scheme V, Na^{+} can substitute Ca^{2+} under $[CO_3]^{2-}$ incorporation. Additionally, Ca^{2+} vacancies can be formed according to substitution scheme II by the partial substitution of $[PO_4]^{3-}$ by $[HPO_4]^{2-}$.

The presence of $[HPO_4]^{2-}$ and a slightly increased amount of $[CO_3]^{2-}$ was confirmed by FT-IR and Raman-spectroscopy for the composites of the C-band[290][290].
Previous investigations have shown, that the incorporation of carbonate into the apatite component of fluorapatite-gelatine nanocomposites drastically influences the lattice parameters.[290] It was demonstrated, that the *a*-parameter decreases and the *c*-parameter increases slightly upon a B-type carbonate incorporation into the apatite crystal structure. As the synthesis of the Sr^{2+}-substituted fluorapatite-gelatine particles was performed under air atmosphere, it might be possible that an increased amount of CO_2 was readily dissolved into the Ca^{2+}-containing solution.

Table 13: Determined lattice parameters, lattice ratios and cell volume of Sr^{2+}-substituted fluorapatite with increasing Sr^{2+}-content.

Sr^{2+}-content [wt-%]	Sr^{2+}-content per unit cell formula	*a*-parameter [Å]	*c*-parameter [Å]	*cla*	V /[Å^3]
0.00	0.00	9.37	6.88	0.734	523.1163
14.26	1.97	9.456(5)	6.950(4)	0.735	538.1835
27.26	3.92	9.525(4)	7.058(5)	0.741	554.552
31.61	4.73	9.566(4)	7.086(6)	0.741	561.5553
33.86	5.15	9.591(9)	7.12(1)	0.742	567.2029
48.04	8.07	9.697(5)	7.193(7)	0.742	585.7543
54.55	9.33	9.764(6)	7.32(1)	0.750	604.3621

2.5 Vibration spectroscopy

The presence of the apatite specific ions and the amide signals of the protein molecules was investigated by FT-IR- and Raman-spectroscopy. Figure 84 (A and B) show representative FT-IR and Raman spectra of strontium substituted fluorapatite-gelatine composites, that were obtained from the M-bands (Sr^{2+}-content 14.26 wt-%). The results are summarized in Table S 15 in appendix B.
The FT-IR spectra of the strontium substituted fluorapatite-gelatine aggregates, which were isolated from the C- and P-Liesegang bands are displayed in Figure S 35 in appendix B. Both IR and Raman spectra exhibit four modes, which can be attributed to the internal vibration of the phosphate group.[170, 174, 292] Additionally, signals corresponding to $[HPO_4]^{2-}$ were detected in the Raman spectra at 1003 cm^{-1} as well as the FT-IR-spectra at 540 cm^{-1} and 864 cm^{-1}. The FT-IR peaks at 1659 cm^{-1} and 1546 cm^{-1} can be attributed to the amide ll and the amide I vibration mode, respectively.[178, 179, 301] The Raman spectra confirm the presence of these groups with signals at 1659-1689 cm^{-1} and 1558-1565 cm^{-1}, respectively.[174] The position of the amide bands indicates that the peptides in the strontium fluorapatite-gelatine composites

have the α -helical configuration.[302] The FT-IR spectra of all samples showed a broad band in the high energy region from 3700 to 2700 cm^{-1}. These were assigned to the amide A and B bands, which typically appear between 3070 - 3300 cm^{-1} and overlap with the stretching modes of water molecules and the vibration modes of the CH groups of the gelatine molecules.[178, 301]

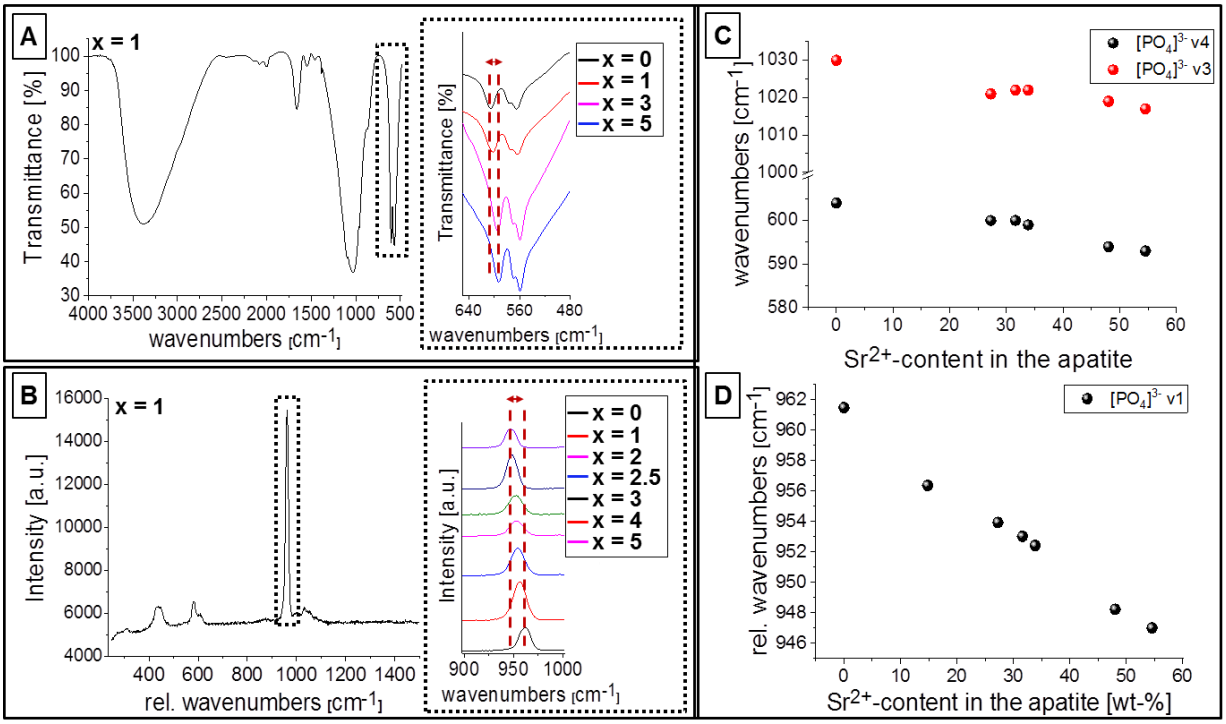

Figure 84: Results of vibration spectroscopic analysis of Sr^{2+}-substituted fluorapatite-gelatine composites. A: Representative FT-IR-spectrum of composites, which were obtained from the M-bands (Sr^{2+}-content 14.26 wt-%); inset: v_4 band of selected substituted fluorapatite-gelatine composites with a highlighted shift of band position. B: Representative Raman-spectrum of composites, which were obtained from the M-bands (Sr^{2+}-content 14.26 wt-%); inset: v_1 band of selected substituted fluorapatite-gelatine composites with a highlighted shift of band position. C, D: Quantification of the shift in wavenumbers of the IR spectra (top) and Raman spectra (bottom).

The FT-IR vibration modes of the phosphate groups of the higher substituted composites were slightly shifted by 7-10 cm^{-1} to lower wavenumbers with respect to the non substituted fluorapatite- gelatine-composites (Figure 84, C). The same trend was observed for the phosphate signals in the Raman spectra (Figure 84, D). As the frequency of a vibration band is dependent on the lattice vibrations, the masses of the present atoms/ions and the strength of the forces between the atoms/ions define the position of the vibration bands in the spectra. Thus, the shift can be explained by different reduced masses between the Sr and the Ca in the Szigeti relationship. Seeing that the bond strengths of Ca-O and Sr-O and the bond force constant are similar (bond strengths of 402.1 kJ/mol and 426.3 kJ/mol, respectively[303]), only the reduced mass would be responsible for shifting the frequency of the vibration to lower wavenumbers.

Furthermore, the FT-IR spectra of composites of the C-Liesegang bands showed characteristic carbonate bands at 1426 and 1457 cm^{-1}.[59] From the position of these peaks, a B-type carbonate substitution was estimated.

2.6 Thermogravimetric analysis

The decomposition of the composites with increasing temperature was investigated by thermogravimetric analysis (TGA). Representative TG graphs of the thermal decomposition of the Sr^{2+}-substituted fluorapatite-gelatine composite materials with a molar ratio between 0 and 5 (with Ca:P:Sr:F = 5-x:5:x:1) are displayed in Figure 85. The data for the thermal decomposition, which is summarized in table Table 14, showed a stepwise mass loss with two steps. The first step with a weight loss of approximately 1 % starts at room temperature and finished at about 200 °C and is related to the release of adsorbed water from the composites. The second step starts at approx. 200 °C with a weight loss of about 3.4-4.5 % and mainly corresponds to the thermal degradation and pyrolysis of gelatine, as well as the loss of the structural water from the apatite channel of the apatite or the decomposition of $[HPO_4]^{2-}$-groups.

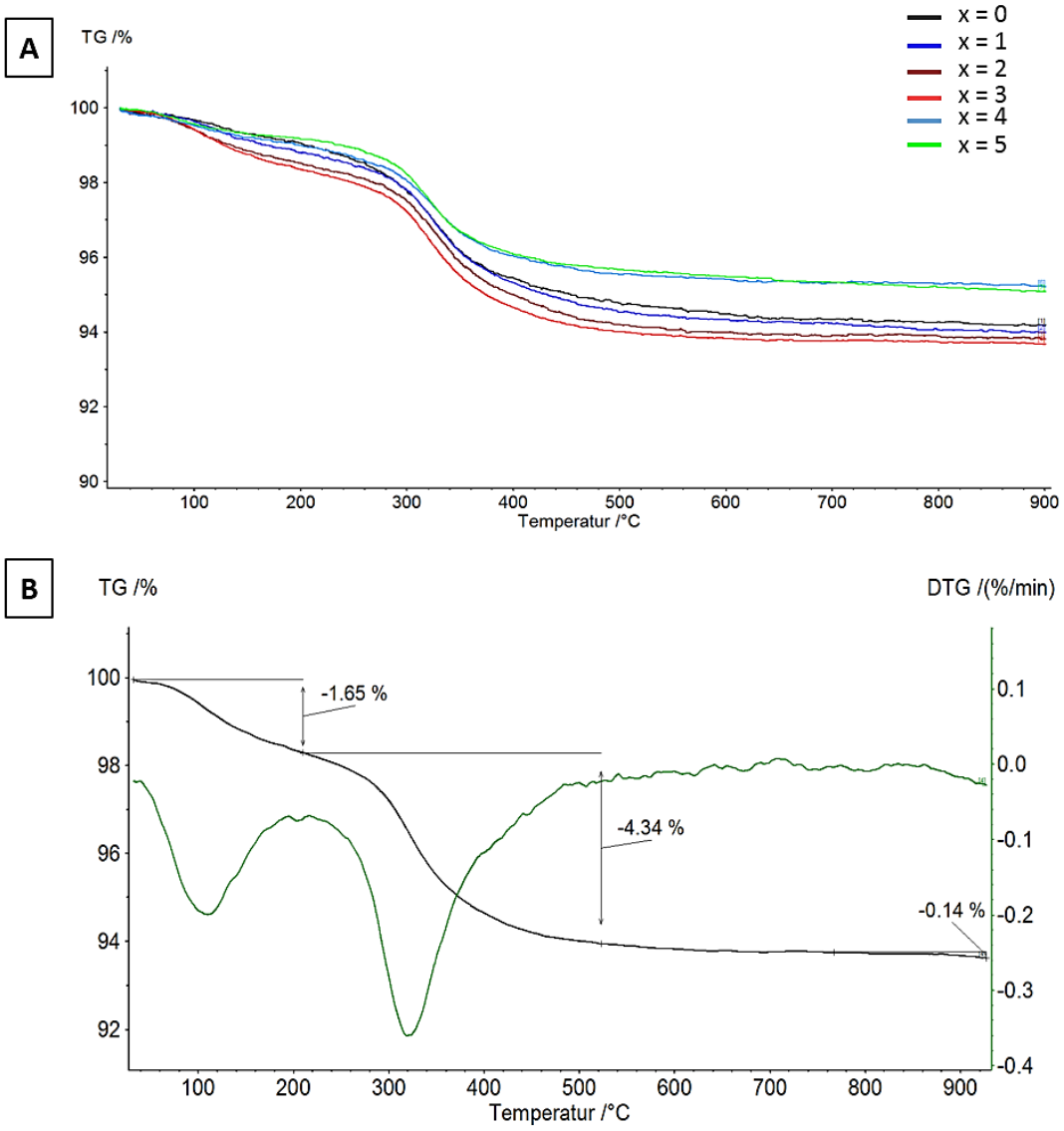

Figure 85: TGA results of the Sr^{2+}-substituted fluorapatite-gelatine composites, which were isolated from the M-Liesegang bands. A: Comparison of all results for different molar ratios (Ca:P:Sr:F = 5-x:5:x:1). B: Representative TG- and DTA result of the composites with a Sr^{2+}-content of about 27 wt-%.

Table 14: TGA results of the Sr^{2+}-substituted fluorapatite-gelatine composites.

Molar ratio[a]	first step [%]	second step [%]	residual mass [%]
x = 0	-0.83	-4.27	94.07
x = 1	-1.26	-4.30	93.94
x = 2	-1.36	-4.52	93.42
x = 3	-1.65	-4.34	93.42
x = 4	-0.87	-3.41	94.93
x = 5	-0.85	-3.6	95.19

[a] molar ratios Ca:P:Sr:F=5-x:5:x:1)

The mass of the residue ranged from approximately 93-95 %. These decomposition steps of the strontium substituted fluorapatite-gelatine composites are similar to previously reported pure and carbonated fluorapatite-gelatine composites.[59]

2.7 Morphology and morphogenesis

The morphology of the strontium substituted fluorapatite-gelatine composites was investigated by SEM. Figure 86 shows a selected sequence of images of mature seeds of fluorapatite-gelatine composites with increasing Sr^{2+}-content. It was observed, that with increasing Sr^{2+}-incorporation into the apatite, the seeds become thinner and elongated. The aspect ratios for the composites increase dramatically with increasing incorporation of Sr^{2+} into apatite from about 4:1 to up to 11:1. This is in accordance with observations of the elongation of hydroxyapatite crystals upon strontium incorporation into the apatite.[284] Herein it was reported, that the morphology of the crystals is drastically influenced by the Sr^{2+}-incorporation into the apatite. The plate-like shape of pure hydroxyapatite became disturbed with low Sr^{2+}-concentrations. The substituted apatites with a high Sr^{2+}-content displayed a well-defined shape, which was elongated in along the crystallographic *c*-axis of apatite.[304, 305]

In previous investigations, it was demonstrated, that carbonated fluorapatite-gelatine composite specimens display clearly rounded and compressed shapes (aspect ratio ~ 2:1) upon increasing carbonate content compared to the pure fluorapatite-gelatine composite.[59] Thus, carbonate ions dramatically decrease the anisotropy of crystals growth. In contrast to these observations, strontium ions have an opposite effect on the growth of apatite-gelatine composites, significantly increasing their anisotropy (aspect ratio ~ 11:1) (see Figure 87).

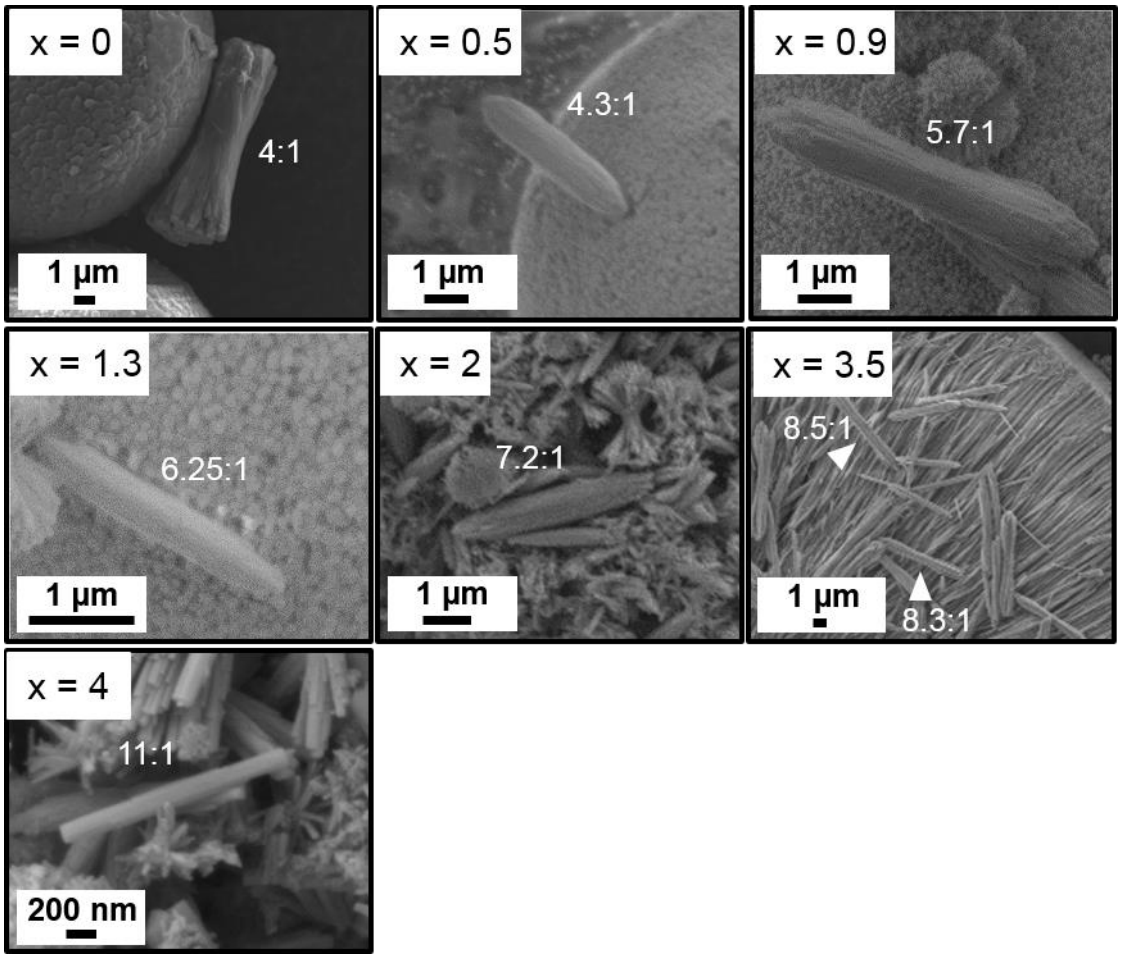

Figure 86: Selected sequence of SEM images displaying the changes in the size of the elongated prisms from the pure fluorapatite-gelatine composites (x=0) upon increasing Sr^{2+}-incorporation (molar ratio: Ca:P:Sr:F = 5-x:5:x:1) with corresponding aspect ratios

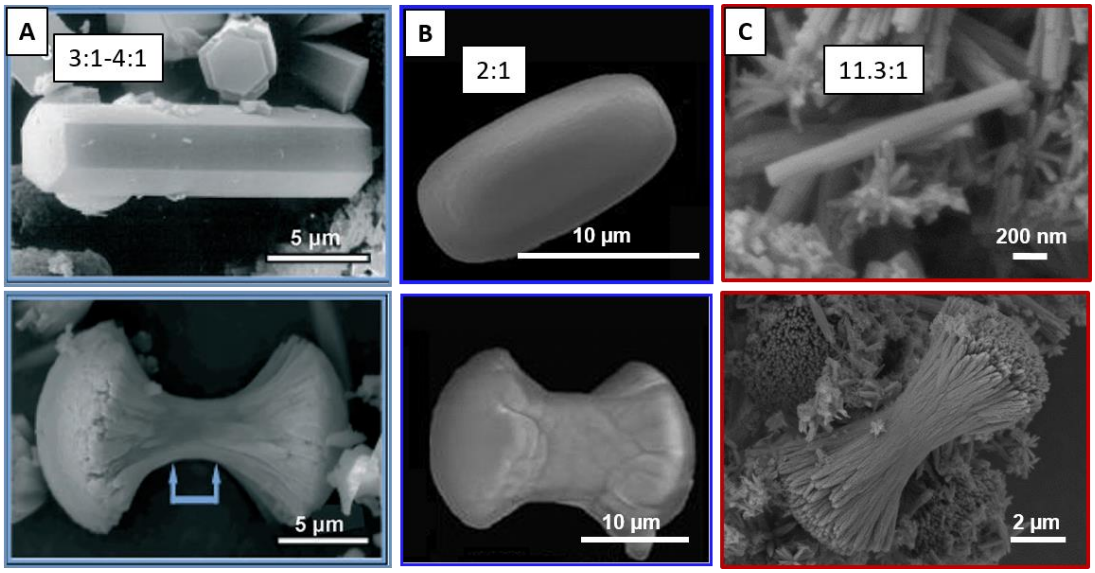

Figure 87: SEM images illustrating the changes of the dumbbell-shaped morphologies of carbonated fluorapatite-gelatine composites (carbonate content ~2 wt-%) (B)[290] and strontium substituted fluorapatite-gelatine composites (Sr^{2+}-content ~56.67 wt-%)(C) to pure fluorapatite-gelatine composites (A). The top row displays the changes of the elongated seeds, and the lower row displays a later dumbbell growth-stage. Reprinted with permission[290]

Molecular dynamics simulations demonstrated that pure fluorapatite-gelatine composites display different sets of morphogenesis mechanisms.[306-308] The preimpregnation of the gelatine by calcium or phosphate ions has an influence on crystal growth and morphology. A so-called “fan-like” morphogenesis is usually found in the apatite-gelatine nanocomposites of the C-Liesegang bands, where the influence of the Ca^{2+} ions causes a stiffening of the gelatine macromolecules. Spherulites, which were grown in these conditions, typically have a “fan-like” morphology at the initial stage of the branching process. They further develop into the spherulite with radial symmetry (without a so-called “double-leaf” or “double-eyes”).[278, 309] The so-called “fractal growth” mechanism results from a phosphate preimpregnation of the gelatine. Herein, the gelatine macromolecule remains flexible during the crystallization.[310, 311] The spherulites, which were grown in these conditions, are characterized by a central “free bridge” and are generally described as having more bend and soft morphologies.[312] Electron holographic investigations of the hexagonal prismatic shaped fluorapatite-gelatine specimen shown that the incorporated gelatine molecules could also induce the formation of intrinsic electric dipole fields, which potentially can influence and direct the further growth process.[289]

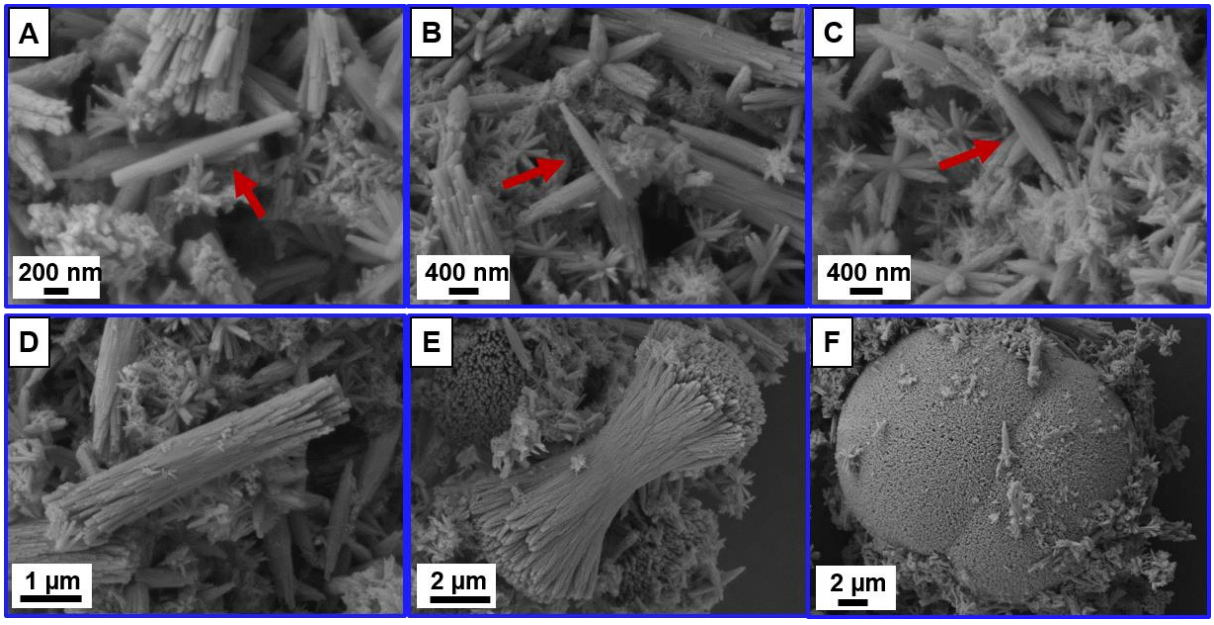

Figure 88: Selected sequence of SEM images demonstrating the developing states of growth of Sr^{2+}-substituted fluorapatite-gelatine composites with a Sr^{2+}-content of 48 wt-% in the apatite component from an elongated seed to a just closed sphere. The red arrows highlight the examples of the hexagonal prisms within this growth series

Figure 88 shows a selected sequence of images illustrating the different growth stages of morphogenesis of strontium substituted fluorapatite-gelatine composites with a gelatine content of about 4.57 wt-% and a strontium content of about 48 wt-%. The growth, in general, starts similar to the pure fluorapatite-gelatine system with an elongated rod-like aggregate (slightly distorted hexagonal prism)(see the prisms in image A-C in Figure 88, which are marked with red arrows), developing via different dumbbell shapes towards a notched sphere. The growth process from the seed to the fully grown spherulite takes up to 9 days. It has to be mentioned that the nuclea-

tion within the gelatine gel appears randomly over time (e.g., due to local pH variations or ion-concentrations) and thus all growth stages can be observed even after 21 days. The Sr^{2+}-bearing fluorapatite-gelatine aggregates could not clearly be assigned to either the fan-like or fractal growth mechanism. The incorporation of Sr^{2+}-ions into the apatite structure promotes branching processes already in the very early stages of morphogenesis. It is well known that the frequency of crystal branching is drastically influenced by the presence of impurities, which could induce internal stress and strain in the growing crystal.[313] Furthermore, due to the high anisotropy of apatite crystals, which were grown in the presence of Sr^{2+}-ions, the branching process, in this case, proceeds in a kinetic regime and the subindividuals initially form on the slow-growing prismatic faces. This “axial-branching” induces the formation of bundle-like aggregates and further have a tendency to form dumbbells with pronounced central “free bridge” and “double-eyes” spherulites at the latest stage of the morphogenesis.[309] The subindividuals within dumbbells and spherulites in the highly substituted Sr^{2+}-fluorapatite-gelatine composites generally display a drastically elongated, needle-like shape in comparison to the pure fluorapatite-gelatine composites (Figure 89). The diameter of the subunits decreased from 580 nm to 83 nm on average upon a strontium incorporation of about 33.8 wt-% (see Figure 90).

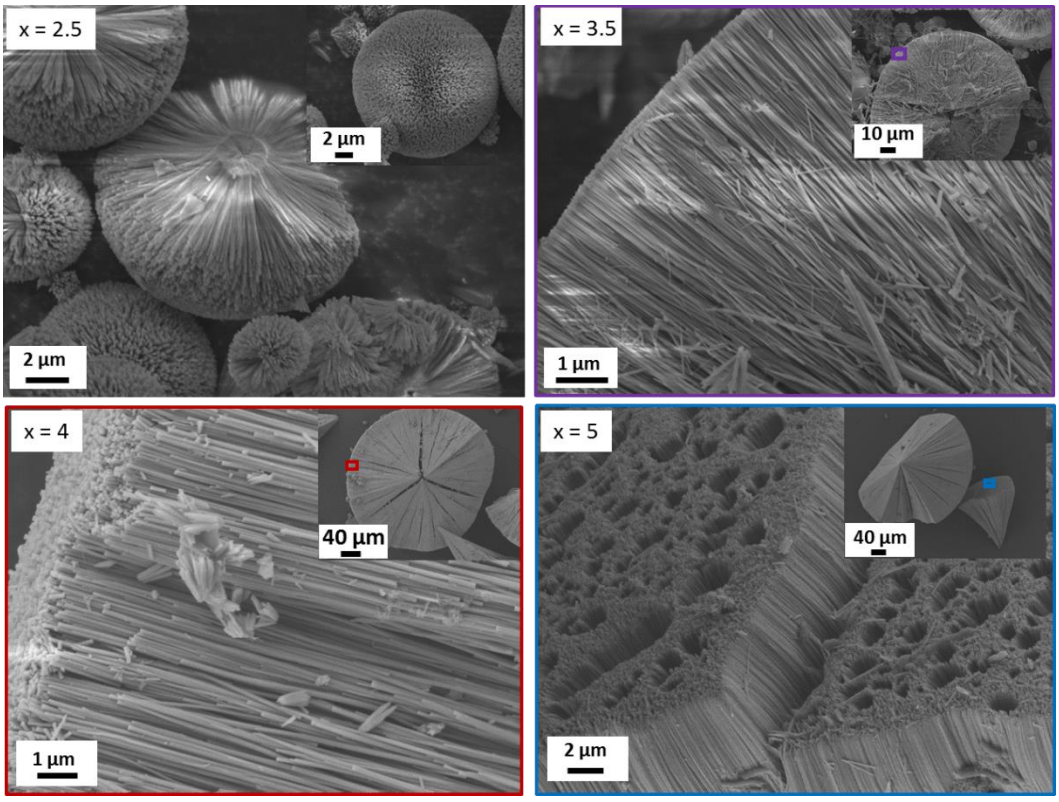

Figure 89: SEM images of the surface area of Sr^{2+}-substituted fluorapatite-gelatine composites demonstrating the elongation of the single subunits upon Sr^{2+}-incorporation into the apatite (molar ratios: Ca:P:Sr:F=5-x:5:x:1)

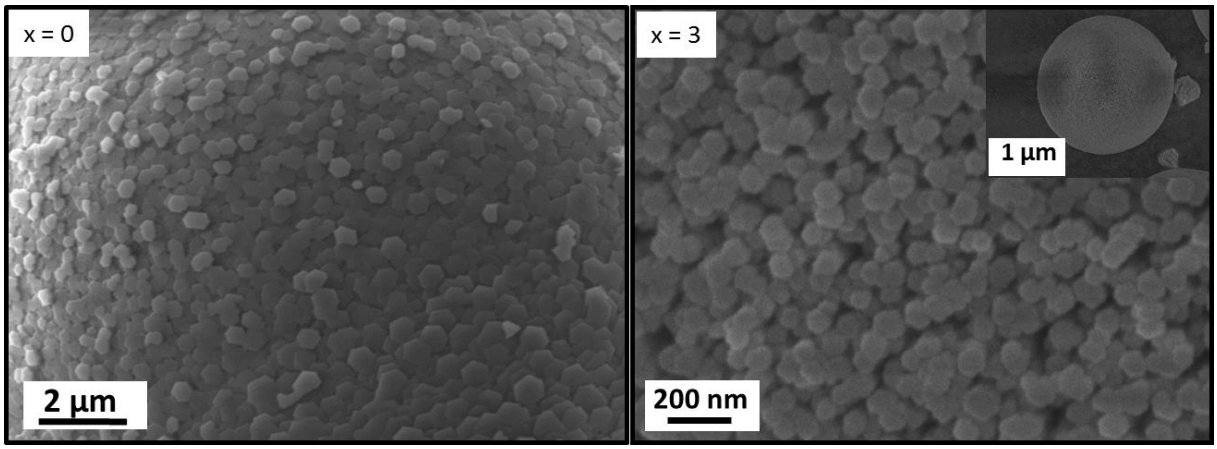

Figure 90: Selected SEM images of the surface of just closed spheres showing the change in the size of the individual subunits upon Sr^{2+}- incorporation into the apatite (molar ratios: Ca:P:Sr:F=5-x:5:x:1)

3. Summary and conclusion

The biomimetic synthesis of organic-inorganic hybrid materials under controlled mineralization conditions is very important for the deeper understanding of the principles of biomineralization. Sr^{2+}-substituted fluorapatite-gelatine composites were synthesized in a gelatine gel using a double diffusion setup. The isolated aggregates were characterized by SEM, chemical analyses, FT-IR spectroscopy, Raman-spectroscopy, XRD, and TGA. It was shown that the lattice parameters *a* and *c* of the isomorphic substituted apatite increase monotonically with increasing strontium content in the apatite crystal structure. The peaks in the IR and the Raman spectra of the phosphate groups of the higher substituted apatite-gelatine composites were slightly shifted to a lower wavenumber with respect to the pure calcium fluorapatite-gelatine composites. TG-analysis confirmed that the synthesized materials have an organic-inorganic composite character, with an average gelatine content between 3-5 wt-%. Based on the chemical analysis, the empirical crystal chemical formula of the Sr^{2+}-substituted fluorapatite-gelatine composites was determined:

$(Ca_xSr_yNa_z\square_{10-(x+y+z)})\ \{[PO_4]_{6-n}\ [HPO_4]_n\ \}\ x\ \{F_p\ [OH]_s,\ (\square,\ H_2O)_{2-(s+p)}\}$
with x= 0-9.75, y= 0-9.33, z= 0.22-0.28, n=0.27-0.79, $s=(x+y+z) \leq 10$, $(p+s) \leq 2$,
$n = (12+s+p-2x-y)$

It was furthermore shown, that the incorporation of strontium into the apatite significantly affects the morphogenesis and morphology of apatite-gelatine composite aggregates. Specifically, an increase in the anisotropy of crystal growth along *c*-axis of apatite was observed. The growth, in general, starts with an elongated rod-like aggregate (slightly distorted hexagonal prism), developing via different dumbbell shapes towards a notched sphere. Herein, it was observed that the incorporation of Sr^{2+}-ions into the apatite structure promotes branching processes already in the very early stages of morphogenesis .

Chapter IV Characterization and biocompatibility of a biomimetic coating of PEEK bone implant materials

1. Introduction

1.1 Bone Implant materials

If a lost bone needs to be replaced, many different materials are available nowadays to fill the bone defects.[280, 314-321] Many different semi- or fully synthetic materials, such as ceramics, bone cements, polymers, metals or composites, have been proposed to treat bone defects.[322-325] Each material has several advantageous properties for a successful implant material. However, there is still much room for improvement. An inherent problem of ceramics and bone cements is their brittleness, which may lead to mechanical failure at the operation site and sometimes to unwanted biodegradation of the material. An inherent disadvantage of metal-based implants is that they are not radiolucent, preventing the use of X-ray- or other imaging procedures for an unobstructed view of the healing of the tissue.[322, 326] Despite this plethora of materials, using autologous bone implants are still the gold standard in clinical medicine.[322] However, using explanted donor bone from the same person has several drawbacks, which set limits the practicability of this technique. One of them is the insufficient amount of autologous bone for larger transplantations, another being the need for a second operation to harvest this bone.[322, 327]
There are several criteria for a successful permanent implant. If non-degradable in the body, the implant material must be non-toxic and must not elicit immunogenic or other adverse biological responses *in vivo.* It has to be resistant to wear and corrosion to reduce the number of debris particles causing inflammatory or immunogenic responses. If particles from the material are released into the body, it must be tolerated by the biological environment and biodegraded or excreted, to avoid accumulation.[322] The implant material should also not swell in the implantation site.[328] Bone implants should have a reliable strength, high toughness and a stiffness matching the bone to minimize stress shielding effects. Stress shielding refers to a reduction in bone density around the implant as a result of the removal of normal stress from the bone by an implant.[329] However, biocompatibility is one of the key factors for a successful bone implant. A material used as an implant is preferably either bioinert or bioactive. Bioinertness entails the ability to elicit no chemical or biological responses between the implant and the tissue. Bioactive materials, which promote a fast ingrowth into the implantation site, are called osseointegrative and form a fast and lasting interface with the bone.[322]
Osseointegration is determined by initial cell-surface interactions. [328, 330, 331] The ability of the biomaterial to allow osteoprogenitor cell adhesion and migration in the early stages of wound healing is crucial for the later steps of the bone formation

cascade.[332] In this study, the general cytotoxicity and biocompatibility of the biomimetic surface coating were evaluated using two different cell lines. Fibroblast and osteoblast cells represent two examples of the types of cells, which bone implants will be in contact with during clinical use. Fibroblasts are a group or family of cells which are present in virtually all tissues.[333] Among other functions, these cells are specialized for the establishment and maintenance of the extracellular matrix structure.[333] Thus they play an important role in cell-cell and cell-substrate interactions. Osteoblasts are important cells in the osseointegration of bone to the implant. Osteoblasts are fully differentiated cells of the osteogenic lineage, which are derived from undifferentiated mesenchymal stem cells.[334, 335] They specialize in the production of the extracellular matrix in bone and to control its mineralization and thus regulate the ingrowth of bone to the implant.[335] Osteoblasts are key cells with regard to implant performance and assessing their behavior on a potential biomaterial may give insight into its likely biocompatibility.

Table 15 lists the major material characteristics, which have been identified to have an influence on the host response to an implant material and which have to be considered when designing an implant surface for improved biocompatibility.[336-339]

Table 15: Major material variables that could influence the host response[339]

Bulk material composition, micro- (or nano)-structure, morphology
Crystallinity and crystallography
Water content, hydrophobic-hydrophilic balance
Elastic constants
Macro-, micro-, nano-porosity
Surface chemical composition, chemical gradients, surface molecular mobility
Surface topography
Surface energy
Surface electrical/electronic properties
Corrosion parameters, ion release profile, metal ion toxicity (for metallic materials)
Degradation profile, degradation product form, and toxicity (for polymeric materials)
Leachables, additives, catalysts, contaminants and their toxicity (for polymeric materials)
Dissolution/degradation profile, degradation product toxicity (for ceramic materials)
Wear debris release profile

Researchers started to functionalize the surface of materials with favorable bulk properties for prosthetic devices to enhance their functionality, e.g., to improve biocompatibility or lower the bacterial attachment. Functionalization of a surface can be divided into three categories: physicochemical, mechanical and biological methods.[340] The physicochemical methods can be further divided into two categories: direct modification techniques and deposition techniques.[328] Direct modification techniques include physical methods and wet chemical methods. Using physical means for surface-modification is advantageous, as they work without direct contact with the sample and without solvents. Common techniques include UV-laser, excimer-, electron beam-, ion beam or plasma-treatment.[328, 341-344] Deposition meth-

ods cause atoms and atomic clusters to be deposited on the substrate surface. Common techniques are plasma coating, laser sintering with inorganic substances, such as hydroxyapatite or vacuum plasma coating.[322, 328] Wet chemical methods are often used to functionalize the surface at the solid-liquid interface selectively.[331, 345, 346]

It is believed, that surface-coatings should be thin, as thicker layers could affect the mechanical and functional properties and could delaminate due to a mismatch in properties between the coating and the bulk material.[345] Too thin layers may, on the other hand, may lead to uneven coverage and might also be susceptible to erosion. For biomaterial applications, the treatment should produce a uniform layer independent of the shape and geometry of the intended material.

1.2 Polyetheretherketone (PEEK)

One of the promising material for bone implant applications is PEEK. Polyetheretherketone (Poly (oxy-1,4-phenyleneoxy-1,4-phenylenecarbonyl-1,4-phenylene)), is a semi-crystalline, high-molecular-weight polymer of the polyaryletherketones (PAEK) polymer family. PAEK are high-performance thermoplastic polymers, consisting of an aromatic backbone interconnected by ketone and ether functional groups (Figure 91). One of the characteristics of PEEK is its high-temperature stability, comprising a glass transition temperature at around 143 °C and a melting temperature of 343 °C and excellent resistance to chemical, thermal, and post-irradiation degradation of the polymer.[328, 347]

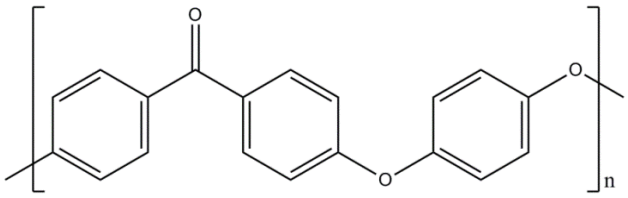

Figure 91: Chemical structure of PEEK.

Exhibiting good biocompatibility, radiolucency, and further advantageous mechanical properties, which are close to that of human cortical bone, PEEK can be engineered as a suitable biomaterial for biomedical as well as biomechanical implants.[348] Ever since the market launch of implantable-grade PEEK in 1998, the polymer has been utilized in plain or as fiber-reinforced material, for example as interbody spinal fusion devices (image A in Figure 92), scaffolds for tissue engineering or as cranio-maxillofacial implants (image B in Figure 92).[328, 349]

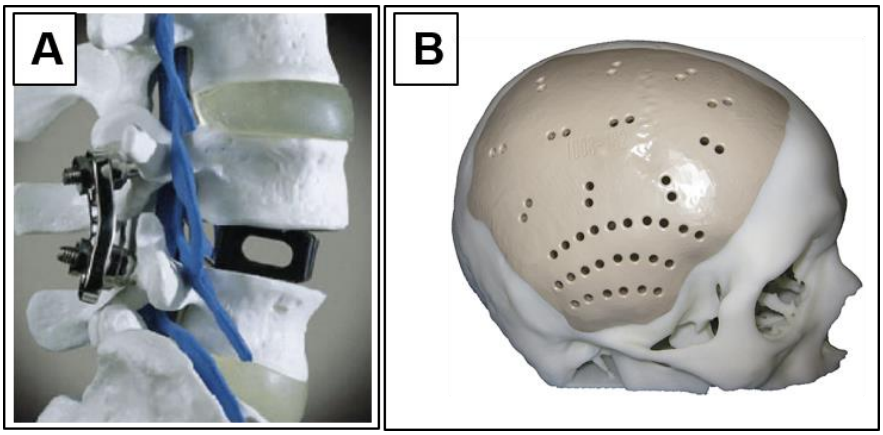

Figure 92: A: Example of a cranio-maxillofacial PEEK implant.[350] B: Carbon fiber reinforced PEEK spine fusion cage for posterior lumbar interbody fusion.[351] Reprinted with permission.

PEEK is considered as bioinert, causing neither toxic or mutagenic effects nor clinically significant inflammation.[352-356] Although inertness and insolubility are desirable properties for a high-performance polymer, it might pose a challenge to its use as a suitable biomaterial, as the bone does not form a direct bond with plain PEEK.[328] This often results in a foreign body reaction at the implant site, leading to fibrous encapsulation of the material, which in return can lead to a loosening of the implant. It is proposed that this is a result of the relatively hydrophobic surface, leading to low surface energy.[328] Thus many strategies have been developed to improve the osseointegration of PEEK into the bone.[357, 358]

1.3 Preliminary work-Engineering the bio-interface of the implant materials

The general aim of the project was the surface functionalization and characterization of PEEK implant materials to combine the excellent bulk properties of PEEK with characteristic compositional and functional properties of mineralized bone tissues. The procedure of preparation and characterization of the surface modification of PEEK was reported by Knaus *et al*.[359, 360] A generalized scheme of the procedure of the surface functionalization is depicted in Figure 93.

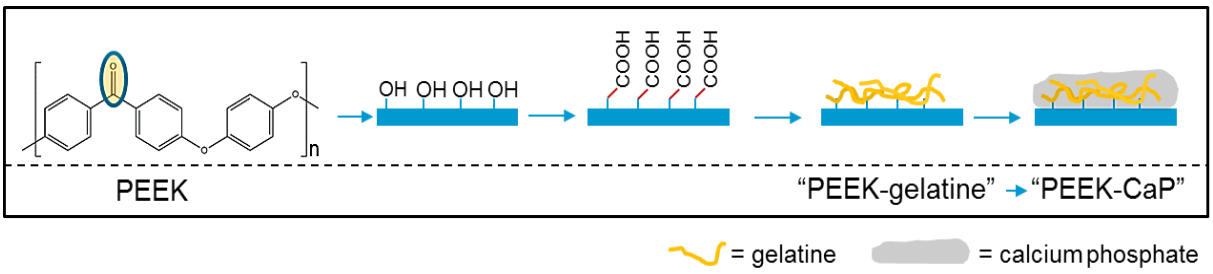

Figure 93: General scheme for the surface functionalization of the PEEK-implant material.

For the surface functionalization, the keto-group was chosen as the connecting point for the attachment of selected organic molecules. For this, the keto-group was reduced, creating hydroxyl-groups for further coupling of linker molecules. Herein, different linker molecules, such as hexamethylene diisocyanate, maleimide or a succinic acid were coupled to the hydroxyl-group. For further studies, the succinic acid-linker has been proposed as most suitable, as the reaction is reliable and established and does not require an inert atmosphere. In the subsequent step, gelatine was coupled to the surface using EDC-chemistry on the carboxylic acid displaying surface. The resulting gelatine-layer, which is covalently attached to the surface of the PEEK, was slowly mineralized with calcium phosphate. This process occurs in a solution containing calcium and phosphate ions in the presence of organic molecules, which inhibit the nucleation of hydroxyapatite crystals to prevent ectopic mineralization. Exemplary SEM images of PEEK-gelatine and PEEK-CaP are displayed in Figure 94. However, a detailed investigation of several material properties of the resulting mineralized coating, as well as the determination of the general biocompatibility for bone implant applications, remained to be investigated.

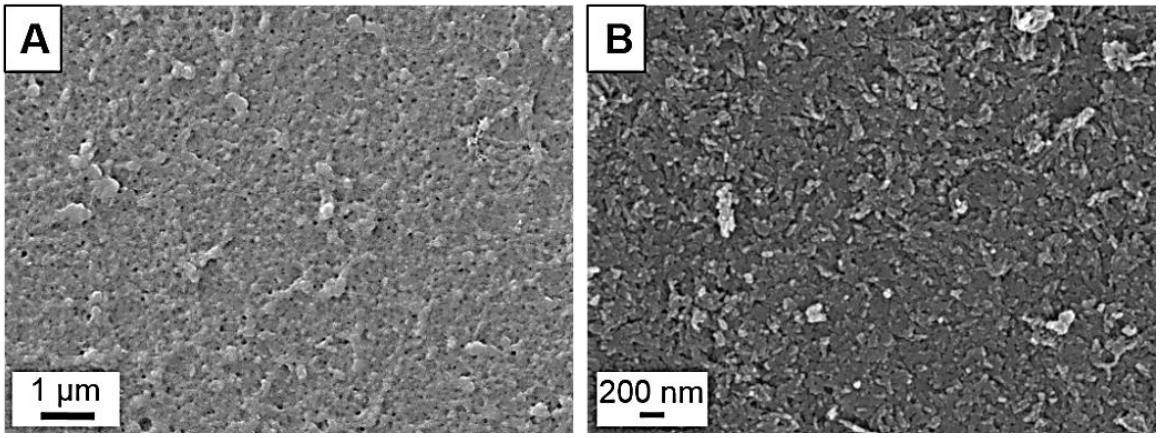

Figure 94: SEM images of freeze-dried PEEK-gelatine (A) and PEEK-CaP (B).

2. Results and Discussion

2.1 Chemical composition of the biomimetic coating

2.1.1 X-ray photoelectron spectroscopy

The chemical composition of the functionalized PEEK-surfaces was investigated by X-ray photoelectron spectroscopy (XPS). Figure 95, A shows the X-ray photoelectron spectrum in the energy range of 0-1400 eV of the gelatin modified PEEK material ("PEEK-gelatine"). The spectrum shows that the main constituents were carbon, oxygen, nitrogen, and molybdenum. These results confirm the presence of gelatine on the surface of the PEEK. The molybdenum peaks originate from the sample holder, which was used during the measurement. Image B shows the high-resolution core-level spectra of O_{1s}, N_{1s}, and C_{1s}.

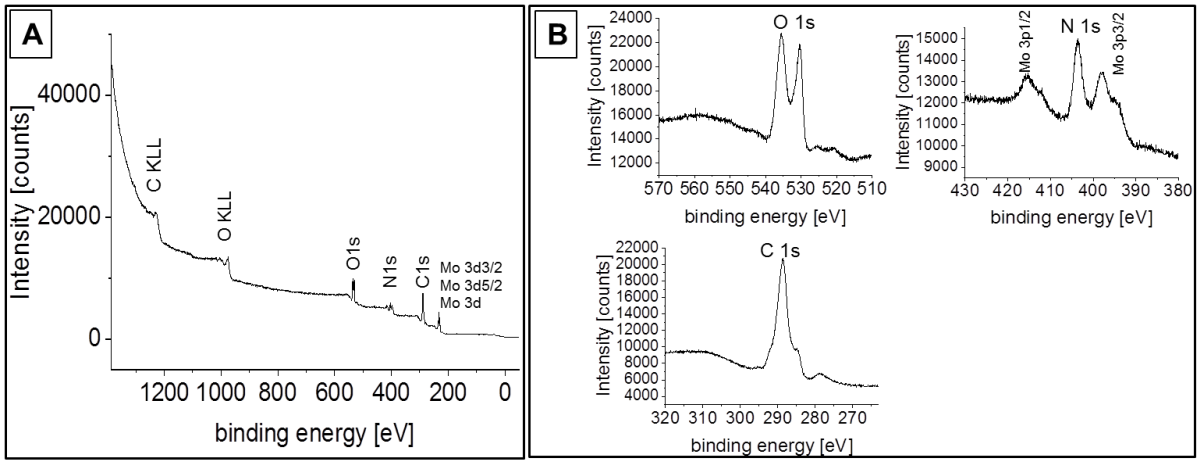

Figure 95: XPS spectra of gelatine, which is coupled to the PEEK surface (PEEK-gelatine). A: Survey spectrum. B: Fine spectra of all element signals. The appearance of molybdenum originates from the sample holder, which was used during the measurement.

The chemical composition of the calcium phosphate-gelatine surface layer on PEEK ("PEEK-CaP") was subsequently investigated by XPS. Image A in Figure 96 shows the wide scan XPS spectrum in the energy range of 0-1400 eV of the mineralized surface of the modified PEEK material. The spectrum shows that the main constituents were carbon, oxygen, nitrogen, calcium, phosphate, and molybdenum. The peaks from molybdenum, as already mentioned, originate from the sample holder during the measurement. Image B in Figure 96 displays the high-resolution core-level spectra of Ca_{2p}, Ca_{2s}, P_{2s}, P_{2p}, O_{1s}, N_{1s}, and C_{1s}. The presence of nitrogen on the surface, albeit weak, indicates that the material has a composite character.

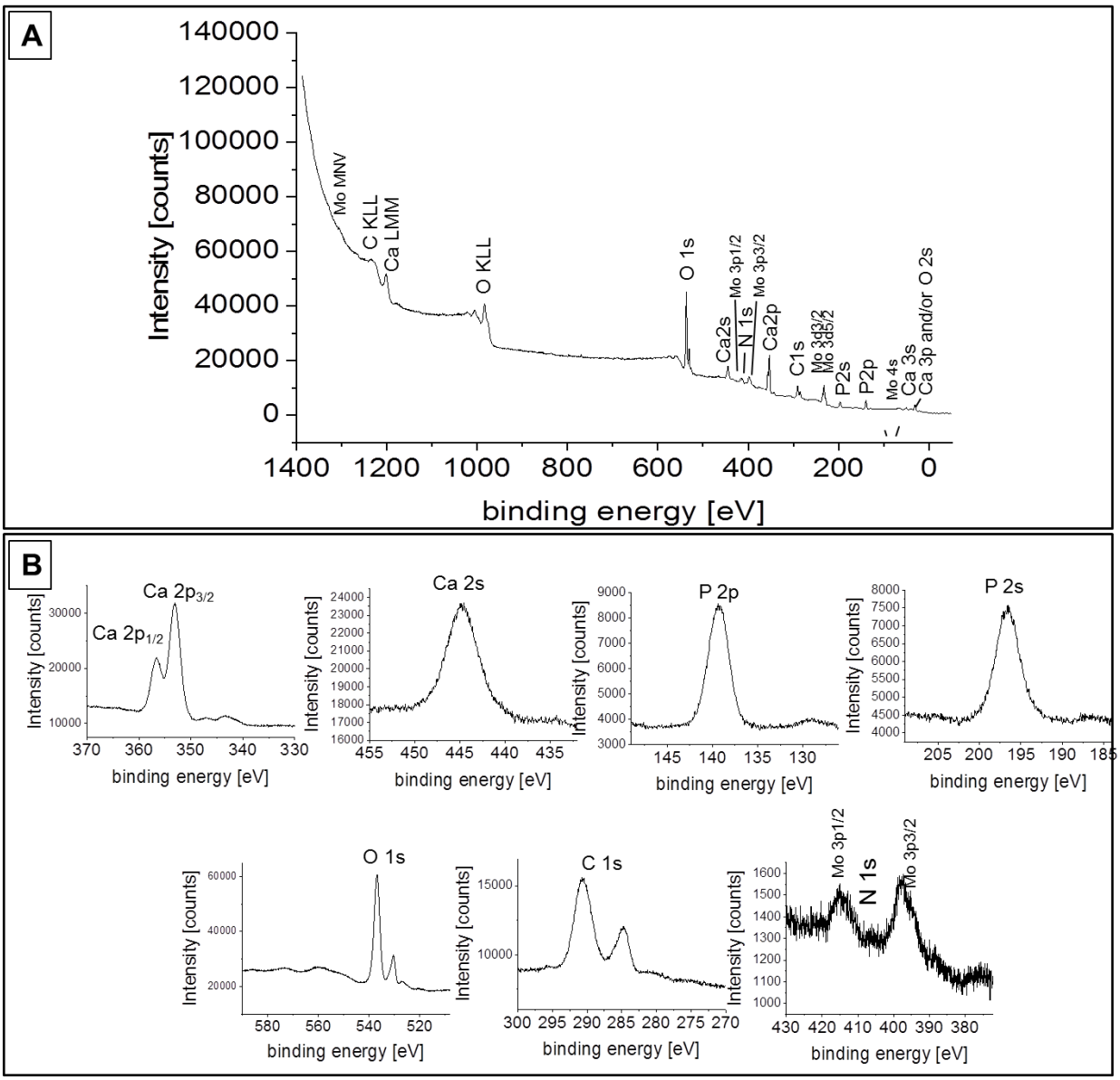

Figure 96: XPS spectra of the mineralized PEEK-surface (PEEK-CaP). A: Survey spectrum. B: Fine spectra of all element signals. The appearance of molybdenum originates from the sample holder, which was used during the measurement.

2.1.2 Grazing incidence X-Ray diffraction

Grazing incidence X-Ray diffraction has been performed to investigate the mineral phase of the calcium phosphate composite on the surface. The results of the non-functionalized PEEK and PEEK-CaP are displayed in Figure 97. The 1D-XRD-pattern of PEEK-CaP was compared to of hydroxyapatite. However, only strong reflexes of the PEEK substrate could be detected as PEEK is a semi-crystalline polymer. No characteristic signals of any calcium phosphate phase could be identified. As the presence of small crystals on the surface was verified by SEM in previous work[359, 360], it is assumed that the calcium phosphate is poorly crystalline or amorphous calcium phosphate. The reflex at ~6° could indicate octacalciumphosphate as the mineral component of the composite.

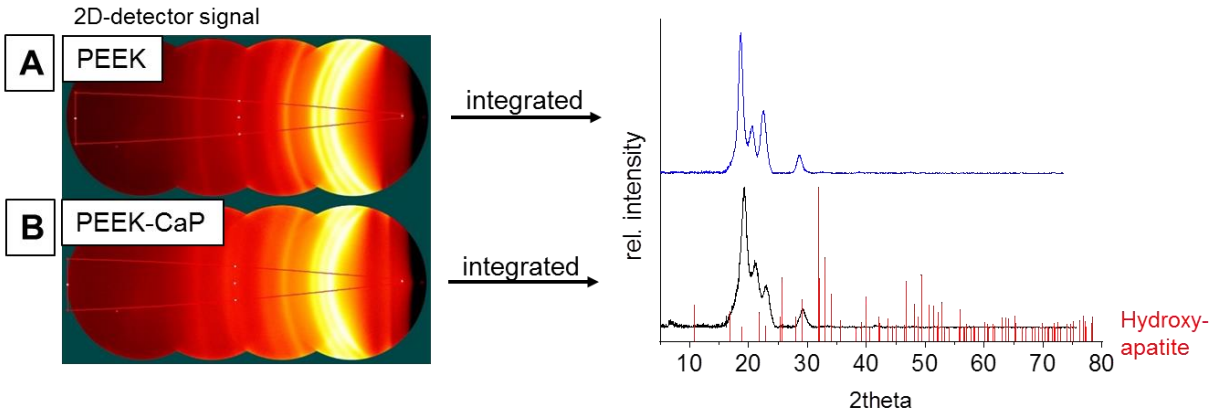

Figure 97: 2D-detector signal and corresponding 1D XRD of the non-modified PEEK (A) and the mineralized gelatine surface of the PEEK material (B).

The reflexes of the PEEK substrate are slightly shifted towards higher angles (~2°) due to a change in crystallinity during the reaction conditions. The color change of the material before and after a functionalization reaction already hinted towards a slight increase in crystallinity of the material (see Figure S 36 in appendix C). Like many semi-crystalline polymers, the crystalline content of PEEK varies depending on its thermal and chemical processing history[361], exhibiting a crystallinity between 0 % and 40 %.[362] The sorption behavior of the material has been studied, and several solvents have been shown to induce plasticization and further crystallization in the polymer.[362] In this study, only a small, thin film of the PEEK-material was used for the functionalization due to the easier handling of the different analysis methods.

2.1.3 Thermogravimetric analysis

TGA was performed to get insight into the amount of gelatine and mineral on the surface of the material. The TG- and corresponding DTG-curve are displayed in Figure 98. The curve of the thermal decomposition of the non-modified PEEK material is comparable to results reported in the literature.[363-366] All modified materials show a mass loss between 150 to about 300°C. Gelatine-apatite nanocomposites of this work (see chapter III, 2.6) and reported results demonstrated such a step for the partial decomposition and simultaneous oxidation of the gelatine component.[290] Thus it is assumed, that this step corresponds to the decomposition of gelatine. The mass loss corresponds to the decomposition of PEEK, which should be associated with the final thermal decomposition of residual organics in the form of carbon dioxide. Generally, it could be observed, that the decomposition temperature and –behavior was different for the non-modified PEEK compared to the modified versions. This step amounts to 2.16 wt-% for PEEK-gelatine and 6.35 wt-% for PEEK-CaP.
Another mass loss was recorded between 400°C – 700°C. Whereas the DTG-curves of the PEEK decomposition displayed a two-step process, the modified versions showed a multistep decomposition within the same range. A residual mass of 0.86 wt-% and 0.36 wt-% for the PEEK-CaP and PEEK, respectively, could be detected. As pure PEEK is composed of carbon and oxygen, it was assumed, that all material would be decomposed at the end of the measurement and thus no residue

would be left. It is still to be determined what the residue of the pure PEEK is composed of. Nonetheless, it is noted that an increase of residual mass between both materials is due to the presence of calcium phosphate, which should remain as calcium oxide at 1000°C at the end of the measurement. The measurement was repeated four times with samples from different batches, and the residual mass always ranges between 0.6-0.9 wt-%. Assuming that the first step corresponds to the thermal decomposition, the amount of gelatine always seems to range between 2-6 wt-%. The difference might be due to inconsistent washing after the coupling step.
It was reported, that the thermal decomposition of carbonated fluorapatite species is a multistep process with overlapping processes.[290] Within that study, the process started at about 200°C and was associated with the release of water and CO_2 as well as the release of products of partial decomposition and simultaneous oxidation of gelatine. The final thermal decomposition of all residual gelatine organics was reached at about 600°C. The complete thermal degradation of the fluorapatite-gelatine composites, which were synthesized within this thesis (see Chapter 3.2.6) was finished at 500°C and also displayed a multistep behavior. The final degradation of gelatine thus may overlap with the onset of the decomposition of the PEEK-substrate.

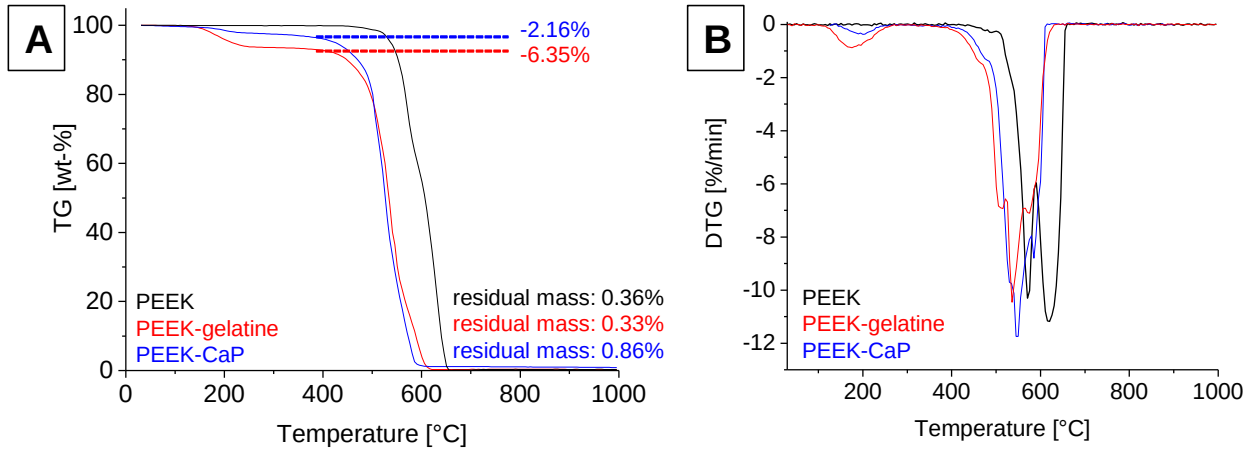

Figure 98: Representative diagrams of the TGA measurements of the non-modified, gelatine-modified and mineralized PEEK material (A) and corresponding DTG-signals (B).

2.2 Modification of the thickness of the biomimetic coating

To demonstrate, that the thickness of the biomimetic coating can be adjusted, repeated gelatine coupling cycles were employed to increase the thickness of the gelatine layer drastically. Figure 99 shows SEM images of the cross-section of different coupling cycles. It can be seen that the thickness increases with more coupling cycles. It has to be noted that the thickness of these layers might be even bigger, as these materials were dried at 40°C in a drying oven and thus, the gelatine matrix might have collapsed upon drying.

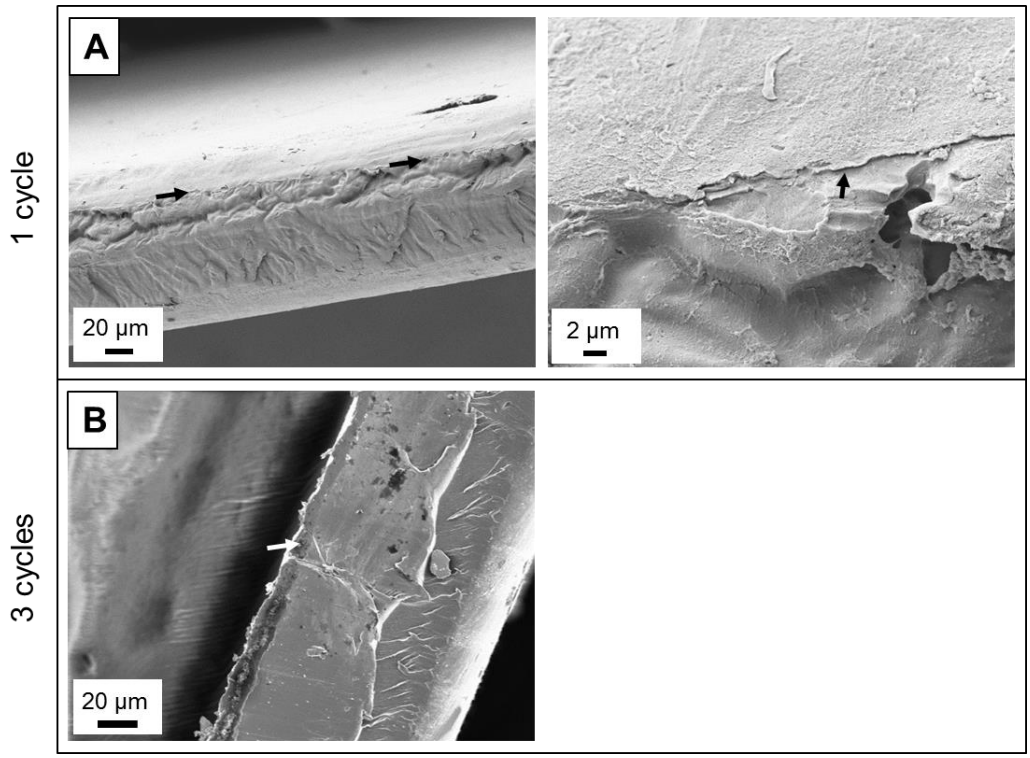

Figure 99: SEM images of PEEK-gelatine after one coupling cycle (A) and three coupling cycles (B).

Thus, it can be concluded, that it is possible to increase the thickness of the surface layer. However, it was generally noted, that the stability of the coating upon the surface gets worse with a thickening of the gelatine layer.

2.3 Surface properties of the biomimetic coating

2.3.1 Contact angle and surface free energy

The surface of the implant interacts strongly with the local tissues and is affected by the local environment. The wettability is an important factor of a surface of an implant to estimate the effect of the implant during the tissue integration. Thus, to get more insight into the wettability and surface free energy of the different PEEK surfaces of this study, the water contact angle was determined. Additionally, the surface free energies and their related disperse and polar fractions were calculated performing additional contact angle measurements with diiodo methane. Figure 100 shows representative examples of a water drop and diiodo methane drop on the different PEEK samples. The results of the mean values of all measurements of the contact angles and surface free energies with their calculated disperse and polar fractions are summarized in Table 16. The results show a decrease in water contact angle of the non-modified PEEK from 93.26° ± 1.45° to 55.29° ± 1.82° of the gelatine coated PEEK and a slight increase to 64.44° ± 3.31° of the calcium phosphate/gelatine coated PEEK material. The mean contact angle of diiodo methane on pure PEEK is 24.91° ± 3.39°, whereas the modified PEEK substrates display an angle of 46.69° ± 1.05° and 43.94° ± 3.64° for the gelatine modified PEEK and mineralized surface respectively.

Even when taking all error values into account, the contact angle changes drastically upon surface modification. The values for the modified PEEK do not change significantly from each other. No significant difference between the surface free energy of all investigated PEEK materials was detected. However, big differences could be observed when comparing the disperse and polar fractions of the surface free energies. Both modified versions of PEEK showed a lower value in the disperse fraction and a higher value in the polar fraction compared with the pure material. The gelatine modified version showed a slightly increased value than the mineralized PEEK. These results imply a general better wettability of the modified PEEK materials.

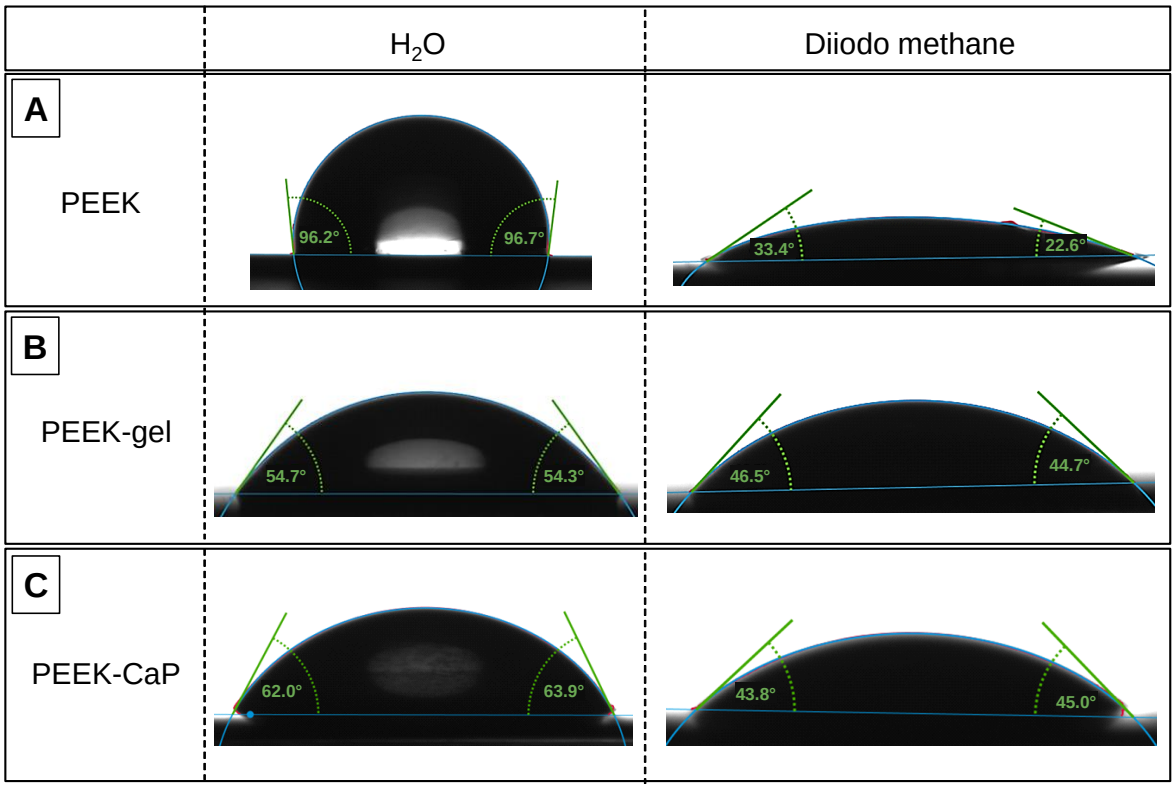

Figure 100: Representative images of the contact angle measurements of the drops of water and diiodomethane on PEEK (A), PEEK-gelatine (B) and PEEK-calcium phosphate (C).

Table 16: Mean values for the contact angles determined for water and diiodo methane, surface free energies and their disperse and polar fractions for the different PEEK samples.

Sample	θ_{H2O} [°]	θ_{CH2I2} [°]	σ_s [mN/m]	σ_s^d [mN/m]	σ_s^p [mN/m]
PEEK	93.26 ± 1.45	24.91 ± 3.39	46.32 ± 1.31	46.18 ± 1.21	0.13 ± 0.10
PEEK-gelatine	55.29 ± 1.82	46.69 ± 1.05	52.67 ± 1.68	36.10 ± 0.57	16.57 ± 1.11
PEEK-CaP	64.44 ± 3.31	43.94 ± 3.64	48.39 ± 3.80	37.57 ± 1.93	10.82 ± 1.87

σ_s: surface free energy

σ_s^d: disperse fraction of the surface free energy

σ_s^p: polar fraction of the surface free energy

Among other surface characteristics, the surface energy and wettability have been shown to influence cell attachment and growth on materials.[367-370] Water is the first component an implant encounters. It is theorized, that the optimal surface for cell attachment allows for good protein adsorption. Thus, an optimal contact angle between 60-70° has been shown to increase the proliferation rates for fibroblasts and osteoblasts.[371-373] This optimal contact angle can vary for different cell lines.[374] It has been hypothesized, that the composition, conformation and the orientation of the adsorbed proteins are important to specific cell interactions with a surface.[336] As proteins and peptides often display a complex structure comprising hydrophilic and hydrophobic parts as well as charged or uncharged areas, the surface charge is an important factor to consider, when designing new biocompatible implant interfaces. The results of this study show that both the gelatine modified- and the calcium phosphate-gelatine modified PEEK material showed favorable water contact angles and good distributions between polar and non-polar surface energies compared to the non-modified version for improved protein adsorption and cell attachment. Since the interaction of a material with biological solutions, such as blood, is rather complex, the relative importance of surface wettability and charge on cell adhesion as well as the influence on cellular morphology, and the cytoskeletal organization remains unclear.[375]

2.3.2 Mechanical stability

The stability of the gelatine layer and the calcium phosphate-gelatine layer on the surface was investigated with a scotch tape test. The layers were found to be very durable, as the attachment was very strong. After the scotch tape test, the layers remained intact even after removal of the adhesive tapes from the coatings. Only very small areas were ripped off (see image B in Figure 101), but further SEM investigations revealed, that beneath the ripped off part gelatine remains as the lowest boundary, not the PEEK substrate.

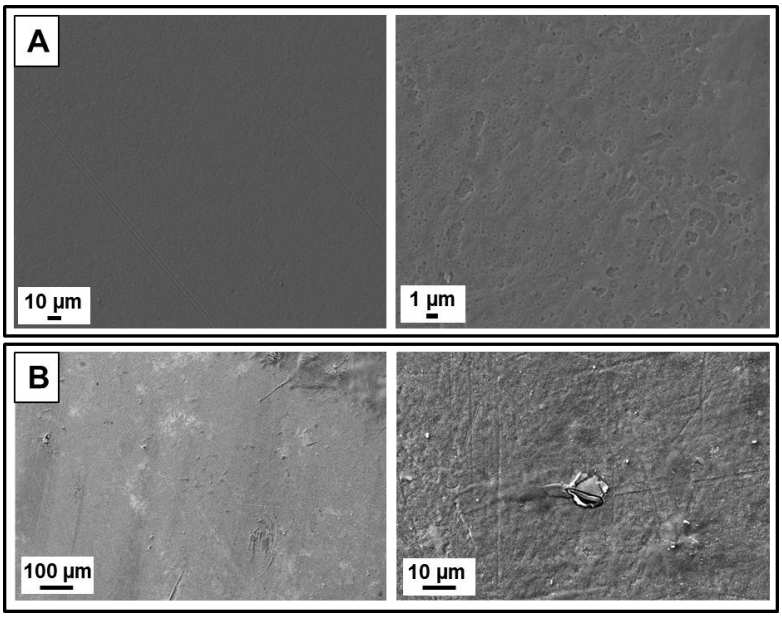

Figure 101: SEM images of the surfaces after the scotch tape tests. A: PEEK-gelatine. B: PEEK-CaP.

2.4 *In vitro* biocompatibility of the biomimetic coating

For the development of novel biomaterials and to improve their performance when they are implanted into the body, a general evaluation of cytotoxicity and biocompatibility is important. Therefore the general biocompatibility for bone implant applications of the biomimetic surface coating and its relative performance in comparison to the non-modified PEEK was evaluated using two different cell lines. Specifically, a fibroblast cell line NIH3T3 and a pre-osteoblastic cell line MC3T3-E1 were used. All assays were performed by standard biomaterial evaluation found in literature and adapted from the DIN EN ISO 10993-5:2009-10, part 5 (Tests for *in vitro* cytotoxicity).

2.4.1 Cell toxicity of the biomimetic coating

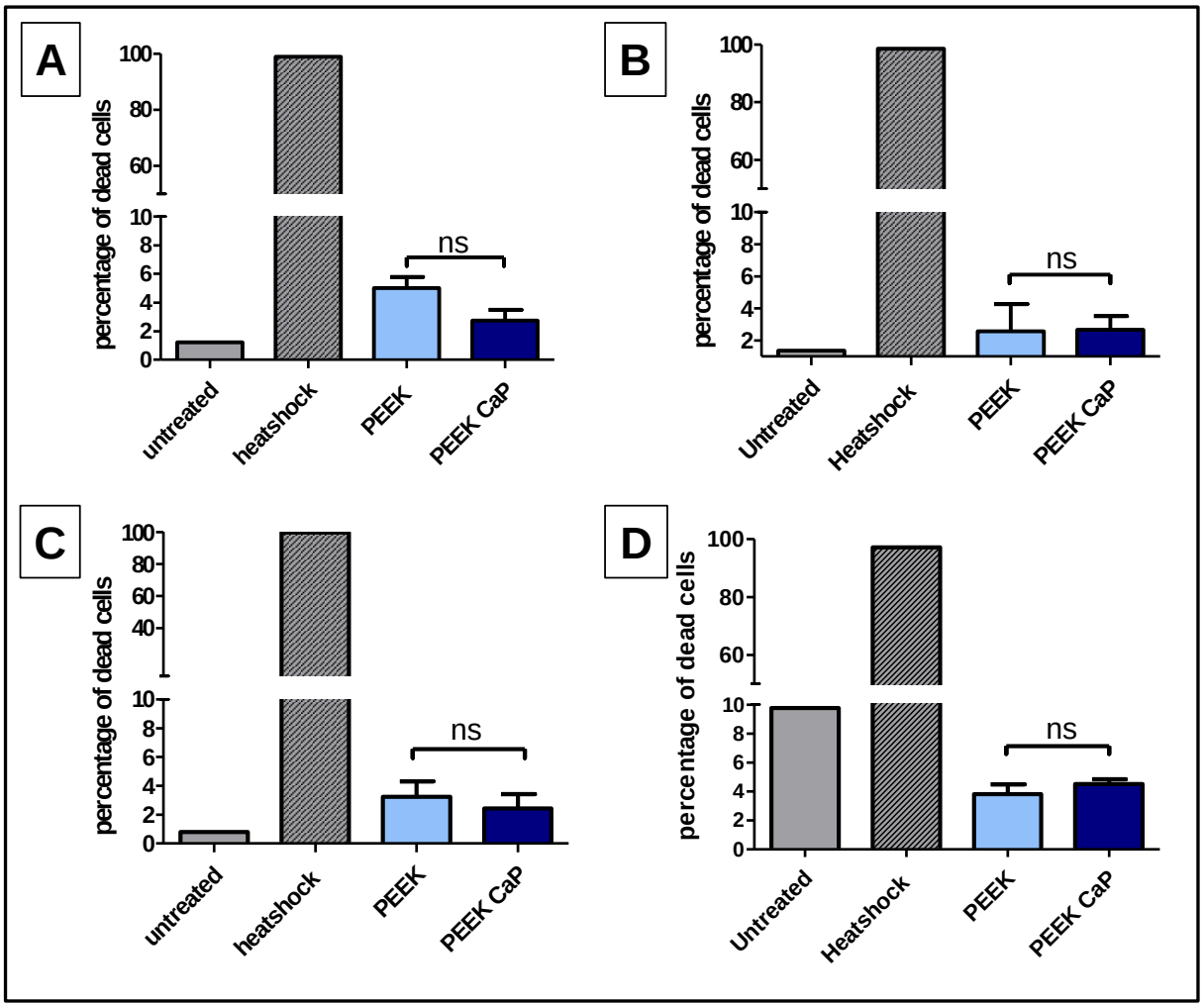

Figure 102: A: Results of the PI flow cytometric toxicity assay of the NIH3T3 fibroblast cells, which were incubated for 2 days with an extract of the different materials. B: Results of the PI flow cytometric toxicity assay of the MC3T3 osteoblast cells, which were incubated for two days with an extract of the different materials. C: Results of the PI flow cytometric toxicity assay of the NIH3T3 fibroblast cells, which were incubated for two days directly on the different materials. D: Results of the PI flow cytometric toxicity assay of the MC3T3 osteoblast cells, which were incubated for two days directly on the different materials. SD of the mean from three technical replicates.

At first, the cellular response to extracts of the material was measured, to evaluate if toxic substances can be extracted from the material. This was realized using a propidium iodide (PI) flow cytometric assay. The different PEEK materials were incubated for 24 h at 37°C in cell culture medium. Then, the extracts were incubated for two days with NIH3T3 fibroblast and MC3T3 osteoblasts cells, respectively. The results of this indirect toxicity assay of fibroblast cells after incubation with an extract of the PEEK materials are summarized in Figure 102, A. A histogram of the single results of all materials can be found in Figure S 37 in the appendix C. For the fibroblasts, the amount of dead cells is 5% for the non-modified PEEK and 2.7% for the modified PEEK-surface, showing no significant difference (P=0.1022) between PEEK and PEEK-CaP. The results of the indirect toxicity assay of the MC3T3 osteoblasts cells are displayed in Figure 102, B. A histogram of the single values of each measurement can be found in Figure S 38 in appendix C. The amount of dead cells is 2.6% for the non-modified PEEK and 2.7% for the modified PEEK-surface and shows no significant difference between the different materials (P=0.9483). These generally low values demonstrate that no toxic substances were extracted from both the non-modified and the modified PEEK-materials. Considering the biomimetic composition of the modified surface, gelatine and calcium phosphate, the only toxic residue might originate from the solvents and agents used for the chemical modification.

To evaluate the general toxicity upon direct contact with the materials, the NIH3T3 fibroblast and MC3T3 osteoblast cells were incubated for two days directly on the surfaces of the different PEEK materials. Dead cells were detected using the same procedure of the PI flow cytometry assay. The results of the fibroblast cells are displayed in image C in Figure 102. The results of the single measurements can be found in Figure S 39. The amount of dead cells is 3.24% for the non-modified PEEK and 2.45% for the modified PEEK-surface, showing no significant difference between the different materials (P=0.6147). The results of the osteoblast cells are displayed in image D in Figure 102. A histogram of the single results for this experiment of each measurement can be found in Figure S 40 in appendix C. This assay showed a noticeable increase of dead cells within the untreated sample, which amounts to 9.75%. The amount of dead cells is 3.81% for the non-modified PEEK and 4.50% for the modified PEEK-surface and shows no significant difference between the different materials (P=0.4106). Generally, these results show, that the material is not toxic and there is no response of the cells, upon direct contact on the different PEEK materials, which might lead to cell death.

2.4.2 Cell viability

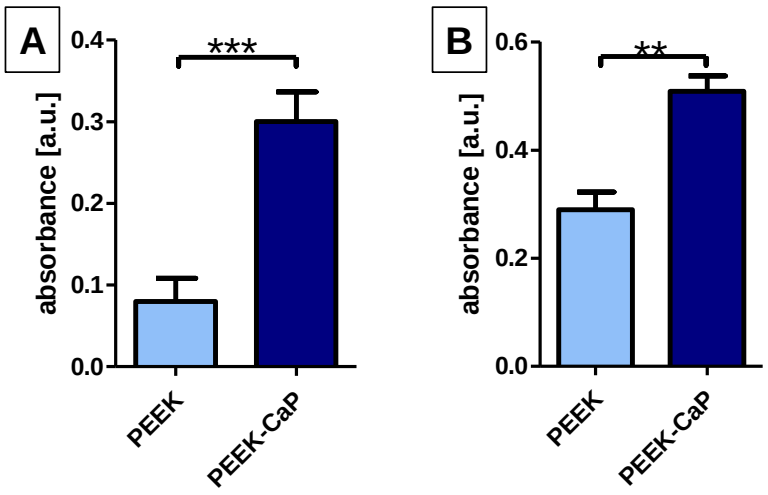

Figure 103: A: Results of the MTT-viability assay of the NIH3T3 fibroblast cells, which were grown in the different PEEK-materials for one day. B: Results of the MTT-viability assay of the MC3T3 osteoblast cells, which were grown in the different PEEK-materials. SD of the mean from three technical replicates.

To evaluate the general metabolic activity of the NIH3T3 fibroblasts on the materials, an MTT-assay was performed three times. The result of one representative assay is displayed in Figure 103, A. The results show, that the general viability is significantly ($P<0.0001$) higher on the calcium phosphate-gelatine modified PEEK in comparison to the non-modified PEEK. The results of the MTT-assay of the MC3T3 osteoblast cells is displayed in Figure 103, B. These results also show that the cellular metabolic activity is good on all investigated PEEK materials. It was observed that the metabolic activity is significantly higher ($P=0.0075$) for the cells, which were grown on the PEEK-CaP surface in comparison to the non-modified PEEK. Thus, these results show, that the cells of both cell lines show an active metabolism on the PEEK materials. Furthermore, these results show, that the metabolic activity is higher on the biomimetic surface coating in comparison to the non-modified version.
The MTT assay is also a useful method for measuring cytotoxicity of biomaterials. It can be used to reveal subtle toxicity effects of some materials, which do not kill the cells rapidly but affect some aspect of cellular metabolism.[376-378] Thus, the results of the viability assays on the different PEEK materials also represent a further aspect of the cytotoxicity evaluation. These results thus confirm, that no toxic substances were extracted from the material, which might negatively affect the cellular metabolism of NIH3T3 fibroblasts and MC3T3 osteoblasts.

2.4.3 Cell attachment

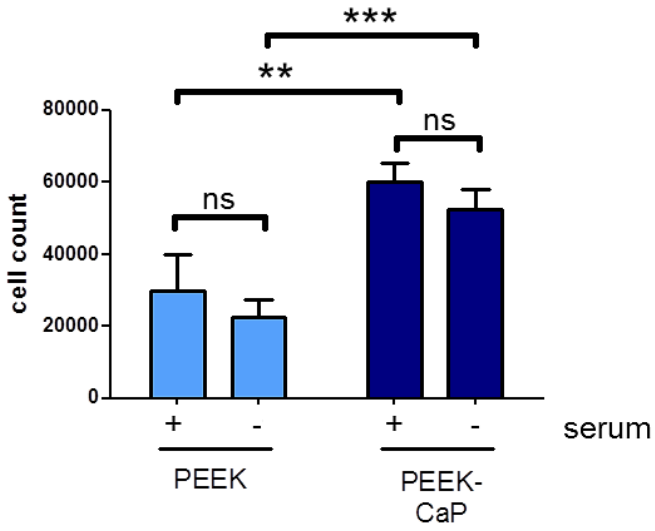

Figure 104: Results of the attachment assay of the NIH3T3 fibroblast cells, which were seeded on the different PEEK-materials in the presence and absence of serum proteins. SD of the mean from four technical replicates.

Cellular adhesion of the NIH3T3 fibroblasts to the modified materials was evaluated. For this, a certain amount of cells were seeded directly onto the different materials and incubated for 6 h. After this time, all non-adherent cells were washed off. After this step, all adherent cells were detached from the material, and the cell number was counted. The results are shown in Figure 104. This assay showed that the cells could adhere significantly better to the modified material by a factor of 2.3 in comparison to the non-modified PEEK (P=0.0001 without serum in the medium and P=0.0020 with serum). This is consistent with the results of the water contact angle measurements and the determination of the surface free energy. As was stated, among other surface characteristics, these two parameters have been shown to influence cell attachment and growth on materials. Herein, an optimal contact angle between 60-70°, which fits to the contact angle for PEEK-CaP, has been shown to increase the attachment and proliferation rates for fibroblasts, especially NIH3T3 fibroblasts.[371-373, 379] This assay was performed in the presence and in the absence of protein serum inside the cell culture medium, to estimate if and to which extend the adherence of the cells is influenced due to serum proteins of the cell culture medium, which might have adsorbed to the surface. The results of this assay showed no significant difference in the cell attachment to the surfaces with or without proteins present in the culture medium (P=0.1682 for the PEEK measurements and P=0.1682 for PEEK-CaP).
The attachment assay was also performed with the MC3T3 osteoblast cells. However, no results could be obtained, as the cells could not be completely detached again by trypsination. By overtrypsination, only cell debris could be detected by the cell counter. However, the SEM- images demonstrate (see Chapter IV 2.2.5), the osteoblast cells do attach to the biomimetic surface coating. Furthermore, it has been shown, that only attached cells produce MTT formazan crystals, whereas nonviable

cells and debris did not reduce the MTT dye.[380, 381] As the viability of the osteoblast cells remained good upon incubation on the modified material, it can be generally assumed, that the cells did indeed attach to the surface.

2.4.4 Cell proliferation

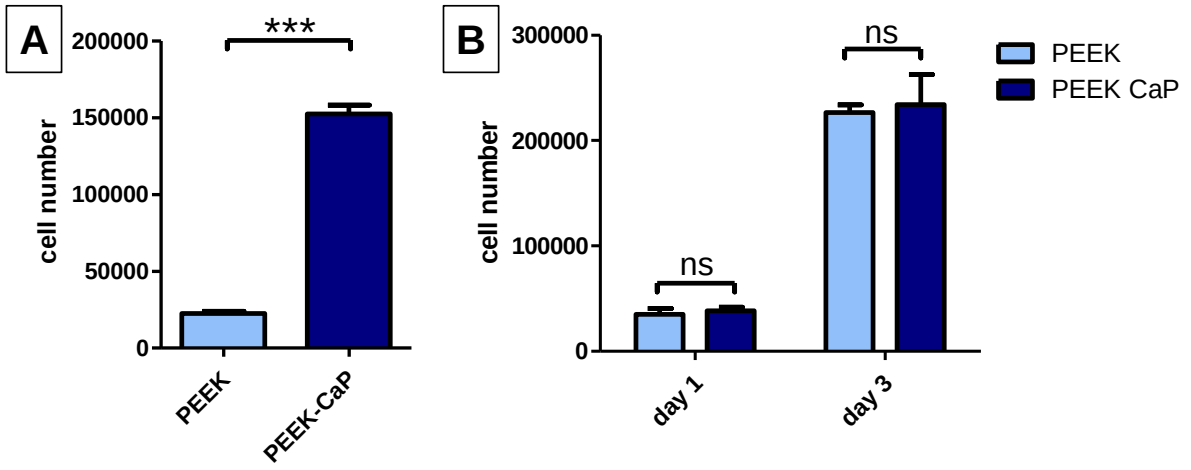

Figure 105: A: Results of the cell proliferation assay of NIH3T3 fibroblast cells, which were grown for one day n the different PEEK materials. SD of the mean from three technical replicates. B: Results of the cell proliferation assay of MC3T3 osteoblast cells, which were grown for one day and three days on the different PEEK materials. Day 1: SD of the mean from six technical replicates. Day 3: SD of the mean from three technical replicates.

The relative proliferation of the NIH3T3 fibroblasts and MC3T3 osteoblasts on the material was evaluated. For this, a certain amount of cells were grown directly on the surface of the different PEEK materials. Afterwards, the cells were detached from the surface via trypsination, and the cell number was determined via a CASY cell counter. The results of the fibroblast proliferation assay are displayed in Figure 105, A. These investigations revealed that the fibroblast cells proliferate significantly better ($P<0.0001$) on the calcium phosphate modified PEEK material by a factor of 4.4 in comparison to the non-modified material. The general low amount of the cells on the pure PEEK might be due to the detachment process during the assay. The cells were detached from the surface of the materials using a Trypsin/EDTA mixture in a buffer, as is standard procedure for the detachment of adherent cells in cell culture. Considering the components of the surface of the modified PEEK, specifically the gelatine and calcium phosphate, the efficiency of the detachment solution might have been lower within this experiment due to a competition reaction. To ensure the detachment of a relatively high amount of cells from the surface, the incubation time within the detachment solution can be prolonged. This, however, entails a higher risk of destroying the already detached cells due to enzymatic digestion. The CASY-cell counter will not count destroyed cells and thus may create an underestimation of the actual cell proliferation. As the general attachment of the fibroblast seemed less on the non-modified PEEK, the cells might have been detached earlier and been digested by the enzyme, which would lead to a generally lower cell count.

The relative proliferation of the osteoblasts on the different PEEK materials was evaluated after 1 and 3 days. The results are displayed in Figure 105, B. These investigations showed no significant increase of the proliferation of the osteoblast cells on the calcium phosphate modified materials (day 1: P=0.6306, day 3: P=0.8125). At first glance, this result appears inconsistent with the viability assay, which showed a significant increase in viability of the osteoblast cells, which grew on the modified PEEK material. Detailed reports on the cellular response of MC3T3-E1 osteoblasts to hydroxyapatite showed, that once the cells attach to the surface, the cells proliferate and subsequently, if the conditions are right, can enter a stage of early differentiation after 24 h, which is marked by the production of an extracellular matrix.[382-385] These studies demonstrated that MC3T3-osteoblast growth is decreased on hydroxyapatite, whereas differentiation is increased. In studies of the influence of the surface roughness of titanium disks on the cellular response of MG63 osteoblasts, it was found that the cells showed a decrease in proliferation and alkaline phosphatase activity when the roughness was increased.[386] Furthermore, collagen synthesis was increased with increasing roughness.[386] This is consistent with the observations of the SEM investigations (see Figure 107, C in chapter IV 2.2.4), where the production of an extracellular matrix of the MC3T3 osteoblasts on the mineralized surface was noted.
There are several potential explanations for the differences observed between the different behavior of the different cell lines, which were used in this study. Cell type specific differences in membrane properties such as phospholipid composition and integrin receptor expression can influence cellular interactions with surfaces. It was reported in the literature, that MC3T3-E1 osteoblast behavior, in contrast to NIH-3T3 fibroblasts behavior, is surface chemistry dependent rather than general surface properties such as wettability.[387, 388]

2.4.5 Cell morphology

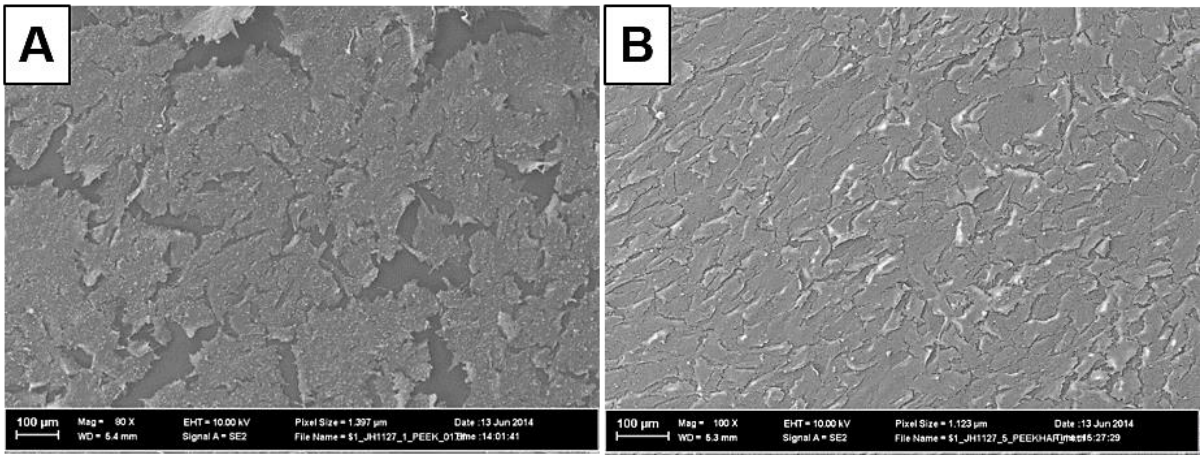

Figure 106: SEM images of NIH3T3 fibroblast cells, which were incubated for one day on the different PEEK-materials.

Figure 106 displays SEM images of the NIH3T3 cells after a growth time of 24 h on the pure PEEK (A) and PEEK-CaP (B). The cells generally adhered to the surfaces. The attached cells were flat and spread over the whole samples. It was observed that

the cells were very densely grown. On the pure PEEK-surface, in contrast to the modified surface, several spots with detached cells could be observed. Some cells may have been washed away during the sample preparation due to bad attachment of the fibroblasts onto the pure PEEK-surface, which indicates weak attachment of the cells on the surface. This demonstrated that fibroblasts can attach to all PEEK surfaces and show a normal morphology.
Figure 107 displays SEM images of the MC3T3 osteoblast cells after a growth time of 24 h on the pure PEEK (A), PEEK-gelatine (B) and PEEK-CaP (C).

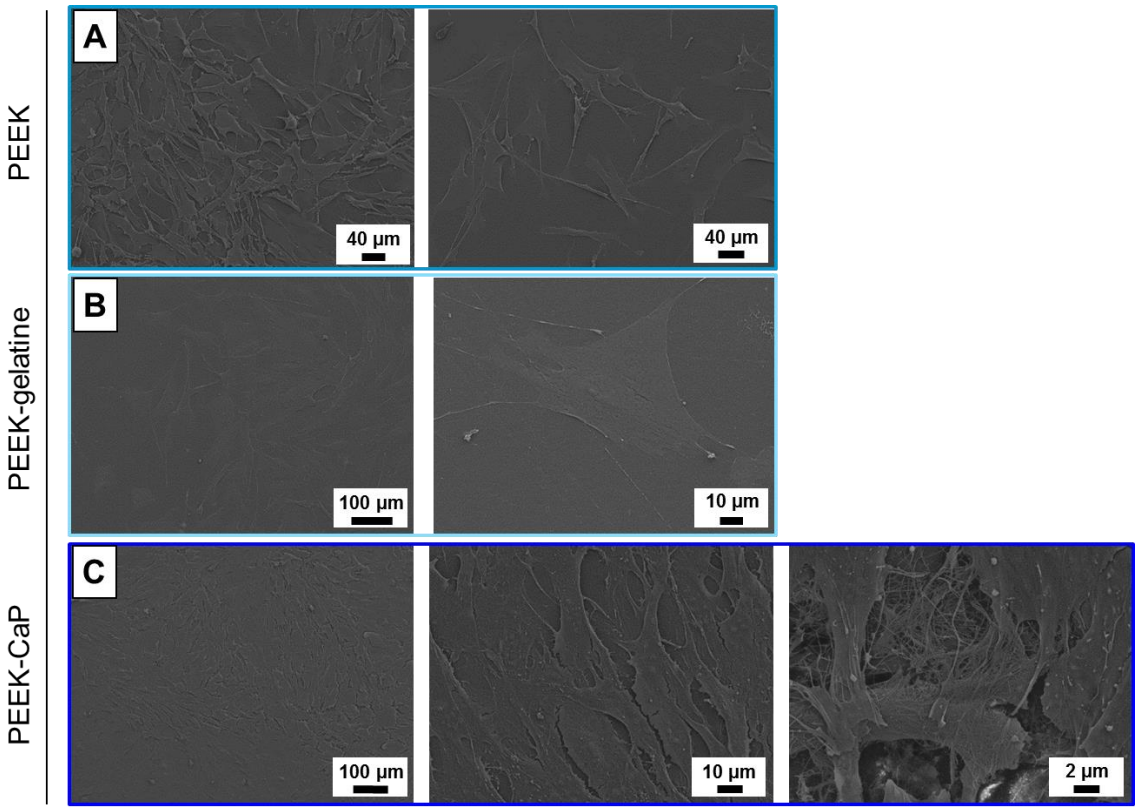

Figure 107: SEM images of MC3T3 osteoblast cells, which were incubated for one day on the different PEEK-materials.

The behavior of the cells on the material differed according to the chemical composition of the surface. On the pure PEEK-surface (image A), the cells were small in size. This might be attributed to the strong hydrophobic surface of the pure PEEK, as was determined by the contact angle measurements and the calculation of the different parts of the surface free energies. In contrast, the cells on the modified surface were very flat, widely spread out and, in the case of PEEK-CaP, very densely grown (see images B and C in Figure 107). Here, in certain areas, single cells could not even be determined anymore. In between these cells, a fibrous network could be detected. As was briefly mentioned in the previous paragraph, the MC3T3-osteoblasts can enter a stage of early differentiation after 24 h if the conditions are favorable. This process is marked by the production of an extracellular matrix. Thus, these results demonstrate, that the MC3T3 osteoblast cells spread well on the surfaces with the biomimetic coating in the initial stages of cell adhesion, which leads to early differentiation of the cells and the production of an extracellular matrix.

3. Summary and conclusion

One prerequisite for a successful bone implant is fast osseointegration. Herein, the implant surface is of utmost importance for the first contact with the human body. To increase the general biocompatibility of PEEK, which is a good candidate material for bone implants, a covalently bound, “bone-like” coating was utilized. In previous work, we described the general method of surface modification, which was further investigated in this study. The surface was shown to display the general compositional characteristics of bone. XPS confirmed the presence of a calcium phosphate-gelatine composite on the surface of the PEEK. This was realized in a covalently bound gelatine layer, which was subsequently mineralized. The results of the scotch tape test showed reasonable stability of the surface coating. Contact angle measurements and the determination of the surface free energies showed an increased wettability of the modified PEEK materials. Furthermore, the general biocompatibility was verified using two different cell lines, fibroblasts and osteoblasts. The fibroblasts and osteoblasts used in this study represent examples of the types of cells which bone implants will be in contact with during clinical use. Indirect and direct toxicity-, viability-, adhesion-, proliferation- assays showed the increase in biocompatibility with the bone-like coating in comparison with pure, non-modified PEEK.

Chapter V Methods

Of Chapter II

1. Specimen and Sample Preparation

All fish used in this study were sexually mature and originated from captivity bred stocks that are fed with the same food (commercial flake food). The specimen preparation was performed by Dr. Ralf Schneider from the group of Prof. Axel Meyer. After euthanizing selected individuals, the lower pharyngeal jaws were dissected, soft tissue, such as muscle and connective tissue, was removed and the samples were fixed in 4% paraformaldehyde (PFA) overnight. Sampling was done in accordance with local ethics regulations (Anzeige T16-13). Subsequently, LPJs were treated with Proteinase K to remove soft tissue residuals, washed with distilled water and then air dried at room temperature.

Removal of selected teeth from LPJ: The lower pharyngeal jaws of the cichlid specimen were briefly washed with water and immersed in a solution of proteinase K (50 µg/ml) in PBS for approximately one hour at room temperature. To reduce the risk of damaging the teeth with the protease, the progress of the removal was controlled visually under a stereomicroscope. When all teeth were removed, the samples were washed two times with distilled water and once with 70 % ethanol and left to air dry at room temperature.

Extracted teeth were embedded in epoxy resin with dispersed Ag-particles and dried. Afterwards, the surface was polished, first with a diamond suspension with a grain size of 0.25 µm and afterwards with an aluminum oxide suspension. The sample preparation for the polishing and the polishing was performed by Dr. Ulrich Burkhardt and Sylvia Kostmann at the Max-Planck-Institut für Chemische Physik fester Stoffe in Dresden.

2. Light Microscopy

Light microscopic images were taken either with a Zeiss Stemi 200-C stereomicroscope, equipped with a AxioCamICc1 camera or a Leica MZ10F Modular Stereomicroscope equipped with a Leica DMC2900 camera.

3. Raman Microscopy

Confocal Raman microscopy imaging was performed at the ETH Zürich with the help of Jana Segmehl and Kirstin Casdorff on embedded and polished tooth samples. All measurements were recorded in backscattering configuration with an InVia Raman microscope (Renishaw, UK) equipped with a motorized xyz stage for mapping. The excitation of Raman Scattering was operated with a linearly polarized diode laser in the near infrared regime (λ = 785 nm). An 50x objective with a numerical aperture (NA) 0.75 (Nikon) was used. The Raman light was detected by an air-cooled charge-

coupled device (CCD) camera behind a spectrometer (InVia) with a spectral resolution of about 1 cm^{-1}. The mapping was recorded with an integration time of 1 s and a laser power of 18 mW in the spectral region between 198 – 2425 cm^{-1} and a step size of 1 µm. The measurement setup as well as the initial data treatment, including cosmic ray removal and baseline correction, was done in Wire (version 4.1, Renishaw, UK). For the baseline correction, the inbuilt automatic intelligent background removal was used. The data was further processed in the Matlab based software Cytospec (version 2.00.01). For intensity profile line scans, the spectra were baseline corrected and the relative phosphate content was determined as the signal intensity at 962 cm^{-1} ($[PO4]^{3-}$ v_2 vibration mode).

4. Attenuated Total Reflection- Infrared Spectroscopy (ATR-IR) and -Microscopy

ATR-IR measurements were conducted with a Perkin Elmer Spectrum 100 FT-IR Spectrometer equipped with a Universal ATR-Sampling Accessory. Different teeth samples were removed from the LPJ, powdered with a mortar and subsequently analyzed. ATR-microscopy was performed on the embedded and polished axial cross-sections with a Bruker Lumos Microscope.

5. Fluorescence Microscopy

Fluorescence microscopy was performed at the University of Konstanz with the help of Dr. Ralf Schneider from the group of Prof. Axel Meyer. LPJs have been dissected and fixed using PFA (4%) over night at 4°C. Then, PFA was replaced by ~10% acetic acid. LPJs were kept at 4°C for 3 weeks and acetic acid was changed every week. LPJs were then embedded in embed medium (Tissue-Tek O.C.T. compound) and sectioned using a microtome cryostat (~25µm). Sections were then stained with Calcofluor White or WGA-FITC. The Sections were investigated with a Zeiss LSM 880 point laser scanning confocal microscope equipped with a GaAsP detector.

6. Nanoindentation

The nanoindentation measurements were performed at the ETH Zürich with the help of Dr. Davide Carnelli in the group of Prof. Stuart and with Dr. Diana Courty in the group of Prof. Spolenakin. Nanoindentation measurements were performed under ambient conditions on a Hysitron TriboIndenter (Hysitron Inc., USA) with a Berkovich diamond indenter. Displacement controlled indentation experiments were performed at 200 nm penetration depth on dry, polished axial cross-sections of the cichlid specimen teeth from the occlusal tip to the basal root area in three parallel rows with 100 indents each, which were interspaced in 3 µm. Each unloading segments of the load vs. displacement curves were evaluated according to the method of Oliver and Pharr[389] to obtain the hardness and indentation modulus.

7. High-Resolution Scanning Electron Microscopy (SEM) /Energy Dispersive X-Ray Spectroscopy (EDXS)

SEM investigations on the polished samples were performed using an ESEM FEI Quanta 200 FEGi system operated in a low (60 Pa) and high vacuum modes and at an acceleration voltage of 15 kV and 5 kV, respectively (FEI Company, Eindhoven, The Netherlands) (measurements were performed by Dr. Elena Sturm at the Max-Planck-Institut für Chemische Physik fester Stoffe, Dresden). The other SEM investigations were performed using a ZEISS Auriga TM Crossbeam Workstation in a high vacuum using variable acceleration voltages. EDXS were acquired using the INCA-system with an Oxford Instruments X-Max detector (UK). If necessary, samples were sputter coated with 5 nm Carbon.

8. Transmission Electron Microscopy (TEM)

For TEM investigations focused ion beam (FIB) thin cuts of the dental hard tissues were prepared by Dr. Matthias Hagner at the University of Konstanz. Microtome cuts of partially demineralized dental hard tissues were prepared at the Electron Microscopy Center at the University of Konstanz by the following procedure. The samples were demineralized at room temperature with a 0.25 M EDTA solution (in H_2O, pH 4) for 4 h. The samples were then washed with water. Fixation was performed in a two-step way in a 3% glutaraldehyde solution (in PBS, pH7.4) at 4 °C for 1 h and 1.5 , respectively. Afterwards, the samples were washed three times with PBS at 4 °C for 30 min each. In preparation for the embedding, the samples were incubated in a graded series of aqueous ethanol solutions (15%, 30%, 50%) for 1 h each. The samples were then washed with a graded series of aqueous ethanol solutions (70%, 80%, 90%, 100%) 10 min each at room temperature. The samples were then embedded in a graded series of Spurr (low viscosity) in propylene oxide (10%, 30%, 50%, 70%, 90%) for 1 h each and again 3x for 3 h in 100% solution, all at 4 °C. The tooth samples were then polymerized at 65 °C for 3 days in an oven. Then the samples were cut into 80-85 nm slices by using a Leica Ultracut UCT ultramicrotome (Leica Microsystems, Wetzlar, Germany) equipped with a Diatome Ultra 45° (Diatome Ltd, Nidau, Switzerland) diamond knife. TEM experiments were carried out using a Zeiss Libra 120 with LaB_6 source at 120 kV acceleration voltage and in-column filter for EELS and EFTEM measurements. HRTEM measurements were performed by means of JEOL JEM-2200FS and FEI Tecnai F20/Cs-corrected TEM operating at 200 kV acceleration voltage. Analysis of the TEM images was done with the Digital Micrograph (Gatan, USA) and JEMS software packages. TEM investigations were performed by Dr. Elena Sturm, Dr. Song Chen, Dr. Marina Krumova at the University of Konstanz and Sebastian Sturm at the Leibniz-Institut für Festkörper- und Werkstoffforschung in Dresden.

9. Atomic Force Microscopy (AFM)

AFM measurements were performed on a JPK nano wizard II ultra. AFM scans were performed in tapping mode. Data visualization was performed with the JPKSPM Data Processing software.

10. Microbeam Wide-angle X-ray Scattering (WAXS) / Small-angle X-ray Scattering (SAXS)

Microbeam scanning small (SAXS) and wide-angle (WAXS) X-ray scattering experiments were performed on the two side polished resin embedded thin samples with the help of Dr. Baohu Wu and Dr. Elena Sturm at the μ-spot beamline at the BESSY II synchrotron radiation facility in Berlin (Germany).[181] X-ray scattering patterns were recorded in transmission mode with a 2D CCD (charge-coupled device) detector (MarMosaic 225, Rayonix, Inc., Evanston, USA) with a pixel size of 73 μm and an array of 3072 × 3072 pixels. The energy of the incident X-ray beam was 15 keV. The beam was further defined by a toroidal mirror together with a silicon (111) double-crystal monochromator with a pinhole size of 30 μm close to the sample. The sample to detector distance (SD) is approximately 310 mm which was calibrated using quartz powder ((NIST, standard Reference Material 1878a). For each two-dimensional diffraction pattern, beam center and tilt corrections were performed using Fit2D.[390] The two-dimensional pattern was integrated to a one-dimensional profile via a radial (Intensity versus q, $q = 4\pi \sin(\theta)/\lambda$, where λ is the wavelength, and θ corresponds to the scattering angle) or azimuthal (Intensity versus azimuthal angle χ) integration and reduction method.

Of Chapter III

1. Synthesis of substituted fluorapatite-gelatine nanocomposites

The fluorapatite-gelatine nanocomposites were grown according to procedures as described in the literature.[278, 290] The growth of the composites was carried out in U-tubes according to the double diffusion technique in which reservoirs of two reagent solutions were separated by a gelatine gel (concentration 10 wt.-%). The pH of the gelatine gel was adjusted to 3.4. The L-shaped tubes of the diffusion cells were filled with buffered aqueous solutions (Tris(hydroxymethyl)-aminomethane 29 g/L, pH 7.4) of $CaCl_2 \times 2H_2O$ (0.1333 M) and Na_2HPO_4/NaF, respectively (molar ratios Ca:P:F of 5:5:1). The addition of fluoride was always delayed by 24 h in order to avoid the formation of calcium fluoride. For the synthesis of strontium-bearing fluorapatite-gelatine nanocomposites $SrCl_2 \times 6H_2O$ was added to the calcium-containing solution in order to obtain molar ratios of Ca:P:F:Sr, with a variation of x in the range between 0 and 5. The temperature was kept constant during the experiments at 25 °C using a water bath. After 3 days the first Liesegang bands were observed within the gelatine matrix. The bands were cut and isolated from the gelatine matrix after growth periods of 21 days. The bands were dissolved in distilled water at 40 °C and centrifuged for 3 min at 3000 rpm to get rid of adhering gelatine. The washing step was repeated for at least three times. Those Liesegang bands, which are located close to the calcium and phosphate sources, are named C and P, respectively. The M bands (middle bands) are located between P and C.

2. Plasma-Optical Emission Spectroscopy (ICP-OES) and CHNS-Analysis

The content of calcium, phosphate, strontium, and sodium of the composites, which were isolated from the M-Liesegang, was determined by inductively coupled plasma-optical emission spectrometry (ICP-OES, Varian, VISTA RL), which was performed by Dr. Gudrun Auffermann at the Max-Planck-Institut für Chemische Physik fester Stoffe in Dresden. The fluoride content was determined by using oxidative combustion connected with ion chromatography (CIC). For this, about 10 mg of the samples were dissolved in 4 mL of 2 M HCl and then diluted with water in a 100 mL volumetric flask.

The amounts of gelatine were calculated on the basis of the N content determined by use of the carrier-gas hot-extraction method combined with the combustion technique by means of the CHNS-analyzer 932 (LECO, USA). The sample weights amounted to 2 mg and combustion was performed in Sn capsules under an O_2 atmosphere.

3. X-ray Powder Diffraction (pXRD)

The phase composition of the composite materials was determined by X-Ray diffraction analysis. The XRD powder data were collected with a Bruker D8 Discover with Cu-Kα radiation equipped with a VÅNTEC-500 2D detector. The lattice parameters were calculated by least-squares refinements using LaB_6 as an internal standard using the WinCSD software package.

4. FT-IR Spectroscopy

Fourier transform infrared (FT-IR) spectra in the region of 4000-380 cm^{-1} were recorded at room temperature using a Bruker spectrometer (IFS 66v/S; Globar (MIR), KBr, DTGS-Detector; Program Opus/IR 3.0.3). The samples were prepared as KBr pellets (2 mg of the sample dispersed and ground in 300 mg KBr). In order to separate overlapping bands the signals were fitted using a Pseudo-Voigt 1 distribution with the software package of Origin 9.0 (OriginLab Corporation; MA, USA).

5. Raman Spectroscopy

Raman spectra were recorded at room temperature using a confocal Raman system MonoVista CRS 750HR/BX51WI from the company Spectroscopy and Imaging. Measurements were done using an excitation Wavelength of 633 nm of a He-Ne laser under a microscope (100x microscope objective, 0.9 NA, MPLN from Olympus) and a 600g grate of the monochromator (Princton Instruments). Spectra were collected with a slit entrance of 100 µm and an acquisition time of 30 s. Overlapping bands were separated in the spectral ranges by fitting with Pseudo-Voigt 1 distributions for the bands. The software package Origin 9.0G (OriginLab Corporation; MA, USA) was used for the least-square fits.

6. Thermogravimetric Analysis

Thermogravimetric analyses (TGA) were performed using a Netzsch simultaneous thermal analyzer 449 F3 Jupiter. The sample weights always were 10 mg. The heating rate was kept at 10 K/min up to 1000 °C under an oxygen atmosphere using aluminum oxide crucibles. Decomposition steps were analyzed using the Netzsch Proteus 6.1 software package.

7. Scanning Electron Microscopy

The morphology of the synthetic aggregates and the tooth samples were studied by scanning electron microscopy (SEM). SEM investigations were either performed by means of an ESEM FEI Quanta 200 FEGi system operated in a low vacuum (60 Pa) mode (FEI Company, Eindhoven, The Netherlands), by means of a ZEISS Auriga TM Crossbeam Workstation with a thermal Schottky field emission cathode in a high vacuum using variable acceleration voltages or a Zeiss 1540XB CrossBeam Focused Ion Beam FE SEM, also in a high vacuum using variable acceleration voltages.

Of Chapter IV

1. Chemical activation of PEEK surface

The synthesis of the reduction of the keto-groups of the PEEK, the coupling of succinic acid as a linker molecule, the subsequent coupling of gelatine and the final mineralization was performed according to [360].
Reaction conditions were used for 1 cm^2 of a PEEK-film-sample.

Reduction of keto-groups (in the following called "PEEK-OH"): 1 mmol $NaBH_4$ was dissolved in 10 mL DMSO and heated to 120 °C under stirring. The PEEK sample was immersed in the solution and stirred at 120 °C for 4 h. The PEEK sample was then washed successively with MeOH (10 min), H_2O (10 min), 0,5 M HCl-solution (25 min), H_2O.

Coupling of succinic acid (in the following called "PEEK-COOH"):
PEEK-OH film was immersed in an ice-cold solution of 0.12 g (1 mmol) succinic acid, 0.2 g (1 mmol) DCC and 1 mg DMAP in THF for 4 h, then stirred for additional 4 days at room temperature. The film was washed successively with THF, H_2O, and EtOH.

Coupling of gelatine (in the following called "PEEK-gelatine"): PEEK-COOH film sample was immersed in a solution of 0.17 g (0.9 mmol) EDC, 0.14 g (0.12 mmol) NHS in 10 mL DMSO and stirred at 37°C for 3 h. The film sample was transferred in a solution of gelatine (1% in DMSO) and stirred for another 3 h at 37 °C. The film sample was washed successively 4x with warm H_2O (37 °C, each 10 min) and then ethanol.

Mineralization (in the following called "PEEK-$CaPO_4$"): A PEEK-gelatine film was immersed in a solution of 20 mL HEPES-buffer (10 mM, pH 7.4), containing $CaCl_2$ (2.7

mM), K_2HPO_4 (1.35 mM) in the presence of poly aspartic acid (10 µg/ml, molecular weight 3800 g/mol) at 37 °C for 4 d. After 4 d, the film was washed H_2O.

2. X-Ray photoelectron spectroscopy

The XPS spectra were obtained with a PHI Quantera SXM equipped with an aluminum anode (15 kV, 1486.6 eV) and a quartz monochromator with the help of Dr. Philipp Erler at the University of Konstanz. The pressures in the measurement-chambers were about $2.5x10^{-6}$ Pa. The direction of the photoelectron collection made angles of 45 ° normal to the sample and the incident X-ray beam. The analysis area was a spot of about 200 µm in diameter. The information depth was estimated to be about 5-10 nm with a detection limit about 0.1-0.5 atom-%. To compensate for charging effects, the binding energies of the Mo_{1S} component of the sample holder was used as a reference. The spectra were analyzed using the CasaXPS software package.

3. Grazing Incidence X-Ray diffraction

The phase composition of the surface coating was determined by giXRD analysis. The data were collected at room temperature with a Bruker D8 Discover with Cu-Kα radiation equipped with a VÅNTEC-500 2D detector at an incidence angle of 1.5°.

4. Thermogravimetric analysis

Thermogravimetric analyses (TGA) were performed using a Netzsch simultaneous thermal analyzer 449 F3 Jupiter. The sample weights were always about 10 mg. The heating rate was kept at 10 K/min under oxygen atmosphere using aluminum oxide crucibles. Decomposition steps were analyzed using the Netzsch Proteus 6.1 software package.

5. Contact angle and surface free energy

Contact angle measurements were performed on an automated Krüss Advance Drop Shape Analysis system. The surface free energy with polar and disperse fractions was determined by these optical contact angle measurements with water and diiodomethane. All measurements were performed at room temperature without any pretreatment of the samples. For each sample, at least 20 measurements were performed and averaged for one drop. Water drop volume was 2 µl, and diiodo-methane drop volume was 0.8 µl. The disperse and polar fractions were calculated by the Advance evaluation software package according to Owens, Wendt, Rabel, and Kaelble.[391, 392]

6. Mechanical stability test

The scotch tape adhesion test was performed on all modified PEEK samples. For this, a scotch tape was placed on the PEEK surface and was smoothed to ensure

good contact with the tape and surface. Within 30 s of application, the tape was removed in a single, fast motion.

7. General cell culture and assay conditions

NIH3T3 mouse fibroblasts were cultured in 7.5 cm^2 culture dishes in Dulbecco's Modified Eagle Medium (DMEM) with 10% fetal calf serum (FCS) and 1% penicillin/streptavidin at 37°C and 5.0% CO_2. Culture medium was changed every two days, and subconfluency of cells and normal morphology was verified.

The MC3T3-E1 osteoblast cells were cultured in 7.5 cm^2 culture dishes in Minimum Essential Medium Eagle (Alpha Modification; α-MEM), supplemented with 5% FCS, 4.5 g/L glucose, 0.1% gentamicin, at 37°C and 5.0% CO_2. Culture medium was changed every two days. For the assays, α-MEM, supplemented with 10% FCS 4.5 g/L glucose, 0.1% gentamicin, 0.1% ascorbic acid was used.

All PEEK-test samples were cut into discs with 1.2 mm and were sterilized either by autoclavation or incubation in 70% EtOH (in H_2O) and dried with an open lid under a sterile hood. All assays were performed in 24-well plates. All growth and incubation periods were unless otherwise stated, performed in a humidified air atmosphere with 5.0% CO_2 at 37 °C. Unless otherwise stated, all tests were performed in three technical replicates.

8. Toxicity assay

Indirect toxicity: The indirect toxicity assays were performed by Tamara Schuhmacher in the group of Prof. Hauck at the University of Konstanz. Dead cells were detected using a propidium iodide (PI) flow cytometric assay. PI is a DNA intercalating agent. As PI cannot cross the cell membrane of living cells, it is often used to stain dead cells in different assays. PEEK and PEEK-CaP slips were washed with acetone, dried and placed in 24 well plates. The slips were subsequently sterilized with 70% ethanol and dried with an open lid under a sterile hood. The assay was performed in technical triplicates. The different PEEK materials were incubated for 1 day at 37°C and 5% CO_2 in α-MEM medium. The next day, cells were seeded into the wells in 24 well plates and incubated with 1 mL of the extract for 2 days at 37°C and 5% CO_2. The supernatant was collected from single wells and transferred into a test tube. The adherent cells were then washed twice with PBS and detached from the surface using trypsin/EDTA mixture. The detachment reaction was stopped using medium containing serum. The detached cells were also transferred into the corresponding test tubes. They were centrifuged at 800 rpm for 5 min. The supernatant was discarded, and cells were taken up in 1 mL PBS +2% FCS +10 µg/mL PI (in PBS) and transferred into a FACS measurement tube. Heatshock treated cells (incubation at 65-70°C for 10-15 minutes) were used as a positive control. The measure-

ment was performed using a BD LSR II FACS using the DiVa software (BD Bioscience) and analyzed with FlowJo software.

Direct toxicity: The toxicity assays were performed by Tamara Schuhmacher in the group of Prof. Hauck at the University of Konstanz. Dead cells were detected using a propidium iodide (PI) flow cytometric assay. PEEK and PEEK-CaP slips were washed with acetone, dried and placed in 24 well plates. The slips were subsequently sterilized with 70% ethanol and dried with an open lid under a sterile hood. The assay was performed in technical triplicates. Cells were seeded into each well in 24 well plates and incubated for 2 days at 37°C and 5% CO_2. The supernatant was collected from the single wells and transferred into a test tube. The adherent cells were then washed twice with PBS and detached from the surface using trypsin/EDTA mixture. The detachment reaction was stopped using medium containing serum. The detached cells were then also transferred into the corresponding test tubes. They were centrifuged at 800 rpm for 5 min. The supernatant was discarded and cells were taken up in 1 mL PBS +2% FCS +10 µg/mL PI (in PBS) and transferred into a FACS measurement tube. Heatshock treated cells (incubation at 65-70°C for 10-15 minutes) were used as a positive control. The measurement was performed using a BD LSR II flow cytometer using the DiVa software (BD Bioscience) and analyzed with FlowJo software.

9. Viability assay

Viability was determined by a 3-(4,5-dimethyl-2-thiazolyl)-2,5-diphenyl-2H-tetrazolium bromide (MTT) assay. Viable cells with an active metabolism are able to convert the MTT into purple colored formazan crystals, which precipitate inside the cells. These crystals can be extracted from the cells and the absorbance measured with a spectrophotometer. The MTT reduction inside the cells thus measures some aspect of general metabolism or an enzymatic activity as a marker for viable cells. After incubation with the test samples, the cell cultures were incubated with a 5 mg/mL MTT solution in PBS for 1-2 h and extracted with isopropanol over night at room temperature. The OD was analyzed at 540 nm with a Thermo Scientific Varioskan Flashspectral photometer. Cell culture medium without cells was used as a negative control, and cell culture wells with no PEEK-test samples were used as positive control.

10. Attachment assay

The cells were incubated on the respective PEEK-samples for 6 h in α-MEM. After incubation, the cell culture medium was removed, and the samples were carefully rinsed once with PBS. The remaining cells were detached by trypsination, spun down at 300 rpm and resuspended in fresh cell culture medium. The cell concentration was determined using a counting chamber.

11. Proliferation assay

The cells were incubated on the respective PEEK-samples for the respective time in supplemented α-MEM. After incubation, the cell culture medium was removed, and the samples were carefully rinsed once with PBS. The remaining cells were detached by trypsination, spun down at 300 rpm and resuspended in fresh cell culture medium. The cell concentration was determined using an Innovatis Casy® Cell Counter. Herein, the proliferation assays of the MC3T3-E1 osteoblast cells were performed by Tamara Schuhmacher in the group of Prof. Hauck at the University of Konstanz.

12. Cell morphology

Cells were grown on the different PEEK-samples for 18 h. The samples were then washed three times with PBS. Fixation was performed in a three-step way in a 2% glutaraldehyde solution (in 0.1 M Na-cacodylate buffer, supplemented with 0.01 M $CaCl_2$ and 0.01 M $MgCl_2$, pH 7) at room temperature. The fixation solution was changed after 10 min, 20 min, and 1 h, respectively. Afterwards the samples were washed three times with PBS. In preparation for critical point drying, the samples were incubated in a graded series of aqueous ethanol solutions (30%, 50%, 70%, 80%, 90%, 96%, and 100%) for 15 min and again two times in 100% ethanol for 30 min each. Critical point drying was performed with a CPD 030 (BAL-TEC AG, Balzers, FL). The samples were coated with a 3 nm platinum layer. SEM investigations were performed with a ZEISS Auriga TM Crossbeam Workstation and ZEISS CrossBeam 1540XB, both operated in a high vacuum using variable acceleration voltages. Herein, the SEM investigations of the NIH3T3 fibroblasts were performed by Dr. Liangfei Tian at the University of Konstanz.

13. Statistics

All data are presented as mean ± S.D. (standard deviation) for n = 3, unless stated otherwise. Statistical analyses were performed by t-test as indicated in the text. Differences were considered statistically significant for $p < 0.05$.

Appendix A

Chapter II Comparative Investigation of Composition-Structure-Properties Relationships of Teeth of Cichlids

2.1 *Astatoreochromis alluaudi*

2.1.2. Chemical composition and distribution

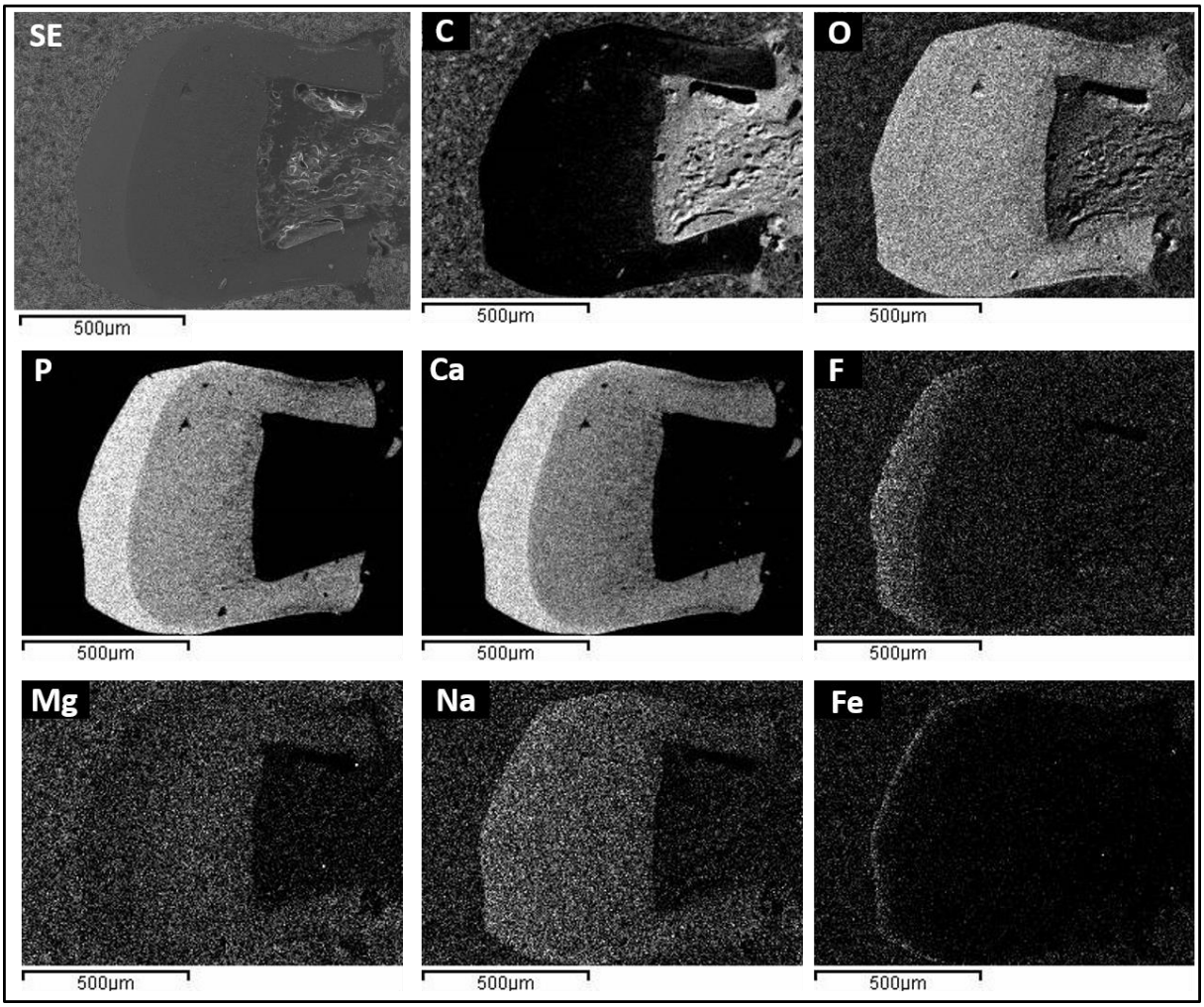

Figure S 1: Secondary electron image (SE) and EDX elemental mappings of the major elemental components of a tooth cross-section of *A. alluaudi.*

Table S 1: Raman vibration modes observed for the polished cross-section of *A. alluaudi* and their assignments.

Vibration mode	Raman position [rel. cm^{-1}]
$[PO_4]^{3-}$ v_1	963
$[PO_4]^{3-}$ v_2	430
$[PO_4]^{3-}$ v_3	1042
$[PO_4]^{3-}$ v_4	589
$[HPO_4]^{2-}$	1003
amide I	1660
amide II	1262
C-H (bending)	1448
B-type $[CO_3]^{2-}$ v_1	1070

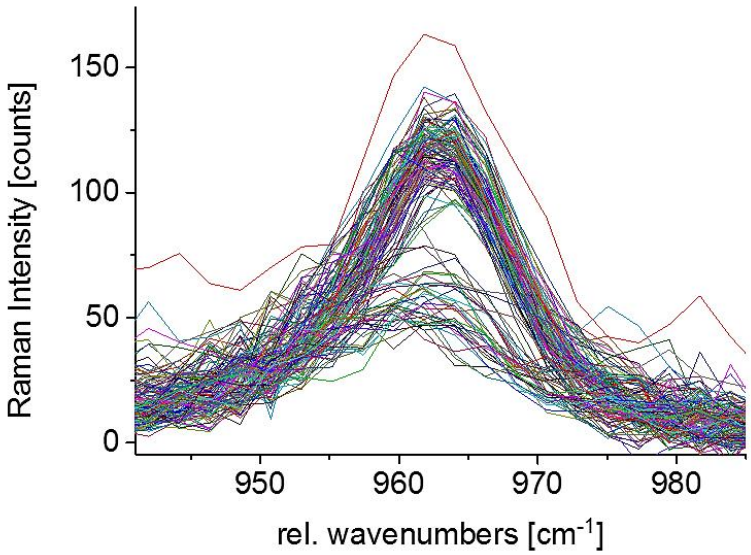

Figure S 2: All collected Raman spectra of the phosphate v_1 band of an axial cross-section of a tooth of *A. alluaudi*.

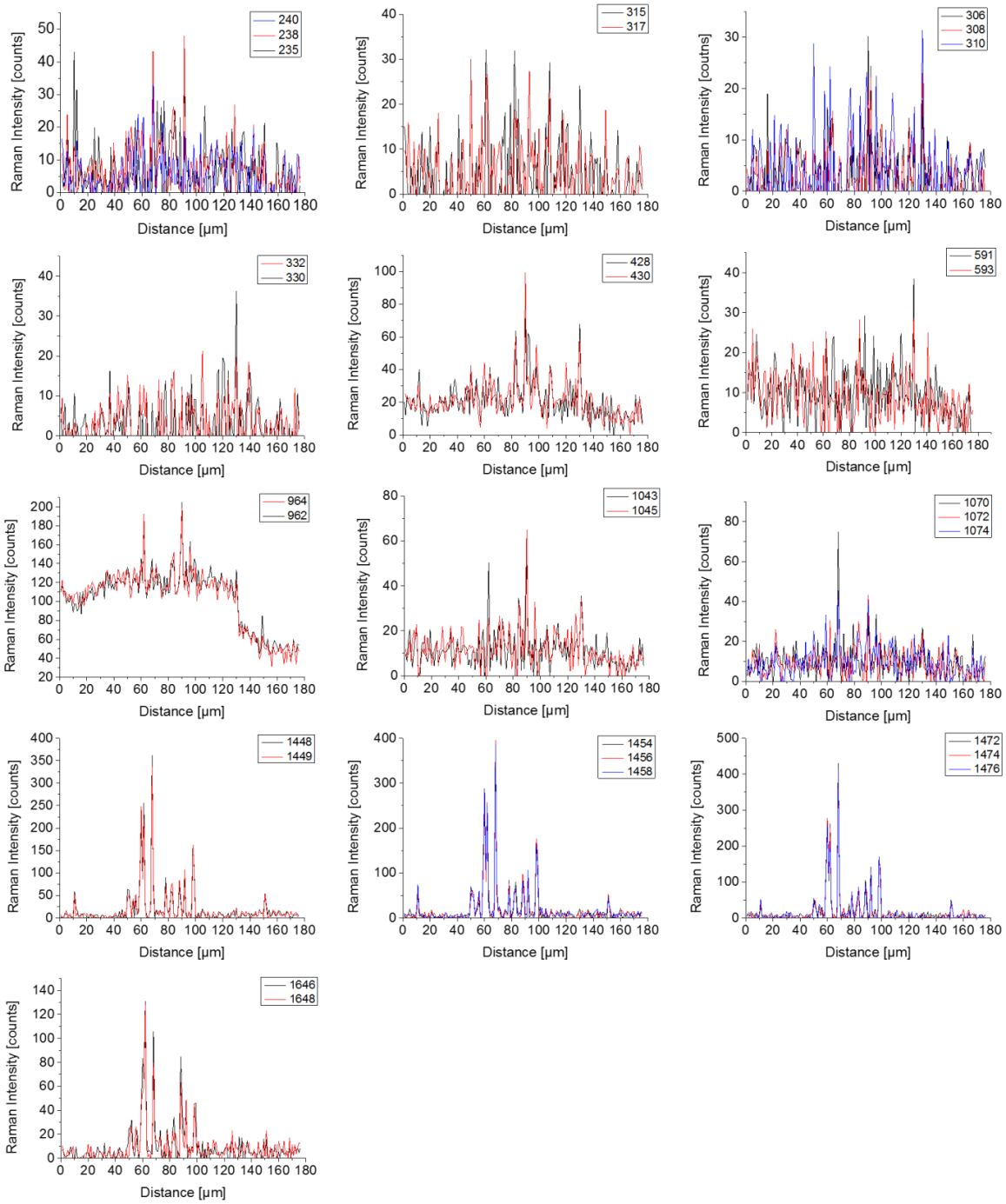

Figure S 3: Raman-line scans of characteristic band positions along the length of a polished axial cross-section of *A. alluaudi.*

Table S 2: IR vibration modes observed for a powdered tooth sample of *A. alluaudi* and their assignments.

Vibration mode	wavenumbers [cm^{-1}]
$[PO_4]^{3-}$ v_1	962
$[PO_4]^{3-}$ v_3	1090 1162
amide I	1644
amide II	1549
amide III	1238
amide A, B	3070-3300
C-H	2854 2924 2959
B-type $[CO_3]^{2-}$ v_2	875
B-type $[CO_3]^{2-}$ v_3	1416 1457
B-type $[CO_3]^{2-}$ v_4	720
NA	1013
NA	1739

NA= not assigned

2.1.3 Ultrastructure of the tooth

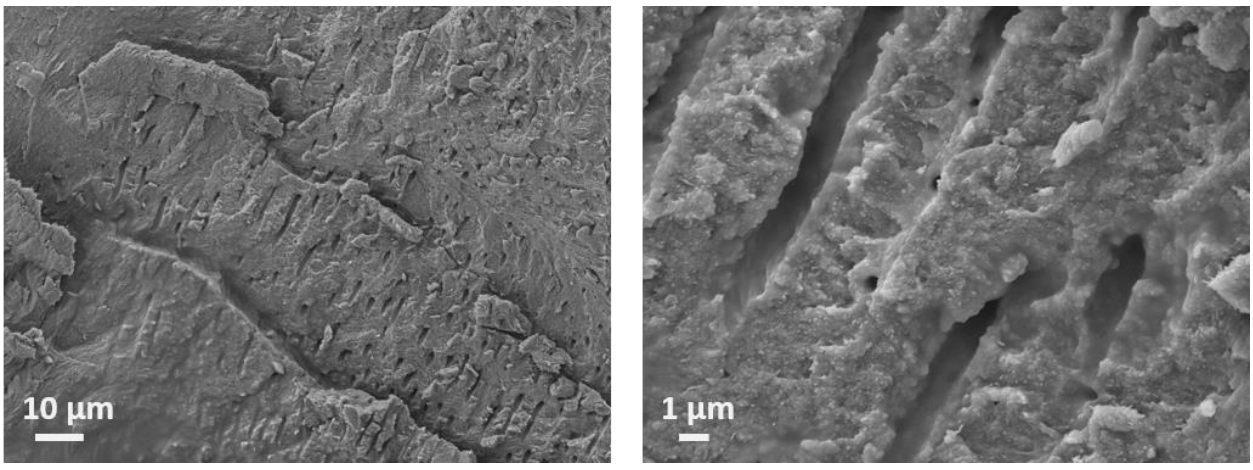

Figure S 4: Scanning electron micrographs of fractured areas of the dentinal tubule area with an approximately axial view on a tooth of *A. alluaudi*.

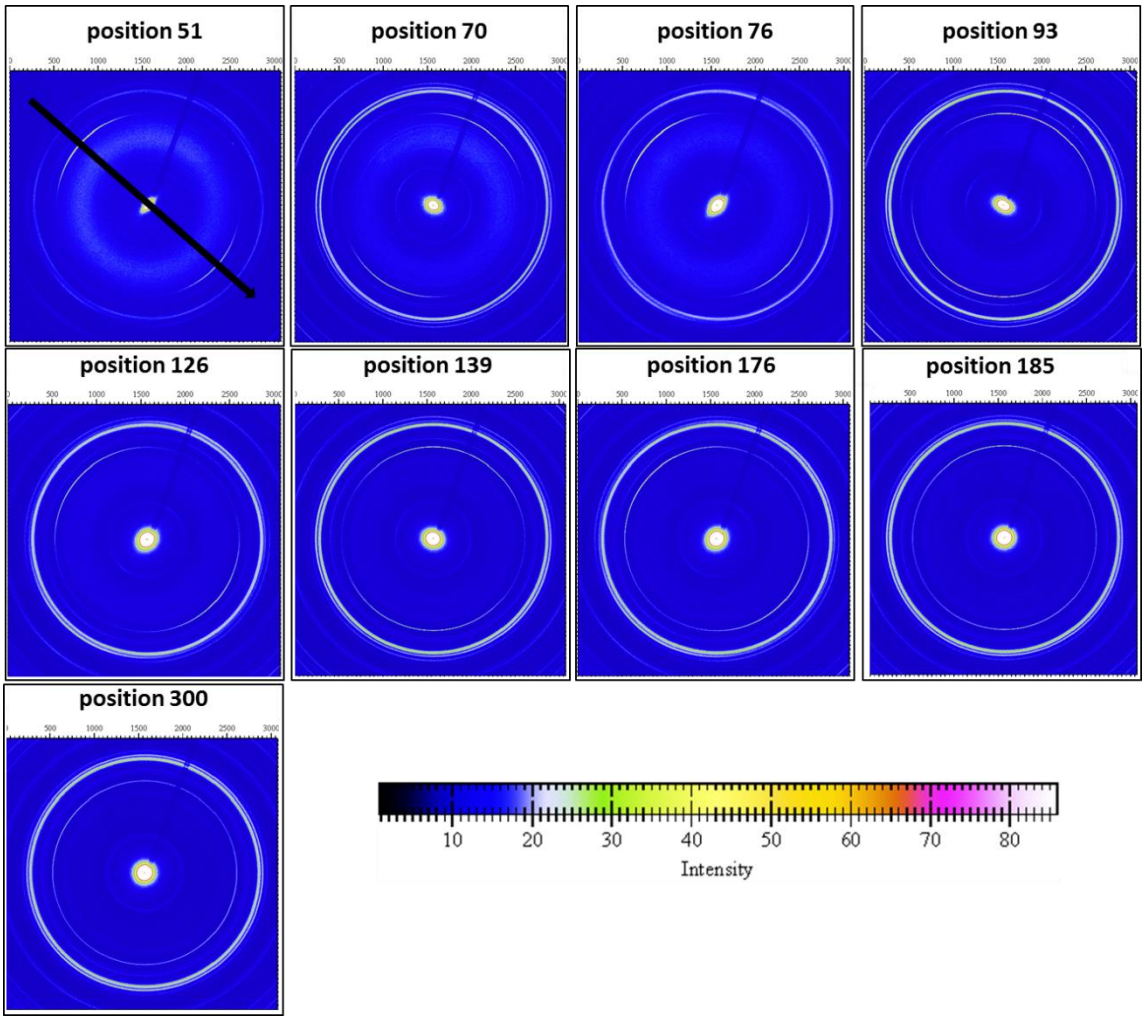

Figure S 5: 2D WAXS/SAXS signals for selected positions (as indicated in the whole map in Figure 18, C) of a transverse cross-section of a tooth of *A. alluaudi*

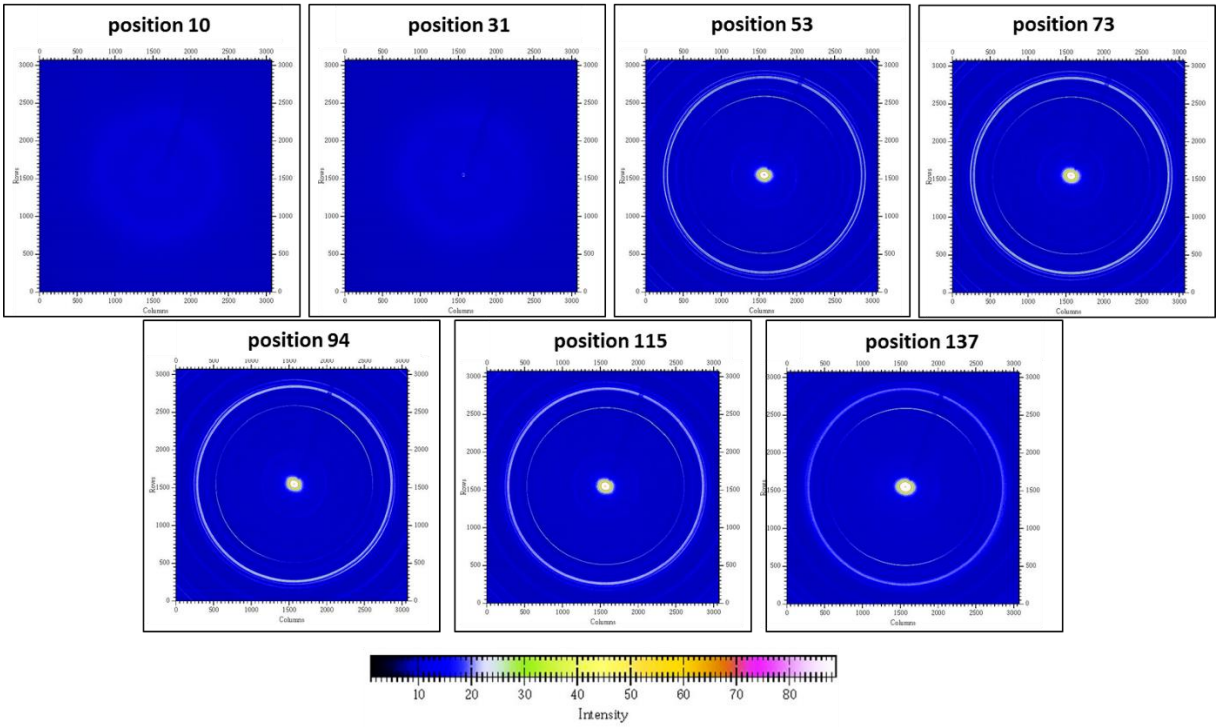

Figure S 6: 2D WAXS/SAXS signals for selected positions (as indicated in the whole map in Figure 21, D)) of an axial cross-section of a tooth of *A. alluaudi.*

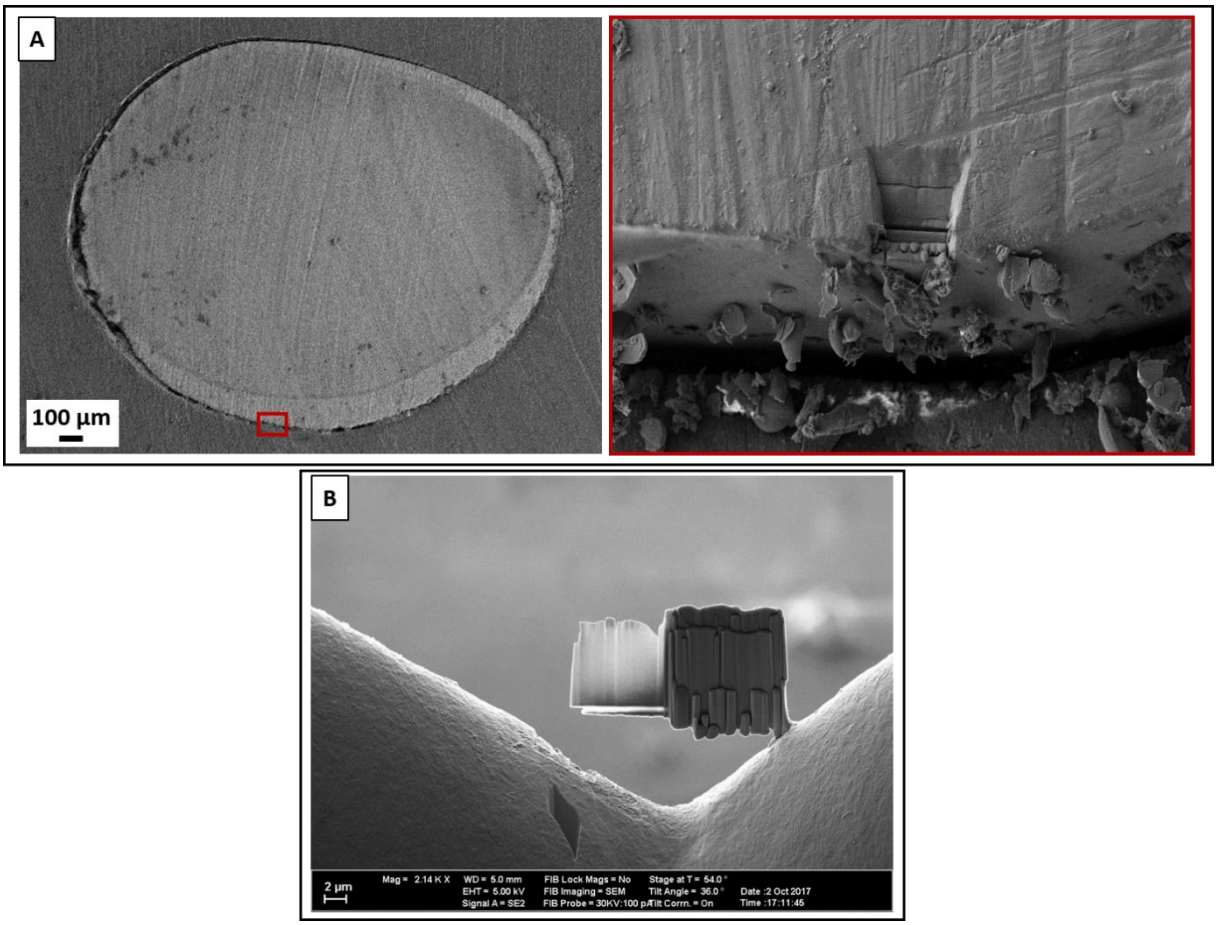

Figure S 7: A: SEM micrograph of the axial polished tooth sample, which was used for the µbeam WAXS/SAXS investigation indicating the location of the FIB milling. B: Respective ultrathin FIB-cut of the tooth sample.

2.2.1 *Haplochromis ishmaeli*

2.2.1.2 Chemical composition and distribution

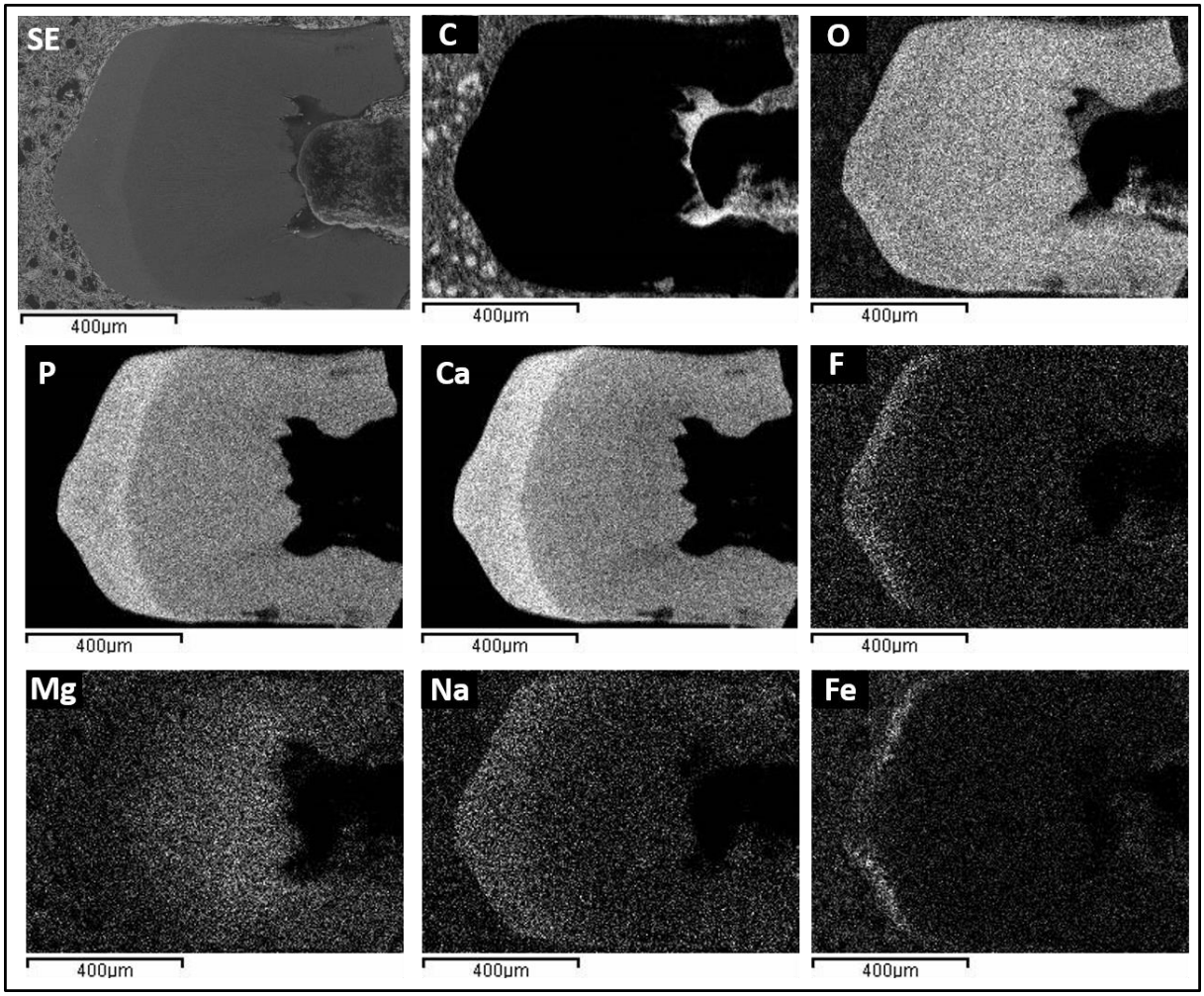

Figure S 8: Secondary electron image (SE) and EDX elemental mappings of the major elemental components of a tooth cross-section of *H. ishmaeli.*

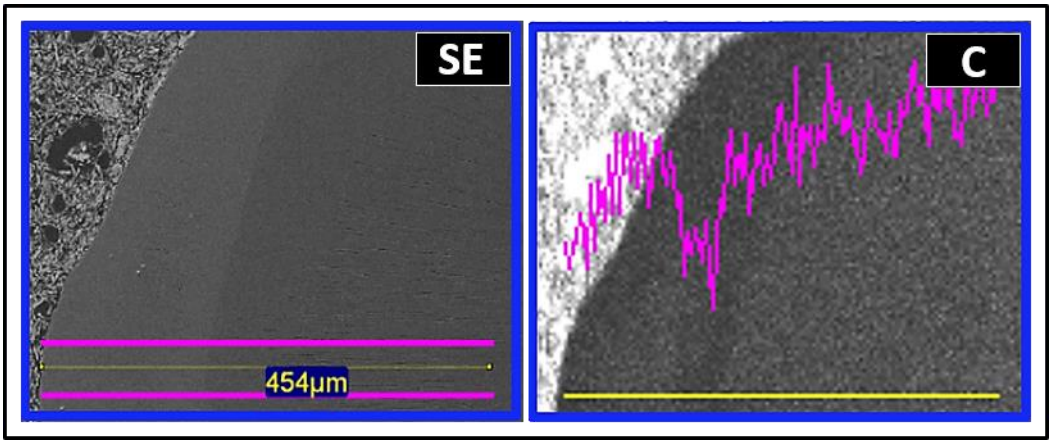

Figure S 9: SEM image and EDX carbon line scan on the polished cross-section of a tooth of *H ishmaeli.*

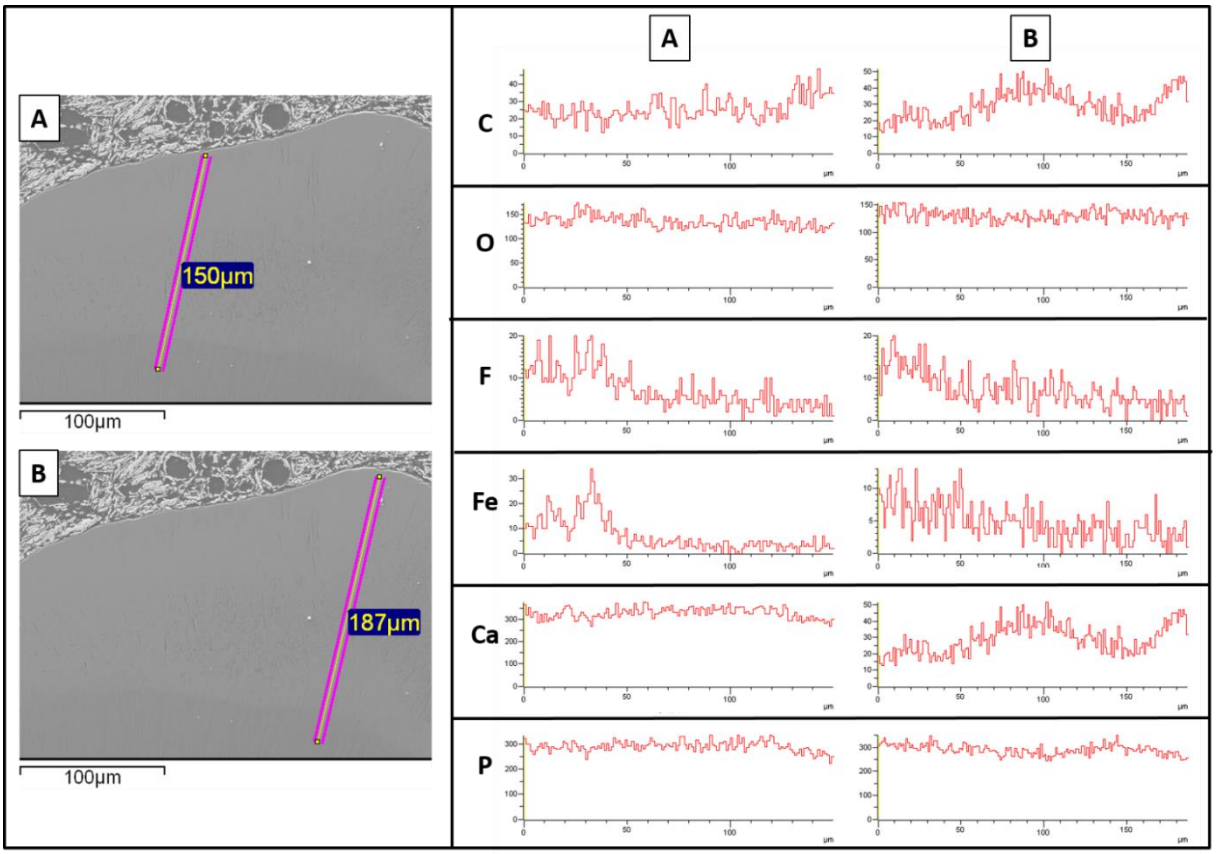

Figure S 10: EDXS-line scans of a polished axial cross-section of *H. ishmaeli.* Comparison of the elemental composition in an area on the left side of the sample (A) and the area of the performed nanoindentation measurements (B).

Table S 3: Raman vibration modes observed for the polished cross-section of a central tooth of *H. ishmaeli* and their assignments.

Vibration mode	Raman position [rel. cm^{-1}]
$[PO_4]^{3-}$ v_1	961
$[PO_4]^{3-}$ v_2	423
$[PO_4]^{3-}$ v_3	1042
$[PO_4]^{3-}$ v_4	592
$[HPO_4]^{2-}$	1004
amide I	1659
$[CO_3]^{2-}$	1049
C-H (bending)	1438

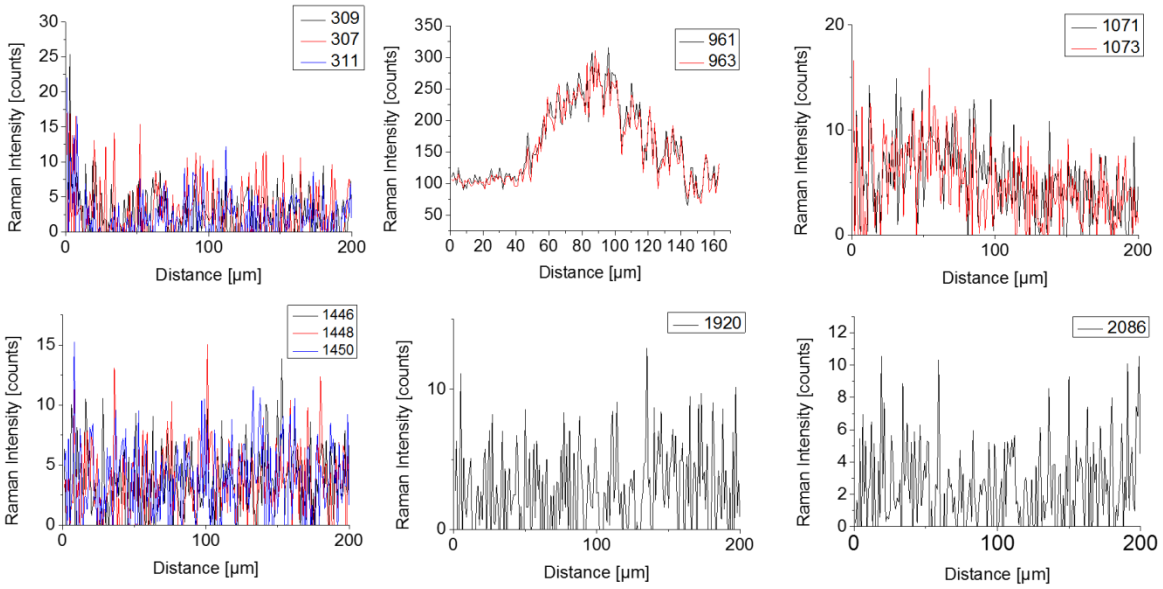

Figure S 11: Raman-line scans of characteristic band positions along the length of a polished axial cross-section of *H.ismaeli.*

Table S 4: IR vibration modes observed for the tooth sample of *H. ishmaeli* and their assignments.

Vibration mode	wavenumbers [cm^{-1}]
$[PO_4]^{3-}$ v_1	963
$[PO_4]^{3}$ v_3	1092 1155
amide I	1643
amide II	1549
amide III	1238
amide A, B	3070-3300
C-H	2855 2925 2961
B-type $[CO_3]^{2-}$ v_2	873
B-type $[CO_3]^{2-}$ v_3	1415 1452
B-type $[CO_3]^{2-}$ v_4	714
NA	1005
NA	1737

NA = not assigned

2.2.1.3 Ultrastructure of the tooth

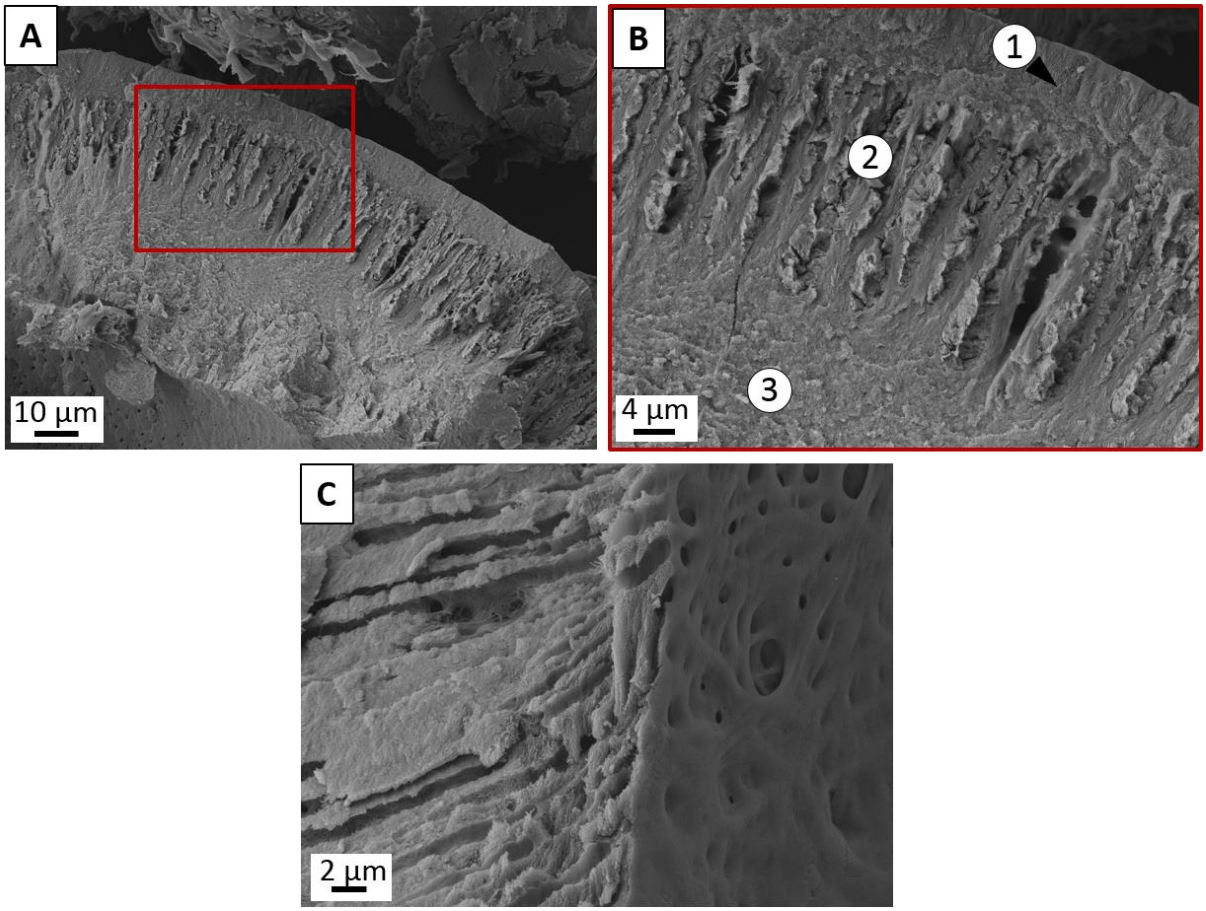

Figure S 12: Scanning electron micrographs of fracture areas of an enameloid cross-section (A), an enlarged area within the enameloid as indicated in A (B) and the dentinal tubule area (B) of teeth of *H. ishmaeli.* Markings (1)-(3) indicate the different structural layers as described in the text in chapter 3.2.1.2.

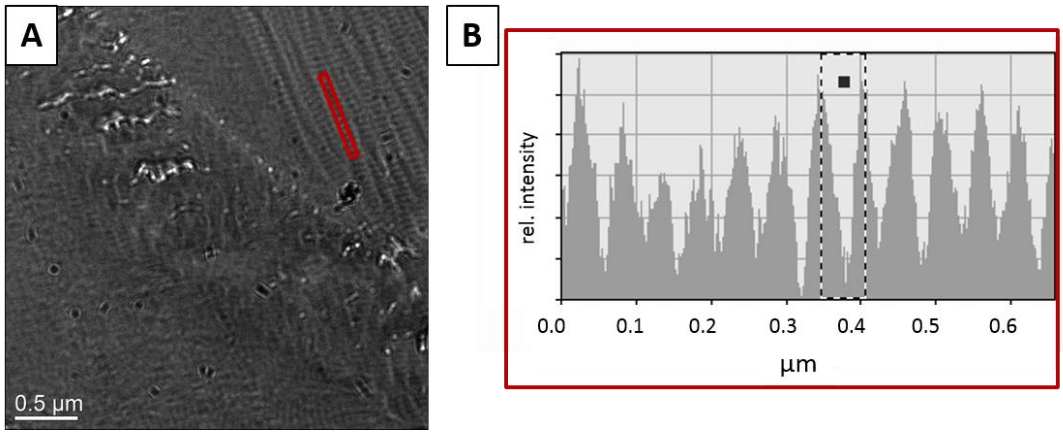

Figure S 13: TEM image of a partially demineralized microtome cut of a tooth of *H. ishmaeli,* displaying mineralized collagen bundles, with the typical collagen fiber cross-striation (A) and an image contrast intensity profile of the area as marked in A along the length of a collagen fiber (B).

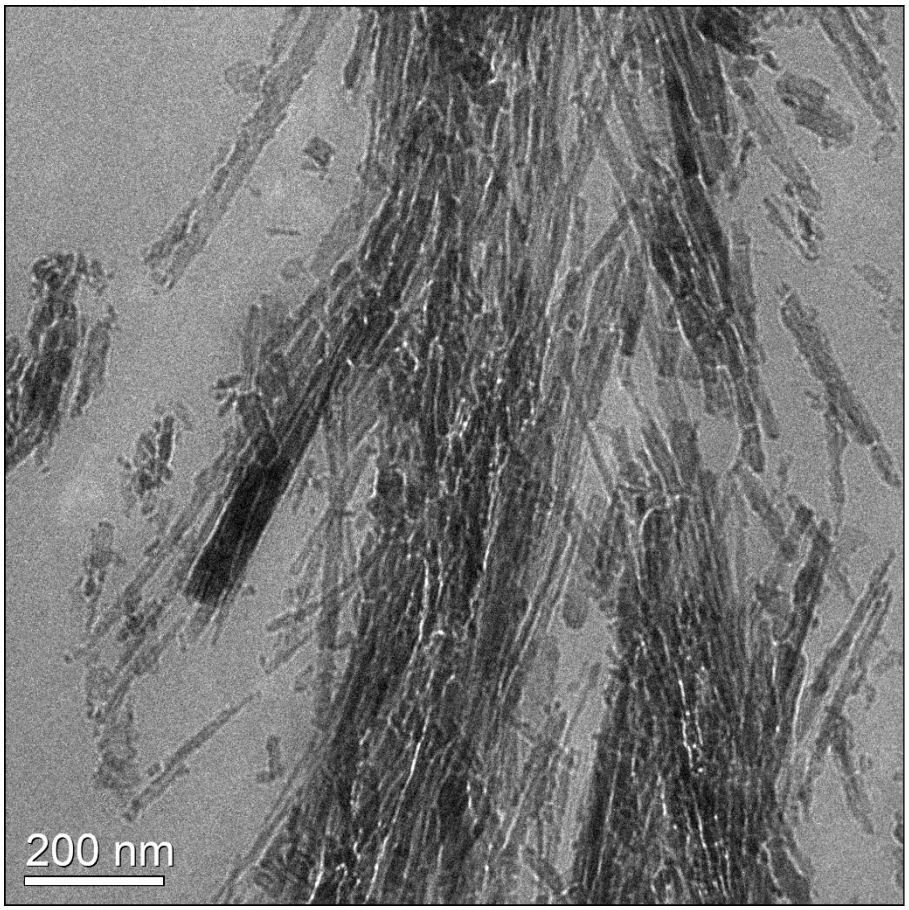

Figure S 14: TEM image of a partially demineralized microtome cut of a tooth of *H. ishmaeli*, highlighting the elongated bundles of crystallites inside the tooth structure.

2.2.1.4 Mechanical properties

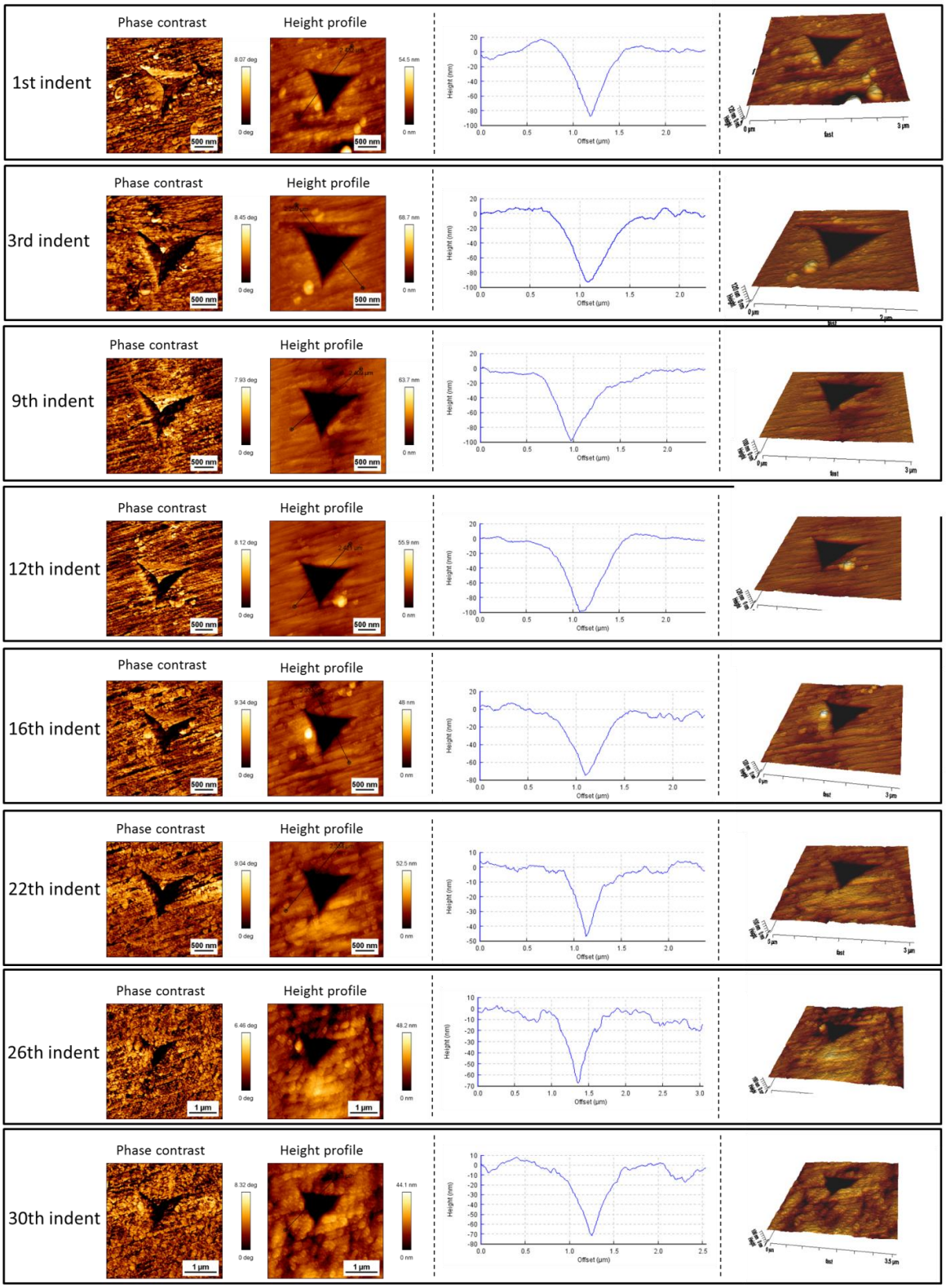

Figure S 15: AFM images (phase contrast and height topography) of selected indents the axial cross-section of a tooth of *H. ishmaeli* along the length of the sample, with indent cross-section profiles and 3D visualization.

2.2.2 *Haplochromis sauvagei*

2.2.2.2 Chemical composition and distribution

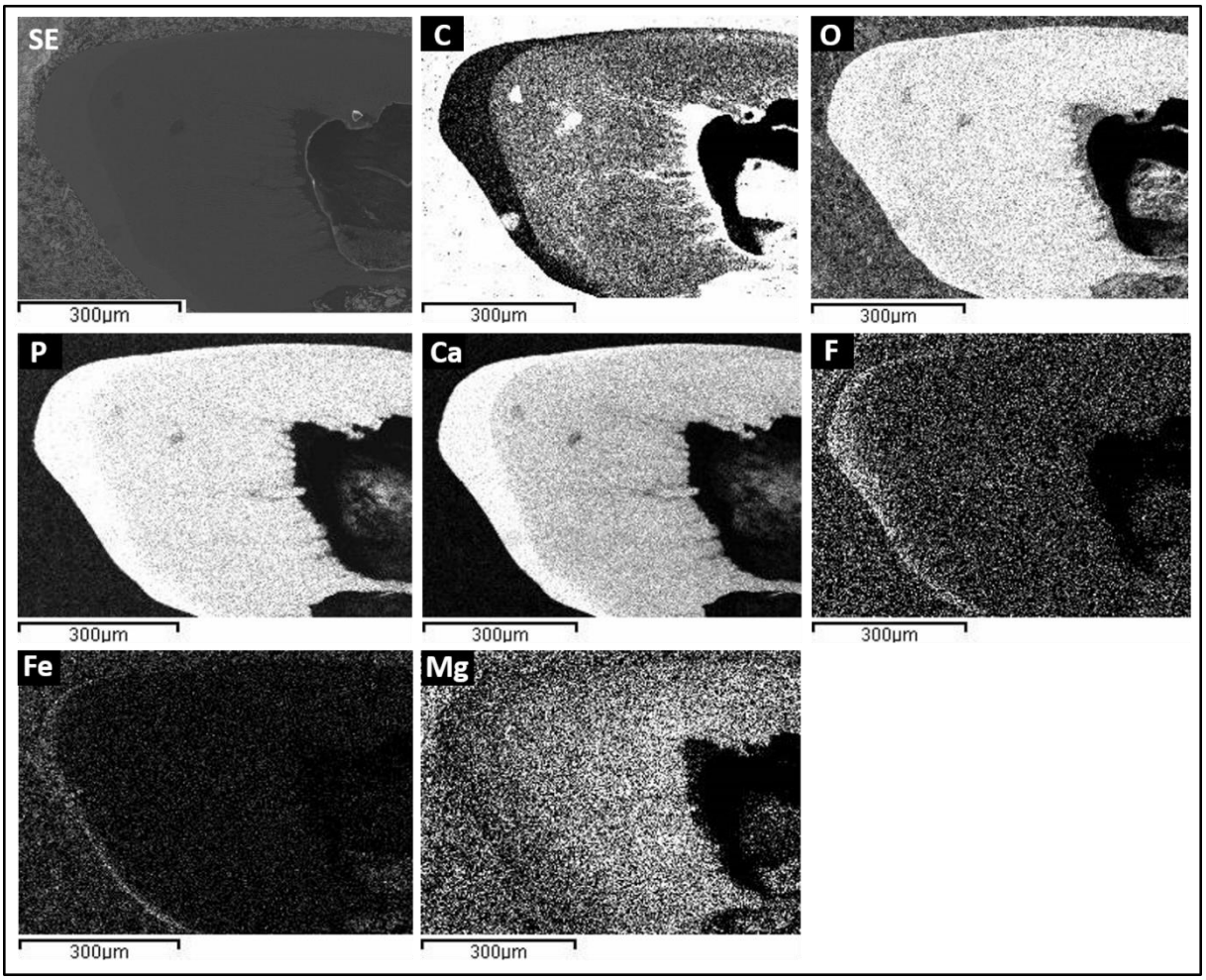

Figure S 16: Secondary electron image (SE) and EDX elemental mappings of the major elemental components of a tooth cross-section of *H sauvagei.*

Table S 5: Raman vibration modes observed for the polished cross-section of a central tooth of *H. sauvagei* and their assignments.

Vibration mode	Raman position [rel. cm^{-1}]
$[PO_4]^{3-}$ v_1	962
$[PO_4]^{3-}$ v_2	430
$[PO_4]^{3-}$ v_3	1045
$[PO_4]^{3-}$ v_4	589
$[HPO_4]^{2-}$	862
amide II	1589
$[CO_3]^{2-}$	1070
C-H (bending)	1453

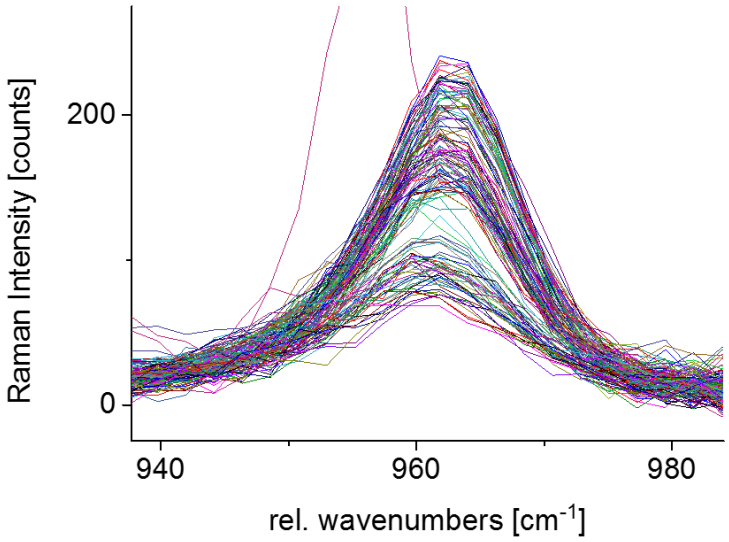

Figure S 17: All collected Raman spectra of the phosphate v_1 band of an axial cross-section of a tooth of *H. sauvagei*.

Table S 6: IR vibration modes observed for a powdered tooth sample of *H. sauvagei* and their assignments.

Vibration mode	wavenumbers [cm^{-1}]
$[PO_4]^{3-}$ v_1	963
$[PO_4]^{3-}$ v_3	1093 1155
amide I	1642
amide II	1544
amide III	1238
amide A, B	3070-3300
C-H	2856 2926 2964
B-type $[CO_3]^{2-}$ v_2	871
$[CO_3]^{2-}$ v_3	1415 1452
B-type $[CO_3]^{2-}$ v_4	714
NA	1012
NA	1738

NA = not assigned

2.2.3 *Haplochromis chilotes*

2.2.3.2 Chemical composition and distribution

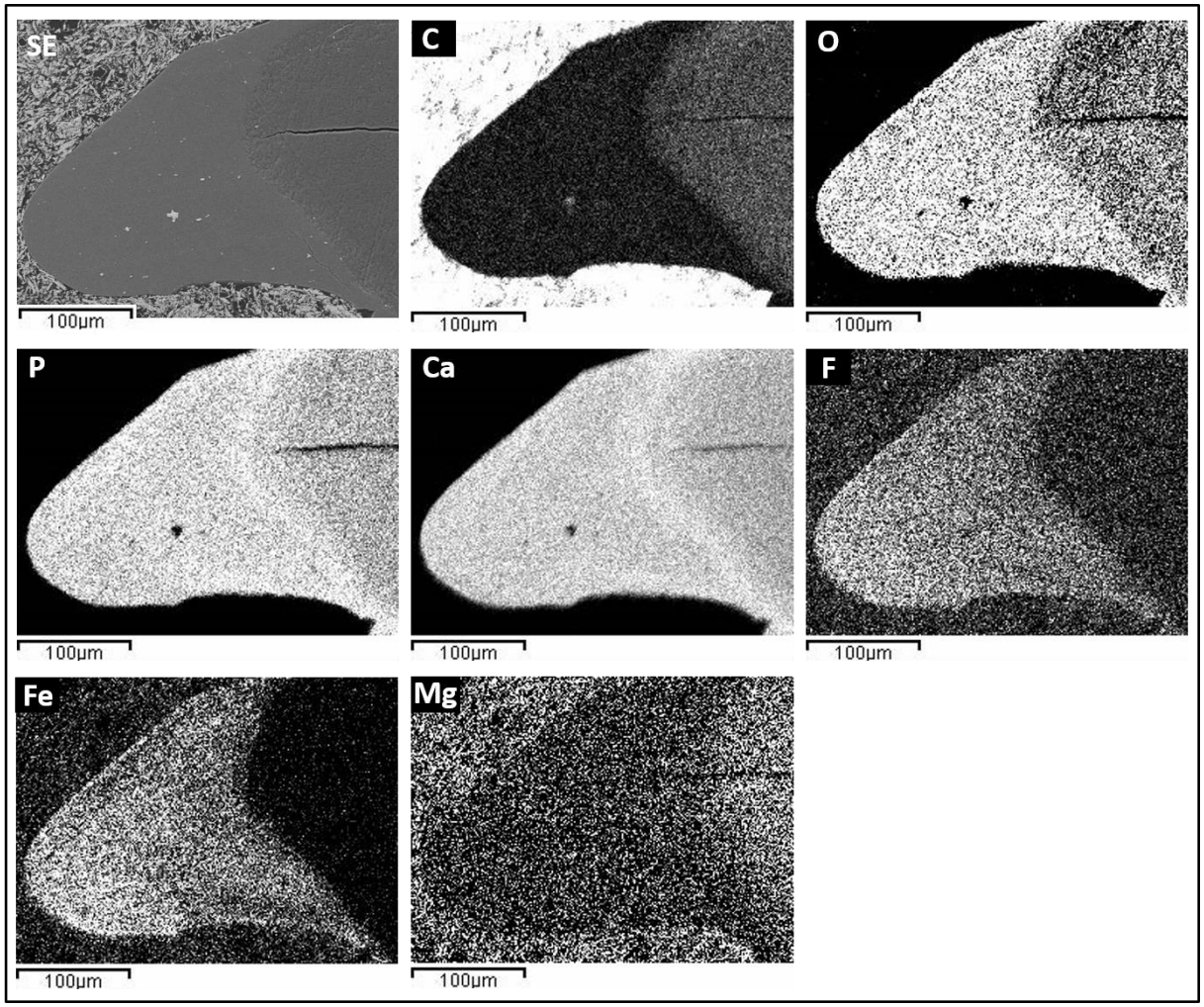

Figure S 18: Secondary electron image (SE) and EDX elemental mappings of the major elemental components of a tooth cross-section of *H chilotes.*

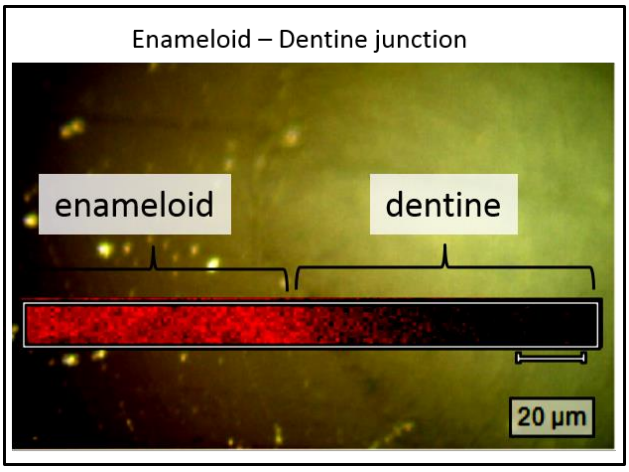

Figure S 19: Light microscopic image of a polished cross-section of a tooth of *H. chilotes* in the enameloid-dentine junction. The square indicates the area for the Raman-measurements.

Table S 7: Raman vibration modes observed for the polished cross-section of a central tooth of *H. chilotes* and their assignments.

Vibration mode	Raman position [rel. cm^{-1}]
$[PO_4]^{3-}$ v_1	961
$[PO_4]^{3-}$ v_2	420
$[PO_4]^{3-}$ v_3	1045
$[PO_4]^{3-}$ v_4	590
$[HPO_4]^{2-}$	1004
amide II	1262
C-H (bending)	1455

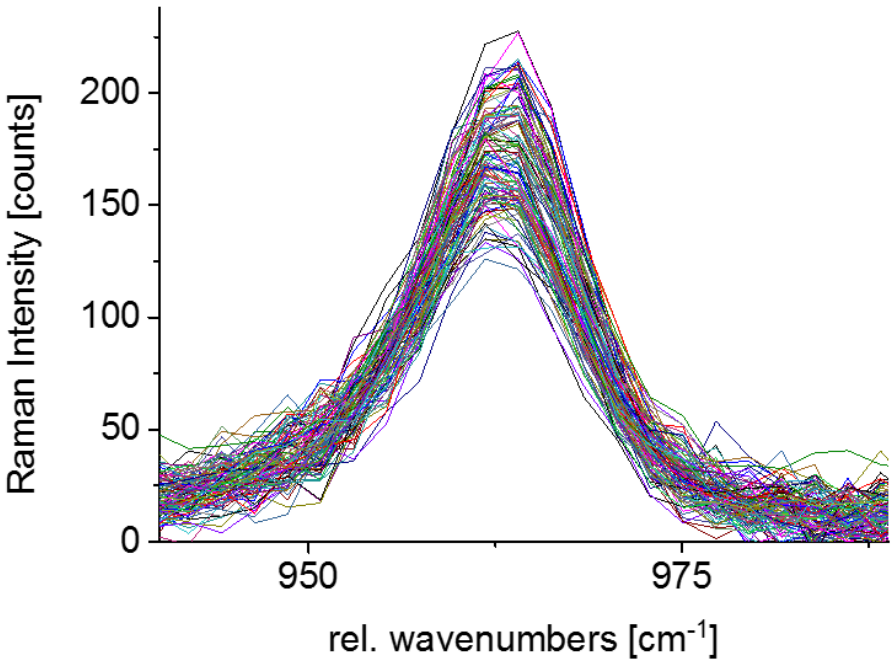

Figure S 20: All collected Raman spectra of the phosphate v_1 band of an axial cross-section of a tooth of *H. chilotes.*

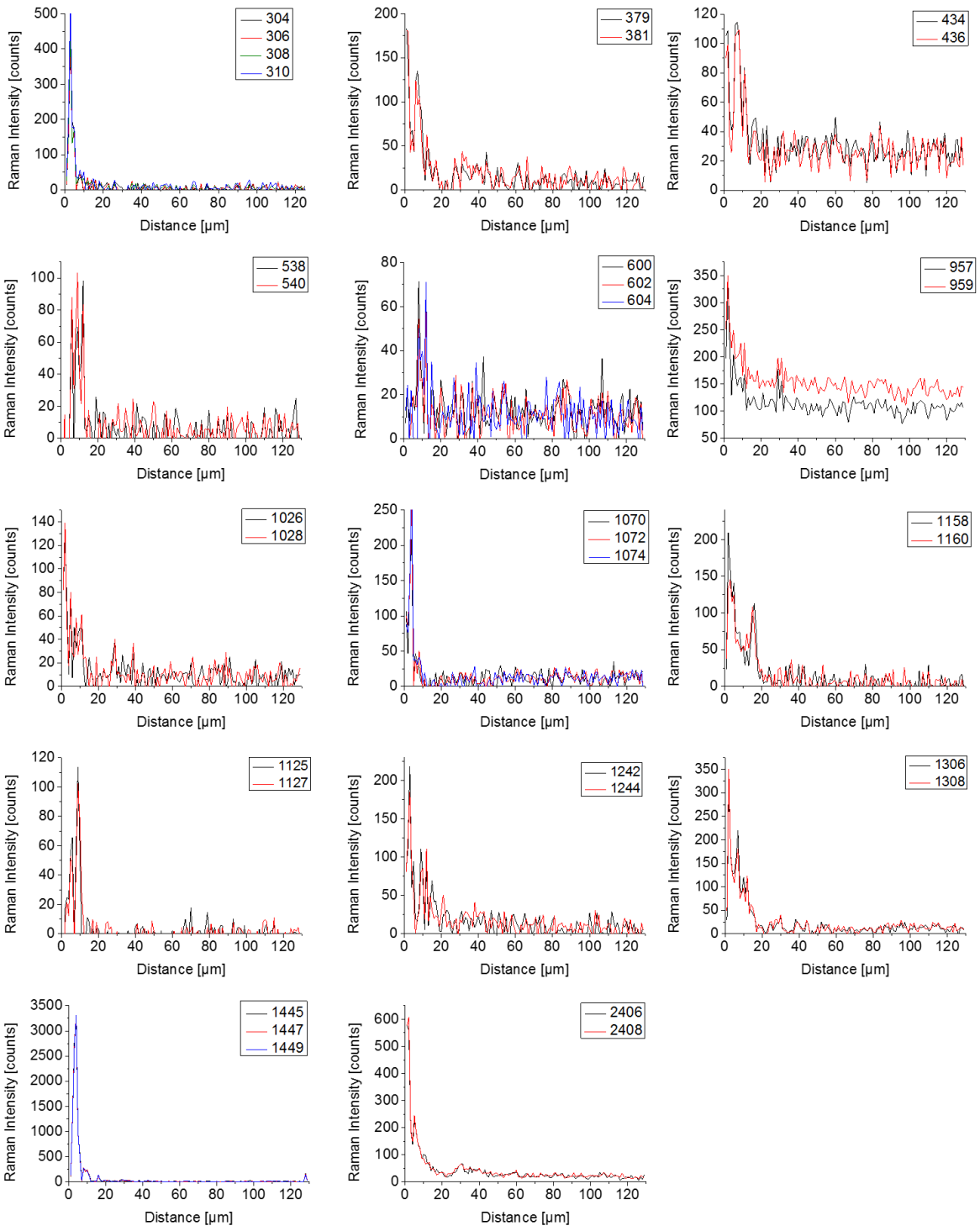

Figure S 21: Raman-line scans of characteristic band positions along the length of a polished axial cross-section of *H. chilotes.*

Table S 8: IR vibration modes observed for a powdered tooth sample of *H. chilotes* and their assignments.

Vibration mode	wavenumbers [cm^{-1}]
$[PO_4]^{3-}$ v_1	963
$[PO_4]^{3-}$ v_3	1093 1155
amide I	1646
amide II	1542
amide III	1240
amide A, B	3070-3300
C-H	2854 2924 2962
B-type $[CO_3]^{2-}$ v_2	874
B-type $[CO_3]^{2-}$ v_3	1413 1456
B-type $[CO_3]^{2-}$ v_4	702
NA	1740

NA = not assigned

2.2.4 *Haplochromis nyererei*

2.2.4.2 Chemical composition and distribution

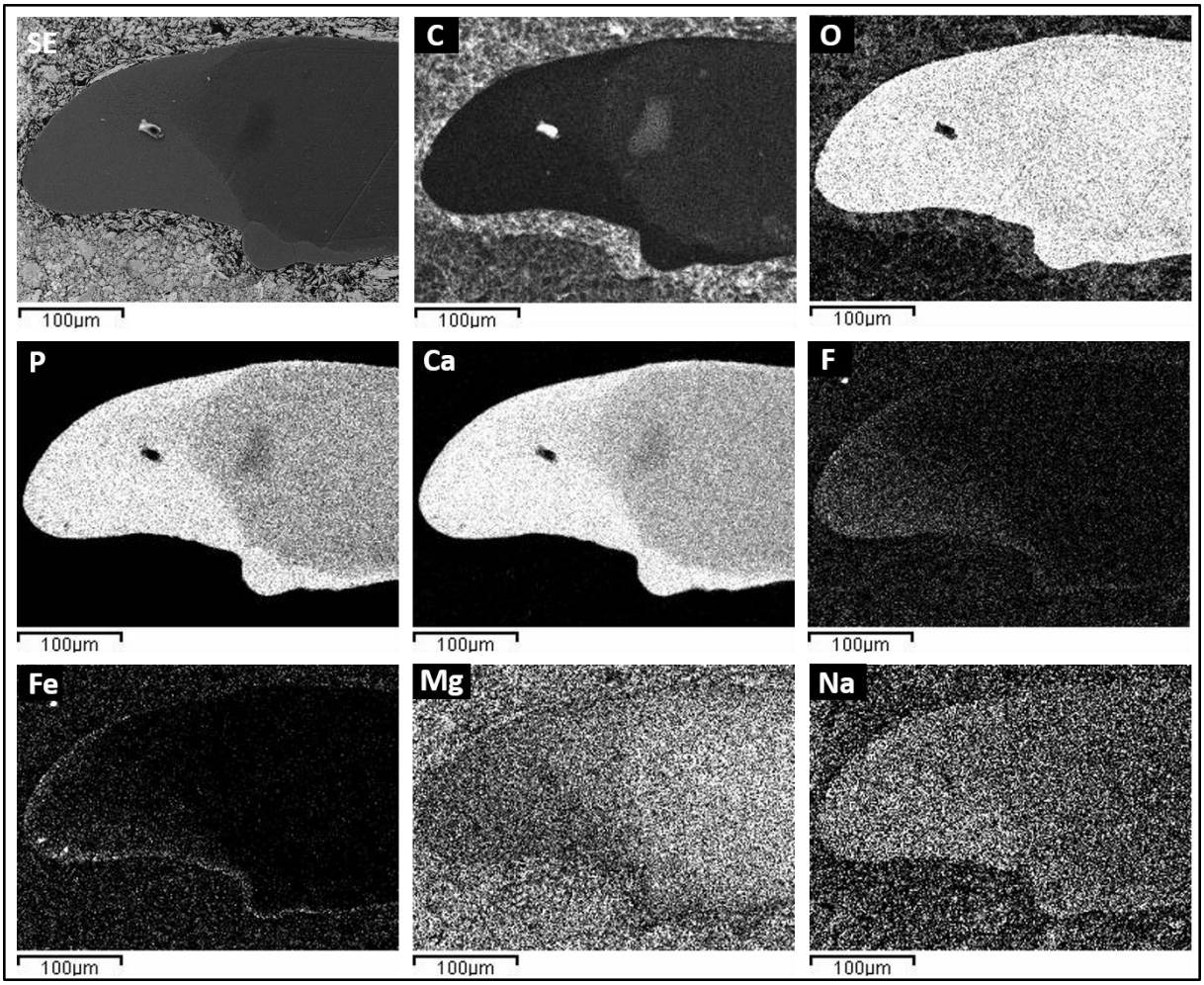

Figure S 22: Secondary electron image (SE) and EDX elemental mappings of the major elemental components of a tooth cross-section of *H. nyererei.*

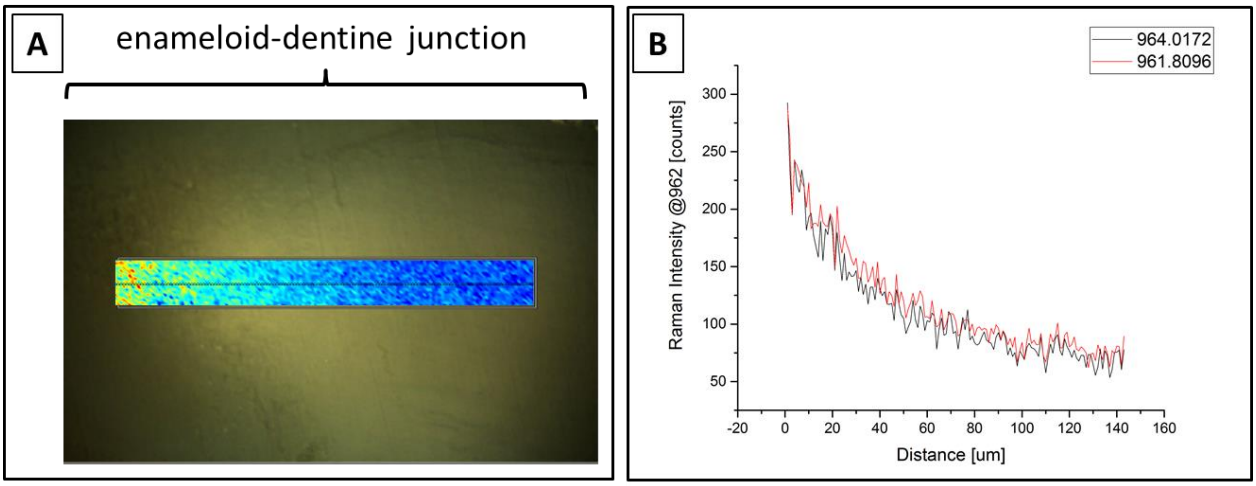

Figure S 23: A: Light microscopic image of a polished cross-section of a tooth of *H. nyererei* at the enameloid-dentine junction. The square indicates the area for the Raman-measurements. B: Line scan of the phosphate v1 vibration mode along the length of the measured area as indicated in A.

Table S 9: Raman vibration modes observed for the polished cross-section of a central tooth of *H. nyererei* and their assignments.

Vibration mode	Raman position [rel. cm^{-1}]
$[PO_4]^{3-}$ v_1	962
$[PO_4]^{3-}$ v_2	431
$[PO_4]^{3-}$ v_3	1043
$[PO_4]^{3-}$ v_4	587
$[HPO_4]^{2-}$	1007
amide II	1570
C-H (bending)	1438

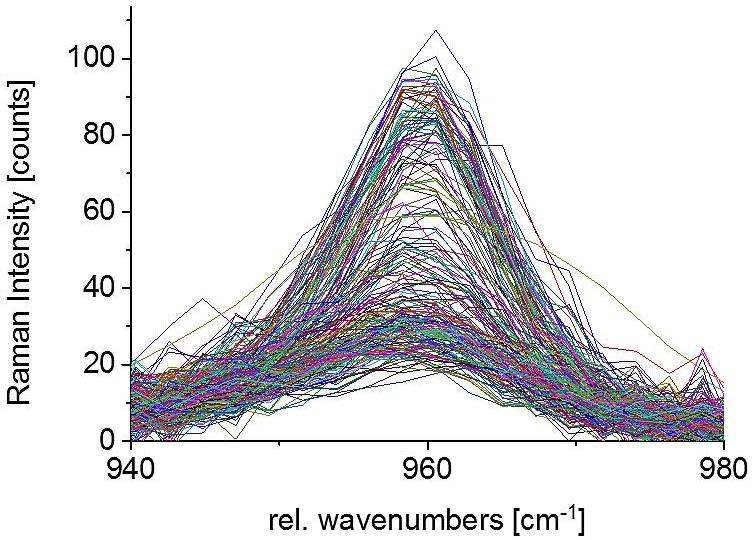

Figure S 24: All collected Raman spectra of the phosphate v_1 band of an axial cross-section of a tooth of *H. nyererei*.

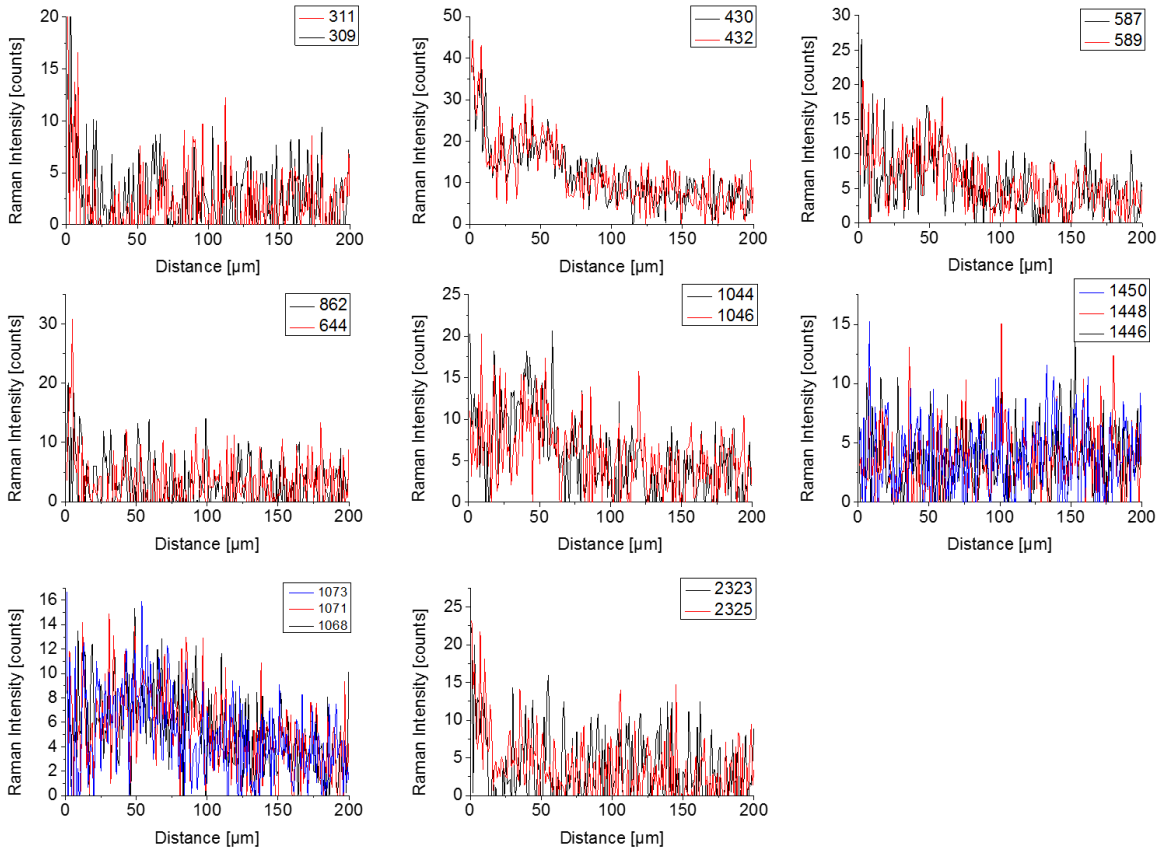

Figure S 25: Raman-line scans of characteristic band positions along the length of a polished axial cross-section of *H. nyererei*.

Table S 10: IR vibration modes observed for a powdered tooth sample of *H. nyererei* and their assignments.

Vibration mode	wavenumbers [cm^{-1}]
$[PO_4]^{3-}$ v_1	964
$[PO_4]^{3-}$ v_3	1093
amide I	1649
amide II	1547
amide III	1240
amide A, B	3070-3300
C-H	2857 2929 2953
B-type $[CO_3]^{2-}$ v_2	871
B-type $[CO_3]^{2-}$ v_3	1415 1454
NA	1008
NA	1740

NA = not assigned

3.2.4.4 Mechanical properties

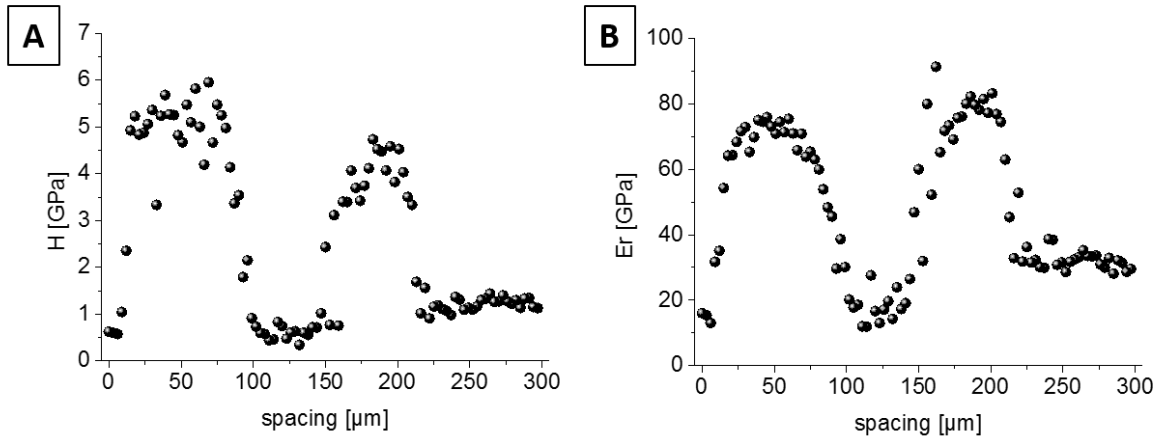

Figure S 26: Nanoindentation results of the hardness (A) and elastic modulus (B) along the axial cross-section of a tooth of the LPJ of *H. nyererei.*

2.3.1 *Mylochromis mola*

2.3.1.2 Chemical composition and distribution

Table S 11: IR vibration modes observed for the tooth sample of *M. mola* and their assignments.

Vibration mode	wavenumbers [cm^{-1}]
$[PO_4]^{3-}$ v_1	960
$[PO_4]^{3-}$ v_3	1014
amide I	1649
amide II	1549
amide III	1241
amide A, B	3070-3300
C-H	2856 2926
B-type $[CO_3]^{2-}$ v_2	866
B-type $[CO_3]^{2-}$ v_3	1416 1451

2.3.2 *Chilotilapia rhoadesii*

2.3.2.2 Chemical composition and elemental distribution

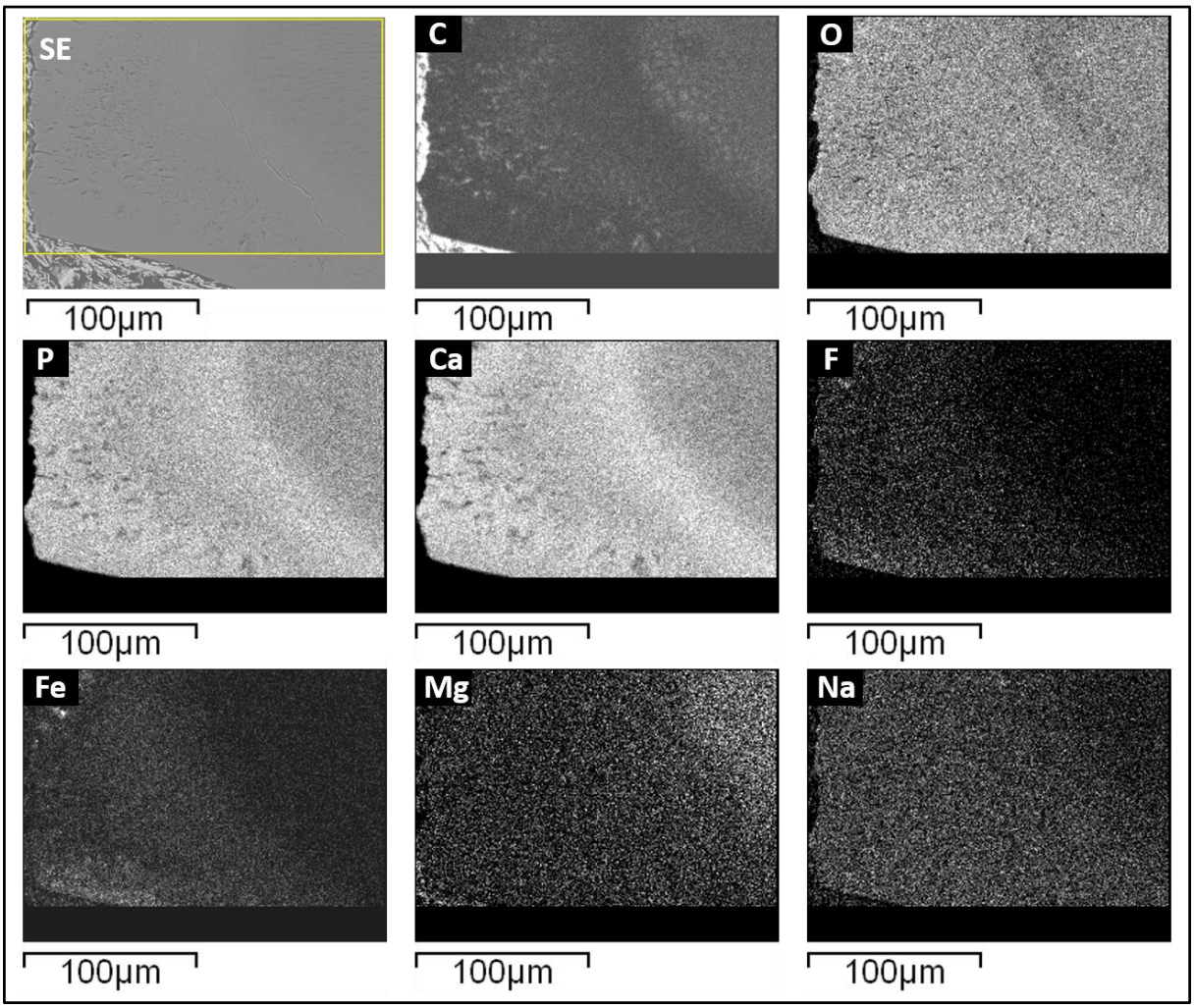

Figure S 27: Secondary electron image (SE) and EDX elemental mappings of the major elemental components of a tooth cross-section of *C. rhoadesii.*

Table S 12: IR vibration modes observed for a powdered tooth sample of *C. rhoadesii* and their assignments.

Vibration mode	wavenumbers [cm^{-1}]
$[PO_4]^{3-}$ v_1	960
$[PO_4]^{3-}$ v_3	1090
$[PO_4]^{3-}$ v_4	
amide I	1645
amide II	1546
amide III	1240
amide A, B	3314
C-H	2933
B-type $[CO_3]^{2-}$ v_2	871
B-type $[CO_3]^{2-}$ v_3	1417 1455

2.3.2.3 Ultrastructure of the teeth

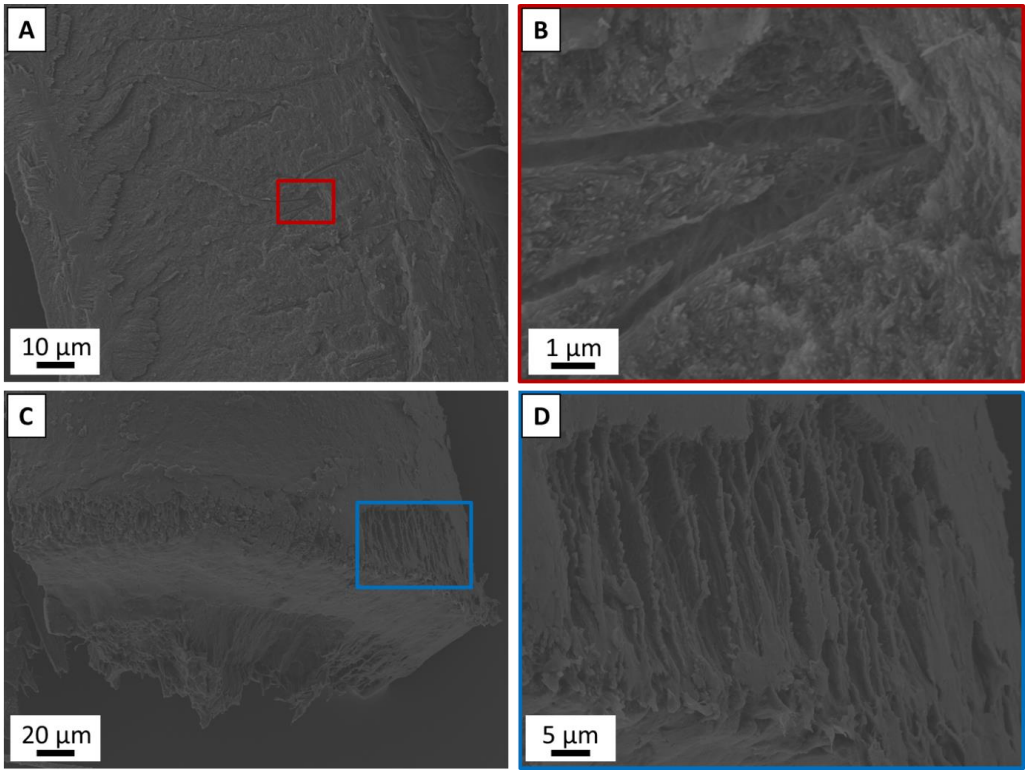

Figure S 28: SEM images of fracture areas of cracked teeth of *C. rhoadesii*. A: Overview of the outer area of a tooth, highlighting the dentinal tubules, which originate at the inner side of the dentine at the pulpa. B: Enlargement of a cross-section of a branching channel of a dentinal tubule, highlighting that this area is constructed of thin mineralized fibers. The position is marked as indicated with the red frame in image A. C: Overview of a basal area of the outer surface of a fractured tooth. D: Enlargement of a delaminated area of the outer surface of a tooth, showing the parallel arrangement of the fibrous ribbons, which run along the length of the whole tooth. The position is marked with a blue frame in image C.

2.3.2.4 Mechanical properties

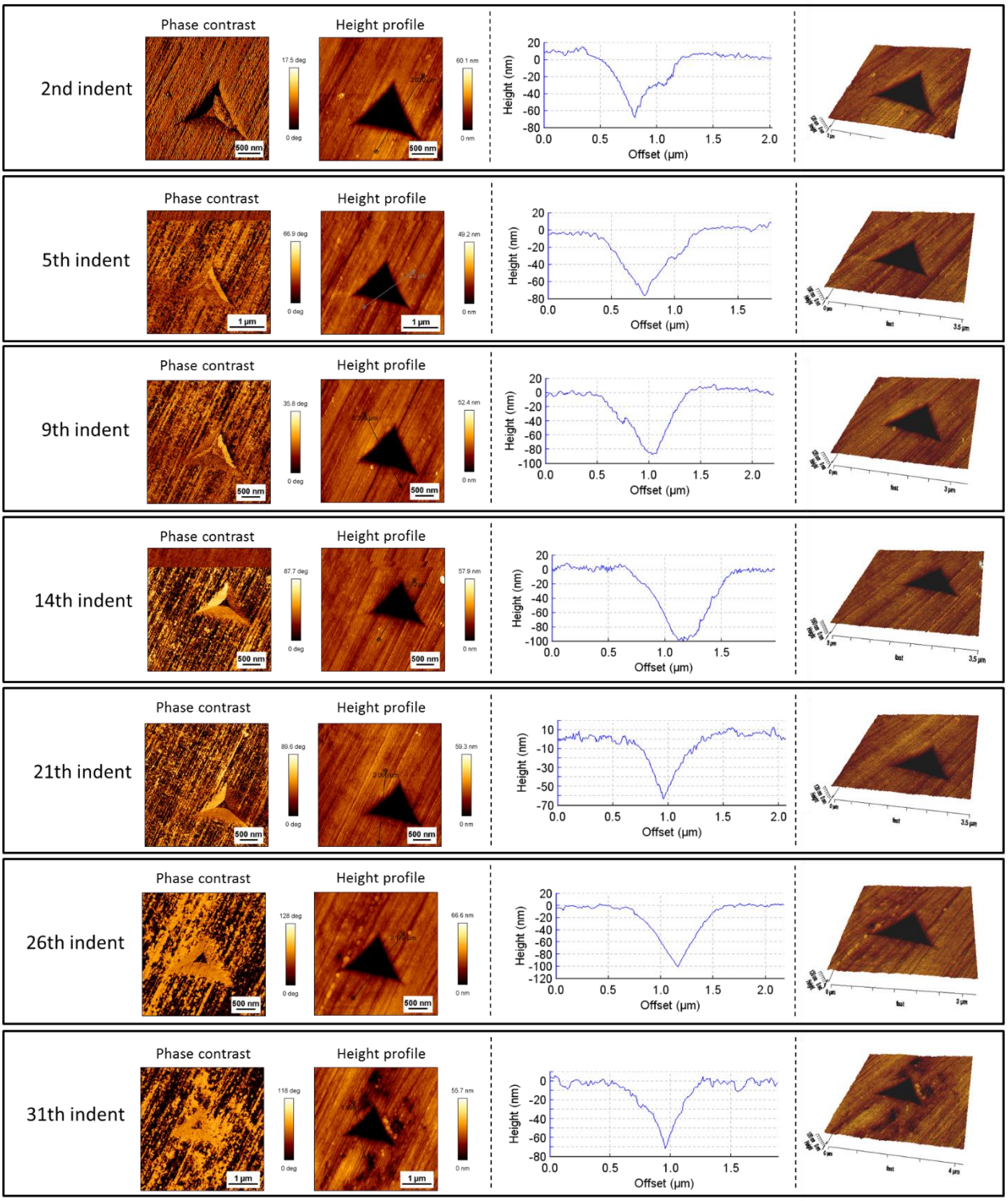

Figure S 29: AFM images (phase contrast and height topography) of selected indents the axial cross-section of a tooth of *C. rhoadesii* along the length of the sample, with indent cross-section profiles and 3D visualization.

2.3.3 *Copadichromis borleyi*

2.3.3.2 Chemical composition and distribution

Table S 13: IR vibration modes observed for the tooth sample of *C. borleyi* and their assignments.

Vibration mode	wavenumbers [cm^{-1}]
$[PO_4]^{3-}$ v_1	958
$[PO_4]^{3-}$ v_3	1015 1088
amide I	1650
amide II	1550
amide III	1240
amide A, B	3070-3300
C-H	2856 2926
B-type $[CO_3]^{2-}$ v_2	867
B-type $[CO_3]^{2-}$ v_3	1419 1451

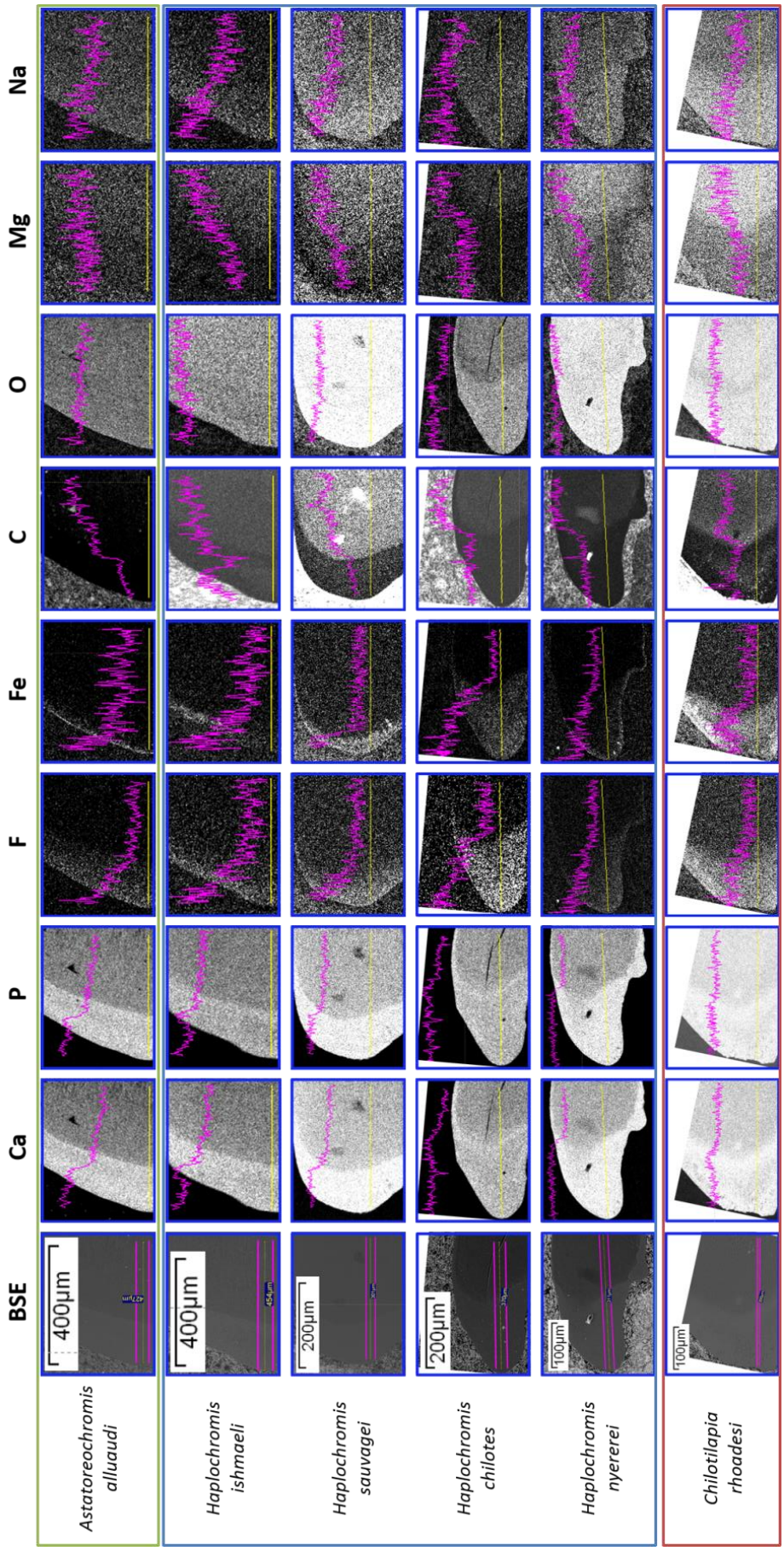

Figure S 30: Overview of EDX-line scans of all investigated species.

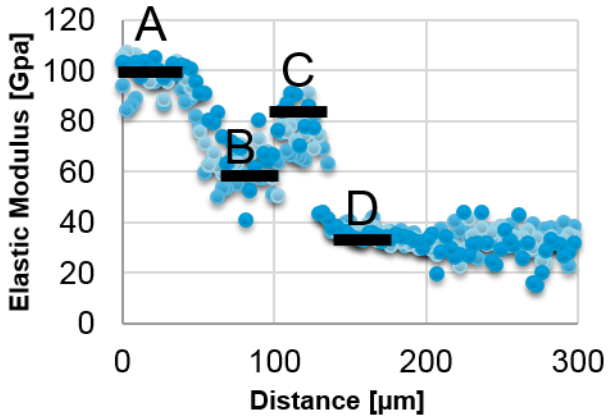

Figure S 31: Example of the determination of the different areas used for the calculation of the averaged values of hardness and elastic modulus and the ratio between them and the dentine.

Appendix B

Chapter III- Synthesis and Characterization of Isomorphic Substituted Fluorapatite-Gelatine Composites

2.3 Chemical composition

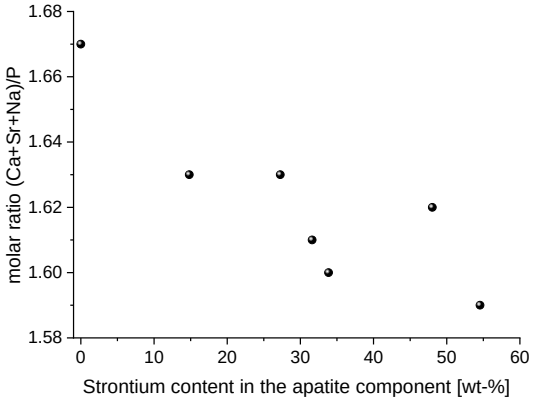

Figure S 32: Molar (Ca+Sr+Na)/P ratio of Sr^{2+}-substituted fluorapatite gelatine composites with increasing Sr^{2+}-content in the apatite component.

Table S 14: Determined empirical formula of the Sr^{2+}-substituted fluorapatite of the fluorapatite gelatine composites.

Starting Sr^{2+}-concentration (x) in solution [a]	Empirical formula
0	$(Ca_{9.72}Na_{0.28})$ $\{[PO_4]_{5.73}$ $[HPO_4]_{0.27}$ $\}$ x $\{F_2\}$
1	$(Ca_{7.56}Sr_{1.97}Na_{0.24}\square_{0.23})$ $\{[PO_4]_{5.33}$ $[HPO_4]_{0.67}\}$ x $\{F_{1.95}$ $[OH]_{0.05}\}$
2	$(Ca_{5.61}Sr_{3.92}Na_{0.23}\square_{0.24})$ $\{[PO_4]_{5.4}$ $[HPO_4]_{0.6}\}$ x $\{F_{1.88}$ $[OH]_{0.12}\}$
2.5	$(Ca_{4.71}Sr_{4.73}Na_{0.23}\square_{0.33})$ $\{[PO_4]_{5.31}$ $[HPO_4]_{0.69}\}$ x $\{F_{1.8}$ $[OH]_{0.2)}\}$
3	$(Ca_{4.24}Sr_{5.15}Na_{0.22}\square_{0.39})$ $\{[PO_4]_{5.21}$ $[HPO_4]_{0.79}\}$ x $\{F_{1.8}$ $[OH]_{0.2}\}$
4	$(Ca_{1.43}Sr_{8.07}Na_{0.23}\square_{0.27})$ $\{[PO_4]_{5.64}$ $[HPO_4]_{0.36}\}$ x $\{F_{1.59}$ $[OH]_{0.41}\}$
5	$(Sr_{9.33}Na_{0.23}\square_{0.44})$ $\{[PO_4]_{5.25}$ $[HPO_4]_{0.75}\}$ x $\{F_{1.65}$ $[OH]_{0.35}\}$

[a] (molar ratios Ca:P:Sr:F = 5-x:5:x:1)

2.4 Phase analysis

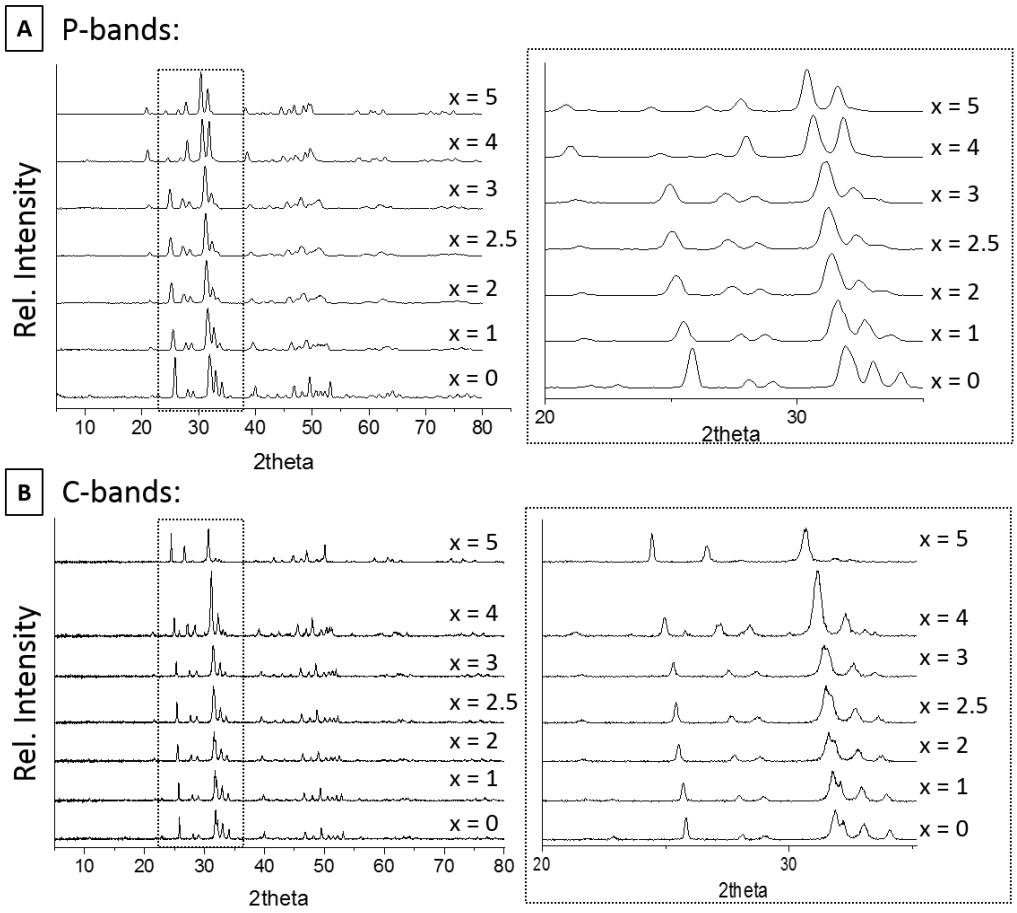

Figure S 33: Results of the pXRD-measurements of Sr^{2+}-substituted fluorapatite-gelatine composites with increasing Sr^{2+}-substitution (with molar ratios Ca:P:Sr:F = 5-x:5:x:1), which were isolated from the P-Liesegang band (A) and from the C-Liesegang band (B) with an enlargement of a range of 15 2theta to visualize the shift in reflex-positions upon increasing Sr^{2+}-incorporation into the apatite.

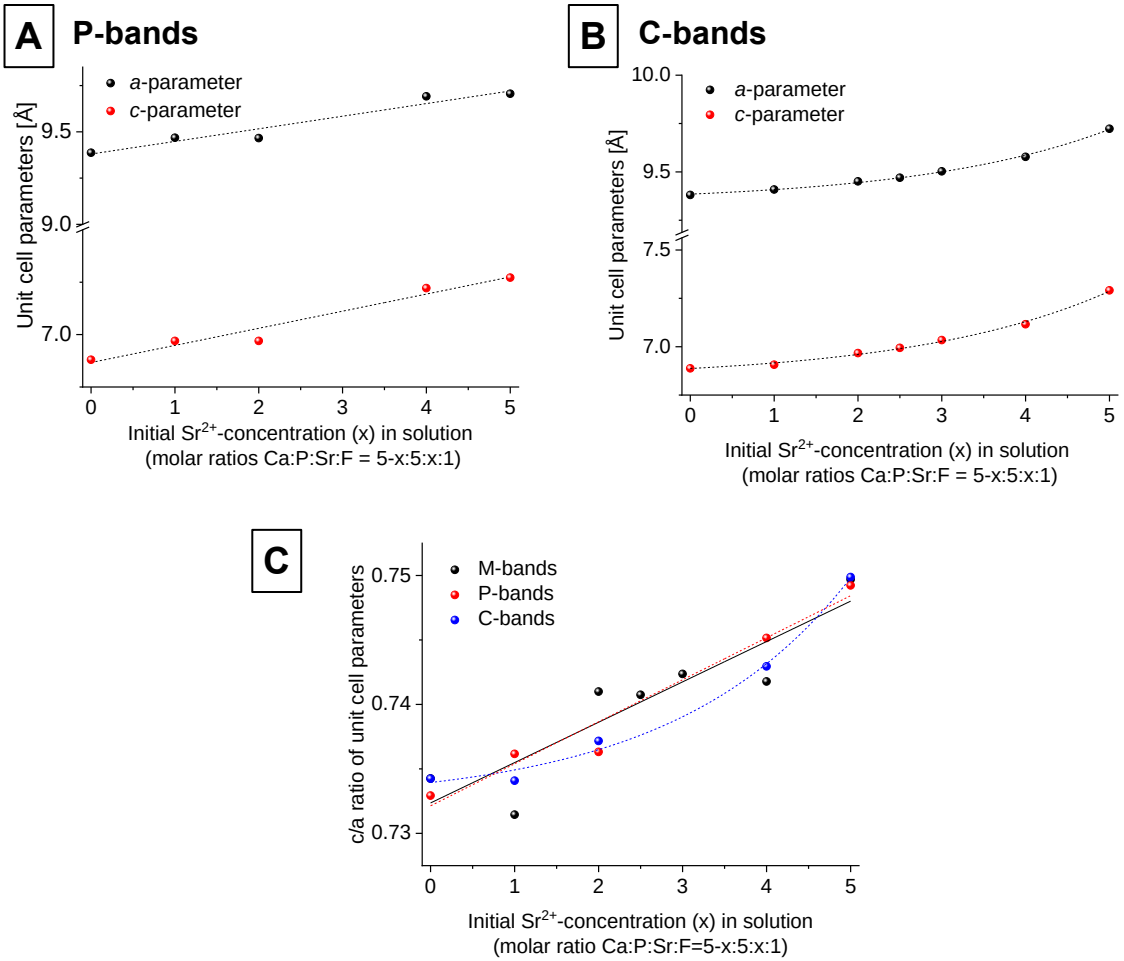

Figure S 34: Changes of lattice parameters *a* and *c* of composites of different Liesegang bands. A: Lattice parameters of P-bands, B: Lattice parameters of C-bands; C: Comparison of c/a ratio from different Liesegang bands with increasing Sr^{2+}-concentration in solution.

2.5 Vibration spectroscopy

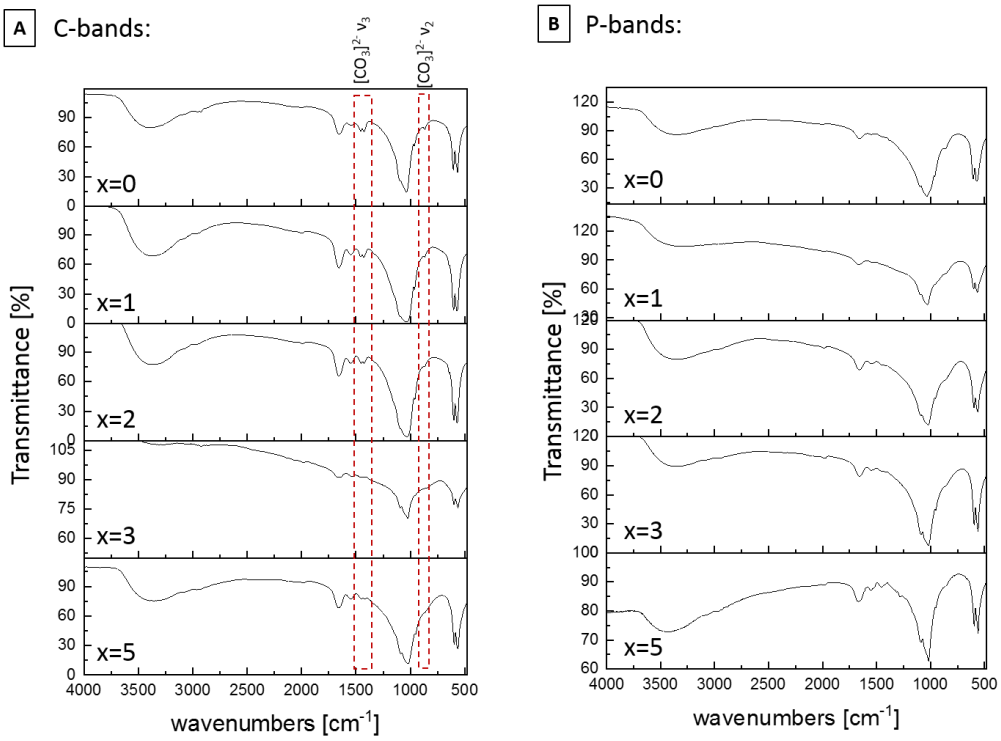

Figure S 35: Results of FT-IR spectroscopic analysis of Sr^{2+}-substituted fluorapatite-gelatine composites, which were isolated from the C-Liesegang- (A) and P-Liesegang-bands (B) (with molar ratios: Ca:P:Sr:F=5-x:5:x:1). Highlighted with the red frame in image A are the B-type carbonate FT-IR vibration modes.

Table S 15: IR and Raman vibration modes of Sr^{2+}-substituted fluorapatite-gelatine composites and their assignments.

Vibration mode	IR position [cm^{-1}]	Raman position [rel. cm^{-1}]
$[PO_4]^{3-}$ v1	949-964	945-960
$[PO_4]^{3}$ v_2	459-469	419-430 442-448
$[PO_4]^{3}$ v_3	1019-1032 1084-1099	1024-1033 1045-1048 1052-1056 1065-1073 1080-1095
$[PO_4]^{3}$ v_4	559-469 570-577 596-606	572-581 593-608 603-623
$[HPO_4]^{2-}$	~540 864	
amide I	1665	1659-1689
amide II	1546	1558-1565
C-H	2934	1457 2938

Appendix C

Chapter IV Characterization and biocompatibility of biomimetic surface modification of PEEK bone implant materials

2.1.2 Grazing incidence X-Ray diffraction

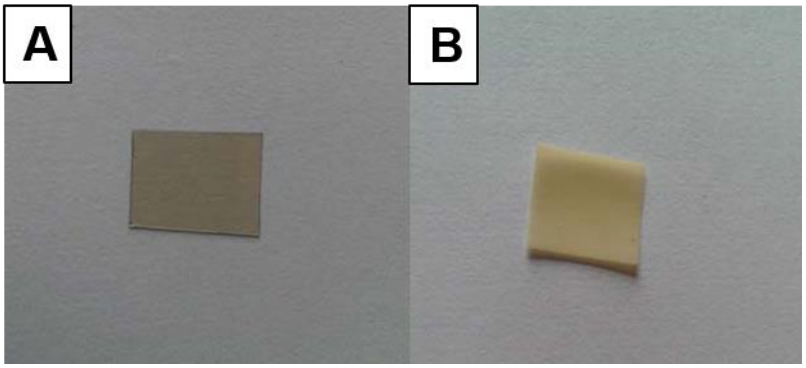

Figure S 36: Images of untreated, amorphous PEEK-film (A) and hydroxylated PEEK (called PEEK-OH) (B). The change in color indicates a change in crystallinity of the PEEK.

2.4.1 Cell toxicity of the biomimetic coating

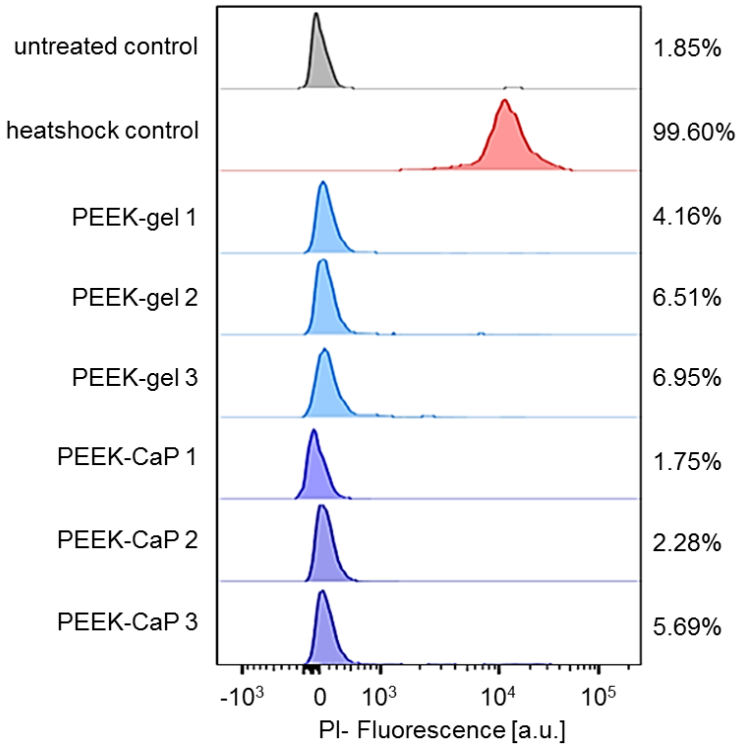

Figure S 37: Histogram of the single results of the PI flow cytometric toxicity assay of NIH3T3-fibroblasts, which were incubated with an extract of α-MEM of the different PEEK materials (incubation time: 1 d). Percentages correspond to dead cells of all counted cell within one measurement.

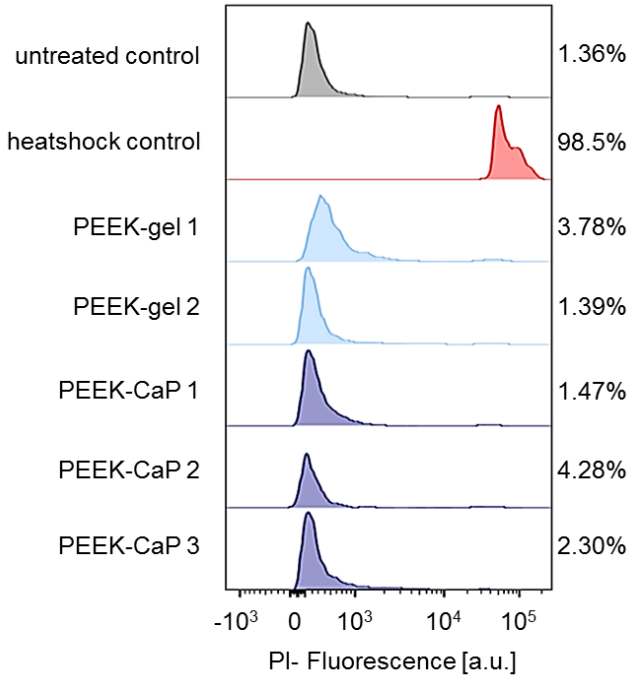

Figure S 38: Histogram of the single results of the PI flow cytometric toxicity assay of MC3T3-E1-osteoblasts, which were incubated with an extract of α-MEM of the different PEEK materials (incubation time: 1 d). Percentages correspond to dead cells of all counted cell within one measurement.

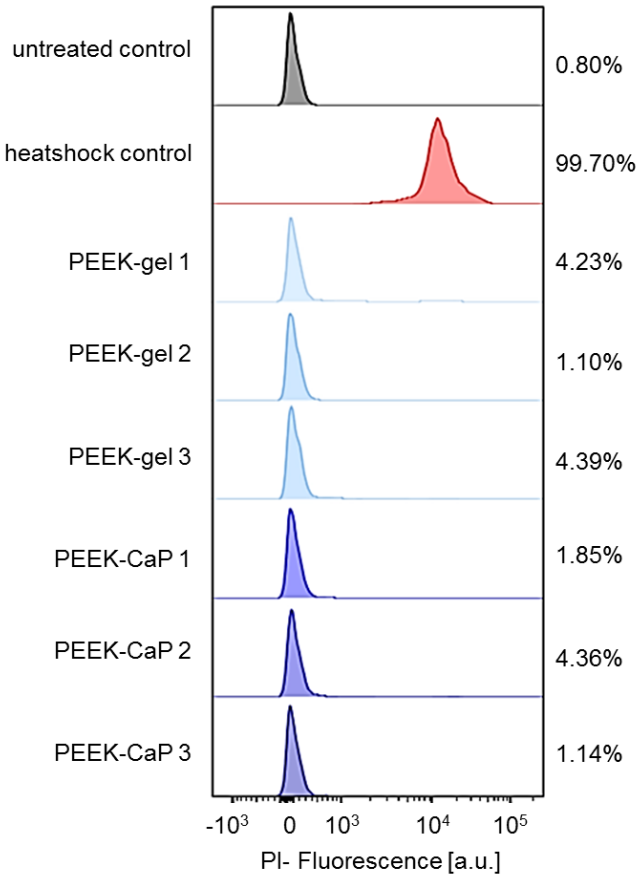

Figure S 39: Histogram of the results of each measurement of the PI flow cytometric toxicity assay of NIH3T3-fibroblasts, which were incubated directly on the different PEEK materials. Percentages correspond to dead cells of all counted cell within one measurement.

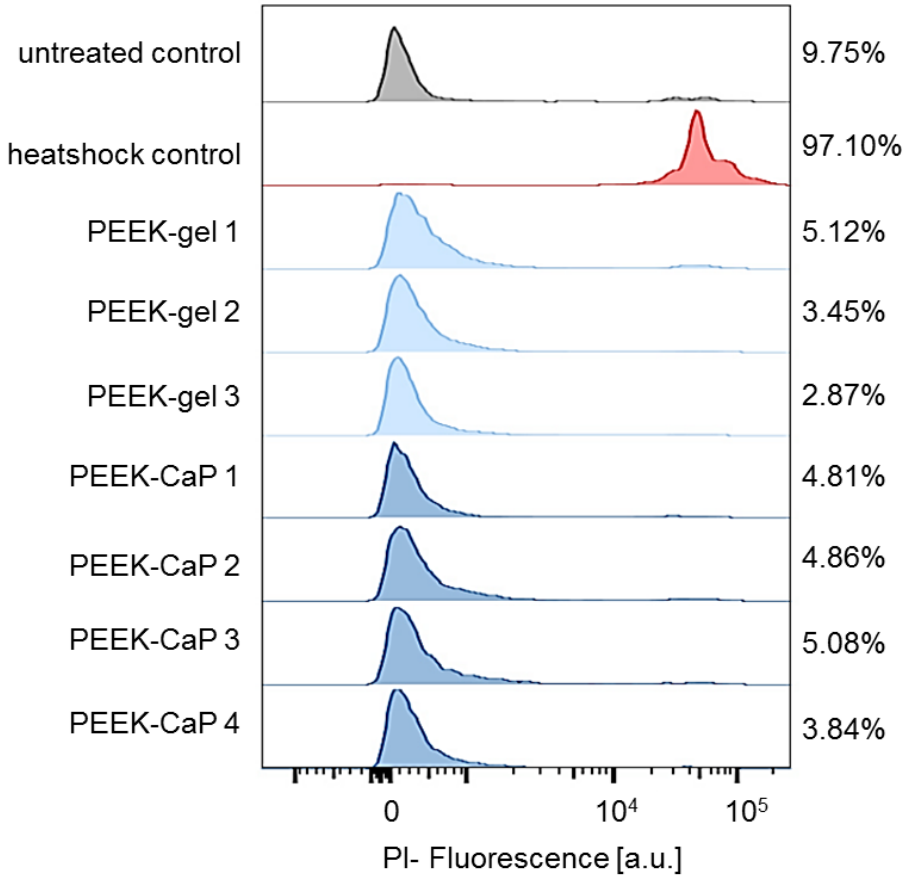

Figure S 40: Histogram of the single results of the PI flow cytometric toxicity assay of MC3T3 osteoblasts, which were incubated directly on the different PEEK materials. Percentages correspond to dead cells of all counted cell within one measurement.

References

1. Losos, J.B., *Convergence, adaptation, and constraint.* Evolution, 2011. **65**(7): p. 1827-1840.
2. Fratzl, P., *Biomimetic materials research: what can we really learn from nature's structural materials?* Journal of The Royal Society Interface, 2007. **4**(15): p. 637.
3. Gruber, P. and S. Gosztonyi, *Skin in architecture: towards bioinspired facades.* WIT Transactions on Ecology and the Environment, 2010. **138**: p. 503-513.
4. Moored, K.W., et al., *Batoid fishes: inspiration for the next generation of underwater robots.* Marine Technology Society Journal, 2011. **45**(4): p. 99-109.
5. Nakata, T., et al., *Aerodynamics of a bio-inspired flexible flapping-wing micro air vehicle.* Bioinspiration & biomimetics, 2011. **6**(4): p. 045002.
6. Combes, S.A., *Materials, structure, and dynamics of insect wings as bioinspiration for MAVs.* Encyclopedia of aerospace engineering, 2010.
7. Gebeshuber, I.C. and M. Drack, *An attempt to reveal synergies between biology and mechanical engineering.* Proceedings of the Institution of Mechanical Engineers, Part C: Journal of Mechanical Engineering Science, 2008. **222**(7): p. 1281-1287.
8. Kwak, M.K., et al., *Towards the Next Level of Bioinspired Dry Adhesives: New Designs and Applications.* Advanced Functional Materials, 2011. **21**(19): p. 3606-3616.
9. Youngblood, J.P. and N.R. Sottos, *Bioinspired Materials for Self-Cleaning and Self-Healing.* MRS Bulletin, 2011. **33**(8): p. 732-741.
10. Jeronimidis, G. and A. Atkins, *Mechanics of biological materials and structures: Nature's lessons for the engineer.* Proceedings of the Institution of Mechanical Engineers, Part C: Journal of Mechanical Engineering Science, 1995. **209**(4): p. 221-235.
11. Carrow, J.K. and A.K. Gaharwar, *Bioinspired polymeric nanocomposites for regenerative medicine.* Macromolecular Chemistry and Physics, 2015. **216**(3): p. 248-264.
12. Tang, Z., et al., *Nanostructured artificial nacre.* Nat Mater, 2003. **2**(6): p. 413-418.
13. Bonderer, L.J., A.R. Studart, and L.J. Gauckler, *Bioinspired Design and Assembly of Platelet Reinforced Polymer Films.* Science, 2008. **319**(5866): p. 1069-1073.
14. Podsiadlo, P., et al., *Ultrastrong and Stiff Layered Polymer Nanocomposites.* Science, 2007. **318**(5847): p. 80-83.
15. Huang, Z.-M., et al., *A review on polymer nanofibers by electrospinning and their applications in nanocomposites.* Composites science and technology, 2003. **63**(15): p. 2223-2253.
16. Shin, S.-H., et al., *A short review: Recent advances in electrospinning for bone tissue regeneration.* Journal of Tissue Engineering, 2012. **3**(1): p. 2041731412443530.
17. Braghirolli, D.I., D. Steffens, and P. Pranke, *Electrospinning for regenerative medicine: a review of the main topics.* Drug Discovery Today, 2014. **19**(6): p. 743-753.
18. Munch, E., et al., *Tough, Bio-Inspired Hybrid Materials.* Science, 2008. **322**(5907): p. 1516-1520.
19. Deville, S., et al., *Freezing as a Path to Build Complex Composites.* Science, 2006. **311**(5760): p. 515-518.
20. Pimpin, A. and W. Srituravanich, *Review on micro-and nanolithography techniques and their applications.* Engineering Journal (Eng. J.), 2012. **16**(1): p. 37-56.
21. Rengier, F., et al., *3D printing based on imaging data: review of medical applications.* International journal of computer assisted radiology and surgery, 2010. **5**(4): p. 335-341.
22. Gross, B.C., et al., *Evaluation of 3D printing and its potential impact on biotechnology and the chemical sciences*. 2014, ACS Publications.
23. Le Duigou, A., et al., *3D printing of wood fibre biocomposites: From mechanical to actuation functionality.* Materials & Design, 2016. **96**: p. 106-114.

24. Dimas, L.S., et al., *Tough composites inspired by mineralized natural materials: computation, 3D printing, and testing.* Advanced Functional Materials, 2013. **23**(36): p. 4629-4638.
25. Maradit Kremers H, e.a. *Prevalence of Total Hip (THA) and Total Knee (TKA) Arthroplasty in the United States*. [cited 2018; Available from: https://www.mayoclinic.org/medical-professionals/clinical-updates/orthopedic-surgery/study-hip-knee-arthroplasty-shows-7-2-million-americans-living-with-implants.
26. NJR. *National Joint Registry Annual Reports 2017*. 2018]; Available from: http://www.njrcentre.org.uk/njrcentre/Reports,PublicationsandMinutes/Annualreports/tabid/86/Default.aspx.
27. FDA. *Guidance Document for Testing Orthopedic Implants with Modified Metallic Surfaces Apposing Bone Or Bone Cement*. 04/28/1994 03/23/2018 [cited 2018.
28. Olszta, M.J., et al., *Bone structure and formation: A new perspective.* Materials Science and Engineering: R: Reports, 2007. **58**(3): p. 77-116.
29. Falini, G. and S. Fermani, *Nucleation and Growth from a Biomineralization Perspective*, in *New Perspectives on Mineral Nucleation and Growth: From Solution Precursors to Solid Materials*, A.E.S. Van Driessche, et al., Editors. 2017, Springer International Publishing: Cham. p. 185-197.
30. Dorozhkin, S.V., *Calcium orthophosphates: Occurrence, properties, biomineralization, pathological calcification and biomimetic applications.* Biomatter, 2011. **1**(2): p. 121-164.
31. Dorozhkin, S.V. and M. Epple, *Biological and medical significance of calcium phosphates.* Angewandte Chemie-International Edition, 2002. **41**(17): p. 3130-3146.
32. Elliott, J.C., *Structure and chemistry of the apatites and other calcium orthophosphates*. Vol. 18. 2013: Elsevier.
33. Ma, G. and X.Y. Liu, *Hydroxyapatite: hexagonal or monoclinic?* Crystal Growth and Design, 2009. **9**(7): p. 2991-2994.
34. Elliott, J.C., P. Mackie, and R. Young, *Monoclinic hydroxyapatite.* Science, 1973. **180**(4090): p. 1055-1057.
35. Nakamura, S., H. Takeda, and K. Yamashita, *Proton transport polarization and depolarization of hydroxyapatite ceramics.* Journal of Applied Physics, 2001. **89**(10): p. 5386-5392.
36. Gobel, C., et al., *Phase formation and morphology of calcium phosphate gelatine-composites grown by double diffusion technique: the influence of fluoride.* Journal of Materials Chemistry, 2004. **14**(14): p. 2225-2230.
37. Tlatlik, H., *Neue Untersuchungen zu Wachstum und Struktur von Fluorapatit-Gelatine-Nanokompositen.* 2008.
38. Glimcher, M.J., *Bone: Nature of the Calcium Phosphate Crystals and Cellular, Structural, and Physical Chemical Mechanisms in Their Formation.* Reviews in Mineralogy and Geochemistry, 2006. **64**(1): p. 223-282.
39. Elliott, J.C., *Calcium Phosphate Biominerals.* Reviews in Mineralogy and Geochemistry, 2002. **48**(1): p. 427-453.
40. M. Golberg, D.S., S. Lecolle, H. Chardin, M. A. Quintana, A. C. Acevedo, G. Gafni, D. and L.V. Dillouya, B. Thonemann, G. Schmalz, P. Bissilamapahou, and J. P. Carreau, *Dental Mineralization.* Int. J. Dev. Biol, 1995. **39**(93).
41. F. Bronner, a.M.F.-C., *Bone Formation*. 2003: Springer.
42. Gross, K.A. and C.C. Berndt, *Biomedical Application of Apatites.* Reviews in Mineralogy and Geochemistry, 2002. **48**(1): p. 631-672.
43. Fratzl, P., *Bone fracture: When the cracks begin to show.* Nat Mater, 2008. **7**(8): p. 610-612.
44. M. Teafard, M.S., M. Ferguson, *Development, Function and Evolution of Teeth*. 2007, Cambridge Univ. Press. 328.
45. Moradian-Oldak, J., *Protein - mediated enamel mineralization.* Frontiers in Bioscience, 2012. **17**: p. 1996-2023.
46. LeGeros, R.Z., et al., *In vitro Caries-like Lesion Formation in F-containing Tooth Enamel.* Journal of Dental Research, 1983. **62**(2): p. 138-144.

47. Miake, Y., et al., *Ultrastructural studies on crystal growth of enameloid minerals in elasmobranch and teleost fish.* Calcified Tissue International, 1991. **48**(3): p. 204-217.
48. Whitenack, L.B., et al., *Young's modulus and hardness of shark tooth biomaterials.* Archives of oral biology, 2010. **55**(3): p. 203-209.
49. Whitenack, L.B., D.C. Simkins, and P.J. Motta, *Biology meets engineering: The structural mechanics of fossil and extant shark teeth.* Journal of Morphology, 2011. **272**(2): p. 169-179.
50. Enax, J., et al., *Structure, composition, and mechanical properties of shark teeth.* Journal of Structural Biology, 2012. **178**(3): p. 290-299.
51. Okazaki, M., et al., *Solubility and crystallinity in relation to fluoride content of fluoridated hydroxyapatites.* Journal of dental research, 1981. **60**(4): p. 845-849.
52. Eslami, H., M. Solati-Hashjin, and M. Tahriri, *Effect of fluorine ion addition on structural, thermal, mechanical, solubility and biocompatibility characteristics of hydroxyapatite nanopowders.* Advances in Applied Ceramics, 2010. **109**(4): p. 200-212.
53. Eslami, H., M. Solati-Hashjin, and M. Tahriri, *The comparison of powder characteristics and physicochemical, mechanical and biological properties between nanostructure ceramics of hydroxyapatite and fluoridated hydroxyapatite.* Materials Science & Engineering C-Biomimetic and Supramolecular Systems, 2009. **29**(4): p. 1387-1398.
54. Elliot, J., *Hydroxyapatite and Chemistry of the Apatites and Other Calcium Orthophosphates*. 1994, Elsevier, Netherlands.
55. Gross, K.A., J. Hart, and L.M. Rodriguez-Lorenzo, *Fluor-hydroxyapatite solid solutions as alternative bioceramics.* Bioceramics 14, 2002. **218-2**: p. 165-168.
56. Frank-Kamenetskaya, O.V., et al., *Refinement of apatite atomic structure of albid tissue of Late Devon conodont.* Crystallography Reports, 2014. **59**(1): p. 41-47.
57. Dorozhkin, S.V., *Calcium orthophosphates.* Journal of Materials Science, 2007. **42**(4): p. 1061-1095.
58. Dorozhkin, S.V., *A review on the dissolution models of calcium apatites.* Progress in Crystal Growth and Characterization of Materials, 2002. **44**(1): p. 45-61.
59. Rosseeva, E.V., et al., *Synthesis, Characterization, and Morphogenesis of Carbonated Fluorapatite−Gelatine Nanocomposites: A Complex Biomimetic Approach toward the Mineralization of Hard Tissues.* Chemistry of Materials, 2008. **20**(19): p. 6003-6013.
60. Hongo, C., et al., *Repetitive interactions observed in the crystal structure of a collagen-model peptide, [(Pro-Pro-Gly)9]3.* J Biochem, 2005. **138**(2): p. 135-44.
61. Rose, A.S., et al., *Web-based molecular graphics for large complexes*, in *Proceedings of the 21st International Conference on Web3D Technology*. 2016, ACM: Anaheim, California. p. 185-186.
62. Rose, A.S. and P.W. Hildebrand, *NGL Viewer: a web application for molecular visualization.* Nucleic Acids Research, 2015. **43**(W1): p. W576-W579.
63. F.Gobeaux, G.M., A.Anglo, P.Panine, P.Davidson, M.-M.Giraus-Guille, E.Belamie, *Fibrillogenesis in Dense Collagen Solutions: A Physicochemical Study.* Journal of Molecular Biology, 2008. **376**: p. 1509-1522.
64. V.Ottani, D.M., M.Franchi, A.Ruggeri, M.Raspanti, *Hierarchical structures in fibrillar collagens.* Micron, 2002. **33**: p. 587-596.
65. M-C.Goh, M.F.P., M.A.Gale, I.Yadegari, M.Edirisinghe, J.Strzelczyk, *Fibril formation in collagen.* Physica A, 1997(239): p. 95-102.
66. M.D.Shoulders, R.T.R., *Collagen Structure and Stability.* Annu Rev Biochem, 2009. **78**: p. 929-958.
67. B.Brodsky, J.A.W., J.A.Ramshaw, *Collagens and Gelatins.* Biopolymers Online, 2005.
68. F.Nudelman, K.P., A.George, P.H.H.Bomans, H.Friedrich, L.J.Brylka, P.A.J.Hilberts, G.de With, A.A.J.M.Sommerdijk, *The role of collagen in bone apatite formation in the presence of hydroxyapatite nucleation inhibitors.* Nature Materials, 2010. **9**: p. 1004-1009.
69. S.Weiner, W.T., *Bone structure: from angstroms to microns.* The FASEB Journal, 1992. **6**: p. 879-885.

70. Reinhard Schrieber, H.G., *Gelatin Handbook*. 2007: WILEY-VCH Verlag GmbH & Co. KGaA. 348.
71. Salzburger, W. and A. Meyer, *The species flocks of East African cichlid fishes: recent advances in molecular phylogenetics and population genetics.* Naturwissenschaften, 2004. **91**.
72. Stiassny, M.L.J. and A. Meyer, *Cichlids of the Rift Lakes.* Scientific American, 1999. **280**.
73. Kornfield, I. and P.F. Smith, *African Cichlid Fishes: Model systems for evolutionary biology.* Annu Rev Ecol Syst, 2000. **31**.
74. Fryer, G., *On the age and origin of the species flock of haplochromine cichlid fishes of Lake Victoria.* Proceedings of the Royal Society of London B: Biological Sciences, 2001. **268**(1472): p. 1147-1152.
75. Fryer, G. and T. Iles, *The cichlid fishes of the Great Lakes of Africa: Their biology and evolution*. Vol. 23. 1972: Oliver & Boyd, Croythorn House.
76. Fryer, G. and T.D. Iles, *The cichlid fishes of the Great Lakes of Africa: their biology and evolution.* 1972.
77. Salzburger, W., et al., *Phylogeny of the Lake Tanganyika cichlid species flock and its relationship to the Central and East African haplochromine cichlid fish faunas.* Syst Biol, 2002. **51**.
78. Sturmbauer, C., et al., *Evolution of the tribe Tropheini from Lake Tanganyika: synchronized explosive speciation producing multiple evolutionary parallelism.* Hydrobiologia, 2003. **500**.
79. Greenwood, P.H., *The haplochromine fishes of the East African lakes*. 1981: Kraus international publications.
80. Greenwood, P., *African cichlids and evolutionary theories.* Evolution of fish species flock, 1984: p. 141-154.
81. Johnson, T.C., et al., *Late Pleistocene desiccation of Lake Victoria and rapid evolution of cichlid fishes.* SCIENCE-NEW YORK THEN WASHINGTON-, 1996: p. 1091-1092.
82. Johnson, T.C., K. Kelts, and E. Odada, *The holocene history of Lake Victoria.* AMBIO: A Journal of the Human Environment, 2000. **29**(1): p. 2-11.
83. Delvaux, D., *Age of Lake Malawi (Nyasa) and water level fluctuations.* Mus R Afr Centr Tervuren (Belg) Dept Geol Min Rapp Ann, 1995. **1995–1996**.
84. Cohen, A.S., M. Soreghan, and C.A. Scholz, *Estimating the age of formation of lakes: An example from Lake Tanganyika, East African Rift system.* Geology, 1993. **21**.
85. Cohen, A., et al., *New palaeogeographic and lake-level reconstructions of Lake Tanganyika: implications for tectonic, climatic and biological evolution in a rift lake.* Basin research, 1997. **9**(2): p. 107-132.
86. Sturmbauer, C., et al., *Lake level fluctuations synchronize genetic divergences of cichlid fishes in African lakes.* Molecular Biology and Evolution, 2001. **18**(2): p. 144-154.
87. Meyer, A., et al., *Monophyletic origin of Lake Victoria cichlid fishes suggested by mitochondrial DNA sequences.* Nature, 1990. **347**.
88. Verheyen, E., et al., *Origin of the superflock of cichlid fishes from Lake Victoria, East Africa.* Science, 2003. **300**(5617): p. 325-329.
89. Salzburger, W., et al., *Out of Tanganyika: Genesis, explosive speciation, key-innovations and phylogeography of the haplochromine cichlid fishes.* BMC Evolutionary Biology, 2005. **5**(1): p. 17.
90. Verheyen, E., et al., *Origin of the superflock of cichlid fishes from Lake Victoria, East Africa.* Science, 2003. **300**.
91. Liem, K.F., *Evolutionary strategies and morphological innovations: cichlid pharyngeal jaws.* Syst Zool, 1973. **22**.
92. Muschick, M., et al., *Adaptive phenotypic plasticity in the Midas cichlid fish pharyngeal jaw and its relevance in adaptive radiation.* BMC Evol Biol, 2011. **11**.
93. Barlow, G.W., in *The Cichlid Fishes. Nature's Grand Experiment in Evolution*. 2000, Perseus Publishing: Cambridge, MA.
94. Barlow, G., *The cichlid fishes: nature's grand experiment in evolution*. 2008: Basic Books.

95. Rijssel, J.C., et al., *Fast adaptive responses in the oral jaw of Lake Victoria cichlids.* Evolution, 2015. **69**(1): p. 179-189.
96. Meyer, A., *Phenotypic plasticity and heterochrony in Cichlasoma managuense.* Evolution, 1987. **41**(6).
97. Gunter, H.M., et al., *Shaping development through mechanical strain: the transcriptional basis of diet-induced phenotypic plasticity in a cichlid fish.* Molecular Ecology, 2013. **22**(17): p. 4516-4531.
98. Meyer, A., *Cost of morphological specialization: feeding performance of the two morphs in the trophically polymorphic cichlid fish, Cichlasoma citrinellum.* Oecologia, 1989. **80**(3): p. 431-436.
99. Stern, D.L., *The genetic causes of convergent evolution.* Nature Reviews Genetics, 2013. **14**(11): p. 751.
100. Rosenblum, E.B., C.E. Parent, and E.E. Brandt, *The molecular basis of phenotypic convergence.* Annual Review of Ecology, Evolution, and Systematics, 2014. **45**: p. 203-226.
101. Witte, F., de Zeeuw, M.P. & Brooks, E., *Haplochromis ishmaeli.* The IUCN Red List of Threatened Species 2010: e.T11074A3249894, 2010.
102. Van Oijen, M., et al., *Haplochromis.* 1991.
103. Witte, F., de Zeeuw, M.P. & Brooks, E., *Haplochromis sauvagei.* The IUCN Red List of Threatened Species 2010: e.T60667A12393156, 2010.
104. Witte, F., de Zeeuw, M.P. & Brooks, E., *Haplochromis chilotes.* The IUCN Red List of Threatened Species 2010: e.T60646A12390707, 2010.
105. Witte-Maas, E. and F. Witte, *Haplochromis nyererei, a new cichlid fish from Lake Victoria named in honour of Mwalimu Julius Nyerere, president of Tanzania.* Brill, Leiden, 1985.
106. Witte-Maas, E.L., *Haplochromis nyererei*. 1985.
107. Daget, J., J.-P. Gosse, and D.F. Thys van den Audenaerde, *Check-list of the freshwater fishes of Africa, Cloffa.* 1984.
108. Konings, A., *Konings's book of cichlids and all the other fishes of Lake Malawi.* 1990.
109. Banyankimbona, G., E. Vreven, and J. Snoeks, *A revision of the genus Astatoreochromis (Teleostei, Cichlidae), East–Africa.* European Journal of Taxonomy, 2013(39).
110. Schneider, R.F., et al., *Regulatory gene networks that shape the development of adaptive phenotypic plasticity in a cichlid fish.* Molecular Ecology, 2014. **23**(18): p. 4511-4526.
111. Greenwood, P. *Environmental effects on the pharyngeal mill of a cichlid fish, Astatoreochromis alluaudi, and their taxonomic implications*. in *Proceedings of the Linnean Society of London*. 1965. Wiley Online Library.
112. Huysseune, A. and J.Y. Sire, *Evolution of patterns and processes in teeth and tooth-related tissues in non-mammalian vertebrates.* European journal of oral sciences, 1998. **106**(S1): p. 437-481.
113. Mills, A., *Structural and chemical organization of teeth*. 2014: Elsevier.
114. Huysseune, A., J.-Y. Sire, and P.E. Witten, *Evolutionary and developmental origins of the vertebrate dentition.* Journal of Anatomy, 2009. **214**(4): p. 465-476.
115. Sire, J.-Y. and A.N.N. Huysseune, *Formation of dermal skeletal and dental tissues in fish: a comparative and evolutionary approach.* Biological Reviews, 2003. **78**(2): p. 219-249.
116. Witten, P.E. and A. Huysseune, *A comparative view on mechanisms and functions of skeletal remodelling in teleost fish, with special emphasis on osteoclasts and their function.* Biological Reviews, 2009. **84**(2): p. 315-346.
117. Weiner, S. and H.D. Wagner, *THE MATERIAL BONE: Structure-Mechanical Function Relations.* Annual Review of Materials Science, 1998. **28**(1): p. 271-298.
118. Kuraku, S. and A. Meyer, *Genomic analysis of cichlid fish 'natural mutants'.* Current Opinion in Genetics & Development, 2008. **18**(6): p. 551-558.
119. Sereno, P.C., et al., *Cretaceous Sauropods from the Sahara and the Uneven Rate of Skeletal Evolution Among Dinosaurs.* Science, 1999. **286**(5443): p. 1342-1347.
120. Carpenter, K., C. Miles, and K. Cloward, *Skull of a Jurassic ankylosaur (Dinosauria).* Nature, 1998. **393**: p. 782.

121. Krause, D.W., et al., *Cosmopolitanism among Gondwanan Late Cretaceous mammals.* Nature, 1997. **390**: p. 504.
122. Carlson, S.J., *Vertebrate dental structures.* Skeletal biomineralization: patterns, processes and evolutionary trends, 1990: p. 235-260.
123. Tchernov, E., *Structure, function and evolution of teeth*. 1992: Freund Publishing House Ltd.
124. Teaford, M.F., M.M. Smith, and M.W. Ferguson, *Development, function and evolution of teeth*. 2007: Cambridge University Press.
125. Line, S.R.P. and P.D. Novaes, *The development and evolution of mammalian enamel: structural and functional aspects.* Braz J Morphol Sci, 2005. **22**(2): p. 67-72.
126. Orvig, T., *Phylogeny of tooth tissues: evolution of some calcified tissues in early vertebrates.* Structural and chemical organization of teeth, 1967: p. 45-110.
127. Berkovitz, B.K. and R.P. Shellis, *The Teeth of Non-mammalian Vertebrates*. 2016: Academic Press.
128. Koenigswald, W. and P.M. Sander, *Glossary of terms used for enamel microstructures.* Tooth enamel microstructure, 1997: p. 267-280.
129. Poole, D., *Phylogeny of tooth tissues: enameloid and enamel in recent vertebrates, with a note on the history of cementum.* Structural and chemical organization of teeth, 1967: p. 111-149.
130. Sasagawa, I. and M. Ishiyama, *The structure and development of the collar enameloid in two teleost fishes, Halichoeres poecilopterus and Pagrus major.* Anatomy and Embryology, 1988. **178**(6): p. 499-511.
131. Sasagawa, I., et al., *Tooth enamel and enameloid in actinopterygian fish.* Frontiers of Materials Science in China, 2009. **3**(2): p. 174.
132. Graham, E.E., *Isolation of enamelinlike proteins from blue shark (Prionace glauca) enameloid.* Journal of Experimental Zoology Part A: Ecological Genetics and Physiology, 1985. **234**(2): p. 185-191.
133. Deutsch, D., et al., *Enamelin and enameloid*, in *Mechanisms and Phylogeny of Mineralization in Biological Systems*. 1991, Springer. p. 73-77.
134. Suga, S., Y. Taki, and K. Wada, *Fluoride concentration in the teeth of perciform fishes and its phylogenetic significance.* Japanese Journal of Ichthyology, 1983. **30**(1): p. 81-93.
135. Suga, S., et al., *Evolution of fluoride and iron concentrations in the enameloid of fish teeth*, in *Mechanisms and phylogeny of mineralization in biological systems*. 1991, Springer. p. 439-446.
136. SUGA, S., K. WADA, and M. OGAWA, *Mineralization pattern and fluoride distribution of the developing and matured enameloid of the shark.* Japanese Journal of Oral Biology, 1978. **20**(1): p. 67-81.
137. Suga, S., K. Wada, and M. Ogawa, *Fluoride concentration in teeth of tetraodontiform fishes and its phylogenetic significance.* Japanese Journal of Ichthyology, 1981. **28**(3): p. 304-312.
138. Prostak, K.S., P. Seifert, and Z. Skobe, *Serum Fluoride Level and Fluoride Content of Enameloid.* Journal of Dental Research, 1991. **70**(9): p. 1266-1271.
139. LeGeros, R. and S. Suga, *Crystallographic nature of fluoride in enameloids of fish.* Calcified Tissue International, 1980. **32**(1): p. 169-174.
140. Suga, S., et al., *Iron Concentration in Teeth of Tetra-odontiform Fishes and its Phylogenetic Significance.* Journal of Dental Research, 1989. **68**(6): p. 1115-1123.
141. Miles, A., *Pigmented enamel*. 1963, SAGE Publications.
142. SELVIG, K.A. and A. HALSE, *The ultrastructural localization of iron in rat incisor enamel.* European Journal of Oral Sciences, 1975. **83**(2): p. 88-95.
143. Stein, G. and P.E. Boyle, *Pigmentation of the enamel of albino rat incisor teeth.* Archives of Oral Biology, 1959. **1**(2): p. 97-105.
144. Anderson, M.A. and B.T. Miller, *Early Iron Deposition in Teeth of the Streamside Salamander, Ambystoma barbouri.* Journal of Herpetology, 2011. **45**(3): p. 336-338.
145. Dumont, M., et al., *Structural and functional characterization of enamel pigmentation in shrews.* Journal of structural biology, 2014. **186**(1): p. 38-48.

146. Weaver, J.C., et al., *Analysis of an ultra hard magnetic biomineral in chiton radular teeth.* Materials Today, 2010. **13**(1–2): p. 42-52.
147. Lowenstam, H., *Goethite in radular teeth of recent marine gastropods.* Science, 1962. **137**(3526): p. 279-280.
148. Lowenstam, H.A., *Opal precipitation by marine gastropods (Mollusca).* Science, 1971. **171**(3970): p. 487-490.
149. Suga, S., Y. Taki, and M. Ogawa, *Iron in the enameloid of perciform fish.* Journal of dental research, 1992. **71**(6): p. 1316-1325.
150. Chen, P.-Y., J. McKittrick, and M.A. Meyers, *Biological materials: functional adaptations and bioinspired designs.* Progress in Materials Science, 2012. **57**(8): p. 1492-1704.
151. Fantner, G.E., et al., *Sacrificial bonds and hidden length dissipate energy as mineralized fibrils separate during bone fracture.* Nature materials, 2005. **4**(8): p. 612.
152. Karam, G. and L. Gibson, *Elastic buckling of cylindrical shells with elastic cores—I. Analysis.* International Journal of Solids and Structures, 1995. **32**(8-9): p. 1259-1283.
153. Thompson, J.B., et al., *Bone indentation recovery time correlates with bond reforming time.* Nature, 2001. **414**(6865): p. 773.
154. Kluge, J.A., et al., *Spider silks and their applications.* Trends in biotechnology, 2008. **26**(5): p. 244-251.
155. Vollrath, F., *Strength and structure of spiders' silks.* Reviews in Molecular Biotechnology, 2000. **74**(2): p. 67-83.
156. Ritchie, R.O., *Mechanisms of fatigue-crack propagation in ductile and brittle solids.* International Journal of Fracture, 1999. **100**(1): p. 55-83.
157. Ritchie, R.O., *Mechanisms of fatigue crack propagation in metals, ceramics and composites: Role of crack tip shielding.* Materials Science and Engineering: A, 1988. **103**(1): p. 15-28.
158. Yeni, Y.N. and D.P. Fyhrie, *A rate-dependent microcrack-bridging model that can explain the strain rate dependency of cortical bone apparent yield strength.* Journal of biomechanics, 2003. **36**(9): p. 1343-1353.
159. Nicolella, D.P., et al., *Ultrastructural characterization of damaged cortical bone using atomic force microscopy.* ASME-PUBLICATIONS-BED, 1999. **42**: p. 319-320.
160. Imbeni, V., et al., *The dentin–enamel junction and the fracture of human teeth.* Nature Materials, 2005. **4**: p. 229.
161. Nalla, R.K., J.J. Kruzic, and R.O. Ritchie, *On the origin of the toughness of mineralized tissue: microcracking or crack bridging?* Bone, 2004. **34**(5): p. 790-798.
162. Nalla, R., J. Kinney, and R. Ritchie, *Effect of orientation on the in vitro fracture toughness of dentin: the role of toughening mechanisms.* Biomaterials, 2003. **24**(22): p. 3955-3968.
163. Nikolov, S., et al., *Revealing the Design Principles of High-Performance Biological Composites Using Ab Initio and Multiscale Simulations: The Example of Lobster Cuticle.* Advanced Materials, 2010. **22**(4): p. 519-526.
164. Yao, H., et al., *Protection mechanisms of the iron-plated armor of a deep-sea hydrothermal vent gastropod.* Proceedings of the National Academy of Sciences, 2010. **107**(3): p. 987-992.
165. Checa, A.G., et al., *Crystallographic control on the substructure of nacre tablets.* Journal of Structural Biology, 2013. **183**(3): p. 368-376.
166. Mutvei, H. and E. Dunca, *Crystalline structure, orientation and nucleation of the nacreous tablets in the cephalopod Nautilus.* Paläontologische Zeitschrift, 2010. **84**(4): p. 457-465.
167. Habelitz, S., et al., *Mechanical properties of human dental enamel on the nanometre scale.* Archives of Oral Biology, 2001. **46**(2): p. 173-183.
168. Wolf, S.E., et al., *Nonclassical crystallization in vivo et in vitro (I): Process-structure-property relationships of nanogranular biominerals.* Journal of Structural Biology, 2016. **196**(2): p. 244-259.
169. Faber, K.T. and A.G. Evans, *Intergranular Crack-Deflection Toughening in Silicon Carbide.* Journal of the American Ceramic Society, 1983. **66**(6): p. C-94-C-95.
170. Antonakos, A., E. Liarokapis, and T. Leventouri, *Micro-Raman and FTIR studies of synthetic and natural apatites.* Biomaterials, 2007. **28**(19): p. 3043-3054.

171. Penel, G., et al., *Infrared and Raman microspectrometry study of fluor-fluor-hydroxy and hydroxy-apatite powders.* Journal of Materials Science: Materials in Medicine, 1997. **8**(5): p. 271-276.
172. Awonusi, A., M.D. Morris, and M.M. Tecklenburg, *Carbonate assignment and calibration in the Raman spectrum of apatite.* Calcified tissue international, 2007. **81**(1): p. 46-52.
173. Rehman, I., et al., *Structural evaluation of human and sheep bone and comparison with synthetic hydroxyapatite by FT-Raman spectroscopy.* Journal of Biomedical Materials Research Part A, 1995. **29**(10): p. 1287-1294.
174. Movasaghi, Z., S. Rehman, and I.U. Rehman, *Raman spectroscopy of biological tissues.* Applied Spectroscopy Reviews, 2007. **42**(5): p. 493-541.
175. Kumar, C.S., *Raman spectroscopy for nanomaterials characterization*. 2012: Springer Science & Business Media.
176. Faria, D.L.A.d., S.V. Silva, and M.T.d. Oliveira, *Raman microspectroscopy of some iron oxides and oxyhydroxides.* Journal of Raman Spectroscopy, 1997. **28**(11): p. 873-878.
177. Wilson, R.M., et al., *Rietveld refinements and spectroscopic studies of the structure of Ca-deficient apatite.* Biomaterials, 2005. **26**(11): p. 1317-1327.
178. Doyle, B.B., E. Bendit, and E.R. Blout, *Infrared spectroscopy of collagen and collagen-like polypeptides.* Biopolymers, 1975. **14**(5): p. 937-957.
179. Montel, G., et al., *New concepts in the composition, crystallization and growth of the mineral component of calcified tissues.* Journal of Crystal Growth, 1981. **53**(1): p. 74-99.
180. Elliott, J.C., Rev. Miner. and Geochem, 2002. **48**(427).
181. Pabisch, S., et al., *Imaging the nanostructure of bone and dentin through small-and wide-angle X-ray scattering*, in *Methods in enzymology*. 2013, Elsevier. p. 391-413.
182. Paris, O. and M. Müller, *Scanning X-ray microdiffraction of complex materials: diffraction geometry considerations.* Nuclear Instruments and Methods in Physics Research Section B: Beam Interactions with Materials and Atoms, 2003. **200**: p. 390-396.
183. Lange, C., et al., *Fetal and postnatal mouse bone tissue contains more calcium than is present in hydroxyapatite.* Journal of structural biology, 2011. **176**(2): p. 159-167.
184. Fischer, A., et al., *Structural purity of magnetite nanoparticles in magnetotactic bacteria.* Journal of The Royal Society Interface, 2011. **8**(60): p. 1011-1018.
185. Koenigswald, W.v., *The variability of the enamel structure at the dentition level.* Tooth Enamel Microstructure. Balkema, Rotterdam, 1997: p. 193-201.
186. Enax, J., et al., *Ultrastructural organization and micromechanical properties of shark tooth enameloid.* Acta biomaterialia, 2014. **10**(9): p. 3959-3968.
187. Prostak, K. and Z. Skobe, *Ultrastructure of the dental epithelium and odontoblasts during enameloid matrix deposition in cichlid teeth.* Journal of Morphology, 1986. **187**(2): p. 159-172.
188. Gantayat, S. and B. Patnaik, *Collagen characteristics of skin and muscle of the ageing teleost, Ophiocephalus punctatus.* Experimental gerontology, 1980. **15**(5): p. 373-387.
189. Prostak, K. and Z. Skobe, *Ultrastructure of the dental epithelium during enameloid mineralization in a teleost fish, Cichlasoma cyanoguttatum.* Archives of oral biology, 1986. **31**(2): p. 73-85.
190. Chen, C.L., et al., *Fluorine in Shark Teeth: Its Direct Atomic-Resolution Imaging and Strengthening Function.* Angewandte Chemie-International Edition, 2014. **53**(6): p. 1543-1547.
191. O'Shea, D.C., M.L. Bartlett, and R.A. Young, *Compositional analysis of apatites with Laser-Raman spectroscopy: (OH,F,Cl)apatites.* Archives of Oral Biology, 1974. **19**(11): p. 995-1006.
192. Freeman, J.J., et al., *Raman spectroscopic detection of changes in bioapatite in mouse femora as a function of age and in vitro fluoride treatment.* Calcified Tissue International, 2001. **68**(3): p. 156-162.
193. Wei, M., et al., *Synthesis and characterization of hydroxyapatite, fluoride-substituted hydroxyapatite and fluorapatite.* Journal of Materials Science-Materials in Medicine, 2003. **14**(4): p. 311-320.

194. Hanesch, M., *Raman spectroscopy of iron oxides and (oxy) hydroxides at low laser power and possible applications in environmental magnetic studies.* Geophysical Journal International, 2009. **177**(3): p. 941-948.
195. Gordon, L.M., et al., *Amorphous intergranular phases control the properties of rodent tooth enamel.* Science, 2015. **347**(6223): p. 746-750.
196. Madsen, M.B., et al., *A study of the sump beaver's dental enamel.* Hyperfine Interactions, 1986. **29**(1-4): p. 1431-1434.
197. LeGeros, R.Z., et al., *Synergistic Effects of Magnesium and Carbonate on Properties of Biological and Synthetic Apatites.* Connective Tissue Research, 1995. **33**(1-3): p. 203-209.
198. Pieters, I.Y., E.A.P. De Maeyer, and R.M.H. Verbeeck, *Influence of Na+ on the Stoichiometry of Carbonated Hydroxyapatite Obtained by the Hydrolysis of Octacalcium Phosphate.* Inorganic Chemistry, 1998. **37**(24): p. 6392-6395.
199. Brauer, D.S., et al., *Nano-and micromechanical properties of dentine: Investigation of differences with tooth side.* Journal of biomechanics, 2011. **44**(8): p. 1626-1629.
200. Meng, J., P. Zhang, and S. Wang, *Recent progress of abrasion-resistant materials: learning from nature.* Chemical Society Reviews, 2016. **45**(2): p. 237-251.
201. Amini, S. and A. Miserez, *Wear and abrasion resistance selection maps of biological materials.* Acta Biomaterialia, 2013. **9**(8): p. 7895-7907.
202. Chan, Y., A. Ngan, and N. King, *Nano-scale structure and mechanical properties of the human dentine–enamel junction.* Journal of the mechanical behavior of biomedical materials, 2011. **4**(5): p. 785-795.
203. Xu, H., et al., *Indentation damage and mechanical properties of human enamel and dentin.* Journal of Dental Research, 1998. **77**(3): p. 472-480.
204. He, L.H. and M.V. Swain, *Understanding the mechanical behaviour of human enamel from its structural and compositional characteristics.* Journal of the Mechanical Behavior of Biomedical Materials, 2008. **1**(1): p. 18-29.
205. Halgaš, R., et al., *Nanoindentation testing of human enamel and dentin.* Ceramics–Silikáty, 2013. **57**(2): p. 92-99.
206. Katti, K.S., B. Mohanty, and D.R. Katti, *Nanomechanical properties of nacre.* Journal of Materials Research, 2006. **21**(5): p. 1237-1242.
207. Li, X., et al., *Nanoscale structural and mechanical characterization of a natural nanocomposite material: the shell of red abalone.* Nano letters, 2004. **4**(4): p. 613-617.
208. Sarikaya, M., et al., *Mechanical Property-Microstructural Relationships in Abalone Shell.* MRS Online Proceedings Library, 1989. **174**: p. null-null.
209. Sarikaya, M., et al., *Mechanical property-microstructural relationships in abalone shell.* MRS Online Proceedings Library Archive, 1989. **174**.
210. Weimer, A.W., *Carbide, nitride and boride materials synthesis and processing*. 2012: Springer Science & Business Media.
211. Buschow, K.J., et al., *Encyclopedia of materials.* Science and technology, 2001. **1**: p. 11.
212. De With, G., *High temperature fracture of boron carbide: experiments and simple theoretical models.* Journal of materials science, 1984. **19**: p. 457-466.
213. Bajaj, D. and D.D. Arola, *On the R-curve behavior of human tooth enamel.* Biomaterials, 2009. **30**(23): p. 4037-4046.
214. Hu, J., et al., *Nanoindentation-Induced Pile-Up in the Residual Impression of Crystalline Cu with Different Grain Size.* Crystals, 2017. **8**(1): p. 9.
215. Oliver, W.C. and G.M. Pharr, *Measurement of hardness and elastic modulus by instrumented indentation: Advances in understanding and refinements to methodology.* Journal of materials research, 2004. **19**(1): p. 3-20.
216. McElhaney, K., J. Vlassak, and W. Nix, *Determination of indenter tip geometry and indentation contact area for depth-sensing indentation experiments.* Journal of Materials Research, 1998. **13**(5): p. 1300-1306.

217. Zhou, L. and Y. Yao, *Single crystal bulk material micro/nano indentation hardness testing by nanoindentation instrument and AFM.* Materials Science and Engineering: A, 2007. **460**: p. 95-100.
218. Massare, J.A., *Tooth morphology and prey preference of Mesozoic marine reptiles.* Journal of Vertebrate Paleontology, 1987. **7**(2): p. 121-137.
219. Evans, A.R. and G.D. Sanson, *The tooth of perfection: functional and spatial constraints on mammalian tooth shape.* Biological Journal of the Linnean Society, 2003. **78**(2): p. 173-191.
220. Evans, A. and G. Sanson, *The effect of tooth shape on the breakdown of insects.* Journal of Zoology, 1998. **246**(4): p. 391-400.
221. Lucas, P., *Basic principles of tooth design.* Teeth: form, function and evolution. New York: Columbia University Press. p, 1982: p. 154-162.
222. Crofts, S.B. and A.P. Summers, *How to best smash a snail: the effect of tooth shape on crushing load.* Journal of The Royal Society Interface, 2014. **11**(92).
223. Sriraman, K.R., S. Ganesh Sundara Raman, and S.K. Seshadri, *Influence of crystallite size on the hardness and fatigue life of steel samples coated with electrodeposited nanocrystalline Ni–W alloys.* Materials Letters, 2007. **61**(3): p. 715-718.
224. Eimar, H., et al., *Regulation of enamel hardness by its crystallographic dimensions.* Acta biomaterialia, 2012. **8**(9): p. 3400-3410.
225. Saber-Samandari, S. and K.A. Gross, *Micromechanical properties of single crystal hydroxyapatite by nanoindentation.* Acta Biomaterialia, 2009. **5**(6): p. 2206-2212.
226. Carnelli, D., et al., *Nanoindentation testing and finite element simulations of cortical bone allowing for anisotropic elastic and inelastic mechanical response.* Journal of Biomechanics, 2011. **44**(10): p. 1852-1858.
227. Carnelli, D., et al., *Orientation and size-dependent mechanical modulation within individual secondary osteons in cortical bone tissue*. Vol. 10. 2013.
228. Jeng, Y.-R., et al., *Human enamel rod presents anisotropic nanotribological properties.* Journal of the Mechanical Behavior of Biomedical Materials, 2011. **4**(4): p. 515-522.
229. Katz, J.L. and K. Ukraincik, *On the anisotropic elastic properties of hydroxyapatite.* Journal of Biomechanics. **4**(3): p. 221-227.
230. Cuy, J.L., et al., *Nanoindentation mapping of the mechanical properties of human molar tooth enamel.* Archives of Oral Biology, 2002. **47**(4): p. 281-291.
231. Braly, A., et al., *The effect of prism orientation on the indentation testing of human molar enamel.* Archives of oral biology, 2007. **52**(9): p. 856-860.
232. Davidson, C.L., I.S. Hoekstra, and J. Arends, *Microhardness of Sound, Decalcified and Etched Tooth Enamel Related to the Calcium Content.* Caries Research, 1974. **8**(2): p. 135-144.
233. Tabor, D., *Hardness Measurements with conical and pyramidal indenters.* The Hardness of Metals. Oxford University Press., Oxford, 1951: p. 95-113.
234. Vlassak, J.J. and W. Nix, *Measuring the elastic properties of anisotropic materials by means of indentation experiments.* Journal of the Mechanics and Physics of Solids, 1994. **42**(8): p. 1223-1245.
235. Buehler, M.J. and S.Y. Wong, *Entropic elasticity controls nanomechanics of single tropocollagen molecules.* Biophysical journal, 2007. **93**(1): p. 37-43.
236. Buehler, M.J., S. Keten, and T. Ackbarow, *Theoretical and computational hierarchical nanomechanics of protein materials: Deformation and fracture.* Progress in Materials Science, 2008. **53**(8): p. 1101-1241.
237. Chen, P.-Y., et al., *Structure and mechanical properties of selected biological materials.* Journal of the Mechanical Behavior of Biomedical Materials, 2008. **1**(3): p. 208-226.
238. Kolednik, O., et al., *Bioinspired Design Criteria for Damage-Resistant Materials with Periodically Varying Microstructure.* Advanced Functional Materials, 2011. **21**(19): p. 3634-3641.
239. Ji, B., *A study of the interface strength between protein and mineral in biological materials.* Journal of biomechanics, 2008. **41**(2): p. 259-266.

240. Gao, H., et al., *Flaw tolerant nanostructures of biological materials*, in *Mechanics of the 21st Century*. 2005, Springer. p. 131-138.
241. Gao, H., et al., *Materials become insensitive to flaws at nanoscale: Lessons from nature.* Proceedings of the National Academy of Sciences, 2003. **100**(10): p. 5597-5600.
242. Preuschoft, H., W.-E. Reif, and W.H. Müller, *Funktionsanpassungen in form und struktur an haifischzähnen.* Anatomy and Embryology, 1974. **143**(3): p. 315-344.
243. Gaspard, D. and J. Nouet, *Hierarchical architecture of the inner layers of selected extant rhynchonelliform brachiopods.* Journal of Structural Biology, 2016. **196**(2): p. 197-205.
244. Nalla, R., J. Kinney, and R. Ritchie, *On the fracture of human dentin: Is it stress-or strain-controlled?* Journal of Biomedical Materials Research Part A, 2003. **67**(2): p. 484-495.
245. Currey, J., K. Brear, and P. Zioupos, *Dependence of mechanical properties on fibre angle in narwhal tusk, a highly oriented biological composite.* Journal of biomechanics, 1994. **27**(7): p. 885891-889897.
246. Break, K., et al., *The mechanical properties of the dentine and cement of the tusk of the narwhal Monodon monoceros compared with those of other mineralized tissues.* Archives of oral biology, 1990. **35**(8): p. 615-621.
247. Currey, J.D., *The effect of porosity and mineral content on the Young's modulus of elasticity of compact bone.* Journal of biomechanics, 1988. **21**(2): p. 131-139.
248. Brunet, F., et al., *Compressibility and thermal expansivity of synthetic apatites, Ca 5 (PO 4) 3 X with X= OH, F and Cl.* European Journal of Mineralogy, 1999. **11**(6): p. 1023-1035.
249. Dötsch, C. and W. Von Koenigswald, *Zur rotfärbung von soricidenzähnen.* Zeitschrift für Säugertierkunden, 1978. **43**: p. 65-70.
250. Heap, P., et al., *An analytical ultrastructural study of the iron-rich surface layer in rat-incisor enamel.* Archives of oral biology, 1983. **28**(3): p. 195-200.
251. Churchfield, S., *The natural history of shrews*. 1990: Cornell University Press.
252. Shellis, R. and B. Berkovitz, *Observations on the dental anatomy of piranhas (Characidae) with special reference to tooth structure.* Journal of Zoology, 1976. **180**(1): p. 69-84.
253. Amini, S., et al., *The role of quasi-plasticity in the extreme contact damage tolerance of the stomatopod dactyl club.* Nature Materials, 2015. **14**(9): p. 943-+.
254. Amini, S., et al., *Textured fluorapatite bonded to calcium sulphate strengthen stomatopod raptorial appendages.* Nature Communications, 2014. **5**.
255. Simha, N.K., et al., *Inhomogeneity effects on the crack driving force in elastic and elastic–plastic materials.* Journal of the Mechanics and Physics of Solids, 2003. **51**(1): p. 209-240.
256. Fischer, F., et al., *Semi-analytical approaches to assess the crack driving force in periodically heterogeneous elastic materials.* International journal of fracture, 2012. **173**(1): p. 57-70.
257. Kolednik, O., et al., *Improvements of strength and fracture resistance by spatial material property variations.* Acta Materialia, 2014. **68**: p. 279-294.
258. Fratzl, P., et al., *Hindered Crack Propagation in Materials with Periodically Varying Young's Modulus—Lessons from Biological Materials.* Advanced Materials, 2007. **19**(18): p. 2657-2661.
259. Kolednik, O., et al., *Improvements of strength and fracture resistance by spatial material property variations.* Acta Materialia, 2014. **68**(Supplement C): p. 279-294.
260. Sistaninia, M. and O. Kolednik, *Effect of a single soft interlayer on the crack driving force.* Engineering Fracture Mechanics, 2014. **130**(Supplement C): p. 21-41.
261. Suresh, S., A.E. Giannakopoulos, and J. Alcalá, *Spherical indentation of compositionally graded materials: Theory and experiments.* Acta Materialia, 1997. **45**(4): p. 1307-1321.
262. Kim, A.S., J. Besson, and A. Pineau, *Global and local approaches to fracture normal to interfaces.* International Journal of Solids and Structures, 1999. **36**(12): p. 1845-1864.
263. Giannakopoulos, A.E., et al., *Elastoplastic analysis of thermal cycling: layered materials with compositional gradients.* Acta Metallurgica et Materialia, 1995. **43**(4): p. 1335-1354.
264. Giannakopoulos, A.E. and S. Suresh, *Indentation of solids with gradients in elastic properties: Part I. Point force.* International Journal of Solids and Structures, 1997. **34**(19): p. 2357-2392.

265. Choi, I.S., M. Dao, and S. Suresh, *Mechanics of indentation of plastically graded materials—I: Analysis.* Journal of the Mechanics and Physics of Solids, 2008. **56**(1): p. 157-171.
266. Suresh, S., *Graded Materials for Resistance to Contact Deformation and Damage.* Science, 2001. **292**(5526): p. 2447-2451.
267. Naleway, S.E., et al., *Structural design elements in biological materials: application to bioinspiration.* Advanced Materials, 2015. **27**(37): p. 5455-5476.
268. Bechtle, S., et al., *Crack arrest within teeth at the dentinoenamel junction caused by elastic modulus mismatch.* Biomaterials, 2010. **31**(14): p. 4238-4247.
269. Miserez, A., et al., *The Transition from Stiff to Compliant Materials in Squid Beaks.* Science, 2008. **319**(5871): p. 1816-1819.
270. Bigi, A., et al., *Morphosynthesis of Octacalcium Phosphate Hollow Microspheres by Polyelectrolyte-Mediated Crystallization.* Angewandte Chemie International Edition, 2002. **41**(12): p. 2163-2166.
271. Kato, T., A. Sugawara, and N. Hosoda, *Calcium Carbonate–Organic Hybrid Materials.* Advanced Materials, 2002. **14**(12): p. 869-877.
272. Yu, S.-H. and H. Colfen, *Bio-inspired crystal morphogenesis by hydrophilic polymers.* Journal of Materials Chemistry, 2004. **14**(14): p. 2124-2147.
273. Yu, S.-H., et al., *Complex Spherical BaCO3 Superstructures Self-Assembled by a Facile Mineralization Process under Control of Simple Polyelectrolytes.* Crystal Growth & Design, 2003. **4**(1): p. 33-37.
274. Meldrum, F.C. and H. Cölfen, *Controlling Mineral Morphologies and Structures in Biological and Synthetic Systems.* Chemical Reviews, 2008. **108**(11): p. 4332-4432.
275. Cölfen, H., in *Topics in Current Chemistry*. 2007, Springer. p. 271.
276. Nudelman, F., et al., *The role of collagen in bone apatite formation in the presence of hydroxyapatite nucleation inhibitors.* Nat Mater, 2010. **9**(12): p. 1004-1009.
277. Wang, Y., et al., *The predominant role of collagen in the nucleation, growth, structure and orientation of bone apatite.* Nat Mater, 2012. **11**(8): p. 724-733.
278. Kniep, R. and P. Simon, *Fluorapatite-Gelatine-Nanocomposites: Self-Organized Morphogenesis, Real Structure and Relations to Natural Hard Materials*, in *Biomineralization I*, K. Naka, Editor. 2007, Springer Berlin Heidelberg. p. 73-125.
279. H. Cölfen, M.A., *Mesocrystals and Nonclassical Crystallization*. 2008: Wiley.
280. Šupová, M., *Substituted hydroxyapatites for biomedical applications: A review.* Ceramics International, 2015. **41**(8): p. 9203-9231.
281. Cabrera, W.E., et al., *Strontium and Bone.* Journal of Bone and Mineral Research, 1999. **14**(5): p. 661-668.
282. Schumacher, M., et al., *A novel and easy-to-prepare strontium(II) modified calcium phosphate bone cement with enhanced mechanical properties.* Acta Biomaterialia, 2013. **9**(7): p. 7536-7544.
283. Capuccini, C., et al., *Interaction of Sr-doped hydroxyapatite nanocrystals with osteoclast and osteoblast-like cells.* Journal of Biomedical Materials Research Part A, 2009. **89A**(3): p. 594-600.
284. Li, Z.Y., et al., *Chemical composition, crystal size and lattice structural changes after incorporation of strontium into biomimetic apatite.* Biomaterials, 2007. **28**(7): p. 1452-1460.
285. Grynpas, M.D. and P.J. Marie, *Effects of low doses of strontium on bone quality and quantity in rats.* Bone, 1990. **11**(5): p. 313-319.
286. Aaseth, J., G. Boivin, and O. Andersen, *Osteoporosis and trace elements – An overview.* Journal of Trace Elements in Medicine and Biology, 2012. **26**(2): p. 149-152.
287. Terra, J., et al., *The structure of strontium-doped hydroxyapatite: an experimental and theoretical study.* Physical Chemistry Chemical Physics, 2009. **11**(3): p. 568-577.
288. Zeglinski, J., et al., *Unravelling the specific site preference in doping of calcium hydroxyapatite with strontium from ab initio investigations and Rietveld analyses.* Physical Chemistry Chemical Physics, 2012. **14**(10): p. 3435-3443.

289. Simon, P., et al., *Embryonic States of Fluorapatite–Gelatine Nanocomposites and Their Intrinsic Electric-Field-Driven Morphogenesis: The Missing Link on the Way from Atomistic Simulations to Pattern Formation on the Mesoscale.* Advanced Functional Materials, 2009. **19**(22): p. 3596-3603.
290. Rosseeva, E.V., et al., *Synthesis, Characterization, and Morphogenesis of Carbonated Fluorapatite−Gelatine Nanocomposites: A Complex Biomimetic Approach toward the Mineralization of Hard Tissues.* Chemistry of Materials, 2008. **20**(19): p. 6003-6013.
291. Sturm, E.V. and H. Cölfen, *Mesocrystals: structural and morphogenetic aspects.* Chemical Society Reviews, 2016. **45**(21): p. 5821-5833.
292. Wilson, R.M., J.C. Elliott, and S.E.P. Dowker, *Rietveld refinement of the crystallographic structure of human dental enamel apatites*, in *American Mineralogist*. 1999. p. 1406.
293. De Maeyer, E.A., R.M. Verbeeck, and D.E. Naessens, *Stoichiometry of sodium (+)-and carbonate-containing apatites obtained by hydrolysis of monetite.* Inorganic Chemistry, 1993. **32**(25): p. 5709-5714.
294. Hughes, J.M., M. Cameron, and K.D. Crowley, *Ordering of Divalent-Cations in the Apatite Structure - Crystal-Structure Refinements of Natural Mn-Bearing and Sr-Bearing Apatite.* American Mineralogist, 1991. **76**(11-12): p. 1857-1862.
295. White, T.J. and D. ZhiLi, *Structural derivation and crystal chemistry of apatites.* Acta Crystallographica Section B, 2003. **59**(1): p. 1-16.
296. Rakovan, J.F. and J.M. Hughes, *Strontium in the apatite structure: Strontian fluorapatite and belovite-(Ce).* Canadian Mineralogist, 2000. **38**: p. 839-845.
297. Swafford, S.H. and E.M. Holt, *New synthetic approaches to monophosphate fluoride ceramics: synthesis and structural characterization of Na2Mg(PO4)F and Sr5(PO4)3F.* Solid State Sciences, 2002. **4**(6): p. 807-812.
298. Michie, E.M., et al., *Predicted energies and structures associated with the mixed calcium strontium fluorapatites.* Journal of Solid State Chemistry, 2008. **181**(12): p. 3287-3293.
299. Goryaeva, A., V. Urusov, and N. Eremin, *Atomistic computer modeling of the local structure and mixing properties of Sr-bearing fluorapatite.* Moscow University Geology Bulletin, 2013. **68**(6): p. 368.
300. Goryaeva, A.M., V.S. Urusov, and N.N. Eremin, *Atomistic simulations of mixing properties and the local structure of the (Ca, Sr)(10)[PO4](6)F-2 solid solution.* European Journal of Mineralogy, 2013. **25**(6): p. 947-955.
301. Camacho, N.P., et al., *FTIR microscopic imaging of collagen and proteoglycan in bovine cartilage.* Biopolymers, 2001. **62**(1): p. 1-8.
302. Rygula, A., et al., *Raman spectroscopy of proteins: a review.* Journal of Raman Spectroscopy, 2013. **44**(8): p. 1061-1076.
303. Lide, D.R., *CRC handbook of chemistry and physics.* 12J204, 2012.
304. Pan, H.B., et al., *Solubility of strontium-substituted apatite by solid titration.* Acta Biomaterialia, 2009. **5**(5): p. 1678-1685.
305. Bigi, A., et al., *Strontium-substituted hydroxyapatite nanocrystals.* Inorganica Chimica Acta, 2007. **360**(3): p. 1009-1016.
306. Busch, S., et al., *Biomimetic morphogenesis of fluorapatite-gelatin composites: Fractal growth, the question of intrinsic electric fields, core/shell assemblies, hollow spheres and reorganization of denatured collagen.* European Journal of Inorganic Chemistry, 1999(10): p. 1643-1653.
307. Kniep, R. and S. Busch, *Biomimetic growth and self-assembly of fluorapatite aggregates by diffusion into denatured collagen matrices.* Angewandte Chemie-International Edition in English, 1996. **35**(22): p. 2624-2626.
308. Harald, T., et al., *Biomimetische Fluorapatit-Gelatine-Nanokomposite: Vorstrukturierung von Gelatine-Matrices durch Ionenimprägnierung und Auswirkungen auf die Formentwicklung.* Angewandte Chemie, 2006. **118**(12): p. 1939-1944.
309. Shtukenberg, A.G., et al., *Spherulites.* Chemical Reviews, 2012. **112**(3): p. 1805-1838.

310. Tlatlik, H., et al., *Biomimetic fluorapatite-gelatine nanocomposites: Pre-structuring of gelatine matrices by ion impregnation and its effect on form development.* Angewandte Chemie-International Edition, 2006. **45**(12): p. 1905-1910.
311. Kawska, A., et al., *The Nucleation Mechanism of Fluorapatite–Collagen Composites: Ion Association and Motif Control by Collagen Proteins.* Angewandte Chemie International Edition, 2008. **47**(27): p. 4982-4985.
312. Kniep, R. and P. Simon, *Fluorapatite-gelatine-nanocomposites: Self-organized morphogenesis, real structure and relations to natural hard materials.* Biomineralization I: Crystallization and Self-Organization Process, 2007. **270**: p. 73-125.
313. Rosseeva, E., P. Simon, and R. Kniep, *Crystal Branching and Spherulite Formation: Similar Shapes↔ Different Mechanisms.* Scientific Reports of Max-Planck-Institute for Chemical Physics of Solids, 2009: p. 181-185.
314. Damien, C.J. and J.R. Parsons, *Bone graft and bone graft substitutes: a review of current technology and applications.* Journal of Applied Biomaterials, 1991. **2**(3): p. 187-208.
315. Witte, F., *Reprint of: The history of biodegradable magnesium implants: A review.* Acta Biomaterialia, 2015. **23**: p. S28-S40.
316. Witte, F., *The history of biodegradable magnesium implants: A review.* Acta Biomaterialia, 2010. **6**(5): p. 1680-1692.
317. Van der Stok, J., et al., *Bone substitutes in the Netherlands – A systematic literature review.* Acta Biomaterialia, 2011. **7**(2): p. 739-750.
318. García-Gareta, E., M.J. Coathup, and G.W. Blunn, *Osteoinduction of bone grafting materials for bone repair and regeneration.* Bone, 2015. **81**: p. 112-121.
319. Dziadek, M., E. Stodolak-Zych, and K. Cholewa-Kowalska, *Biodegradable ceramic-polymer composites for biomedical applications: A review.* Materials Science and Engineering: C, 2017. **71**: p. 1175-1191.
320. Tajbakhsh, S. and F. Hajiali, *A comprehensive study on the fabrication and properties of biocomposites of poly(lactic acid)/ceramics for bone tissue engineering.* Materials Science and Engineering: C, 2017. **70**: p. 897-912.
321. O'Neill, R., et al., *Critical review: Injectability of calcium phosphate pastes and cements.* Acta Biomaterialia, 2017. **50**: p. 1-19.
322. Matthias Epple, E.B., *Handbook of Biomineralization*. 2007: WILEY-VCH.
323. B.D.Ratner, S.J.B., *Biomaterials: Where We Have Been and Where We Are Going.* Annu. Rev.Biomed.Eng. , 2004. **6**: p. 41-75.
324. B.D.Ratner, S.J.B., *New Ideas in Biomaterials Science - A Path to Engineered Biomaterials.* Journal of Biomedical Materials Research, 1993. **27**: p. 837-850.
325. S.-M Kim, J.-H.J., S.-M.Lee, M.-H.Kang, H.-E.Kim, Y.Estrin, J.-H.Lee, J.-W.Lee, Y.-H.Koh, *Hydroxyapatite-coated magnesium implants with improved in vitro and in vivo biocorrosion, biocompatibility, and bone response.* J. Biomater. Res. A, 2013.
326. Wirtz, T.P., *Herstellung von Knochenimplantaten aus Titanwerkstoffen durch Laserformen*, in *Fakultät für Maschinenwesen*. 2005, Rheinisch-Westfälischen Technischen Hochschule Aachen.
327. J.F.Keating, M.M.M., *Substitutes for Autologous Bone Graft in Orthopaedic Trauma.* The Journal of Bone & Joint Surgery, 2001. **83-B**(1): p. 3-8.
328. M.Kurtz, S., *PEEK Biomaterials Handbook*. 2011: William Andrew.
329. W.-T.Lee, J.-Y.K., Y.-J.Lim, S.-K.Kim, H.-B.Kwon, M.-J. Kim, *Stress shielding and fatigue limits of poly-ether-ether-ketone dental implants.* J. Biomed. Mater. Res. Part B, 2012. **100B**: p. 1044-1052.
330. D.A.Puleo, A.N., *Understanding and controlling the bone-implant interface.* Biomaterials, 1999. **20**: p. 2311-2321.
331. Y.Förster, C.R., W.Schneiders, R.Bernhardt, J.C.Simon, H.Worch, S.Rammelt, *Surface modification of implants in long bone.* Biomatter, 2012. **2**(3): p. 149-157.

332. C.Morrison, R.M., C.MacDonald, A.Wykman, I.Goldie, M.H.Grant, *In vitro biocompatibility testing of polymers for orthopaedic implants using cultured fibroblasts and osteoblasts.* Biomaterials, 1995. **16**: p. 987-992.
333. Ziats, N.P., K.M. Miller, and J.M. Anderson, *In vitro and in vivo interactions of cells with biomaterials.* Biomaterials, 1988. **9**(1): p. 5-13.
334. Davies, J., *In vitro modeling of the bone/implant interface.* The Anatomical Record, 1996. **245**(2): p. 426-445.
335. Duplomb, L., et al., *Concise Review: Embryonic Stem Cells: A New Tool to Study Osteoblast and Osteoclast Differentiation.* STEM CELLS, 2007. **25**(3): p. 544-552.
336. Harvey, A.G., E.W. Hill, and A. Bayat, *Designing implant surface topography for improved biocompatibility.* Expert review of medical devices, 2013. **10**(2): p. 257-267.
337. Yao, X., R. Peng, and J. Ding, *Cell–material interactions revealed via material techniques of surface patterning.* Advanced materials, 2013. **25**(37): p. 5257-5286.
338. Liu, X. and S. Wang, *Three-dimensional nano-biointerface as a new platform for guiding cell fate.* Chemical Society Reviews, 2014. **43**(8): p. 2385-2401.
339. Williams, D.F., *On the mechanisms of biocompatibility.* Biomaterials, 2008. **29**(20): p. 2941-2953.
340. A.S.Hoffman, *Surface Modification of Polymers: Physical, Chemical, Mechanical and Biological Methods.* Macromol. Symp., 1996. **101**: p. 443-454.
341. P.Laurens, B.S., F.Decobert, F.Arefi, J.Amouroux, *Modifications of polyether-etherketone surface after 193 nm and 248 nm excimer laser radiation.* Applied Surface Science, 1999(93-96): p. 138-139.
342. Kim Shyong Siow, L.B., Sunil Kumar, Hans J.Griesser, *Plasma Methods for the Generation of Chemically Reactive Surfaces for Biomolecule Immobilization and Cell Colonization.* Plasma Process. Polym., 2006. **3**: p. 392-418.
343. N.Inagaki, S.T., T.Horiuchi, R.Suyama, *Surface Modification of Poly (aryl ether ether ketone) Film by Remote Oxygen Plasma.* Journal of Applied Polymer Science, 1998. **68**: p. 271-279.
344. C.-M.Chan, T.-M.K., H.Hiraoka, *Polymer surface modification by plamas and photons.* Surface Science Reports, 1996. **24**: p. 1-54.
345. K.Duan, R.W., *Surface modifications of bone implants through wet chemisty.* Journal of Materials Chemistry, 2006. **16**: p. 2309-2321.
346. O.Noiset, Y.-J.S., J.Marchand-Brynaert, *Fibronectin adsorption or/and covalent grafting on chemically modified PEEK film surfaces.* J. Biomater.Sci.Polymer Edn, 1999. **10**(6): p. 657-677.
347. S.M.Kurtz, J.N.D., *PEEK Biomaterials in Trauma, Orthopedic, and Spinal Implants.* Biomaterials, 2008. **28**(32): p. 4845-4869.
348. Wang, H., et al., *Mechanical and biological characteristics of diamond-like carbon coated poly aryl-ether-ether-ketone.* Biomaterials, 2010. **31**(32): p. 8181-8187.
349. Jackson, S. *First Use of Laser-Sintered PEEK for Craniofacial Implants*. 2011 20.6.2013]; Available from: http://news.thomasnet.com/companystory/First-Use-of-Laser-Sintered-PEEK-for-Craniofacial-Implants-843325.
350. Lethaus, B., et al., *A treatment algorithm for patients with large skull bone defects and first results.* Journal of Cranio-Maxillo-Facial Surgery, 2011. **39**(6): p. 435-440.
351. Kurtz, S.M. and J.N. Devine, *PEEK biomaterials in trauma, orthopedic, and spinal implants.* Biomaterials, 2007. **28**(32): p. 4845-4869.
352. Godara, A., D. Raabe, and S. Green, *The influence of sterilization processes on the micromechanical properties of carbon fiber-reinforced PEEK composites for bone implant applications.* Acta Biomaterialia, 2007. **3**(2): p. 209-220.
353. Wenz, L., et al., *In vitro biocompatibility of polyetheretherketone and polysulfone composites.* Journal of Biomedical Materials Research Part A, 1990. **24**(2): p. 207-215.
354. Rivard, C.H., S. Rhalmi, and C. Coillard, *In vivo biocompatibility testing of peek polymer for a spinal implant system: a study in rabbits.* Journal of Biomedical Materials Research Part A, 2002. **62**(4): p. 488-498.

355. Nieminen, T., et al., *Amorphous and crystalline polyetheretherketone: Mechanical properties and tissue reactions during a 3-year follow-up.* Journal of Biomedical Materials Research Part A, 2008. **84A**(2): p. 377-383.
356. Katzer, A., et al., *Polyetheretherketone—cytotoxicity and mutagenicity in vitro.* Biomaterials, 2002. **23**(8): p. 1749-1759.
357. Ma, R. and T. Tang, *Current Strategies to Improve the Bioactivity of PEEK.* International Journal of Molecular Sciences, 2014. **15**(4): p. 5426-5445.
358. Kurtz, S.M., *PEEK Biomaterials Handbook*. 2011: Elsevier.
359. Cölfen, H., L. Tian, and J. Knaus, *Material für knochenimplantate und verfahren zu dessen herstellung*. 2016, Google Patents.
360. Knaus, J., *Surface-modification of PEEK-implant Material*. 2013, University of Konstanz: Konstanz.
361. Herrod-Taylor, A., *The Crystallisation of Poly (Aryl Ether Ether Ketone) (PEEK) and its Carbon Fibre Composites*, in *School of Metallurgy and Materials*

College of Engineering and Physical Sciences. 2011, University of Birmingham. p. 135.
362. C.J.Wolf, J.A.B., M.A.Grayson, D.P.Anderson, *Solvent-induced crystallinity in poly(aryl-ether-ether-ketone).* Journal of Polymer Science Part B: Polymer Physics, 1992. **30**(3): p. 251-257.
363. Perng, L.H., C.J. Tsai, and Y.C. Ling, *Mechanism and kinetic modelling of PEEK pyrolysis by TG/MS.* Polymer, 1999. **40**(26): p. 7321-7329.
364. Salin, I.M. and J.C. Seferis, *Kinetic analysis of high-resolution TGA variable heating rate data.* Journal of Applied Polymer Science, 1993. **47**(5): p. 847-856.
365. Patel, P., et al., *Investigation of the thermal decomposition and flammability of PEEK and its carbon and glass-fibre composites.* Polymer Degradation and Stability, 2011. **96**(1): p. 12-22.
366. Patel, P., et al., *Mechanism of thermal decomposition of poly(ether ether ketone) (PEEK) from a review of decomposition studies.* Polymer Degradation and Stability, 2010. **95**(5): p. 709-718.
367. Hallab, N.J., et al., *Evaluation of metallic and polymeric biomaterial surface energy and surface roughness characteristics for directed cell adhesion.* Tissue engineering, 2001. **7**(1): p. 55-71.
368. Shen, H., et al., *Combining oxygen plasma treatment with anchorage of cationized gelatin for enhancing cell affinity of poly (lactide-co-glycolide).* Biomaterials, 2007. **28**(29): p. 4219-4230.
369. Harnett, E.M., J. Alderman, and T. Wood, *The surface energy of various biomaterials coated with adhesion molecules used in cell culture.* Colloids and Surfaces B: Biointerfaces, 2007. **55**(1): p. 90-97.
370. Van der Valk, P., et al., *Interaction of fibroblasts and polymer surfaces: relationship between surface free energy and fibroblast spreading.* Journal of Biomedical Materials Research Part A, 1983. **17**(5): p. 807-817.
371. Kang, I.K., et al., *Attachment and growth of fibroblast cells on polypeptide derivatives.* Journal of Biomedical Materials Research Part A, 1989. **23**(2): p. 223-239.
372. Tamada, Y. and Y. Ikada, *Fibroblast growth on polymer surfaces and biosynthesis of collagen.* Journal of Biomedical Materials Research Part A, 1994. **28**(7): p. 783-789.
373. Kennedy, S.B., et al., *Combinatorial screen of the effect of surface energy on fibronectin-mediated osteoblast adhesion, spreading and proliferation.* Biomaterials, 2006. **27**(20): p. 3817-3824.
374. Van Wachem, P., et al., *Adhesion of cultured human endothelial cells onto methacrylate polymers with varying surface wettability and charge.* Biomaterials, 1987. **8**(5): p. 323-328.
375. Vogler, E.A., *Water and the acute biological response to surfaces.* Journal of Biomaterials Science, Polymer Edition, 1999. **10**(10): p. 1015-1045.
376. Zhang, Y., et al., *Analysis of the cytotoxicity of differentially sized titanium dioxide nanoparticles in murine MC3T3-E1 preosteoblasts.* Journal of Materials Science: Materials in Medicine, 2011. **22**(8): p. 1933-1945.

377. Damoulis, P.D. and P.V. Hauschka, *Nitric Oxide Acts in Conjunction with Proinflammatory Cytokines to Promote Cell Death in Osteoblasts.* Journal of Bone and Mineral Research, 1997. **12**(3): p. 412-422.
378. Lee, K.-H. and E.-M. Choi, *Myricetin, a naturally occurring flavonoid, prevents 2-deoxy-d-ribose induced dysfunction and oxidative damage in osteoblastic MC3T3-E1 cells.* European Journal of Pharmacology, 2008. **591**(1): p. 1-6.
379. Webb, K., V. Hlady, and P.A. Tresco, *Relative importance of surface wettability and charged functional groups on NIH 3T3 fibroblast attachment, spreading, and cytoskeletal organization.* Journal of biomedical materials research, 1998. **41**(3): p. 422-430.
380. Ciapetti, G., et al., *In vitro evaluation of cell/biomaterial interaction by MTT assay.* Biomaterials, 1993. **14**(5): p. 359-364.
381. Green, L.M., J.L. Reade, and C.F. Ware, *Rapid colormetric assay for cell viability: application to the quantitation of cytotoxic and growth inhibitory lymphokines.* Journal of immunological methods, 1984. **70**(2): p. 257-268.
382. Owen, T.A., et al., *Progressive development of the rat osteoblast phenotype in vitro: reciprocal relationships in expression of genes associated with osteoblast proliferation and differentiation during formation of the bone extracellular matrix.* Journal of cellular physiology, 1990. **143**(3): p. 420-430.
383. Lian, J.B., et al., *Transcriptional control of osteoblast differentiation*. 1998, Portland Press Limited.
384. Quarles, L.D., et al., *Distinct proliferative and differentiated stages of murine MC3T3-E1 cells in culture: An in vitro model of osteoblast development.* Journal of Bone and Mineral Research, 1992. **7**(6): p. 683-692.
385. Shu, R., et al., *Hydroxyapatite accelerates differentiation and suppresses growth of MC3T3-E1 osteoblasts.* Journal of Biomedical Materials Research Part A, 2003. **67**(4): p. 1196-1204.
386. Bächle, M. and R.J. Kohal, *A systematic review of the influence of different titanium surfaces on proliferation, differentiation and protein synthesis of osteoblast-like MG63 cells.* Clinical Oral Implants Research, 2004. **15**(6): p. 683-692.
387. Webb, K., V. Hlady, and P.A. Tresco, *Relationships among cell attachment, spreading, cytoskeletal organization, and migration rate for anchorage-dependent cells on model surfaces.* Journal of biomedical materials research, 2000. **49**(3): p. 362.
388. Schneider, G.B., et al., *The effect of hydrogel charge density on cell attachment.* Biomaterials, 2004. **25**(15): p. 3023-3028.
389. Oliver, W.C. and G.M. Pharr, *An improved technique for determining hardness and elastic modulus using load and displacement sensing indentation experiments.* Journal of materials research, 1992. **7**(6): p. 1564-1583.
390. Hammersley, A., *FIT2D: a multi-purpose data reduction, analysis and visualization program.* Journal of Applied Crystallography, 2016. **49**(2): p. 646-652.
391. Owens, D.K. and R. Wendt, *Estimation of the surface free energy of polymers.* Journal of applied polymer science, 1969. **13**(8): p. 1741-1747.
392. Kaelble, D., *Dispersion-polar surface tension properties of organic solids.* The Journal of Adhesion, 1970. **2**(2): p. 66-81.